

Low Temperature Metallization for Silicon Solar Cells

Dissertation
zur Erlangung des Grades

"Doktor der Naturwissenschaften"

im Promotionsfach Chemie
am Fachbereich Chemie, Pharmazie und
Geowissenschaften
der Johannes Gutenberg-Universität
in Mainz

Aline Gautrein
geb. in Wadern

Mainz, 2015

Erster Berichterstatter:

Zweiter Berichterstatter:

Datum der mündlichen Prüfung: 22.09.2015

Für meine Familie

Erklärung

Die vorliegende Arbeit wurde in der Zeit von Januar 2011 bis Juni 2015 unter Anleitung von (Name gestrichen wegen Datenschutz), Johannes Gutenberg Universität Mainz, Institut für Anorganische und Analytische Chemie und (Name gestrichen wegen Datenschutz) vom Fraunhofer Institut am Fraunhofer Institut für Solare Energiesysteme, Bereich Silizium Solarzellen - Entwicklung und Charakterisierung, in Freiburg angefertigt.

Ich erkläre hiermit, dass ich die vorliegende Arbeit selbständig und ohne fremde Hilfe verfasst habe. Alle verwendeten Quellen und Hilfsmittel sind vollständig angegeben.

Freiburg, 22.09.2015
Aline Gautrein

Contents

Contents	i
Abstract	vii
Deutsche Zusammenfassung	ix
Nomenclature	xi
List of Figures	xv
List of Tables	xxi
1 Introduction	1
1.1 Motivation	1
1.2 Scientific relevance of the approach	4
1.2.1 State of the art	4
1.2.2 New metallization concepts evaluated in this work	7
1.3 Outline	8
2 Theoretical Background	9
2.1 Silicon Solar Cells	9
2.1.1 Basic principles and loss mechanisms	9
2.1.2 Two-Diode Model	14
2.1.3 Series resistance and metallization induced losses	15
.	15
2.2 Metal-semiconductor contact	17
2.2.1 Schottky contact	18
2.2.2 Ohmic contact	20
2.2.3 Printed and fired contacts	23
2.2.4 Present contact model	24
2.3 Production prozess of crytsalline silicon solar cells . .	30
2.4 Nanoparticles, particle sintering and stabilization . . .	31

2.4.1	Nanoparticles	31
2.4.2	Nanoparticle synthesis	33
2.4.3	Particle sintering and stabilization	35
2.4.4	Thermal sintering	39
2.4.5	Chemical sintering	39
2.4.6	Other sintering methods	41
2.4.7	Comparison with liquid phase sintering	43
2.5	Hetero junction with Intrinsic Thin Layer Cells	45
2.5.1	Working principle	45
2.5.2	Challenges of metallization	47
2.6	Transparent Conductive Oxides - TCOs	48
2.6.1	General overview	48
2.6.2	Working principle	50
2.6.3	Indium Tin Oxide	52
2.6.4	Other TCOs	55
2.7	Surface energy and work of adhesion	56
3	Metallization Techniques	61
3.1	General demands on metallization for solar cells	61
3.2	Printing techniques	62
3.2.1	Screen printing	62
3.2.2	Aerosol jet printing	64
3.2.3	Ink jet printing	65
3.3	Plating techniques	66
3.3.1	Basic principles	67
3.3.2	Electroplating	68
3.3.3	Electroless plating	68
3.3.4	Light induced plating (LIP)	69
3.4	Temperature sensitive cell concepts	71
3.4.1	Sputtering and thermal evaporation	71
3.4.2	Direct plating	73
3.4.3	Seed-and-plate	73
3.5	Printed metal inks and pastes	74
4	Characterization Methods	77
4.1	I-V Curve	78
4.1.1	Dark I-V curve	78
4.1.2	Illuminated I-V Curve	79
4.2	I_{SC} - V_{OC} characteristics - $SunV_{OC}$ measurement	81

4.3	Four point probe measurement	82
4.3.1	Line resistance	83
4.3.2	Contact resistance measurement	84
4.4	Thermal gravimetric-differential scanning analysis - TG-DSC	90
4.5	Determination of sintering temperature	92
4.6	Cross section preparation	92
4.7	SEM/EDX and FIB	92
4.8	Confocal microscope	93
4.9	Electroluminescenz measurement	94
4.10	Cyclic voltammetry	95
4.11	Tape test	96
4.12	Goniometer measurements	96
5	Nanoparticle based Metallization on ITO	97
5.1	Introduction	97
5.2	Experimental	100
5.2.1	Nanoparticle characterization	100
5.2.2	Effects on particle sintering	102
5.2.3	Ink and paste printing	106
5.2.4	Sintering	107
5.2.5	Line resistivity	109
5.2.6	Contact formation to ITO	112
5.2.7	Chemical sintering with in-built chemical sintering agent	115
5.3	Results and discussion	116
5.3.1	Nanoparticle synthesis and characterization	116
5.3.2	Influences on particle sintering	122
5.3.3	Printing results	131
5.3.4	Sintering results	136
5.3.5	Line resistivity of silver nanoparticle inks and pastes	145
5.3.6	Contact formation to ITO	155
5.3.7	Chemical sintering with in-built chemical sintering agent	162
5.4	Summary	169
6	Influence of Sample Surface on Metallization	173
6.1	Introduction	173

6.2	Experimental	174
6.2.1	Contact angle measurements on ITO	174
6.2.2	Influence of surface properties on metallization characteristics	175
6.3	Results and discussion	178
6.3.1	Solvents on ITO surface	178
6.3.2	Influence of surface properties on metallization characteristics	182
6.4	Chapter Summery	186
7	Seed-and-Plate on ITO	189
7.1	Introduction	189
7.2	Experimental	190
7.2.1	Selective copper plating on HIT solar cells with TiPdAg seed-layer	190
7.2.2	Cyclovoltammetric measurements on ITO	191
7.3	Results and discussion	192
7.3.1	Plating results	192
7.3.2	CV measurement results	196
7.4	Summary	199
8	MOD Ink Metallization of Silicon Solar Cells	201
8.1	Introduction	201
8.2	Experimental	203
8.2.1	Ink formulation	204
8.2.2	Tempering process	208
8.2.3	Aerosol jet printing	209
8.2.4	Screen printing	210
8.2.5	Plating	211
8.2.6	Contact formation model	211
8.2.7	Contact quality	215
8.2.8	Conductivity, contact resistance and cell results	216
8.3	Results and discussion	217
8.3.1	Ink formulation	217
8.3.2	Tempering process	224
8.3.3	Aerosol jet print of MOD inks	228
8.3.4	Screen printing of MOD pastes	229
8.3.5	Plating on the MOD seed-layer	231
8.3.6	Contact formation model	235

8.3.7	Contact quality	249
8.3.8	Conductivity, contact resistance and cell results	251
8.3.9	Comparison to high temperature metallization pastes	254
8.4	Chapter Summary	257
9	Summary and Outlook	259
	Publications	265
	Bibliography	267
	Danksagung	285
A	Appendix	287
A.1	Theory	287
A.1.1	Additional data for Chapter 2	287
A.1.2	Additional data for Chapter 3	290
B	Appendix	293
B.1	Measurements	293
B.1.1	Additional data for Chapter 5	293
B.1.2	Additional data for Chapter 7	295
B.1.3	Additional data for Chapter 8	296

Abstract

The present work studies the suitability of new metallization technologies for contacting advanced and standard industrial silicon solar cells. The technologies are special in terms of process temperatures: all metallization concepts presented here are processed at low to medium temperatures between 200 °C and 500 °C. Thus, new metallization routes for temperature sensitive cell concepts are accessible and production costs for standard cell production can be reduced.

The work was inspired by metallization approaches developed for printed flexible electronics.

The work addresses new metallization concepts for advanced temperature sensitive solar cell developments as well as for established standard silicon solar cells.

For the advanced solar cell designs the potential of metallization approaches based on silver nanoparticles is evaluated. A basic understanding of the influences of organics included and necessary for ink and paste formulations on the sintering behavior of silver nanoparticles will be analyzed in detail. In addition, a new sintering process, *chemical sintering*, is used and further developed to meet the demands for metallization of solar cells. As a result, very low lateral and contact resistance values are measured, which could not be demonstrated for other comparable low temperature metallization techniques with exception of the laborious process of evaporated and sputter metals.

A basic understanding of the standard substrate surface of the addressed solar cell approaches, ITO, is developed, in order to make proper formulation of metallization inks possible.

It is demonstrated that selective plating on a metallic seed-layer on ITO is possible, without protection of the conductive ITO surface.

For standard industrial solar cells a new metallization ink, firstly formulated at Fraunhofer ISE, is evaluated. The ink is free of lead and free of particles. Compared to a thick film metallization paste, which is typically used, the ink contains a very low amount of silver and is able to contact the emitter through the anti-reflection coating

at temperatures far below the firing temperature of standard thick film metallization pastes.

On the basis of the current contact formation model, which has been developed for thick film metallization pastes, a new model for the contact formation by this ink is proposed.

It is demonstrated that the novel metallization approaches discussed in this work, can be combined with the advanced metallization technology “seed-and-plate” which is currently under development and in first test phases in industry.

Deutsche Zusammenfassung

Die vorliegende Arbeit untersucht die Eignung neuer Metallisierungstechnologien zur Kontaktierung neuer Solarzellgenerationen sowie von standardisierten industriellen Siliziumsolarzellen. Das Besondere der neuen Technologien sind ihre Prozesstemperaturen: Alle hier vorgestellten Metallisierungsverfahren werden bei niedrigen bis mittleren Temperaturen prozessiert. Auf diese Weise, werden neue Arten der Metallisierung für temperaturempfindliche Solarzellenkonzepte verfügbar und die Produktionskosten für Standardsolarzellen gesenkt.

Die Arbeit wurde durch neue Metallisierungsansätze für druckbare und flexible Elektronik inspiriert.

Die Arbeit befasst sich mit neuen Metallisierungsverfahren für weiterentwickelte temperaturempfindliche Solarzellenkonzepte als auch für etablierte Siliziumsolarzellen.

Für neue Solarzellenkonzepte wird die Eignung von Metallisierungsverfahren auf Basis von Silbernanopartikeln evaluiert. Die Grundlagen für das Verständnis des Einflusses zugesetzter und notwendiger Organik in Tinten- und Pastenformulierungen auf das Sinterverhalten von Silbernanopartikeln wird detailliert untersucht. Darüber hinaus wird ein neues Sinterverfahren, das so genannte "chemische Sintern" angewandt und weiterentwickelt, um den Anforderungen an die Metallisierung von Solarzellen gerecht zu werden. Im Ergebnis können sehr niedrige Werte für die laterale Leitfähigkeit als auch für den Kontaktwiderstand erreicht werden, die mit vergleichbaren Niedertemperaturmetallisierungsverfahren außer mit thermischen Verdampfen oder Sputtern von Metallen bisher nicht erreicht werden konnten.

Ein grundlegendes Verständnis für die normalerweise verwendete Substratoberfläche der angewandten Solarzellenkonzepte, ITO, wird entwickelt, um angepasste Zusammensetzungen der Metallisierungstinten formulieren zu können.

Um die Vorteile des weiterentwickelten Metallisierungsansatzes "seed and plate" nutzen zu können, wird gezeigt, dass das selektive elektrochemische Abscheiden von Metall auf Metallsaatschichten auf ITO

möglich ist, ohne dass die leitfähige ITO-Oberfläche geschützt werden muss.

Für Siliziumsolarzellen wird eine neue Metallisierungstinte, die am Fraunhofer ISE entwickelt wurde, getestet. Die Tinte ist blei- und partikelfrei. Die Tinte enthält im Vergleich zu den sonst üblicherweise verwendeten Metallisierungspasten sehr wenig Silber und ist in der Lage den Emitter der Solarzelle durch die Antireflexionsschicht bei Temperaturen zu kontaktieren, die weit unter den üblichen Feuertemperaturen für Vollaufbaumetallisierungspasten liegen.

Auf Grundlage des derzeit gültigen Kontaktbildungsmodell für Vollaufbaumetallisierungspasten wird ein neues Kontaktbildungsmodell, welches auf die hier vorgestellte Tinte angewandt werden kann, vorgeschlagen.

Es wird gezeigt, dass die in dieser Arbeit vorgestellten neuen Metallisierungsansätze zusammen mit der weiterentwickelten Metallisierungstechnology “seed-and-plate”, die sich noch sowohl in der Entwicklung als auch in Anwendung in ersten industriellen Pilotlinien befindet, angewandt werden kann.

Nomenclature

<i>mpp</i>	Maximum power point	DIM	Diiodmethane
<i>pFF</i>	Pseudo fill factor	DOD	Drop on demand
AgAc	silver acetate	DSC	Differential scanning analysis
ARC	Anti-reflection coating	EB	Electron beam
AZO	Aluminium zinc oxide	EC	Ethyl cellulose
bcc	Space-centered cubic	EC	European Community
BSF	Back surface field	EDX	Energy dispersive X-ray spectroscopy
CA	Capping agent	EL	Electroluminescenz
CCD	Charged-coupled device	EWT	Emitter wrap through
CER	Contact end resistance test structure	FF	Fill factor
CFR	Contact front resistance test structure	FIB	Focused ion beam
CIJ	Continuous ink jet	HA	Heptylamine
CNL	Charge neutrality level	HEC	Hydroxy ethyl cellulose
CV	Cyclic voltammetry	HIT	Hetero Junction with Intrinsic Thin Layer
Cz	Czochralski	IBC	Interdigitated Back Contact
DA	1-dodecylamine	IEA	International Energy Agency
		IHP	Inner Helmholtz plane

ITO	Indium Tin Oxide	RoHS	Restriction of Hazardous Substances
LED	Light emitting device	RoHS	Restriction of Hazardous Substances
LIP	Light induced plating	SEM	Scanning electron microscope
M3D	Maskless Mesoscale Material Deposition	SHJ	Silicon hetero junction
mc	Multicrystalline	TCO	Transparent conductive oxide
MOCVD	Metal organic chemical vapor deposition	TEM	Transmission electron microscope
MOD	Metal organic decomposition	TG	Thermo-gravemetry
MWT	Metal wrap through	TLM	Transfer line methode
NMP	N-methyl-2-pyrrolidon	umg	upgraded metallurgical
O	Oxidized species	FZ	Float zone
OHP	Outer Helmholtz plane	V_D	Drop volume
PAA	Poly(acrylic acid)	β	Current efficiency
PDAC	Poly(diallyldimethylammonium chloride)	χ	Distance
PECVD	Plasma enhanced chemical vapor deposition	η	Efficiency
PET	Poly(vinyl terephtalate)	γ_{sl}	Interfacial tension
PH	Phenylhydrazine	ν	Stoichiometric coefficient
PL	Photolithography	ϕ	Electrostatic potential
PVP	Poly(N-vinyl-2-pyrrolidone)	ϕ_n	Contact barrier height
R	Reduced species	ρ_c	Resistivity
		ρ	Specific resistance
		σ	Charge density

σ_s	Surface energy	j	Diode current density
σ_s, σ_l	Surface tension of solid, liquid	j_{02}	Current density of space charge region
σ_s^D	Dispers part of surface energy	j_0	Saturation current density
σ_s^P	Polar part of surface energy	j_{Ph}	Photon current density
	Electron mobility	j_{SC}	Short circuit current density
Θ	Contact angle	l	Length
ε_{EA}	Electron affinity	L_T	Transfer length
		M	Molare mass
ε_M	Metal work function	m	Mass
ε_M	Semiconductor work function	N	Electron density
		n	Free electron density
ε	Energy level	n_1, n_2	Ideality factor
		N_D	Number of doped atoms
ζ	Zeta Potential	P_{mpp}	Power at maximum power point
A	Area	P_{Ph}	Phonon power
c_{max}^{Nu}	Maximum monomer concentration	Q	Charge (number of electrons)
c_{min}^{Nu}	Minimal monomer concentration	q	Elementary charge
e	Elementary charge	R	Resistance
F	Faraday constant	R_c	Contact resistance

R_P	Parasitic shunt resistance	W_{12}	Work of adhesion
R_{Sh}	Sheet resistance	w_c	Contact length
R_S	Series resistance	z	Number of electrons
t	Thickness	λ	Wavelength
t_D	Time	τ	Charge carrier lifetime
U_c	Contact voltage	E	Energy
U_E	External voltage	E_F	Fermi Energy
V	Voltage	E_P	Photon energy
v_{ER}	Evaporation rate	E_G	Band gap energy
V_{OC}	Open circuit voltage	k	Boltzmann constant
W	Contact width	T	Absolute temperature

List of Figures

1.1.1	Depletion of fossil energy sources	2
1.2.1	Silver demand by Solar Industry	5
2.1.1	Loss mechanisms	12
2.1.2	Exploitation of solar spectrum	13
2.1.3	Two-diode model	15
2.1.4	Series resistance of a solar cell	15
2.1.5	Optical impact of finger shapes	17
2.2.1	Band energy of seperated metal and semiconductor .	18
2.2.2	Band energy of Schottky contact	18
2.2.3	Current transport mechanisms for Schottky contacts	20
2.2.4	Barrier heights of metal - silicon contacts	20
2.2.5	Band energy of ohmic metal - semiconductor contact	21
2.2.6	Band energy of specific contact	22
2.2.7	Contact resistivities for silver - silicon contacts . . .	22
2.2.8	Silicon solar cell	24
2.2.9	Temperature gradient of fast firing process	25
2.2.10	Contact formation model	27
2.2.11	TEM image of silver - silicon contact	28
2.2.12	Current paths for silver - silicon contacts	29
2.3.1	Industrial solar cell processing sequence	31
2.4.1	SEM image of silver nanoparticles	32
2.4.2	Dependence of gold melting-point from particle size .	33
2.4.3	Nanoparticle synthesis: top down and bottom up ap- proach	34
2.4.4	Size control of nanoparticle synthesis according to La Mer	34
2.4.5	Particle sintering mechanisms	36
2.4.6	Particle stabilization	37
2.4.7	Chemical sintering	40
2.4.8	Thermal simulation of photonic curing process	42

2.5.1	Structure of HIT cell	46
2.5.2	Thermal budget of cell process	47
2.6.1	Optical spectra of TCO	49
2.6.2	CNL position in In_2O_3	52
2.6.3	Chrystal structure of In_2O_3	53
2.6.4	Energy band structur of In_2O_3	54
2.6.5	Transmittance and reflectance of ITO	55
2.7.1	Contact angle on solid surface	56
2.7.2	Surface energy calculation according to Rabel	58
2.7.3	Interaction between solid surface and liquid	59
3.2.1	Working principle of screen printing	63
3.2.2	Scheme of Aerosol jet printer	64
3.2.3	Working principle CIJ printer	66
3.2.4	Working principle DOD printer	66
3.3.1	Scheme of LIP process	70
3.3.2	Photograph of multiple cell wafer	71
3.4.1	Photolithographic metallization process	72
3.4.2	Seed-and-plate metallization stack	74
4.1.1	Dark IV-curve	78
4.1.2	Illuminated IV-curve	80
4.1.3	Influence of resistance on IV-curve	81
4.2.1	Comparison of IV- and SunsV_{OC} measurement [1]	82
4.3.1	Four point probe measurement set-up	83
4.3.2	Illustration of TLM measurement structure	85
4.3.3	Illustration of transfer length	85
4.3.4	Relationship of contact length and contact resistance	87
4.3.5	TLM measurement plot	88
4.3.6	Simplified TLM measurement structure	89
4.4.1	Scheme of TG measurement setup and DSC sample holder	91
4.4.2	Schematic TG-DSC signals	91
4.8.1	3D LEXT image	94
4.9.1	Electroluminescenz image of a silicon solar cell	95
5.2.1	Chemical structure of (hydroxy)ethyl cellulose	105
5.2.2	Sample structure of contact resistance measurement samples	112

5.2.3	Sample structure of contact resistance measurement samples	114
5.3.1	SEM image of silver nanoparticles synthesized according to Li	117
5.3.2	SEM image of particles with varying metal precursor to capping agent ratio	117
5.3.3	SEM image of particles with varying metal precursor to reducing agent ratio	118
5.3.4	SEM image of particles with varying reaction temperature	118
5.3.5	SEM image of particles with reducing agent drop rate	119
5.3.6	SEM image of particles with different capping agents	119
5.3.7	SEM image of particles with doubled concentration and synthesis volume	120
5.3.8	SEM image of particles according to Li and Peng . .	121
5.3.9	Sintered 1-heptylamine capped silver nanoparticles .	123
5.3.10	Dependence of nanoparticle sintering temperature from particle size	123
5.3.11	TG-DSC measurement of capping agents	126
5.3.12	Nanoparticle formation with PVP capping	127
5.3.13	Particles before and after chemical sintering	128
5.3.14	Silver particles capped with 1-heptylamine unstable at room temperature	129
5.3.15	Instability of silver nanoparticles	129
5.3.16	Inks with additive variation after chemical sintering .	130
5.3.17	Ink jet samples	132
5.3.18	Cross section of ink jet sample	132
5.3.19	Aerosol jet sample	133
5.3.20	LEXT image of aerosol jet samples	134
5.3.21	Silver nanoparticle paste	135
5.3.22	Microscope measurement of screen printed finger . .	136
5.3.23	SEM images of differently treated nanoparticles . . .	137
5.3.24	SEM images of temperature impact on chemical sintered particles	138
5.3.25	SEM images of thermal sintered particles	139
5.3.26	TG-DSC measurement of hydroxy ethyl cellulose . .	141
5.3.27	Sintered silver nanoparticle paste with ethyl cellulose	142
5.3.28	Cross section of nanoparticle paste with ethyl cellulose	142

5.3.29	SEM images of temperature impact on chemical sintered paste with HEC	143
5.3.30	SEM images of sintered silver nanoparticle paste with hydroxy ethyl cellulose	144
5.3.31	SEM images of thermal sintered paste with HEC	145
5.3.32	Line resistivities of nanoparticle ink samples	146
5.3.33	Line resistivity comparison of chemically and thermally sintered ink samples	148
5.3.34	Line resistivities of screen printed samples	149
5.3.35	Image of screen printed samples	151
5.3.36	Line resistivity comparison of chemically and thermally sintered screen prints	152
5.3.37	Line resistivity comparison of screen printed samples with EC and HEC	153
5.3.38	Line resistivity comparison of ink and screen printed samples	154
5.3.39	Normalized contact resistance of silver nanoparticle ink to ITO	155
5.3.40	Cross sections of particles of different quality	157
5.3.41	Normalized contact resistance of silver nanoparticle paste to ITO	158
5.3.42	Normalized contact resistance of silver nanoparticle pastes with EC and HEC	159
5.3.43	Normalized contact resistance of silver nanoparticle paste and ink to ITO	160
5.3.44	Current sweep measurement	162
5.3.45	Sinter islands on NaCl sintered sample	164
5.3.46	Magnified image of sinter islands	164
5.3.47	Nanoparticles outside of sinter islands	165
5.3.48	Sinter cubes with NH_4Cl	167
5.3.49	Sintering of inks with different silver amount	168
5.3.50	Inks including NH_4Cl	168
6.2.1	Sample structure of contact resistance measurement samples	175
6.2.2	Process flow ITO aging experiment	177
6.2.3	Photograph of tape test sample	178
6.3.1	Goniometer pictures on textured silicon surface with ITO	179

6.3.2	Contact angle development on textured silicon with ITO	180
6.3.3	Goniometer pictures on planar silicon surface with ITO	181
6.3.4	Contact angle development on planar silicon with ITO	181
6.3.5	Contact angle change of water on ITO	183
6.3.6	Contact angles of water on treated ITO	184
6.3.7	Surface energy calculations	186
7.2.1	Cell structure of HIT solar cell for plating	190
7.3.1	Photograph of non plated and plated cell sample . .	192
7.3.2	Copper plating on HIT cells with and without cleaning	192
7.3.3	SEM image of copper plating on seed-layer on ITO .	194
7.3.4	EDX measurements of ITO at the cell edge	195
7.3.5	Cyclovoltametric measurements	197
8.3.1	Chemical structures of metal neodecanoates	219
8.3.2	Evaluation of evaporation rate of Xylene:NMP solutions	219
8.3.3	Silver neodecanoate	220
8.3.4	Photograph of Zn and Bi neodecanoate solution series	220
8.3.5	Bismuth neodecanoate content solution series	221
8.3.6	Zinc content variation in three component solution .	221
8.3.7	MOD ink dilution series	222
8.3.8	MOD ink stability	223
8.3.9	Etching results of Bi variation in MOD ink	225
8.3.10	DSC measurement of metal organyls with Si_3N_4 . . .	226
8.3.11	MOD ink on SiN_x coated wafer	227
8.3.12	LEXT images of Aerosol printed MOD ink	228
8.3.13	Photographs of screen-printed MOD ink samples . .	230
8.3.14	LIP plating setup	232
8.3.15	Photographs of plating on MOD seed layer	233
8.3.16	Details on MOD seed layers	234
8.3.17	Pure bismuth neodecanoate on SiN_x	236
8.3.18	Layer sequence of MOD ink metallization	237
8.3.19	Influence of Bi/Ag proportion on SiN_x -etching	238
8.3.20	EDX analysis of MOD ink etching on SiN_x	239
8.3.21	Pore etching in SiN_x layer	240
8.3.22	Silver dendrites in ARC pore	240
8.3.23	Silicon etching with silver in HF	241
8.3.24	Silicon nitride etching by MOD ink residues	243

8.3.25	EDX spectra of MOD ink residues	244
8.3.26	Contact points with silver crystallites of MOD ink in SiN _x -layer	246
8.3.27	Influence of silver deposited silver amount on SiN _x - etching	247
8.3.28	Etching results on SiN _x layers of varying thickness .	248
8.3.29	High metal concentration in ARC layer from MOD ink	250
8.3.30	Contact point formation by MOD ink	251
8.3.31	Cave formation under contact points	251
8.3.32	SunsV _{OC} and IV-measurement of MOD ink metalized cell	252
8.3.33	Fully metallized cell contacted with MOD ink	253
8.3.34	Electroluminescence image of fully metalized cell con- tacted with MOD ink	254
8.3.35	Silver crystallite imprints	256
A.1.1	Fermi-diract distribution	287
A.1.2	Pneumatic impactor and virtual impactor	291
A.1.3	Aerosol printing head	291
B.1.1	TG-DSC measurement of EC	293
B.1.2	Linkam TS 1500	294
B.1.3	Organic residues in nanoparticle ink	294
B.1.4	Illustration of Helmholtz-plane	295
B.1.5	TG-DSC measurement of silver neodecanoate	296
B.1.6	TG-DSC measurement of bismuth neodecanoate . .	297
B.1.7	TG-DSC measurement of zinc neodecanoate	297
B.1.8	TG measurement of reaction of metal neodecanoates with Si ₃ N ₄	298
B.1.10	SunsV _{OC} measurements of MOD ink cell batch . . .	299
B.1.9	MOD ink etching results at different temperatures .	300

List of Tables

3.3.1 Reducing agents for electroless plating	69
5.2.1 Nanoparticle synthesis: Varied parameters	101
5.2.2 Details of silver nanoparticles	103
5.2.3 Details of additives	105
5.2.4 Salt concentrations in PAA capped nanoparticle silver inks	116
5.3.1 Particle sizes and sintering temperatures	124
5.3.2 Sinter salt results for NaCl	163
5.3.3 Sinter salt results for KCl	166
5.3.4 Sinter salt results for HCl	166
5.3.5 Sinter salt results for NH ₄ Cl	167
6.3.1 Experimental results on ITO	185
8.2.1 Xylene/NMP mixtures for solvent evaluation	204
8.2.2 Bismuth to silver neodecanoate proportions	213
8.2.3 Etching times for silicon nitride etching	214
A.1.1 Properties relevant to TCO materials and applications	288
A.1.2 TCO materials for various applications	289
B.1.1 Mass loss of metal neodecanoates	296
B.1.2 Influence of Bi-/Ag-ratio on SiN penetration	301

1 Introduction

1.1 Motivation

The worlds energy demand rises every year. Within the last 40 years the demand almost doubled from 4 672 Mteo¹ in 1973 to 8 979 Mteo in 2012 [2]. The share in the primary fossil energy sources of oil, natural gas and coal was 66% in 2012 [2].

This dependence on primary fossil energy sources has several crucial disadvantages which have impact on the safety and well-being on the worlds population already today.

First, primary fossil energy sources are naturally limited. Figure 1.1.1 shows the time until the depletion of those energy sources in years, assuming 2012 consumption.

According to [3] with 33.1% crude oil is still the dominating energy source for energy production today. At the same time, it is also the most limited resource. Although according to Figure 1.1.1 resources of gas and coal would ensure our energy production for 4000 years, especially the extensive usage of coal would lead to massive pollution of the environment.

Along with energy consumption also the emission of CO₂ rose from 15 633 Mt in 1973 to 31 734 Mt in 2012 [2]. CO₂ is known to be a greenhouse gas and its concentration in the atmosphere influences the worlds climate. The consequences of this change can already be seen today (rise of number of weather extremes, sea-level rising) and the consequences for the population are unpredictable. Assuming a change of the energy mix in favor of coal this problem would even be tightened. The so-called “450” scenario of the International Energy Agency (IEA) includes the limitation of CO₂ concentration in the air to 450 ppm [2]. This would limit global warming to 2 °C but even this optimistic scenario will not be able to totally prevent certain environmental and global consequences caused by climate change. In

¹Mteo = Million tonnes of oil equivalent)

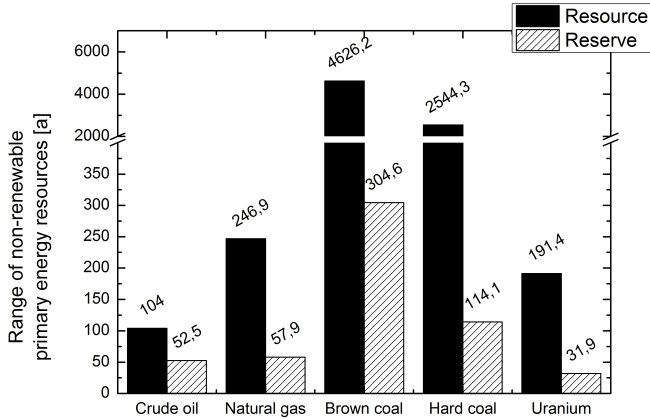


Figure 1.1.1: Depletion of fossil energy sources in years assuming 2012 consumption. Resources: all sources of raw material known or assumed today, including technically deducible and non-deducible sources. Reserves: today technically deducible raw material sources including already used sources (based on data from [3])

addition, to the risks for climate and nature, environmental pollution especially of the air involves the risk of causing health problems.

Apart from the pollution problem the limit of the availability of fossil energy resources also entails the risks of international and national crises in a scramble to the access of those resources. Energy prices already rose within the last decades² and will rather further rise than decrease in the future [3].

Even considering the “New politics” scenario from the IEA the world energy consumption will further rise about 11 % by 2020 and even 36 % by 2035³[2].

Nuclear power is an at least questionable alternative to primary

²Rise of energy prices up to 800% from 1990 to 2013[2])

³The “New politics” scenario would cause a global warming of 3.5 °C in the long term [2].

fossil resources in terms of waste disposal and safety.

To ensure the well-being and further development of the worlds population a massive change in the global energy concept has to be made.

A promising way to avert these negative impacts of fossil energy source consumption is to rise the amount of renewable energies within the global energy mix and even totally substitute primary fossil energy sources by renewables in the long term.

The amount of energy from the sun sent to the earth (outside the atmosphere) is about $5.36 \times 10^{24} \text{ Ja}^{-1}$ [4]. Almost 70 % of this impact reaches the earth's surface. Based on the energy consumption of $3.38 \times 10^{18} \text{ Ja}^{-1}$ in 2012 the *daily* energy impact of the sun on the earth's surface equates 3000 times our *annual* demand. In other words, the amount of energy provided by the sun exceeds our demand by a factor of 1 million. Thus, the sun can be seen as an unlimited energy resource.

In most cases renewable energies use the energy of the sun directly (photovoltaic) or indirectly (wind, biomass, thermal solar power). Technologies for the conversion of the sun's energy have been developed and are already introduced into the market to some extend. However, due to the relatively short time of development (around thirty years, except for waterpower, compared to around 150 years for energy conversion of fossil fuels), there is a lot of potential and also need for optimization.

Costs for energy rise, thus, there is pressure to significantly increase the cost-effectiveness of renewable energies. This will also lead to independence from governmental support.

Besides the already mentioned reduction of negative impacts caused by fossil fuels, the further development of renewables will provide more independence of countries with no or little access to fossil fuels. By installation of many small energy producers energy production becomes independent of large power plants. The decentralization of energy production provides new possibilities for both: developed and so-called underdeveloped countries.

1.2 Scientific relevance of the approach

1.2.1 State of the art

Solar electricity can already compete with grid electricity at a price of 0.10-0.20 €/kWh [5]. However, there is still potential for even further optimization.

The most efficient way to increase the cost-effectiveness of renewable energies is to increase their conversion efficiency and reducing production costs at the same time. In case of crystalline silicon solar cells, optimization is already very advanced, especially on the laboratory scale.

The photovoltaic sector is dominated by technologies based on crystalline silicon (90%) [5]. Especially the metallization of these concepts has potential of reducing the production costs [6, 7].

Silver consumption

Standard silicon solar cells as well as more advanced cell concepts use silver as material for contact formation to the front side of the cells. Thick film metallization pastes contain 70-90 wt% silver [8, 9]. The cost of silver per solar cell is around 0.03 US\$/Wp [7]. Silver is a noble metal and its price has been rising within the last decades by around 400 % from 2004 to 2013. Figure 1.2.1 shows the development of silver demand by solar industry over the last years including the silver price development.

Nevertheless with further demand of energy supply and the pressure to change the world's energy mix a reduction of silver consumption by solar industry is required to make sure that this changes keeps affordable.

Energy costs

Beside the costs for the materials, also the high energy consumption during production causes high €/kWh prices.

Standard silicon solar cells are being contacted with thick film pastes which have to be “fired” to form contact to the emitter of the cell. This process is done at around 800-900 °C. This high thermal impact does not only consume a lot of energy but can also lead to cell damage by warping of the wafers, causing micro cracks within the material, which reduces cell efficiency [10].

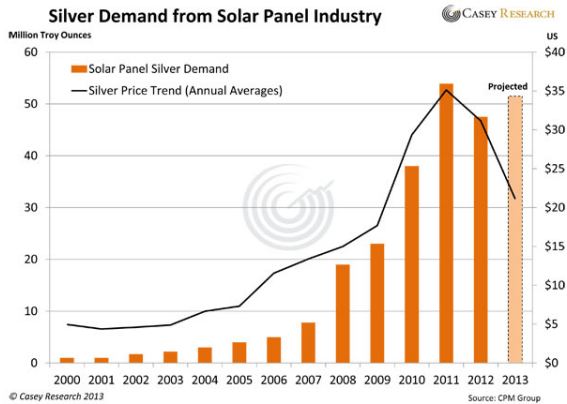


Figure 1.2.1: Silver demand by solar industry until 2012 including silver price trend (reprint with permission from [6])

Material and printing technique

Besides silver, high firing metallization pastes also contain lead, which is necessary to pursue the anti-reflection coating which is applied to the front side of the solar cell. Lead is toxic and is, therefore, forbidden to use in electrical devices by the EC directive 2011/65/EU (Restriction of Hazardous Substances - RoHS). For lack of alternatives, solar cells are still excluded from this restriction but this is likely to change in the near future.

Silver thick film metallization pastes are applied by screen printing, which is a non-contactless printing technique. For saving material, silicon cells tend to use thinner base material (today around 200 μm), which improves the risk of wafer breakage when applying the metallization paste by screen printing.

Standard cell concepts

While alternative cell concepts are still under development, the standard industrial cell concepts still demands further improvement.

Currently a more advanced metallization concept called “seed-and-plate” is being developed and aims to separate contact formation to the emitter and lateral current transport. This allows for independent optimization of both.

The contact is still formed by high temperature metal pastes or inks, which are being fired at high temperatures to make contact to the emitter. This *seed-layer* is then thickened by electrochemical metal deposition, which forms the lateral conductive layer. By introducing a diffusion barrier of nickel, also copper⁴ can be used to form the lateral conductive layer [12]. This concepts reduces the silver consumption, however, the problem of contact firing is still present.

Direct plating is also under development. In this process, the anti-reflection coating (ARC), which covers the front side of the solar cell and which is non-conductive has to be opened by etching or laser ablation. This method possesses high efficiency potential but also owns its own problematic with ARC opening, adhesion failures and short-circuiting the cell [13, 14].

Alternative cell concepts

Alternative and more advanced cell concepts as the HIT⁵ solar cell are processed at low temperatures and do even reach very high efficiencies. The world record has been set by Panasonic with a HIT-IBC⁶ solar cell reaching 25.6% cell efficiency [15]. Thus, advanced cell concepts combine both principles for improving the competitiveness of solar cells: low manufacturing costs and high efficiency.

However, these low temperature cell concepts have special demands on metallization. They can't be contacted with high temperature firing pastes. The metallization techniques to contact those cell types used today are evaporation of the metal through a shadow mask or a photolithographic mask⁷ and thick film metallization with polymeric silver pastes.

Evaporation of metal through a mask is a complicated and, therefore, very expensive approach and is not suitable for industrial mass production.

Polymeric silver pastes, which are screen printed on the wafer, contain high amounts of silver and, measured on the consumed silver amount, demonstrate low conductivity, limiting the efficiency.

⁴Copper has a high diffusion constant within silicon and damages the cell. The degradation is fast. Silver is no barrier against copper ions [11].

⁵Hetero junction with intrinsic thin layer

⁶Hetero junction with intrinsic thin layer - interdigitated back contact

⁷The techniques is described in more detail in Section 3.4.1.

1.2.2 New metallization concepts evaluated in this work

Standard cell concepts

Standard solar cell designs are still the dominant cell concept on the market, which demands further improvements for the metallization.

The principle of separating contact formation and lateral conductivity is a promising route to lower production costs and even improve the cell efficiency. “Seed-and-plate” will, therefore, be the base for the approach introduced in this work. Contact formation however, will not be done by a high temperature firing paste. Instead, the potential of a particle- and lead-free metallization ink based on metal organics, will be analyzed. The *metal organic decomposition* (MOD) ink contains metal organics which can be reduced to the metals and/or decompose to the corresponding oxides and form contact to the emitter of the cell at moderate temperatures < 500 °C. The metal concentration is relatively low (~ 26 wt%) and the ink can be printed with cost efficient and contactless printing techniques like ink jet or aerosol jet printing. Ink jet and aerosol jet are low cost metallization techniques, which require relatively cheap and compact equipment and are applicable to various substrates [16, 17]. In addition, printing of very narrow line widths < 10 μm is possible [18–22]. Thus, MOD inks might be a good alternative to the standard thick film metallization technique by reducing silver consumption, processing temperature, avoidance of hazardous substances and enabling the use of contactless application processes.

Alternative cell concepts

A cost efficient metallization method would allow new cell concepts to enter the commercial solar cell market instead of being left at the laboratory level.

An advanced method for contacting temperature sensitive substrates could be the metallization with silver nanoparticles. Metal nanoparticles sinter far below the melting temperature of the corresponding bulk material [23]. Nanoparticles can be introduced in an ink formulation and can thus, be applied by fast and cheap printing techniques like ink jet printing or aerosol jet printing. In addition, the sintering of the nanoparticles permits higher conductivity than the pure touch of single silver particles or flakes as present in polymeric silver pastes.

1.3 Outline

The present work aims on the evaluation of low temperature metallization for silicon solar cells. This requires general knowledge about the basics of solar cells, nanoparticle sintering (Chapter 2) and metallization techniques (Chapter 3). The techniques used in this work to characterize the results of the experimental work are described in Chapter 4. The analysis of inks and pastes on the basis of silver nanoparticle inks to estimate their suitability as alternative metallization concept for temperature sensitive solar cell concepts is described in Chapter 5. These low temperature metallization inks and pastes are intended to be mainly applied to ITO⁸. The special challenges of contacting ITO with inks and pastes are addressed in Chapter 6.3.2. Because the seed-and-plate approach is a very promising way of lowering processing temperatures and reducing the amount of silver applied to a solar cell, the feasibility of plating on metal seed-layers on ITO is investigated in Chapter 7. Low temperature metallization for standard solar cells based on MOD inks was also investigated and a new metallization approach was tested and analyzed. Especially the contact formation process for this new metallization method to the emitter was studied in detail. A contact formation model for this kind of metallization is proposed (chapter 8).

⁸Indium tin oxide

2 Theoretical Background

This chapter explains the theoretical basics for this work. In Section 2.1 the fundamental working principle of silicon solar cells is introduced. The different contact types between metal and semiconductor, as well as, the current contact formation model of common industrial metallization on silicon solar cells is explained in Section 2.2. Section 2.4 introduces the fundamentals of metal nanoparticles, the sintering of nanoparticles and their stabilization. A main part of this work deals with the metallization on transparent conductive oxides, which are introduced in Section 2.6.3. For metallization the interdependency of substances is important and Section 2.7 explains some of the basic theories.

2.1 Silicon Solar Cells

2.1.1 Basic principles and loss mechanisms

Basic principles

The information given here and further details can be found in the literature: [4, 23–33] etc.

The ability of silicon solar cells to convert sunlight in an electrical current is based on two characteristics: silicon is a semiconductor and - in case of a solar cell - equipped with a p-n junction.

A semiconductor possesses an electrical band gap which separates the allowed energetic states through a band gap energy E_G . The band below this energy gap is called the valence band and is fully occupied at $T = 0$ K. The electrons are fixed to the nucleus and are not able to move throughout the lattice. Conduction is impossible. The next allowed state for electrons is named conduction band. Energies described by the conduction band exhibit energies $E \geq E_G$. The

Fermi energy E_F ¹ lies within the band gap.

At $T = 0$ K no energy states above the Fermi-level are occupied. At higher temperatures electrons gain thermal energy (due to lattice oscillations and bond loosening), thus, the electrons are able to overcome the energy gap and occupy higher energy levels in the conduction band. In the valence band void energetic states - *holes* - are left behind enabling electrons to move around in the valence band. These effects result in a minimal conductivity.

To further improve the conductivity of the semiconductor more free charge carriers (electrons and holes) have to be created. More electrons have to possess energies higher than the band gap energy to occupy states in the conduction band. As the energy gap in semiconductors is relatively small this additional energy can be provided by photons emitted by the sun. The electrons absorb the energy of a photon with a sufficient amount of energy and can be lifted in the conduction band. Photons with smaller energy amounts than the band gap $E_P < E_G$ are not absorbed and pass through the material. Photons with $E_P > E_G$ lift the electrons at higher states above the band edge within the conduction band.

The law of conservation of energy and the law of conservation of momentum must be fulfilled. Silicon is an indirect semiconductor. Therefore, the maximum of the valence band edge and the minimum of the conduction band edge are located at different crystal momentums. To fulfill the conservation of momentum an electron has to absorb a phonon in addition to the photon. The probability of absorption of two particles (photon and phonon) is essentially smaller than the absorption of only one particle. Thus, absorption of light in direct semiconductors is higher than that of indirect semiconductors.

By the excitation of the electron an “electron-hole pair” is created and adds to higher conductivities. The band gap for silicon is 1.12 eV (at $T = 300$ K) which corresponds to a wavelength of about $\lambda = 1100$ nm (visible wavelengths of light is around $\lambda = 400$ -700 nm) of incident photon to lead to an excitation [4].

¹The Fermi energy is defined by the Fermi-Dirac distribution which is given by $f(E) = \frac{1}{1 + \exp\left(\frac{E - E_F}{kT}\right)}$, with E_F the Fermi energy, k the Boltzmann constant and T the absolute temperature in K. The Fermi energy is defined as the energy at which the occupation probability of this energy state is 0.5. The Fermi-Dirac distribution is graphically given in Figure A.1.1 in the appendix A.1.1.

Electrons and holes occupying energy states at the band edge in an ideal semiconductor² can only lower their energy by recombination. The probability of a recombination is relatively small as a phonon is additionally needed. Excited carriers, therefore, remain in their energy rich states for a certain amount of time which is known as *lifetime* τ . Within this time carriers move randomly around the lattice. The distance which is passed by the carriers within τ is called *diffusion length*.

To further rise the amount of charge carriers in a semiconductor one can provide those additional charge carriers by *doping* the material. Doping means to replace some of the silicon atoms in the lattice through foreign atoms with more valence electrons (additional negative charge carriers \rightarrow n-type doping) than silicon or less valence electrons (additional positive charge carriers \rightarrow p-type doping). An undoped material is called *intrinsic*. Silicon is a group IV element. To add holes to silicon an element of group III (typically boron) is used as dopant. To add electrons a group V element is needed (typically phosphorus). The Fermi energy is also shifted by doping: to higher energies and closer to the conduction band edge in n-type materials and to lower energies and closer to the valence band gap for p-type semiconductors.

By bringing both doping type materials into contact a *p-n junction* is created. To reach thermal equilibrium electrons move from the n-type material to p-type material to balance the concentration differences of electrons and holes (Fermi energies reach same energy level). The moving charge carriers leave behind exposed charges on dopant atom sides which are fixed to the lattices and are, therefore, unable to move. The fixed charges built up an electrical field which is directed against the movement of the charge carriers and rises until the field energy equals the diffusion energy of electrons and holes. Close to the p-n junction less charge carriers are present at both sides of the junction. This region is called the *depletion region* or *space charge region* and is typically only a few nanometer thick.

Electrons, which are present in excess in n-type silicon are called *majority carriers*. Holes on the other hand are very limited and are called *minority carriers* (for p-type semiconductors the definitions are vice versa). The p-n junction separates the electrons and the holes

²Ideal semiconductor: without defects

to the n-contact and the p-contact, respectively. Under illumination electron-hole pairs are generated continuously and thus, are present in excess in comparison to the pure doping effect. The Fermi level splits into two quasi-Fermi levels which are shifted to the valence and conduction band. This separation defines the maximal achievable voltage of the solar cell. The created charge carriers can be extracted using metals contacting the front and the rear side of the device, respectively.

Loss mechanisms

Different physical and constructive induced losses limit the conversion efficiency of silicon solar cells. An overview over the different loss mechanism is given in Figure 2.1.1.

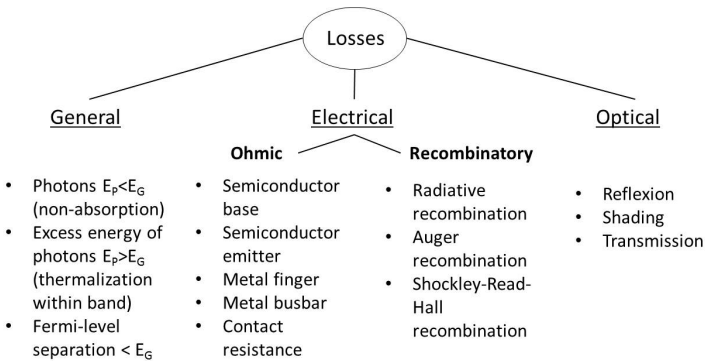


Figure 2.1.1: Loss mechanisms in solar cells (retraced from [12])

Ohmic losses are discussed in chapter 2.1.1. Within this section most relevant loss mechanism are briefly discussed. More detailed information can be found in the given literature.

General and recombination losses

Most relevant losses are given by the limitation of the semiconductor to fully absorb all wavelength of the solar spectrum.

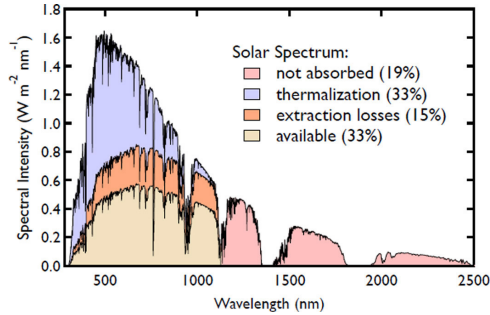


Figure 2.1.2: Exploitation of solar spectrum by silicon (reprint with permission from [34])

All photons with long wavelengths, which energy is smaller than the silicon band gap are not able to excite an electron from the valence band to the conduction band. Photons with shorter wavelengths, thus higher energy, provide additional energy which is released through thermal energy and is lost. The maximum voltage achievable by a solar cell is not directly given by the band gap but by the quasi-Fermi level splitting.

Losses through recombination occur, when an electron-hole pair recombines. The released energy can also be reabsorbed by recombination through a second electron. This is referred to as “Auger recombination”. The electron releases the additional energy by collision with the crystal lattice. Those losses limit the efficiency of silicon solar cell to approximately 29%. These limits are hard to overcome and can only be approached by optimization of the cell structure.

Most relevant recombination loss is the Shockley-Read-Hall recombination. This mechanism describes recombination of charge carriers via defect levels of impurities, such as dopants, other elementary impurities and crystal lattice defects.

Optical losses

Reflexion occurs on the surface of the semiconductor due to light refraction at the atmosphere/semiconductor interface. Technically re-

reflectance of light can be decreased by texturing the surface³ and applying an *anti-reflection coating* (ARC)⁴ which also serves as a passivation layer⁵.

Optical losses also occur due to shading of the active cell area by the metallization on the front side.

2.1.2 Two-Diode Model

To be able to describe the most relevant electrical mechanisms in a solar cell one uses an equivalent model. Simply a solar cell is considered as a diode, which is described by equation 2.1:

$$j = j_0 \left(\exp \left(\frac{qV}{kT} \right) - 1 \right) - j_{Ph} \quad (2.1)$$

with q representing the *elementary charge*, j_0 the *saturation current density* which is the sum of the saturation current density of emitter and base and j_{Ph} the current density of a photon. V is the voltage, k the Boltzmann constant and T the temperature. As a solar cell is not a simple diode, the diode model is extended by a second diode that represents the recombination of the *space charge region* (j_{02}), the *parasitic shunt resistance* or *parallel resistance* (R_P)⁶, and the losses caused by the *series resistance* (R_S). The equivalent circuit diagram is given in Figure 2.1.3.

³Texturing redirects the impacting sunlight partially back to the solar cell surface and thus, increases the chance of absorption. Also, the optical path length within the solar cell is increased.

⁴The ARC layer is matched to the used semiconductor. Refractive index and layer thickness are chosen in order to achieve destructive interference of light, which is reflected at the ARC/semiconductor interface with light reflected at the ARC/air interface. This leads to a reduced total reflectance.

⁵Surfaces and interfaces are typically locations of high defect concentration. A passivation layer reduces the number of defects and, therefore, the Shockley-Read-Hall recombination.

⁶The parallel resistance represents the electrical barrier quality between the n-type and p-type region of the solar cell. The higher the resistance the better: less charge carriers are able to recombine by parasitic currents within the space charge region, which do not contribute to the electrical power generation.

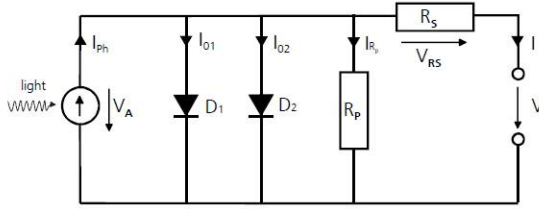


Figure 2.1.3: Equivalent circuit diagram of the two-diode model [35]

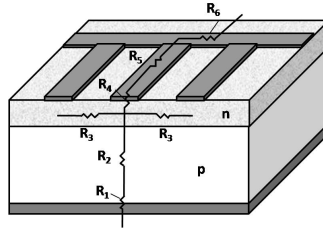


Figure 2.1.4: Composition of series resistance in a simple silicon solar cell (retraced from [24])

A solar cell is, therefore, more precisely described by equation 2.2

$$j(V) = j_0 \left(\exp \left(\frac{q(V - jR_s)}{n_1 kT} \right) - 1 \right) \quad (2.2)$$

$$+ j_{02} \left(\exp \left(\frac{q(V - jR_s)}{n_2 kT} \right) - 1 \right) + \frac{V - jR_s}{R_p} - j_{ph}$$

The *ideality factors* n_1 and n_2 describe the quality of both diodes. Their values for an ideal solar cell are $n_1 = 1$ and $n_2 = 2$. In real solar cells those parameters can strongly differ from the ideal values.

2.1.3 Series resistance and metallization induced losses

The series resistance is composed of several resistances which are illustrated in Figure 2.1.4

The different resistances are:

- R_1 : Resistance of metal-semiconductor contact to the base (usually rear side)
- R_2 : Resistance of semiconductor base
- R_3 : Resistance of emitter, called R_{Sh}
- R_4 : Resistance of metal-semiconductor contact to the emitter (usually front side)
- R_5, R_6 : Resistance of metallic contacts (finger and busbar)

The contributions of R_1 and R_2 to R_S are normally negligible and, therefore, not discussed any further.

The resistance of the emitter R_3 is given by the doping concentration. High doping concentrations lead to low R_{Sh} values but also favor higher Auger recombination. Therefore, technical tendency goes to lower doping concentrations and higher sheet resistances. Due to the increased sheet resistance the metal grid design includes shorter finger distances and a higher value of fingers per cell area. Also, the metal-semiconductor contact R_4 is strongly influenced by the doping concentration of the emitter (see Section 2.2). High ohmic emitters make higher demands on the metallization than low ohmic emitters.

The resistances of the metal contacts themselves R_5, R_6 should be as low as possible and are mainly defined by the metal itself, as well as the quality of the metallization medium. For example, plated contacts are normally very dense and are of very high quality regarding R_5 and R_6 . Screen printed contacts compose of single particles which are sintered together during the metallization process and are, therefore, less dense compared to plated contacts.

The metallization also contributes to optical losses of the solar cell: The metallization on the front side leads to shading of the active cell area. To keep shading losses as low as possible, very narrow fingers and an optimal grid design are aspired. The form of the fingers themselves can lower the shading effect but is difficult to influence.

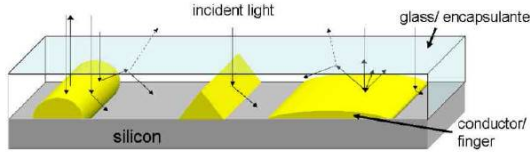


Figure 2.1.5: Finger shapes and their impact on optical properties [12]

2.2 Metal-semiconductor contact

The metal contact on a solar cell enables the collection and conduction of the current generated in the cell to lead it out of the semiconductor. To avoid electrical losses, contact resistivity between the semiconductor and the metal has to be avoided or be at least as small as possible. The reason for the occurrence of a contact resist is the difference in *work function*. The work function is the amount of energy which is necessary to transport an electron at the Fermi level into the vacuum level. For metals the work function ε_M is a material constant but can be influenced by surface properties.

For semiconductors the *electron affinity* ε_{EA} is also a material constant and is defined as the energy difference between the lowest conduction band edge and the vacuum energy level. In analogy to the work function of a metal one can define the *work function of a semiconductor* ε_{SC} , which is not a constant but can be strongly affected by the doping level of the material. Furthermore, in intrinsic semiconductors the Fermi level is normally located within the band gap, thus, there are no electrons on the Fermi level. Figure 2.2.1 shows a schematic illustration of the band energy of a separated metal and n-type semiconductor with ε_{F_M} being the Fermi level of the metal, ε_C the conduction band level, ε_V the valence band level, ε_{Vac} the vacuum level and $\varepsilon_{F_{SC}}$ the Fermi level of the semiconductor.

By contacting metal and semiconductor thermodynamic equilibrium must be reached: charge carriers diffuse through the contact until the Fermi levels of both metal and semiconductor reach the same energy level.

The two limiting cases for the contact formation between metal and semiconductor will be discussed in the following Sections 2.2.1

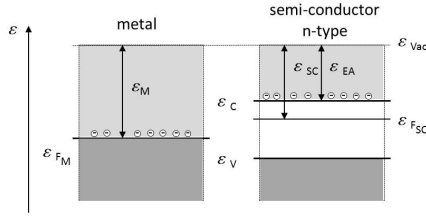


Figure 2.2.1: Band energy scheme of separated metal and n-type semiconductor ($\epsilon_M > \epsilon_{SC}$) (retraced from [26])

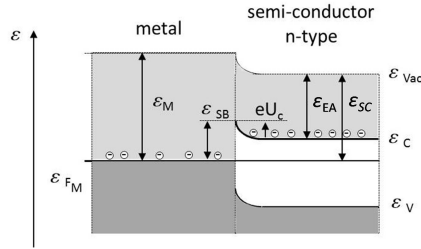


Figure 2.2.2: Band energy scheme of Schottky metal n-type semiconductor contact (retraced from [26])

and 2.2.2.

2.2.1 Schottky contact

A *Schottky contact* is formed if either

- a) $\epsilon_M > \epsilon_{SC}$ and n-type semiconductor
- b) $\epsilon_M < \epsilon_{SC}$ and p-type semiconductor

Here we will only discuss case a).

In case metal and semiconductor are in contact, diffusion of charge carriers occur until the Fermi energy levels are in thermal equilibrium. The band energy scheme is shown in Figure 2.2.2.

Due to the smaller work function of the semiconductor is compared to the metal's, electrons diffuse into the metal. Inside the semiconductor a depletion region is formed and a positive contact voltage U_c builds up. This voltage prevents further diffusion of electrons into

the metal. On the metal side, a narrow region of excess electrons is formed. The energy levels inside the semiconductor descent with the amount of $(\varepsilon_M - \varepsilon_{SC}) = eU_c$.

Without an external current no further diffusion of electrons is possible. Electrons diffusing from metal into the semiconductor have to overcome the *Schottky barrier* with the energy $\varepsilon_{SB} = \varepsilon_M - \varepsilon_{EA}$. Electrons diffusing from semiconductor to metal need to get over an energy barrier with the amount eU_c (see Figure 2.2.2).

Dependent on the polarity of an *external voltage* U_E applied to the contact, a current flow can be induced. In case a positive voltage is applied to the semiconductor, electrons are torn from the junction. The energy bands further descend and the barrier for electrons flowing from the semiconductor to the metal rises to $e(U_c + U_E)$. No current flow can be measured. Electrons flowing from metal to semiconductor have to overcome the Schottky barrier. Electrons rich of energy can overcome the Schottky barrier. A small cutoff current can be measured, which increases with increasing applied voltage. Due to surface effects and the *Schottky effect* (influence of cutoff current) the measured cutoff current is always higher than the theoretical one.

If a negative external voltage is applied to the semiconductor, the energy barrier between metal and semiconductor is reduced and electrons can pass the barrier and a current flow from semiconductor to the metal can be measured.

In solar cells a Schottky contact is usually formed. Depending on the work function of the metal and the doping concentration a current flow can be measured. Depending on the doping concentration of the semiconductor three mechanisms, which are illustrated in Figure 2.2.3 can occur: a) *thermionic emission*, b) *thermionic field emission* and c) *field emission*. Thermionic emission occurs for moderate barrier heights and doping concentrations $< 1 \times 10^{17} \text{cm}^{-3}$. Charge carriers can overcome the Schottky barrier through thermal activation. Field emission describes the current transport by tunneling through a very thin Schottky barrier and occurs for very high doping concentrations $> 1 \times 10^{20} \text{cm}^{-3}$. This effect is often used for solar cell contact formation and is described further in the following section. Thermionic field emission is a combination of the two mechanisms described and occurs for doping concentrations between 1×10^{18} - $1 \times 10^{21} \text{cm}^{-3}$ [35–37].

The measured barrier height against the metal work function for different metals on n-type silicon is given in Figure 2.2.4 from [27].

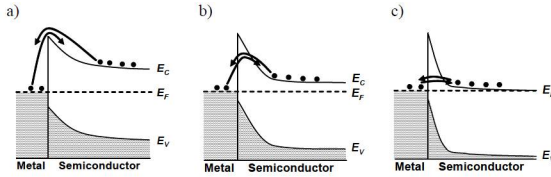


Figure 2.2.3: Current transport mechanisms for Schottky contacts: a) thermionic emission, b) thermionic field emission, c) field emission [38]

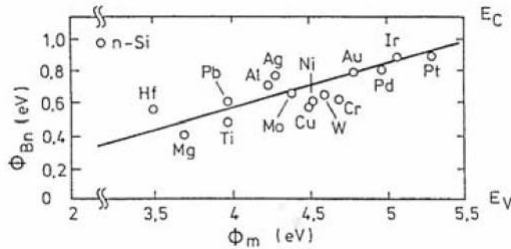


Figure 2.2.4: Barrier heights as function of metal work function for different metals on n-type silicon ([27] © 1984 IEEE)

2.2.2 Ohmic contact

The ohmic contact is the desired contact type for the metallization of solar cell applications. Ohmic contact provides transport of charge carriers with minimal losses and, thus, better performance of the cells. The energy band scheme of an ohmic contact between a metal and a n-type semiconductor is shown in Figure 2.2.5. As for the Schottky-contact there are two cases for which an ohmic contact formation is possible, vice versa to the Schottky contact.

- a) $\varepsilon_M < \varepsilon_{SC}$ and n-type semiconductor
- b) $\varepsilon_M > \varepsilon_{SC}$ and p-type semiconductor

Now, the work function of the semiconductor is higher than the metal one. Therefore, electrons diffuse from the metal to the semiconductor. On the semiconductor side an excess of electrons builds up a negative voltage U_c towards the metal. This voltage prevents fur-

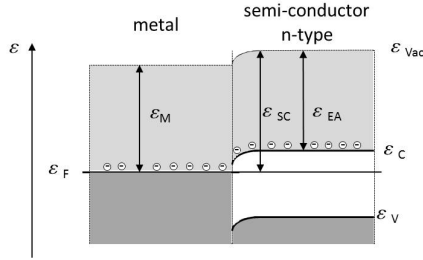


Figure 2.2.5: Band energy scheme of ohmic metal n-type semiconductor contact (retraced from [26])

ther electron transport. Due to excess of free electrons on the metal side, no depletion can be detected. No Schottky barrier is induced but a very small energy mismatch of $(\varepsilon_M - \varepsilon_{EA})$, which is small or even negative.

An external voltage applied to this contact leads to an almost unhindered current flow over the contact, independent of polarity.

An ohmic contact can also be reached by applying very high doped layer between metal and semiconductor. Figure 2.2.6 shows the band energy scheme. By very high doping of the semiconductor, the Fermi level can be raised over the conduction band edge. Through contact formation a very thin *space charge region* is formed between metal and semiconductor. Electrons are able to tunnel this energy barrier and enable a current flow between metal and semiconductor. Especially for the contact between metal and n-type semiconductor this contact design is used and is called *selective emitter*.

A simulation of the contact resistance in dependence of the *doping concentration* (number of doped atoms) N_D corresponding to different theories for silver as contact metal with a Schottky barrier height of 0.78 eV was done by Schubert [39] and is illustrated in Figure 2.2.7.

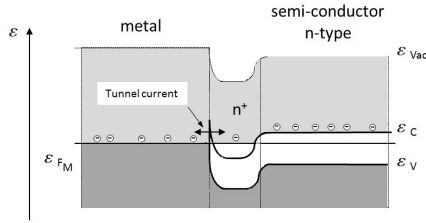


Figure 2.2.6: Band energy scheme of metal semiconductor contact with highly doped semiconductor surface (retraced from [26])

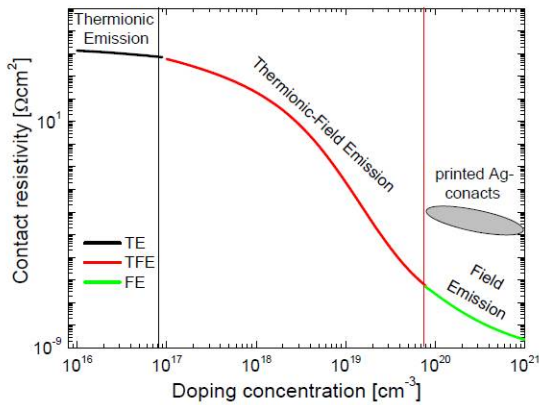


Figure 2.2.7: Simulation of theoretical resistivity ρ_c as a function of the doping concentration N_D for silver and a barrier height of 0.78 eV. Different current transport mechanisms are marked and the the region of contact resistivity for printed and fired contacts on silicon solar cells is illustrated [35, 39]

2.2.3 Printed and fired contacts

To contact solar cells the bulk metal can be applied to the cell by sputtering or evaporation through a shadow mask or a mask applied by a photolithographic process⁷. Those processes are cost intensive, therefore, only used for high efficiency cell concepts or on laboratory scale. For conventional crystalline silicon solar cells more cost efficient metallization methods have to be used. In industrial production the metals are applied through screen printing of metal pastes which have to be “fired” in a high temperature process to contact the emitter and base of the cell. Firing temperatures lie between 850 to 900 °C. For front side metallization a paste containing up to 90 wt% silver, 5 wt% glass and organics (solvent, rheological and other organic additives) are used. Silver has the highest electrical conduction value of all metals [40]. The specific line resistant of bulk silver is $1.58 \times 10^{-8} \Omega\text{m}$ [40]. Copper, for example, has a similar value but is able to diffuse through the silicon to the p-n junction causing shunts and destroying the cell, thus, can not be used in firing pastes. Alternatives like plated nickel-copper stacks with nickel as diffusion barrier for copper are being developed [12] and are necessary because copper makes up only 1% of the price of silver.

The paste is applied in a design called H-pattern (e.g. with 3 bus bars 1.5 mm in width and 60-80 fingers perpendicular to the bus bars and 60-80 μm wide). The goal is to print as narrow fingers as possible to avoid losses through shading of the active cell area, recombination losses at the metal-semiconductor interface, to gain high adhesion to silicon by using only minimal amount of silver. A typical front side metallization pattern is shown in Figure 2.2.8.

The glass phase in the front side paste is necessary to penetrate the anti-reflection coating (typically SiN_x), which is highly stable against chemicals and high temperatures. One important component in the glass is lead, which is toxic. The eruption directive 2011/65/EG

⁷Photolithography is a process from semiconductor industries. The process allows the application of very thin metallic patterns. A photo resist is printed on the solar cell and the grid pattern is transferred by light exposure to the photo resist. Dependent on the photo resist the exposed or the unexposed part of the resist is washed away and the metal is applied via evaporation or sputtering. The photo resist has to be removed (lift-off) again. The process is extremely complex and therefore quite expensive in relation to the total cost arguable for a solar cell. More details are given in Section 3.4.1

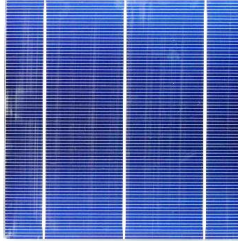


Figure 2.2.8: Typical H-pattern on silicon solar cell [1]

(RoHS) provides, that no certain hazardous substances like lead are allowed to be used in electronic devices. Solar cells are temporarily excluded but with further development one has to expect that solar cells will be included in the directive in the near future.

The contact formation by conventional metal pastes is less efficient than the contacts applied by sputtering or evaporation. To avoid losses due to metallization, development of contact formation procedures aim to form ohmic contacts on the rear and even the more critical front side of the solar cell. The contact formation process is complex and even up to now not fully understood. The current contact model will be discussed briefly in the following section.

2.2.4 Present contact model

Contact formation theory

Contact formation between a thick film silver paste and silicon solar cells is done in a drying and fast firing furnace. The temperature curves of the two processes are illustrated in Figure 2.2.9. At first there is the drying furnace where the biggest part of the solvents evaporates out of the paste at around 250 °C. The second process is firing of the cell, and the process is further divided into three main parts:

1. Organic burnout
2. Firing/Sintering
3. Cool down

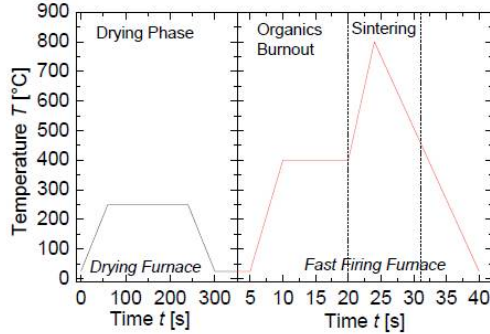
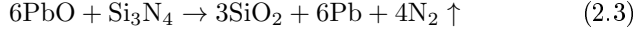


Figure 2.2.9: Temperature gradient in a fast firing furnace for thick film metalized silicon solar cells [41]

Within the drying zone solvents are evaporated to avoid explosively fast evaporation of solvent and organics during high temperature treatment causing local blast of metallization. In the following zone further organics like binders and polymer additives are burned out at around 400 °C. Organic burn out is done up until 550 °C. The glass temperature of the lead glass is already exceeded and first silver particle sintering starts. Above 550 °C glass is molten and wets the silver particle surface as well as the silicon nitride surface. Rearrangement of silver particles takes place and further sintering occurs above 580 °C (Figure 2.2.10 a)). Kalio adds that silver particle rearrangement occurs several times during the whole firing procedure [41]. In the next high temperature zone between 800-900 °C real contact formation with penetration of the *anti-reflection coating*, ARC, takes place. After reaching the peak temperature, the cells are rapidly cooled down to room temperature. Heating and cooling is done very quickly (> 50 °C/min) [42].

The contact formation model described here is based on the findings of Gunnar Schubert, Matthias Hörteis, Andre Kalio and Hong et. al. [35, 39, 41, 43].

Referred to Schubert and Hörteis [35, 39] etching reaction of the silicon nitride penetration takes place according to equation 2.3 (Figure 2.2.10 b))

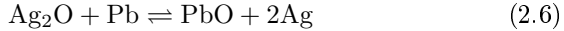


In the range of 700-800 °C silicon is oxidized by lead oxide and incorporated into the glass (Figure 2.2.10 c)):

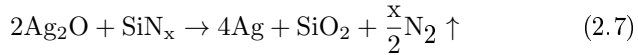


Parallel to the penetration of silicon nitride Schubert suggests that silver crystallites form out of a liquid silicon-glass or liquid silicon-lead-silver phase (Figure 2.2.10 d-f)). He concludes that molten lead is the main driving force of the reaction.

Hong et al. suggested that liquid lead reduction and further a liquid lead phase are only possible by absence of silver. Silver oxide would suppress the reduction of PbO by oxidation according to the following reactions [43]:



Additionally silver oxide reduces silicon nitride and penetrates the ARC.



Hörteis argues that the silver crystallite formation cannot be explained by silver ion diffusion originating from the glass layer [35]. According to his thesis the amount of silver dissolved in the glass would be too little. The silver would precipitate rather from a liquid Pb-Ag or Bi-Ag phase caused by the redox reactions 2.32.4 and 8.5, 8.6, respectively [35].

Kalio observed that evaporated silver on a pure silicon surface is able to form a glass layer on top of the silicon wafer at curing temperatures of 550 °C and a duration of 3 s [41]. But only on wafers with a very high doping concentration (phosphorus doping) crystallite formation at 750 °C curing temperature could be observed. Silver and silicon form an eutectic mixture at 833 °C [44] which is far higher than the temperature observed by Kalio. This effect is called selective corrosion and has already been described by Schatt [45]. The silver crystallite

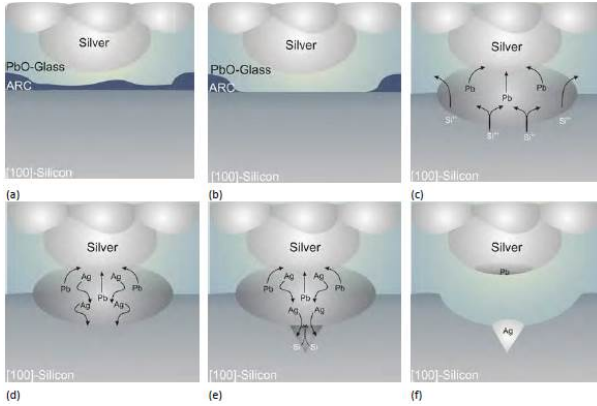


Figure 2.2.10: Simplified contact formation model according to Gunnar Schubert; a) cross section of thick-film silver metallization after organic burn out on (100) silicon wafer with an anti-reflection coating (ARC); b) ARC penetration through glass; c) glass reaction with silicon and melt formation of liquid lead and silver; d) silver diffusion to silicon surface through lead-silver melt; e) dissolving of silicon and silver penetration; f) silver crystallite formation after cool down [39]

formation is supported by lattice failures and impurities (for example, through doping) of the silicon surface [46, 47]. Suganuma showed that silver and the (111) crystal surface on pyramids of alkaline textured (100) silicon wafers have a well fitting lattice match, which enables silver to precipitate on the silicon surface [48].

The back contact is usually formed by aluminum. An aluminum paste is screen-printed at the back and is co-fired with the front-side. Aluminium partially diffuses into the silicon, which leads to a highly doped p^+ -region (aluminum provides one electron less to the lattice than silicon) and the *back surface field* (BSF)⁸ is formed. It acts as a passivation layer for the back side similar to the ARC of the front side.

⁸The back surface field is formed by a highly doped region at the rear side of the solar cell. It forms a passivation layer at the back side.

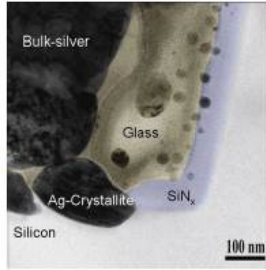


Figure 2.2.11: TEM image of interface of paste applied silver - silicon contact: direct silicon/silver crystallite/silver bulk contact [51]

Current transport at the metal semi-conductor interface of paste applied contacts

Theoretically, the current has several possible paths to cross the metal semiconductor interface:

- a) silicon \rightarrow silver bulk
- b) silicon \rightarrow silver crystal \rightarrow silver bulk
- c) silicon \rightarrow silver crystal \rightarrow thin glass layer \rightarrow silver bulk
- d) silicon \rightarrow silver crystal \rightarrow interstitial traps in glass \rightarrow silver bulk
- e) silicon \rightarrow silver precipitation in glass \rightarrow silver bulk

Assuming that the wettability of the glass on the silver particles is very high, which is necessary for effective liquid phase sintering⁹ [49] and all surfaces should be wetted, path a and b are quite unlikely assuming no glass between the silicon and silver or silver crystallite and silver bulk, respectively. However, those paths are postulated to be the main current flow paths by Cabrera and Hörteis [50]. Hörteis observed direct silicon/silver crystallite/silver bulk contact in TEM measurements (Figure 2.2.11)

Cabrera showed experimentally that most of the current is transported from silicon to silver (crystallites) especially at pyramidal tips where less or even no glass is found [50, 52].

⁹Liquid phase sintering is discussed in Section 3.5 in more detail.

Paths c and d are postulated by Schubert. Electrons are able to tunnel a very thin glass layer (<5 nm) [53] or through interstitial traps in the glass layer [39].

The current path through glass tunneling (e) is postulated by Dupont [54].

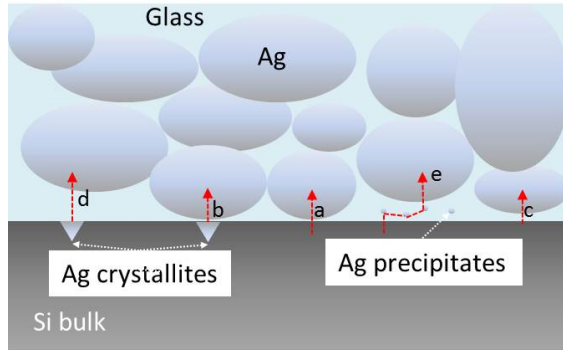


Figure 2.2.12: Possible current paths on the metal semiconductor interface of paste applied silver metallization on crystalline silicon solar cells

2.3 Production prozess of crytsalline silicon solar cells

Further details to the topic in this Section as well as alternative cell concepts can be found in literature [4, 24].

In this section the technological route for production of “standard” silicon solar cells is described. The process is schematically illustrated in Figure 2.3.1.

High quality silicon material lowers recombination losses within the material. This high purity silicon material is used. Typically highly purified monocrystalline material (FZ¹⁰ or Cz¹¹, multicrystalline (mc) silicon or upgraded metallurgical-grade silicon¹² (umg) is used. The resulting effecencies for monocrystalline cells are higher due to less recombination losses at grain boundaries.

The wafers get sawn out of the silicon block or brigg. The material usually owns a basic p-type doping of around 10^{16} cm^{-3} . The surface gets chemically cleaned and the surface damages resulting from sawing and causing recombination at the surface is etched. Within the same process, the surface gets textured¹³, which improves the optical properties.

To develop the emitter, the wafer surface is diffused with phosphorus, using a POCl_3 atmosphere and heating the wafers to 800-900 °C. POCl_3 concentration, temperature and duration decide about the doping concentration and depth. A phosphorous glass remains at the surface after the diffusion and has to be removed by etching. In the same process step, the emitter which is short circuiting the cell over the edges is separated from the rear by single side wet-chemical etching¹⁴. The complete surface of the wafer is now n-type doped. The emitter is usually several nm thick and owns a surface concentration of 10^{21} cm^{-3} .

In the next step an ARC layer of SiN_x with a thickness of 70-

¹⁰“Float-Zone” material with very high purity

¹¹“Czochralski” silicon with high purity

¹²Silicon material with less purity and ten times cheaper than mc-silicon

¹³Alkaline anisotropic etch with $\text{KOH} + \text{isopropanole}$ for monocrystalline silicon, resulting in random pyramids, acidic isotropic etch with $\text{HF} + \text{HNO}_3$ on mc-silicon (anisotropic etch due to multiple crystal orientations not possible)

¹⁴Alternatively the so called “laser edge isolation” is used: After the co-firing step, the front emitter gets isolated from the rear side by a laser.

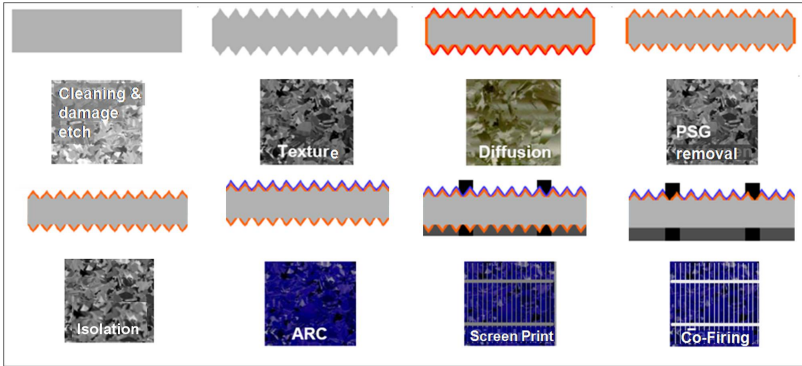


Figure 2.3.1: Silicon solar cell production scheme: Top rows: Cross sectional pictograms of monocrystalline silicon solar cells. Bottom rows: Top view pictograms of mc-solar cells [12]

75 nm, is applied to the wafer surface. This process is typically done by *plasma enhanced chemical vapor deposition*, PECVD. The ARC layer enhances the optical and electrical surface properties.

The rear side is almost full area screen printed with aluminium paste. At the soldering spots a paste of aluminium and silver is used. The front side is standardly contacted by screen-printed silver paste. Both cell sides are simultaneously contacted by co-firing at temperatures >800 °C. The firing of the back side leads to overcompensation of the n-type doping of the wafer rear-side by p-type aluminium, recreating the back-surface field (BSF).

2.4 Nanoparticles, particle sintering and stabilization

2.4.1 Nanoparticles

Particles with diameters within a size range of 1-100 nm are called *nanoparticles* (Figure 2.4.1).

Due to their very high specific surface (surface to volume ratio), nanoparticles have unique physical and chemical properties:

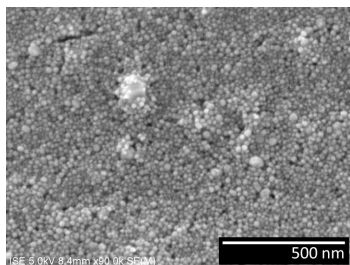


Figure 2.4.1: SEM image of nearly monodispers silver nanoparticles

- very high surface energy and surface tension
- very high surface charge
- high chemical reactivity
- surface forces become more influencing compared with mass forces
- special optical properties.

For metallization, especially high surface energy, high surface charges and the higher chemical reactivity are important.

Due to the high chemical reactivity nanoparticles can be used as catalysts in reaction. On the other hand, nanoparticles have to be stabilized or protected against unwanted reactions e.g. oxidation, which can be very rapid.

Due to the high surface charge, nanoparticles are able to form stable suspensions without additional stabilizers or emulgators. The surface charge yields to an repelling effect between the particles in (water based or ionic) solutions. But this effect is counteracted by the high surface tension, which causes agglomeration of single particles to lower the surface energy. Therefore, particle stabilization without additional stabilizers is only possible for low particle concentration.

However, the high surface energy and tendency to agglomerate can also be used technically: metal nanoparticles possess melting temperatures far below the melting temperature of the corresponding bulk material (down to 10 %). This has experimentally been shown on gold

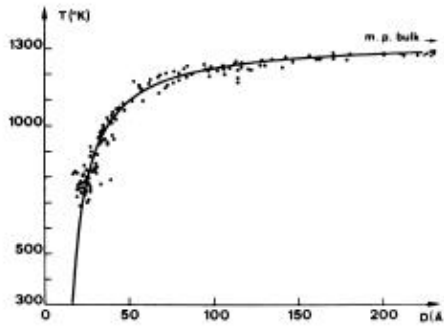


Figure 2.4.2: Experimental and theoretical melting-point temperatures of gold nanoparticles dependent of size (Reprinted figure with permission from [23] Copyright 1976 by the American Physical Society)

nanoparticles by Buffat [23] and is called *thermodynamic size effect*. Figure 2.4.2 shows the melting temperature drop of gold nanoparticles against the particle size.

Therefore metal nanoparticles are used in inks and pastes for low temperature metallization approaches (150–300 °C) [55–65]. Because of its nobility and high conductivity especially silver is used as nanoparticle within this formulations.

2.4.2 Nanoparticle synthesis

Two basic approaches can be used to synthesize nanoparticles:

- the *top down* approach
- the *bottom up* approach

Figure 2.4.3 illustrates both approaches:

When using the top down approach nanoparticles are produced by breaking the bulk material, e.g., by milling. This approach is suitable especially for porous materials but not for ductile materials e.g. metals like silver.

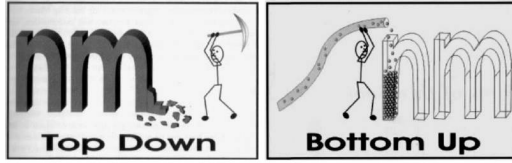


Figure 2.4.3: Illustration of top down and bottom up approaches [66]

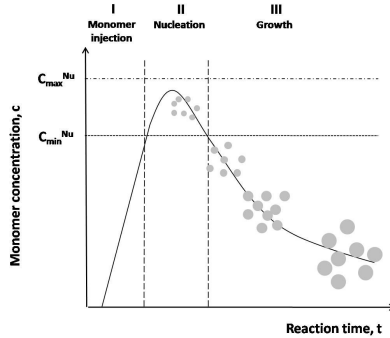


Figure 2.4.4: Illustration of size control of nanoparticle synthesis in the framework of La Mer model

In this case the bottom up approach is used. The nanoparticles are synthesized starting from ions or decomposing molecules, which form so called *seeds*, a cluster of only a few atoms of the material, which then grow to nanoparticles. Also, foreign seed materials can be used to trigger the growth of the particles.

The control of the growth process can be difficult depending on the material. The key to monodispers nanoparticle growth is control and separation of the nucleation and growth phase during the synthesis, respectively. The principle is illustrated in Figure 2.4.4.

The La Mer model describes the time dependency of nanoparticles nucleation and growth. During the injection time (I) the monomer concentration increases rapidly. At a threshold concentration c_{min}^{Nu} self nucleation appears and monomer concentration gradually decreases. As long as the critical level of monomer concentration c_{max}^{Nu} is not reach

further nucleation is suppressed. With further monomer transport the particle growth continuous. At a certain point so called “Ostwald ripening” appears and smaller particles are redissolved in favour for bigger particles. At this point the particles grow in different speed and no monodispers product can be collected. With even longer reaction times particle saturation appears and the particles participate from the solution [67].

Important factors in nanoparticle synthesis are: temperature, heating rate, educts, capping agents (which stabilize the nanoparticles and also control growth rate), potential reducing agents and timing. More detailed information about the synthesis of nanoparticles, control of size and shape can be found in the literature [67–70].

2.4.3 Particle sintering and stabilization

The sintering of particles is the welding of particles below their melting temperature. The direct sintering of powders (ceramic or metal) is called *solid-state sintering*. The connection of the single particles is formed via diverse diffusion mechanisms which are illustrated in Figure 2.4.5:

According to Hajmrle [28] particle sintering takes place in several stages which include different diffusion mechanisms which are dependent on the temperature and activation energy, respectively. In their work Hajmrle et al. [28] describe the sintering of silver particle between 2-50 μm in diameter. Due to the lower melting point of nanoparticles compared to the corresponding bulk material one can assume a drop of sintering temperature as well. Hajmrle assumes that the sintering mechanism below 570 $^{\circ}\text{C}$ (for particles of 2-50 μm in diameter) is based on two mechanisms: initial plastic deformation of the material, which takes place as long as the neck radius is small and the surface tension is still high. With increase of the sintering neck, surface tension drops and plastic deformation is no longer possible.

The second possibility is the diffusion of solid at the grain boundary. Grain boundary diffusion has the lowest activation energy of all mentioned diffusion paths and, therefore, the most likely one. Grain boundary diffusion is also dependent on the angle between particle and sintering neck. Therefore, particle rotation can be observed during particle sintering. The energy required for grain boundary formation counteracts the diffusion process. Initial sintering takes place until

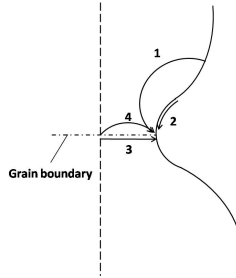


Figure 2.4.5: Illustration of sintering mechanisms of two particles. Contact point of two particles and atom diffusion paths are shown: 1-Volume diffusion (no particle approach), 2-Surface diffusion (no particle approach), 3-Grain boundary diffusion (particle approach), 4-Volume diffusion (particle approach) (retraced from [28])

surface tension has reach equilibrium with grain boundary formation energy. For further sintering more energy and higher temperatures are needed. At this point the metallic layer has still a porous structure, thus, the maximum reachable conductivity will always be lower than the bulk conductivity of the corresponding dense metal [28].

At temperatures between 570 -720 °C (particles 2-50 μm) several diffusion mechanisms occur: boundary diffusion, surface diffusion and volume diffusion. At temperatures above 720 °C only volume diffusion appears [28].

Those diffusion processes lead to further reduction of the pores between the particles. In addition, the degree of crystallinity rises and consequently the conductivity rises. In ideal cases, at adequate temperature and sintering time a bulk is formed and the maximal conductivity can be reached.

Below a certain particle diameter, which is depending on material and particle shape, sintering occurs at very low temperatures, even at room temperature. The only requirement is a direct contact between the particles to start the sintering process.

Due to the Brownian motion of nanoparticles in suspensions the particles have to be stabilized in ink and paste formulations to avoid agglomeration and sedimentation of the particles through collision. Since

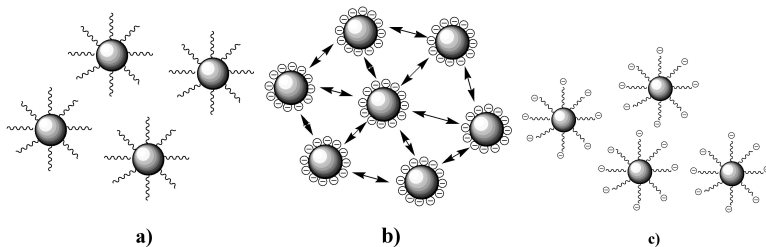


Figure 2.4.6: Illustration of particle stabilization mechanisms: a) steric b) electrostatic c) electrosteric

metals have a much higher density, metallic nanoparticles are more challenging to disperse and high concentrations of metal nanoparticles in solution are difficult to achieve. To avoid the aggregation, the particles get stabilized already during synthesis with a dispersant. This *capping agents* are coordinated (adsorbed) via an *anchor group* to the metal surface and ideally possess a high affinity to the metal.

There are three mechanisms (Figure 2.4.6) which prevent particles from collision. The capping agents are chosen depending on the stabilization mechanism that should be used and the ink formulation.

1. Sterical stabilization
2. Electrostatic stabilization
3. Electrosteric stabilization

1. Sterical stabilization is most often used for formulations in organic solvents and provides highest possible metal concentrations. The capping agent is a bulky polymer which ideally contains an anchor group with high affinity to the metal. The organic solvent is chosen fitting to the polymer: The polymer uncoils and stretches out into the solution. The bulky surrounding around the particle keeps particles at distance longer than the effective range of attracting van der Waals forces. Additional dispersants in the ink formulation which can also interact with the capping agent can further stabilize the dispersion. Most popular capping agent used for this kind of stabilization is poly(N-vinyl-2-pyrrolidone) (PVP). PVP is often used during the synthesis

of metal nanoparticles especially silver nanoparticles as it allows good control of size and even shape of the particles and acts as a very good dispersant for the formed particles in dispersion [64, 71–75].

2. In solvents with high dielectric constants, such as water, electrostatic stabilization can be used. In this case, the capping agent contains charged functional groups (for e.g. carbonyls for basic dispersions or amines for acidic dispersions). An electrostatic double shell is formed around the particles and keeps them from aggregation via electrostatic repulsion. A crucial size in this kind of dispersion is the surface potential of the particles: the higher the potential, the higher the electrostatic repulsion and the more stable the dispersion. The zeta potential ζ is most often used to describe the surface potential of particles in dispersions. Dispersions with zeta potentials $|\zeta| > 35 - 40$ mV are considered as stable (for electrolyte concentrations $< 10^{-2}$ mol · dm⁻³) in water [64]. Increase in ionic strength leads to decrease of the electric double layer and to collision of particles. At high metal ion concentrations, which are needed during the synthesis of the nanoparticles, the electric double layer is rather small. Thus, high concentrations of particles stabilized only via electrostatic stabilization are hard to realize.
3. Electrosteric stabilization is a combination of both mechanisms described above. Bulky polymeric capping agents with charged functional groups, *polyelectrolytes*, are used to keep the particles to hang at poise. This mechanism is most often used in aqueous dispersions. Often used capping agents for this kind of stabilization are: poly (acrylic acid) salts (PAA), carboxymethyl cellulose sodium salts, block co polymers with acidic groups (like Disperbyk 190 from Byk Chemicals) and others [64]. Electrostatic stabilization is very effective and a good choice to stabilize particles with high densities like silver.

To initiate the sintering of particles the capping agent has to be removed from the surface. To achieve the removal several sintering methods are possible and described in the following sections.

2.4.4 Thermal sintering

Thermal sintering is the most often used method to achieve the connection between nanoparticles and form a conducting metal layer. Due to the drop of melting temperature of metallic nanoparticles and the high surface potential of nanoparticles, the sintering temperature is also drastically reduced and the contact between two particles can trigger the sintering of the particles even at room temperature. The aim is to get values as close to silver bulk conductivity as possible ($1.58 * 10^{-8} \Omega\text{m}$). After printing the ink dries and the solvent evaporates. Capping agents, dispersants and other high molecular ink components remain between the single particles and prevent particle sintering. To also eliminate high molecular organics, temperatures between 200-350 °C are normally necessary [16, 65, 76–79]. The aim for low temperature metallization is its use on temperature sensitive substrates like poly(vinyl terephthalate) (PET) or polycarbonate. For this reason a lot of effort has been undertaken to reduce the sintering temperature of the metal nanoparticle inks [16, 65, 80–82]. Ink formulation and particle stabilization has been optimized by using short capping agents (oligomers for example 1-dodecylamine [61]), which evaporate at lower temperatures or capping agents which decompose. Curing temperature could be lowered down to 150 °C [61, 81]. Using shorter capping agents also means to lower the dispersion ability, therefore, the maximal concentration of metal part in the ink and shelf life. Another possibility is to further reduce particle size.

2.4.5 Chemical sintering

As already mentioned, to start the sintering process, the capping agent has to be removed from the metal particle surface to enable particles to touch. If bulky polymers are used to keep the particles at distance one can trigger sintering by forcing the polymers around the particles to recoil. In this case distance between particles becomes too short and attractive van der Waals forces become effective. The particles touch and sintering starts. In case of polyelectrolytes the recoilition of the stabilizing polymer can be forced by adding a chemical with opposite charge. The zeta potential in dispersion will drop and particles start to agglomerate and to sinter. This mechanism has been demonstrated by Magdassi et al. on silver nanoparticles capped with the anionic poly-

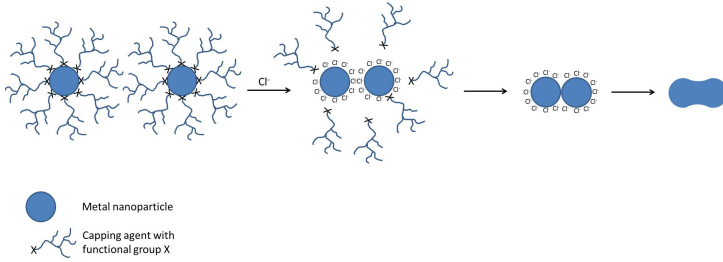


Figure 2.4.7: Illustration of chemical sintering through substitution with chlorine as sintering agent

electrolyte poly(acrylic acid) (PAA) and the cationic polyelectrolyte poly(diallyldimethylammonium chloride)(PDAC) as electrolyte.[83]

The capping agent coordinates to the metal particle surface via an anchor group which is most likely a functional group containing a hetero atom like nitrogen, oxygen, sulfur, phosphorus or halides. Another method to get the particles in close contact is to remove those capping agents from the surface of the metal. This can be achieved by substitution of the stabilizing agent by small molecules or even ions with higher affinity to the metal than the functional group of the capping agent (e.g. chlorine). Throughout this work the substituting chemical is named *sintering agent*. Figure 2.4.7 illustrates the process of chemical sintering via substitution:

The sintering agent is applied to the ink after deposition. For simplicity chlorine is used within this explanation. The chlorine ions have a higher affinity to the metal surface than the anchor group “X” (see Figure 2.4.7). It coordinates to the surface of the particles and ousts the capping agent from the metals surface. Since chlorine is much smaller than the bulky polymer, metal nanoparticles get into contact and the sintering process starts.

This way of sintering has also been invented and first demonstrated by Zapka et al. [84] and further developed by Grouchko et al. and Magdassi et al.[60, 79]. The sintering agents can be applied by printing a solution containing the sintering agent on top of the dried ink [85] or by evaporation with vapor, e.g., HCl vapor [60].

2.4.6 Other sintering methods

There are several other sintering methods which are all based on the concept of thermal sintering. The methods differ from classical thermal sintering by the way of energy input. The energy input that heats up the metal nanoparticles and starts the sintering process can be realized by

1. photonic sintering
2. microwave sintering
3. electrical sintering
4. plasma sintering.

1. When using photonic sintering the printed grid becomes cured using flash lights, lasers and other light sources. A commercially available technique for flash light sintering on temperature sensitive substrates has been developed by NovaCentrix (USA). The “PulseForge” uses high energetic light flashes with tunable light intensity, flash duration and number [86]. The flash light heats up the printed ink on top of the substrate to a maximum temperature T_{max} . Via conduction through the much thicker substrate (compared to the printed layer) the film cools down. Shortly after the light flash, substrate and applied printing reach thermal equilibrium at moderate temperatures as can be seen from Figure 2.4.8. The substrate facing the printing does get heated usually far beyond its working temperature. However, because of the short time period of heat application ($\sim 40 \mu\text{s}$) the substrate does not get significantly damaged.[29].

The method is only effective on substrates which have a low thermal conductivity. Otherwise the thermal energy which is produced by the nanoparticles by light absorption, gets transferred through the good thermal conductivity of the particles and the substrate to the chuck. For samples with high thermal conductivity, very high light intensities and number of flashes have to be used, which can already damage the substrate [29].

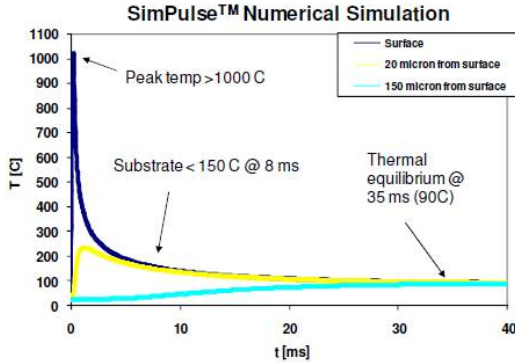


Figure 2.4.8: Thermal simulation of photonic curing process ($300 \mu\text{s}$, $1 \text{ J}/\text{cm}^2$) for a $1 \mu\text{m}$ thick silver film on $150 \mu\text{m}$ PET (© 2011 NSTI <http://nsti.org>. Reprinted and revised, with permission, from Nanotech, pp.220-223, June 13-16, 2011. Boston, U.S.A.[29])

Conductivities of $20 \text{ m}\Omega/\text{sq}$ and a resistivity of 4 times of bulk silver for silver nanoparticle inks and $150 \text{ m}\Omega/\text{sq}$ and 40x bulk resistivity of copper for copper thin films could be achieved [87]. The appearance is the same as for thermally cured films.

Lasers are also used for curing metal ink prints which have the advantage of very high precision. Metallic conducting lines of $6 \mu\text{m}$ width could be sintered, which is by far more precise than ink jet printing ($20\text{-}50 \mu\text{m}$) and can otherwise only be reach by photolithographic techniques [55].

2. Microwave heating is already used for sintering of dielectrics and chemical reactions [57]. The microwave radiation is absorbed due to charge carrier coupling of rotating dipoles. However, absorption depth is strongly dependent on the material. For metals like Ag, Au and Cu it is only $1\text{-}2 \mu\text{m}$. Due to good thermal conductivity of the metals the sintering is also effective in slightly thicker films than the penetration depth ($\sim 4 \mu\text{m}$). Still, microwave sintering is not appropriate for thick film applications. Resistivities of 5 % of bulk silver could be reached [57]. A fur-

ther reduction of resistivity down to 34 % of bulk resistivity of silver has been reached by printing and thermally curing an antenna grid prior to the printing of a silver grid line. The antenna design absorbed a higher amount of microwave radiation. However, sintering effect was still dependent on starting conductivity of the printed silver test line [58].

3. Electrical sintering uses dissipation to sinter the nanoparticles in printed patterns. To make this method work a minimal conductivity must already exist. This is typically not the case for metallic nanoparticle inks and a pre-curing step at low temperatures is necessary. Further, an electrical contact has to be made to the patterns what slows fabrication significantly down [64]. Conductivities as low as 50 % of bulk silver could be reached [56].
4. Plasma sintering combines two effects which triggers the sintering of metal nanoparticles: the ions generated during the process destroy the capping agents surrounding the nanoparticles which enables the particles to come into contact. At the same time the particles partially absorb the plasma energy and heat up, which further stimulates the sintering process. The thermal conductivity of the substrate plays an important role regarding the final quality and conductivity of the printed pattern that can be reached through plasma sintering: the lower the thermal conductivity of the substrate the higher is the conductivity reachable by plasma sintering. Lower thermal conductivity of the substrate prevents the heat generated within the particle pattern to be drawn away which leads to more effective particle sintering [59]. Conductivities as low as 2.5 to 3x of the bulk conductivity of silver could be reached [59, 64].

2.4.7 Comparison with liquid phase sintering

Solid-state sintering is a rather slow process with limited reachable density and requires quite high activation energies and, therefore, high temperatures. Only the thermodynamic size effect allows nanoparticles to sinter at low temperatures as described above. Sintering has already been used industrially to sinter ceramics and alloys at higher

temperatures close to the melting point of the bulk materials. Sintering times and temperatures have been quite high which lead to the development of the *liquid phase sintering* process: a low melting material is added to the powder that should be sintered together. In case of silicon solar cell metallization, silver is the powder and a lead glass forms the liquid phase. To reach ideal wetting of the solid particles typically 5-15 % of glass are used [49]. The liquid phase is chosen in such a way, that the solid is soluble in the liquid. When the melting point of the glass is reached, surface atoms of the silver powder are dissolved in the liquid glass phase. As diffusion in liquids is much higher than in the solid state, sintering occurs faster, more effective and at lower temperatures. Capillary forces additionally pull the solid grains together [49]. Liquid phase sintering can also be divided into three phases[41]:

1. Rearrangement: Solid particles get wetted by the liquid phase and capillary forces densify the solid phase.
2. Solution and precipitation: Solid particles get dissolved into the liquid phase and precipitate again. Here a process called *Ostwald ripening* occurs: small particles are getting redissolved and bigger particles grow further. The amount of liquid determines diffusion distance and amount. Densification is influenced by the solubility of the solid in the liquid. At the same time of liquid phase sintering, solid-state sintering also occurs between neighboring particles. Besides dissolution of particles in the liquid, also liquid can be dissolved inside the solid phase: swelling occurs.
3. Final densification: This stage is reached as soon as solid-state sintering becomes dominant. The liquid is encapsulated inside voids of the solid phase and liquid diffusion over longer distances is no longer possible. The highest densification can only be reached with very long sintering times comparable to pure solid-state sintering.

Comparing solid-state sintering of metal nanoparticles and liquid phase sintering of metal powders two facts attract attention:

The sintering temperature is strongly influenced by the size and capping agent of the metal nanoparticles which can be pushed down to

even room temperature as already discussed above. For liquid sintering the process temperature is dependent on the melting temperature of the liquid phase and the solubility of the solid phase inside the liquid.

At higher temperatures and for longer sintering times solid-state sintering of nanoparticles can reach much higher densities compared to liquid phase sintering. This is due to the liquid phase which will always remain in the solid layer after cooling, in case boiling temperature of the liquid phase is not reached which is generally not the case. Additionally, almost completely dense solid phases can be reached at low temperatures (compared to the melting temperature of the corresponding bulk material) at short sintering times with solid-state sintering of metal nanoparticles, shown in Section 5.

2.5 Hetero junction with Intrinsic Thin Layer Cells

Knowledge and principles discussed in this chapter and further details can be found in the literature: [5, 30]

2.5.1 Working principle

The key of silicon hetero junction devices is the separation of the (ohmic) contacts, which are highly recombination active, from the crystalline silicon surface by introducing a buffer layer with a slightly wider band gap than the base material [88]. Ideally the buffer layer should act like a semi-permeable membrane for carrier extraction: electrons should slowly diffuse through the buffer layer to allow a high voltage to be built up, but fast enough to avoid excessive recombination [4]. In addition, the interface state density should be minimal; otherwise, the buffer layer would even enhance recombination. Amorphous silicon is a promising candidate for such a buffer layer, as it has a slightly wider band gap than crystalline silicon and can be easily doped, p-type and n-type.

Hetero junction with intrinsic thin layer (HIT) solar cells were first introduced by Sanyo, Japan in 1990 [89]. Fuhs, et. al., studied the a-Si:H/c-Si hetero structure in 1974 [90]. It has been shown, that amorphous silicon provides excellent surface passivation to crystalline

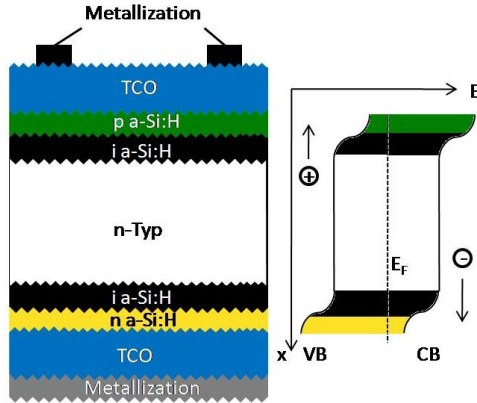


Figure 2.5.1: Structure of HIT solar cell including the band diagram

silicon [91] and the first solar cell devices with amorphous silicon have been reported by Hamakawa et al. in 1983 [92]. However, the fill factors (FF) of those cells were rather low and further investigation of the a-Si:H/c-Si junction revealed high interface state densities. Sanyo, Japan solved this problem by introducing an intrinsic a-Si:H layer as buffer to the p-type a-Si:H layer in 1990. They called the structure *hetero junction with intrinsic thin layer* - or short HIT [89]. This invention was the major breakthrough for the hetero junction concept. The cell structure designed and further developed from Sanyo, Japan is shown in Figure 2.5.1.

As base material n- or p-type crystalline silicon is used. Front and rear side are passivated with a very thin (~ 5 nm) layer of intrinsic amorphous silicon (a-Si:H(i)). The good ability of passivating the c-Si surface is explained by hydrogenation of *dangling bonds* (unsaturated bonds) at the silicon surface [91]. Depending on the base material the emitter is formed by p-type or n-type doped a-Si:H layer of a thickness around 15 nm, respectively. The *back surface field* (BSF) is formed by a layer of a-Si:H(n) or a-Si:H(p) layer which is also 15 nm thick. The front side is contacted with a full area *transparent conductive oxide* (TCO) layer (thickness 70-80 nm), which is again contacted by a metal grid. Amorphous silicon has a quite low conductivity which makes a more conductive contact layer necessary for collection and transport

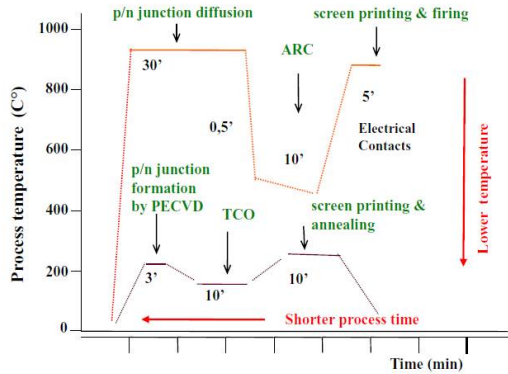


Figure 2.5.2: Scheme of thermal budget and processing time for c-Si cell and SHJ cell processing estimated by Zeman [30]

of charge carriers. The rear side can also be covered with TCO, but is not obligatory. The rear side can also be directly contacted by a metal.

The main advantages of the hetero junction cell structure are high values for the *open circuit voltage* (V_{OC}), which can be > 740 mV. This high voltage leads to very high efficiencies and has led to a new world record for silicon based single junction solar cells of $\eta = 25.6$ % as recently demonstrated by Panasonic using the more advanced IBC-HIT¹⁵ cell structure [15].

2.5.2 Challenges of metallization

Amorphous silicon as buffer and passivation layer provides an additional advantage compared to conventional crystalline solar cells. All process steps can be performed at low temperatures (< 250 °C), which saves energy costs in production and avoids process-induced material and cell degradation caused by high temperature process steps. An estimated scheme for the thermal budget and processing time for conventional silicon solar cells and *silicon hetero junction* (SHJ) cells from [30] is shown in Figure 2.5.2.

¹⁵interdigitated back contact - hetero junction with intrinsic thin layer

As can be seen the metallization of conventional silicon solar cells is done at temperatures around $T = 800\text{-}900\text{ }^\circ\text{C}$. However, amorphous silicon is very sensitive to high temperatures and degrades [93]. The metallization is, therefore, done by thermal evaporation or sputtering. Both processes require a photolithographic masking of the cell area, which is a very cost intensive process and is normally only used for high efficiency lab scale cells but not in industrial production. Polymeric screen printing pastes with low curing temperatures around $200\text{ }^\circ\text{C}$ are well suited. The pastes have to reach high conductivities and provide a low contact resistance to the underlying TCO layer at the same time. Current polymer pastes reach conductivities around $10 \cdot 10^{-8} - 15 \cdot 10^{-8} \Omega\text{m}$ which is still 4 to 6 times higher compared to normal screen printing pastes. In addition, silver consumption is high which raises the production costs.

Indium tin oxide (ITO) which is mostly used as TCO for HIT cells acts as a good barrier against metal ion diffusion including copper, which has a very high diffusion coefficient in silicon and damages the cell. Thus, copper pastes and plated copper contacts either by direct plating or deposited on a seed-layer are alternative metallization techniques [5].

A third alternative is provided by silver nanoparticles which sinter at very low temperatures ($< 300\text{ }^\circ\text{C}$) and are thus promising candidates for the development of low temperature sintering inks and pastes for full metallization concepts or seed-and-plate processing, respectively. The suitability and requirements on such low sintering nanoparticle inks and pastes was investigated within this work and will be discussed in detail in Chapter 5.

2.6 Transparent Conductive Oxides - TCOs

Knowledge and principles discussed in this chapter and further details can be found in the literature [31].

2.6.1 General overview

A variety of new electronic applications like flat screens, touch displays, organic electronics, thin film applications like coated windows and solar cells, need materials with a high conductivity and high trans-

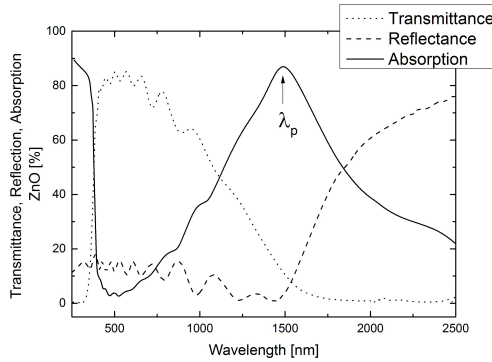


Figure 2.6.1: Optical spectra of typical ZnO transparent conducting oxide (T : Transmittance, A : Absorption, R : Reflection) (data from [31])

parency in the visible range of light at the same time. Conductive materials like metals possess in general a *free electron gas*: the electrons are free to move throughout the conduction band. Due to the absence of a band gap, metals are nontransparent conductors. The free electrons are able to absorb almost every optical energy independent of wavelength. Semiconductors normally have small band gaps, which can easily be overcome by electrons; for example, through thermal energy or light induced energy. However, the small band gap leads also to absorption in the visible spectrum of light and is, therefore, not useable for applications mentioned above. *Transparent conductive oxides*, TCOs, possess wide band gaps around 3.0 eV and are transparent for the visible wavelengths. Doping provides additional electrons which are free to move inside the conductive band, which is the reason why TCOs often have very high conductivities. Therefore, TCOs meet both criteria of transparency and high electrical conductivity in certain limits. Figure 2.6.1 shows optical reflection, transmittance and absorption spectra for ZnO as TCO coated on glass.

A variety of TCOs is known today and for each application one has to choose according to its needs. An overview about different TCOs and their properties are given in tables A.1.1 and A.1.2 in the

appendix (2). Most often used TCOs are: SnO_2 , In_2O_3 , InSnO and ZnO .

2.6.2 Working principle

Most relevant characteristics of TCOs are their optical and electrical behavior in terms of conductivity and contact formation to metals or other semiconductors.

As can be seen from Fig. 2.6.1 the material is quite transparent in the visible spectrum between 400-700 nm, due to its wide band gap. The oscillations which can be detected in this region are caused by thin film interference effects. At shorter wavelength below 400 nm spectral absorption is high, because now the energy is high enough for electron excitation from the valence to the conduction band. At higher wavelength around 1000 nm transmittance starts to decrease while reflection starts to increase from 1500 nm and above, due to the activation of plasmons¹⁶. Also, the absorption of light occurs and reaches its maximum at the *plasma wavelength*, λ_p , as indicated in Fig. 2.6.1. The plasma wavelength shifts to shorter wavelengths when *electron density*, N , in the conduction band is increased; for example, through doping:

$$\lambda_p \sim 1/\sqrt{N} \quad (2.8)$$

In case of very high electron concentrations the shift can be so intense, that it decreases even the visible wavelength transmittance [31].

For the resistivity of semiconductors equation 2.9 applies:

$$R_{Sh} = 1/e\mu nt \quad (2.9)$$

Here e is the electronic charge, μ the electron mobility, n the free electron density and t , the thickness of the semiconductor. Three parameters can be adjusted in order to influence the sheet resistivity of a semiconductor. However, for TCOs some constrictions have to be considered: in case of application in solar cells the thickness t has a fixed value between 65-80 nm, because the TCO also serves as anti-reflection coating. The thickness of the TCO plays an important role

¹⁶The collective oscillation of conduction band electrons

for the optical characteristics. The electron density can't be increased limitlessly because the transparency will simultaneously decrease according to equation 2.8. So, only the electron mobility is suitable to further decrease sheet resistance in TCOs, which should be used in solar cell applications [94].

As already mentioned TCOs are wide band gap semiconductors. That means the Fermi level lies within the band gap and the materials are non-conductive. In order to obtain conductive materials, the oxides have to be doped. Most of the TCOs known and used so far are n-type semiconductors. This means elements with more valence electrons than the host metal occupy lattice sites instead of the host metal and/or fill in interstices. The additional electrons fill the conduction band which leads to very high conductivities.

As discussed in Chapter 2.2 semiconductors form Schottky- or ohmic contacts to metals of which the barrier height ϕ_n can be estimated from the electron affinity rule:

$$\phi_n = \varepsilon_M - \varepsilon_{EA} \quad (2.10)$$

with ε_M , the work function of the metal and ε_{EA} , the electron affinity of the semiconductor.

This rule is actually not quite correct for metals on typical semiconductors. The semiconductor possesses mid gap states filled up to a certain energy, which can be called the *charge neutrality level* (CNL) [31]. These states in the "forbidden" band gap arise from impurities within the crystal lattice or from surface states which are equal to the number of surface atoms. In neutral semiconductors those states are half filled. Surface states can also occur from impurities on the surface or imperfections in the lattice [95]. According to Bardeen [95] a high number of surface states lead to a metal-semiconductor contact, which is largely independent of the metal work function. For most ionic oxides the CNL energy lies near the center of the energy gap. In case of the transparent oxides the CNL is effectively in the middle of the average band gap over the Brillouin zone¹⁷. The lowest conductive

¹⁷The Brillouin zone describes a polyeder in the reciprocal space. The Brillouin zone is constructed by connecting each lattice point from any point and erecting a perpendicular plane in the middle of each reciprocal lattice vectors.

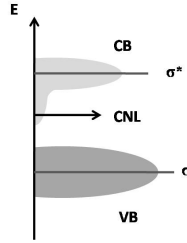


Figure 2.6.2: CNL position in In₂O₃ (retraced from [31])

band in TCOs like SnO₂ or In₂O₃, is formed by s-states¹⁸ from Sn and In, respectively. Those bands have rather broad minima which are well below the average conduction band energy. This causes the CNL to lie close to or even inside the conduction band as in In₂O₃ for example [31].

The surface states cause another phenomenon regarding the ability of a semiconductor to be doped: For large band gap semiconductors with a lot of surface states (or defect states) within the band gap, donor electrons can effectively lower their energy by falling in a lower lying energy states within the band gap. Thus, those electrons are not free to move and are, therefore, lost in terms of current transport. Hence, if the number of surface states is significantly higher than the doping concentration, effective doping is impossible. The Fermi level can not be further influenced by doping. This effect is called *Fermi level pinning* [31].

2.6.3 Indium Tin Oxide

Indium tin oxide, ITO, is the most commonly used TCO for solar cell applications today. It combines the highest conductivity, plasma frequency and good transparency at the same time (see Table A.1.2). This work focuses on the metallization on ITO and some of its chemical and physical properties will be discussed briefly in the following

¹⁸The orbitales of atoms joined in a crystal or amorphous material form the energy bands or energy states. For example: s-states are the energy levels formed by the joined s-orbitals.

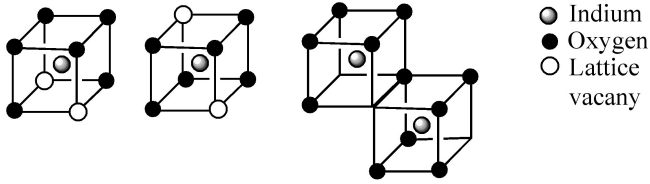


Figure 2.6.3: Chrystal structure of In_2O_3 (retraced from [96, 97])

sections.

Chemical structure

Indium oxide which is most often used for electronic applications crystallizes in the bixbyite structure, a cubic space-centered (bcc) crystal class. Each elementary cell contains 80 atoms. Each In atom is surrounded by six oxygen atoms which are in the corners of the cubic. In the bixbyite structure 1/4 of the anions is missing either on the space diagonal or the face diagonal (see Figure 2.6.3) The lattice constant is 1.0117 nm.

In indium tin oxide, indium is substituted by Sn-atoms and forms interstitial bonds with oxygen either as SnO or SnO_2 . If Sn^{2+} substitutes an In atom it acts like a trap for electrons and reduces the conductivity of the material. Sn^{4+} adds one more electron to the lattice compared to indium which is build in the conduction band. This and the missing interstitial oxygen account for the high conductivity in ITO. ([97]).

The source of the additional electrons is also an explanation for the possibility to control ITO conductivity properties during synthesis by magnetron sputtering or activated electron beam (EB) evaporation [31]. The oxygen pressure during deposition determines the conductivity: the higher the oxygen pressure during synthesis the more SnO species are formed, thus, reducing the concentration of charged donor species Sn^{4+} ([98]). Under reducing conditions, Sn donors can be activated. Therefore, conductivity and also transparency can be varied over a wide range by varying oxygen pressure during deposition.

The energy band structures of In_2O_3 and In_2O_3 with oxygen defects calculated by Medvedeva et al. ([32]) are shown in Figure 2.6.4

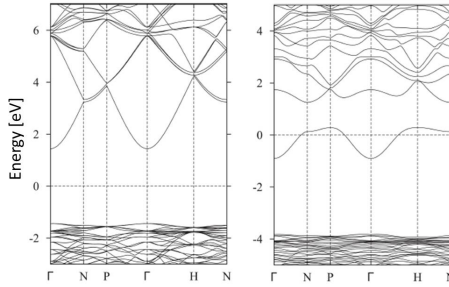


Figure 2.6.4: Energy band structure of In_2O_3 (left) and In_2O_3 with oxygen defects (right). Due to the lack of oxygen atoms the Fermi energy shifts into the conduction band and causes very high conductivity (Reprinted figure with permission from [32] Copyright 2010 by the American Physical Society)

The highest valence band in In_2O_3 is built by hybridized $\text{O}2p$ and $\text{In}5d/4p$ electrons. The $5s$ electrons of indium form the lowest conduction band. Shifting the Fermi level into the conduction band by removing oxygen atoms or doping leads to very high conductivity. This is why ITO can be called a *degenerated semiconductor* and is considered to act like a metal.

Properties

Properties of ITO which are most interesting for application in solar cells are electrical conductivity and optical properties.

High quality indium tin oxide films reach resistivities as low as $1.5\text{-}2.0 \times 10^{-4} \Omega\text{cm}$. According to equation 2.9, the resistivity is inversely proportional to charge carrier density and mobility. Due to scattering effects on grain boundaries and impurities ITO has a quite low charge carrier mobility compared to In_2O_3 . Many parameters during deposition influence the growth of ITO crystals, e.g.: sample surface, gas pressures, deposition times and deposition temperature. Higher deposition temperatures can increase the crystallinity of ITO which also increases charge carrier mobility. However, for new applications on temperature sensitive substrates this is not an option [97].

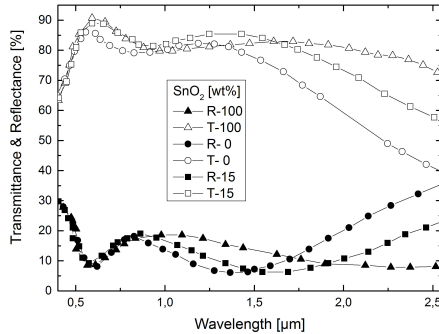


Figure 2.6.5: Transmittance and reflectance of ITO films with varying Sn doping concentration (data from [31])

As already mentioned a conductivity increase by doping is limited due to the decrease of optical properties like transparency and reflectance. For increasing carrier density the transparency decreases and reflectance increases. This is shown in Figure 2.6.5.

Chemical etching of ITO is possible with acids. However, the sensitivity against acids is very dependent on the deposition quality.

ITO is quite temperature stable. However, annealing effects occur but are also dependent on the quality of the initially deposited ITO layer.

2.6.4 Other TCOs

Indium is a rare earth metal, quite expensive and only available in a limited amount. Therefore, the ever growing flat-panel and solar cell industry is looking for cheaper and easier available alternatives.

One alternative are TCOs based on ZnO. One that is more closely observed is aluminum zinc oxide (AZO). Like most TCOs, AZO is a n-type semiconductor. Compared to ITO the conductivity of AZO is lower but transparency is comparable. Since it is not yet as extensively observed as ITO, deposition on large area is still a problem.

Another family of TCOs is based on SnO₂. The most often used

representative of this family is fluorine doped tin oxide: $\text{SnO}_2:\text{F}$. It is the cheapest TCO with the highest work function so far. It is mostly used as coating in energy efficient windows.

Another approach to gain high conductivities and transparencies at the same time is a stack deposition of $\text{ZnO}:\text{Ag}:\text{ZnO}$: silver nanowires or a thin film of silver (<10 nm) is deposited between a stack of zinc oxide films.

More detailed information about the theory of this topic is given in [99]

2.7 Surface energy and work of adhesion

Young formulated a correlation about the interfacial tension at a point of the three-point-contactline formed by a liquid resting on a solid surface and surrounded by a gas phase, which is schematically shown in Figure 2.7.1.

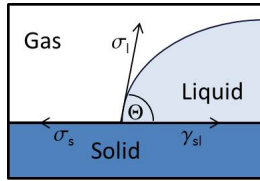


Figure 2.7.1: Contact angle formation on a solid surface according to Young [33]

σ_s and σ_l describe the surface tension of the solid and liquid phase, respectively, γ_{sl} is the *interfacial tension* between solid and liquid phase and Θ is the contact angle between the vectors of γ_{sl} and σ_l . Young formulated the correlation between those parameters as follows [33]:

$$\sigma_s = \gamma_{sl} + \sigma_l \cos \Theta \quad (2.11)$$

The interdependency of the gas phase with the solid phase and the liquid phase, respectively, is neglected.

The interfacial tension γ_{sl} is a function of the surface tension of the different phases. According to Fowkes only congeneric interdependen-

cies between the phases can occur [100]. That means only a pure dispersive (unpolar) part of phase one can interact with the unpolar or dispersive parts of phase two. Same holds for the polar parts of the phases. Thus, the interfacial tension (for the dispersive parts of phases 1 and 2) can be calculated from equation 2.12:

$$\gamma_{12}^D = \sigma_1 + \sigma_2 - 2\sqrt{\sigma_1^D \sigma_2^D} \quad (2.12)$$

The index D implies the dispersive part.

Whereas all molecules own a dispersive part (originating from Van-der-Waals-forces), only some molecules also have polar parts. The electronegativity of different atoms of a molecule cause a polarisation of the molecule, which is the source for the polarity of a molecule. Owens, Wendt, Rabel and Kaelble deduced from this model that the surface tension of a liquid can be formulated as the sum of the polar part of the surface tension and the dispersive part [101]:

$$\sigma = \sigma^D + \sigma^P \quad (2.13)$$

The index P implies the polare part.

By measuring the contact angle of at least two different liquids with known polar and dispersive parts of their surface tension, the *surface energy* of a surface can be determined.

According to Rabel [102] the surface energy can be calculated from the linear equation 2.14. This method is also known as method by Owens, Wendt, Rabel and Kaelble (OWRK).

$$\frac{(1 + \cos\Theta)\sigma_l}{2\sqrt{\sigma_{l^D}}} = \sqrt{\sigma_s^P} \sqrt{\frac{\sigma_l^P}{\sigma_l^D}} + \sqrt{\sigma_s^D} \quad (2.14)$$

To get more precise results one should measure more than two liquids, which is the minimum. If using only a few liquids the polarity of those liquids should differ as much as possible. Often used liquids are diiodmethane (DIM) (unpolar) and water (polar).

If the surface energy tensions and the interfacial tension are known the *work of adhesion* can be calculated. According to Dupré [103] adhesion and interfacial tension are correlated:

$$W_{12} = \sigma_1 + \sigma_2 - \gamma_{12} \quad (2.15)$$

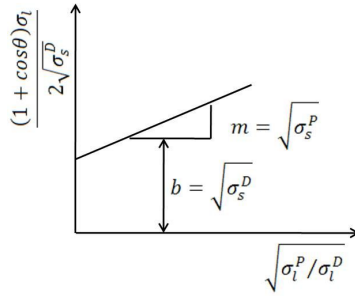


Figure 2.7.2: Surface energy: Calculation of dispersive and polar part according to Rabel [102]

The work of adhesion is a measure of the adhesion strength of two surfaces. The theory of adhesion is complex and numerous forces influence the adhesion between two solid surfaces. As for the surface energy, one can divide the most important forces of adhesion into dispersive forces like Van-der-Waals forces and polar forces caused by electronegative elements on the surface. In general, one can say, that only surfaces owning the same attractive forces are able to adhere. The principle is illustrated in Figure 2.7.3.

Dispersive and polar forces are illustrated by yellow and grey hands, respectively. A liquid which possesses similar surface characteristics (polar (P) and dispersive (D)) as the solid it is applied on, will show high work of adhesion, a small contact angle and a small value for the interfacial tension or surface energy, respectively. According to equation 2.15 surfaces which possess high surface energies before getting into contact to each other (high σ value) are likely to interact more strongly with a second surface if the characteristics fit (low value for γ_{12}) and, thus, show better adhesion to it.

The same considerations hold for solid - solid interaction. Besides pure attractive forces, also diffusion and chemical reactions can play an important role regarding the adhesion.

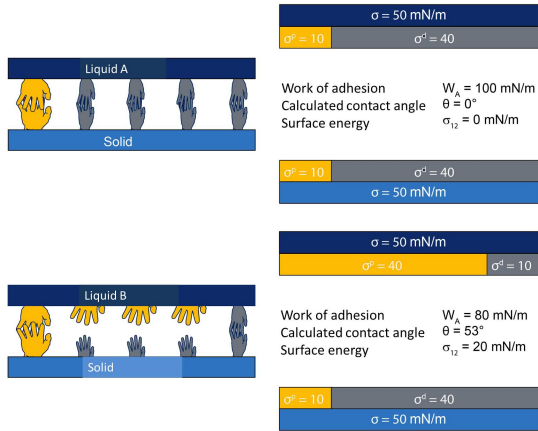


Figure 2.7.3: Illustration for good (top) and bad (bottom) interaction between a solid surface and a liquid (retraced from [104])

3 Metallization Techniques

This chapter addresses the processes and demands on the metallization of solar cells. Section 3.1 explains the general requirements the metallization has to fulfill to be used on solar cells. Different metallization techniques are used today. The two most important techniques are printing of metal containing inks and pastes, discussed in Section 3.2 and chemical deposition of metals or plating, respectively. Several plating techniques can be used today and are the subject of Section 3.3. The special demands of temperature sensitive cell concepts require also special metallization techniques which is addressed in Section 3.4.

3.1 General demands on metallization for solar cells

Solar cells separate charge carriers by a large area p-n-junction. Both sides of the junction have to be contacted separately on the rear and the front side. As conducting material, usually metal is used which has a very high conductivity but no light transmittance when thicker than a few nanometer. To avoid transport losses and gain maximal power output it would be desirable to contact the whole cell area. This is easily realizable for the rear side. In order to reach high cell performances, as much light as possible has to be able to enter the cell through the front side. To avoid shading losses, the front side metallization needs to cover only a minimal cell area.

To gain minimal sheet resistance, and hence, power output; one tries to keep the metallization fingers as narrow and high as possible. In other words, the aspect ratio¹ should be as high as possible. The bus bars, which are connected to the fingers and which are able to transport high amounts of current are wider than the fingers. They are also used to connect the single cells via soldering to each other

¹Aspect ratio = height/width

to get a module. The design of the metallization grid is always a compromise between optical losses and series resistance. In general, today's metallization of industrial produced solar cells reaches shading of 7-10 % of the total cell area.

Newer concepts try to realize both contacts on the back side of the solar cell (e.g., MWT - metal wrap through solar cell, EWT - emitter wrap through solar cell, IBC - interdigitated back contact solar cell). Those cell concepts are more difficult to realize and are not yet suitable for industrial mass production.

Another crucial aspect is the contact resistance between metal and semiconductor. As described in chapter 2.2, the band levels of metal and semiconductor do not match, which leads to a more or less high contact resistance. The aim of solar cell metallization is to achieve as low contact resistances as possible to reduce series resistance. In addition, the contact area is an area of high recombination activity. Both emitter and metallization have to be optimized to gain a minimum of losses.

A third aspect is the chemical and mechanical stability of the metal - semiconductor contact. Low adhesion between metal and semiconductor complicate module integration and may result in higher contact resistance. In addition, bad mechanical stability may result in short life time of the cells and modules. Chemical stable contacts must not degenerate during operation or damage the cell, as is the case for chopper contacts directly contacting the emitter.

From the industrial point of view, the cost effectiveness is another crucial aspect which has to be considered. Easy processes with high yield (low wafer breakage), low material and machinery costs and high cell efficiencies are desired. As a key parameter the cost per watt peak (€W_p^{-1}) can be considered. However, higher production costs can be overcompensated by higher efficiencies.

3.2 Printing techniques

3.2.1 Screen printing

Screen printing is the established metallization technique for standard industrial solar cells. It is a relatively cheap metallization technique with a very high throughput. The general working principle is shown

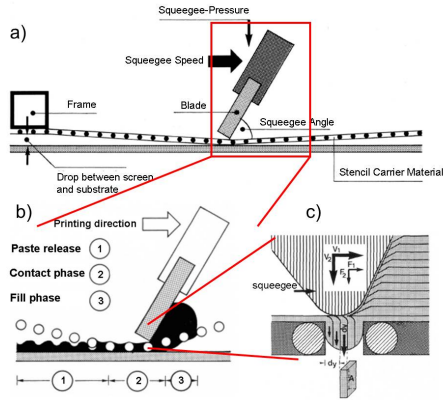


Figure 3.2.1: Working principle of screen printing a) Overview and general process parameters, b) different phases of paste transfer from screen to substrate, c) detailed look at the paste transfer mechanism [12]

in Figure 3.2.1.

To print the desired design onto the substrate the printing medium (color, metal paste) is passed through a screen with a squeegee. The screen consists of a mesh of fibers, which are partially covered by a polymer film. Only the areas, where the printing medium is desirable, the screen is open. During printing the screen gets locally pressed against the substrate by the squeegee. Due to the tension of the mesh, the medium is released and applied to the substrate. The printing result depends on a variety of factors: mesh tension, mesh opening, fiber diameter, pressure applied by the squeegee, snap-off distance (distance between mesh and substrate), substrate surface and paste characteristics.

Screen printing technique and even more important paste formulation, improved significantly during the last five years, leading to formally broad screen printed fingers of $\sim 100 \mu\text{m}$ down to $50\text{-}60 \mu\text{m}$ and good aspect ratios. Seed-layer printing even achieves narrower lines. Double printing can achieve lines with higher aspect ratios than single print.

The optimization of the print image is always a compromise to mesh

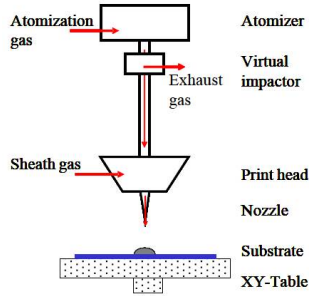


Figure 3.2.2: Scheme of Aerosol jet printing system [35]

durability. The fibers have to be made thinner to allow for narrower line printing. The mesh loses tension with each printing step, which leads to line broadening. The mesh, therefore, has to be removed after around 20000 cells (around 10 hours of production) unless the mesh did break already [105].

The main disadvantage of screen printing is the fact of the necessity of making contact between substrate and screen (and squeegee) [17]. Although improvements in technology lowered the amount of breakage, with the trend to thinner substrates, it is likely that further problems regarding this issue will occur [12].

The screen mesh is usually made of stainless steel and coated dependent on the paste chemistry. The meshes are usually defined by mesh/inch and the thread size.

3.2.2 Aerosol jet printing

The metal aerosol printer uses a Maskless Mesoscale Material Deposition (M3D) technique from OPTOMECH INC., USA. Using an optimized ink, lines of 10 μm width can be deposited contactlessly [19]. It was designed to close the gap between photolithographically defined structures ($< 100 \text{ nm}$) which is normally used for electronic production and thick film printing ($\sim 40 - 50 \mu\text{m}$ and even $\sim 100 \mu\text{m}$ for polymeric low temperature thick film pastes).

A scheme of the aerosol jet printing system is shown in Figure 3.2.2.

The ink has to be nebulized to create an aerosol which is then

concentrated in a virtual impactor and finally focused and deposited on the substrate through the printing head. The demands on an ink for aerosol jet printing are less rigid than for screen printing pastes or ink jet inks. Although an optimum of particle size and viscosity exists, basically every ink can be printed as long as it is able to be nebulized and particle size is small enough to not clog printing nozzles. An upper limit for particle size of silver inks was found to be $d < 0.5\mu\text{m}$ with narrow size distribution and a viscosity with $\eta_{\text{vis}} < 1\text{Pa} \cdot \text{s}$ [35].

More details on the working principle of the aerosol jet printing system can be found in the Appendix A.1.2.

3.2.3 Ink jet printing

Ink jet printing is vastly known as a consumer printing system. Due to several advantages over other printing techniques, ink jet printing is getting more and more interesting for industrial applications. Some of these advantages are: reduction of manufacturing costs, higher quality output, process integration from analogue to digital, wide variety in substrates, waste reduction, mass customization, etc. Especially for solar cell demands, the achievable low line widths of $< 35\mu\text{m}$ are important [20, 22].

There are several ink jet printing techniques known. They can roughly be sub-divided in *continuous ink jet* (CIJ) and *drop-on-demand* (DOD) ink jet systems.

The CIJ technology uses a pump which sends a continuous stream of drops through a nozzle from a reservoir. The drops get exposed to an electric field to gain a charge and then pass a deflection field, which determines where the drops land. Excess drops are getting recycled. Figure 3.2.3 shows the working principle.

A very high throughput can be achieved with this technology. However the resolution of the printed patterns is rather poor.

The technique which is currently more of industrial interest is drop-on-demand (DOD). Drops are only ejected when required. There are several techniques implemented to realize the DOD system.

One is the thermal DOD, which is most often used in commercial available desktop ink jet printers. A resistive heating element within the ink chamber heats up the ink up to 350-400 °C which causes the fluid to evaporate. A small bubble is formed. The bubble causes a drop to eject from the nozzle (Figure 3.2.4). Very small droplets can

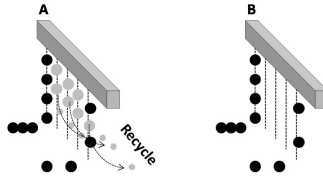


Figure 3.2.3: Working principle of CIJ (A) technology and DOD (B) (retraced from [17])

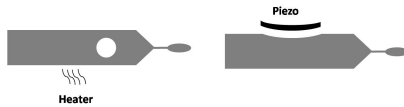


Figure 3.2.4: Schematic drawing of thermal DOD print head (left) and piezo DOD print head (right) (retraced from [17])

be produced and high print resolutions can be achieved. Production costs are relatively low but the print heads have special demands on the ink.

The piezo DOD technique uses the property of piezo crystals to distort when a current is applied. The piezo squeezes the ink chamber and a drop is released (Figure 3.2.4). The piezo DOD technique is the most interesting one for industrial use. It provides the highest freedom for ink formulation and longest print head life. Compared to thermal DOD printers the devices are more cost intensive. A piezo DOD printer has been used for sample preparation within this work.

3.3 Plating techniques

Plating processes realize the electrochemical deposition of metals either directly onto the substrates or on a seed-layer deposited by other metallization techniques (for example, evaporation/sputtering or ink/paste deposition). In the following, the different plating techniques are described. More detailed information can be found in the literature [106–109].

3.3.1 Basic principles

The electrochemical processes described here consider a system containing electrodes (semiconductors or metals where charges are transferred) and a surrounding electrolyte which is an ionic conductor. Within this system, the reaction between ions of the electrolyte and the conductors or semiconductors are observed. A *redox* process occurs. This process involves two reaction types: the *reduction* of a species and the *oxidation* of another one at the same time. None of the reactions can occur without the other as electrons are transferred from one species involved in the redox system to the other (equation 3.1). An oxidized species O with the oxidation number z is reduced to the reduced species R. ν is a stoichiometric coefficient. The reduced species does not necessarily need to be reduced to the neutral element, however, this is usually the case for plating processes.



A process which involves electron transfer can be called “Faradaic” and the amount of electroactive species which reacted can be calculated by Faraday’s law:

$$Q = nzF \quad (3.2)$$

with Q the charge (number of electrons), n the amount of reacted electroactive species (in mol), z the number of electrons needed for the reaction of one species involved in the redox system and F the Faraday constant ($96485.34 \text{ As mol}^{-1}$).

In the case of metal plating, electrons are transferred from the metal or semiconductor (or a reduction species inside the electrolyte) to the metal ions in the electrolyte. The ions are being reduced to elemental metal and crystallize on the surface of the conductor. The amount of deposited metal can be calculated from equation 3.3:

$$m = \beta \frac{MQ}{zF} \quad (3.3)$$

with m being the metal mass deposited, M the molar mass of the metal and β the current efficiency of the electrolyte (percentage of Faradaic current within the process).

Electrochemical processes can run in two directions. The case of a spontaneous reaction which occurs until the chemical potentials (or

Fermi-level) between electrolyte and reduced metal are even is called *galvanic cell*. A current flow can be observed during the process. A voltage can be measured between the electrodes: a positive voltage at the cathode and a negative one at the anode. The reduction does always take place at the cathode and the oxidation of the redox reaction at the anode.

For systems where a current has to be applied to run the redox reaction, the cathode has to be negatively charged and the anode positively. A setup running this way is called an *electrolytic cell*.

3.3.2 Electroplating

The electrochemical deposition of metals is typically an electrolytic cell, where a working electrode is dissolved via an external potential and ions from the electrolyte are deposited on the negatively charged substrate (in this case, the solar cell). The metal ions are usually dissolved as complexes (Me^{z+}) coordinated by a complexant X :



Dissolution (oxidation) of the counter anode should ideally take place at the same amount as the reduction process.

The form of the deposited layer varies depending on the set potential. The crystal growth can, e.g., be layer by layer or dendritical [12] and can lead to highly porous deposition layers.

In order to reach desirable layer properties, it is favorable to choose a potential which is not too cathodic although more cathodic potentials lead to higher deposition rates. Nucleation rate and charge transfer rate will be kept constant by choosing a fixed potential during the whole process.

3.3.3 Electroless plating

While electroplating uses a current source to reduce and oxidize the metal ions and metals, respectively, the metal ions used in electroless plating baths are reduced by chemical reducing agents. Strictly speaking, electroless plating is not a electrochemical process and is also called *chemical metal deposition*.

Table 3.3.1: Reducing agents used in chemical metal deposition processes, operating pH values and standard potentials of electron releasing reactions (retraced from [12])

Reducing Agent	pH	E^0 [V vs NHE]
Sodium Hypophosphite NaH_2PO_2 : $\text{H}_2\text{PO}_2^- + \text{H}_2\text{O} \rightleftharpoons \text{H}_2\text{PO}_3^- + 2\text{H}^+ + 2\text{e}^-$	4-6	0.499
Sodium Hypophosphite NaH_2PO_2 : $\text{H}_2\text{PO}_2^- + \text{H}_2\text{O} \rightleftharpoons \text{H}_2\text{PO}_3^- + 2\text{H}^+ + 2\text{e}^-$	7-10	1.57
Sodium Borohydride NaBH_4 : $\text{BH}_4^- + 8\text{OH}^- \rightleftharpoons \text{B}(\text{OH})_4^- + 4\text{H}_2\text{O} + 8\text{e}^-$	12-14	1.24
Hydrazine H_2NNH_2 : $\text{N}_2\text{H}_4 + 4\text{OH}^- \rightleftharpoons \text{N}_2 + 4\text{H}_2\text{O} + 4\text{e}^-$	8-11	1.16
Formaldehyde HCOH : $\text{HCOH} + \text{H}_2\text{O} \rightleftharpoons \text{HCOOH} + 2\text{H}^+ + 2\text{e}^-$	0	0.056

The reducing agent, which is often a hydrogen containing chemical, becomes oxidized during the process. The reducing agent is metastable in solution and typically needs a catalyst to decompose and initialize the redox reaction for metal deposition. Those catalysts are, for example, metal surfaces or surfaces of semiconductors, depending on the chemical design of the reducing agent. An overview of common reducing agents used for electroless plating is given in Table 3.3.1.

Electroless plating is quite slow but allows for very homogeneous metal deposition, if the depletion of reaction species is avoided.

3.3.4 Light induced plating (LIP)

Metal deposition on solar cells can also be done by using the photovoltaic effect of the cell to produce the current which is necessary to reduce the metal. Basically, the solar cell is immersed into the electrolyte and irradiated with light of a certain wavelength. This causes the n-doped side (for p-type solar cells the emitter, which is in general on the front side) to adopt a negative potential reducing the metal

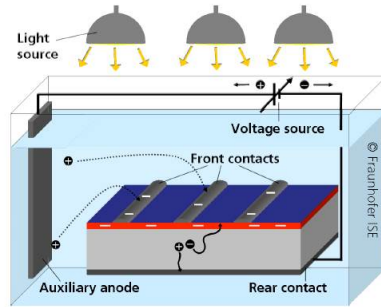


Figure 3.3.1: Schematic drawing of working principle of LIP process [12]

cations from the electrolyte and to deposit on, e.g., a seed-layer or an opening in the anti-reflection coating (laser opened or chemically etched). The corresponding oxidation process can be shifted from the p-doped side to another electrode, for example, a metal electrode from the same material as the metal dissolved in the electrolyte. In this way, the electrolyte is continuously replenished. The idea for LIP was first formulated in a patent from the 1970s [110]. A schematic drawing of the setup of LIP with a solar cell is shown in Figure 3.3.1.

If the conductivity of the used dissolved metal in the electrolyte is sufficiently high, a conductive layer is deposited onto the substrate. The deposition is very uniform even if the seed-layer is interrupted or the emitter is only poorly contacted. As long as the current can pass through the emitter/seed-layer interface to the seed-layer/electrolyte interface the LIP process works. If no contact is formed between seed-layer and emitter, no current can pass and the LIP process does not work. Thus, a working process can also serve as evidence for contact formation.

In order to control the potential ratio between p- and n-type areas of the semiconductor one can either adjust the light intensity or contact the p-type area, which is set to a negative potential against a metal in the electrolyte with a voltage source. The choice of the potential also allows for simultaneous plating of p- and n-type area [12].

The rear side can also serve as anode: the solar cell is fully immersed into the electrolyte and the front surface is set to a negative potential

by illumination. The rear side adopts a positive potential due to the presence of holes allowing the rear side to dissolve into the electrolyte. The rear side should then be fully metalized with the metal to be plated. The solar cell does not have to be contacted at all for this process.

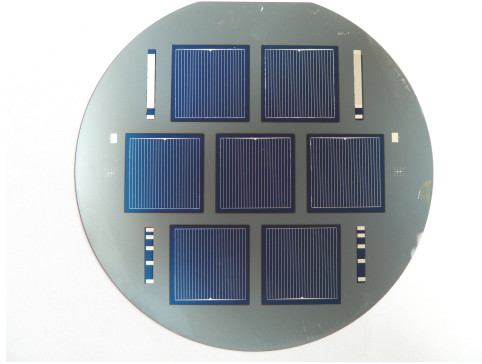


Figure 3.3.2: Photograph of several single cells produced on one 4" wafer. The blue areas are coated with ITO. The metal grid appears silver white.

The LIP process is especially advantageous for the metallization of small separated cells on one wafer where it would be difficult to contact each single seed-layer (usually evaporated metal), because the front side does not have to be contacted.

3.4 Temperature sensitive cell concepts

3.4.1 Sputtering and thermal evaporation

The application of metals via thermal evaporation or sputtering has been the dominant metallization technique for silicon solar cells before screen printing. Due to some very valuable advantages, like very low contact resistance and narrow and defined feature size, these techniques are still used for high efficiency solar cells, lab scale applications and cell concepts, where a low series resistance R_s is crucial. Since the technique does not require high temperature steps, it is also used

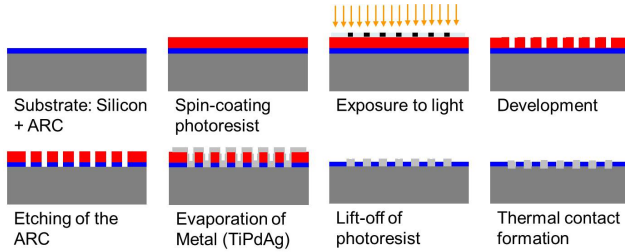


Figure 3.4.1: Metallization process by photolithographical structuring, metal evaporation and lift-off (retraced from [12])

for contacting temperature sensitive (and high efficiency) solar cells. However, the process is not suitable for high throughput industrial solar cell fabrication due to very high processing costs. The metals used for the metallization (with the exception of full area aluminum metallization) are very expensive. In general, a metal stack of titanium, palladium and silver is used. Titanium has a very low contact resistance to silicon (see also Figure 2.2.4). Palladium, which is the most expensive, serves as oxidation inhibitor for titanium and as diffusion barrier for silver. The whole process consists of eight steps, which is far too much for industrial processing. Apart from the high costs caused by the high number of process steps, evaporation and sputtering have a very low yield of material as most of the metal is deposited on the facility chamber and the masking. Moreover, the photolithographic process generates large volumes of hazardous waste [16]. Figure 3.4.1 shows the schematic metallization process for grid metallization by sputtering or thermal evaporation including the photolithographic masking step.

Alternatively to the costly photolithographical structuring, evaporation can also be done through a shadow mask. However, the resulting metal grids are not as narrow and defined as can be achieved by photolithography [17].

Industrially used printing techniques using low temperature sintering inks or pastes based on nanoparticles could be a more economical alternative.

3.4.2 Direct plating

Direct plating of metal layers is another alternative for the metallization of thermally sensitive substrates. Direct plating on silicon solar cells can be done if the anti-reflection coating has been opened, for example, by laser processing or etching. For structured metallization the latter also needs a masking step in advance. For ITO covered cell concepts, e.g., the HIT solar cell, an insulating and structuring mask has to be applied onto the ITO at first, otherwise the whole cell area will be covered with metal due to the high conductivity of ITO itself. In addition, the adhesion of metals on ITO is very poor. Silver does not adhere to ITO without adhesion promoters. When evaporated, titanium serves as adhesion promoter. Unfortunately, titanium can't be electrochemically applied from aqueous electrolytes due to its position in the electrochemical series [40].

3.4.3 Seed-and-plate

In the seed-and-plate approach the metallization layer forming the contact to the emitter (or ITO, respectively), called seed-layer, and the metal layer forming the lateral conductive bulk, which has to transport the current, are applied independently. The seed-layer can be applied by the photolithographic process described above or by printing an ink or a paste. The second lateral conductive layer is usually applied by plating techniques. The technique is not limited to just two layers. Figure 3.4.2 shows a cross section of a multi-layer metallization stack. The metals were analyzed with EDX.

The main advantage of this approach is to be able to optimize the contact formation to the emitter (or ITO, respectively) by choice of the metal or special ink formulation independently from the conductive layer.

As has been described in Section 3.4.1 titanium forms a very good contact to silicon and is used on high efficiency solar cells. However, for the lateral conductivity, silver or copper are more suitable. Plating is faster and cheaper than thermal evaporation or sputtering, therefore, application of the conductive layer by plating is more economic.

Further cost reduction can be achieved by applying the seed-layer through inks and pastes which can be formulated specifically for contact formation, which normally means higher amounts of glass in the

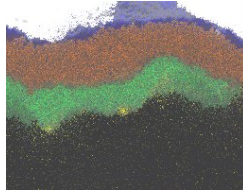


Figure 3.4.2: SEM image of cross section of multi-layer metallization stack; Yellow: silver seed-layer, Green: nickel diffusion barrier, Red: copper conductive layer, Blue: Tin capping layer [12]

ink; which in turn causes worse lateral conductivity. By using the seed-and-plate approach, an optimized seed-layer ink or paste for contact formation can be used. A very dense and highly conductive current transport layer can be applied electrochemically on top.

Since ITO acts as a barrier for copper [111] the metal can be used as conductive layer on HIT solar cells, which significantly reduces the production costs. However, copper does not adhere to ITO, and an additional seed-layer has to be applied first.

The separation of contact formation and lateral conductivity carries big potential to optimize the metallization fitting to every cell concept. However, seed-and-plate requires at least one more processing step compared to standard thick film metallization by screen printing, which is why it is not yet used in industrial production.

3.5 Printed metal inks and pastes

Low-temperature curing polymer pastes

Low-temperature curing polymer pastes are dispersions of polymers and silver flakes or silver particles. The size of the silver particles is usually in the micrometer range. The polymer within the paste is either a thermoplast and the pastes contain higher amounts of solvents. Careful choice and control over the curing temperature prevents entrapment of solvent within the paste and thus, formation of pores. The second kind of pastes contains a thermoset. The molecules polymerize during the curing step and form a rigid three-dimensional network.

Low-temperature curing polymer pastes can be applied either by screen printing or stencil printing². The rheology of polymer pastes is completely different compared to normal high temperature firing screen printing metallization pastes. Achieved finger widths are still too high (around 100 μm). The best polymer paste reaches specific conductivity values of $10 \cdot 10^{-8}$ - $15 \cdot 10^{-8}$ Ωm , which is still 4 to 6 times higher compared to high temperature firing pastes and even 10 times higher than bulk silver (specific conductivity of $1.58 \cdot 10^{-8}$ Ωm) [5][112]. In addition, the silver consumption for the metallization based on polymer pastes in relation to the achievable conductivity is very high.

Inks based on metallic nanoparticles

The requirements for metallic nanoparticle inks are the same as for conventional color inks. Major differences arise out of the fact that a conductive pattern has to be formed by the metallic particles after printing. As the main application focuses on thermally sensitive materials, the ink should be processable at temperature below 200 °C. It should be long term stable and provide minimal printer maintenance.

The main ingredient of an ink is the solvent. Metallic nanoparticle inks can be based on water or organic solvent formulations, depending on the capping of the metallic particles and the substrate. The second main component of the formulation are the metal nanoparticles. Their size differs in most commercially available inks between 20 nm and 50 nm but is never >100 nm. Metal particles have a very high density and their stabilization in high concentrations is a special challenge for ink formulation to avoid agglomeration and precipitation of the particles. In addition, aside from the two main components solvent and conductive particles, the ink contains diverse additives which adjust printing characteristics like rheology, surface tension and wettability. For piezoelectric ink jet inks, the viscosity should be between 8-15 cP and surface tension between 25-35 dyne/cm [17]. For some application adhesion promoters are also needed [16].

The chemical formulation of the inks is a tricky task as all components have to be very accurately selected. Additives and solvents have

²Stencils are thin foils of stainless steel, in which a pattern is chemically etched or cut out with a laser. Openings of down to 15 μm can be achieved [5].

to be removed after printing and drying. Organic residues of the additives could form layers between the conductive metal particles and avoid the formation of highly conductive metal grids. In addition, none-noble metals like Cu or Al oxidize very rapidly in air, which is an additional problem for the stabilization of the particles within the ink to avoid oxidation [28]. In case of copper, NovaCentrix developed a CuO nanoparticle ink which contains a reducing agent [113, 114].

To avoid the oxidation problem, silver as a noble metal is mostly used in conductive nanoparticle inks.

4 Characterization Methods

This chapter introduces the different characterization methods which were used in this work, and their theoretical background . Section 4.1 introduces the standard method for solar cell characterization: the I-V curve measurement. Section 4.2 addresses a characterization method independent of the metallization of the solar cell, the “Suns V_{OC} ” method. Very important for this work was the determination of the metallization characteristics which were done with the four-point-probe method and TLM measurements, which are discussed in Section 4.3. Information about chemical reactions which occurred during the contact formation process could be observed with the thermal gravimetric-differential thermo analysis method which is discussed in Section 4.4. The understanding and interpretation of the collected data is easier, if one can observe the contact area and the metallization on the solar cell itself, directly. This can be done on the sub-micrometer scale, by preparation of cross sections and observation by SEM, EDX and FIB . These methods are explained in Sections 4.6 and 4.7. Dimensions and shape of the metallization are crucial for solar cell performance and can closely be observed by 3D imaging with a confocal microscope (Section 4.8). Further information, about the plating process on the cells can be collected by measuring a cyclic voltammetry diagram (Section 4.10). Not only the metallization characteristics themselves but also the contact to the cell is of importance. Also, mechanical properties especially, the adhesion to the surface is important. A very simple test to evaluate the same is the “tape test” and is explained in Section 4.11. A first estimation of adhesion prior to the metallization can be done by knowing the surface characteristics of the cells and also the metallization substance. An relatively simple way of determining surface properties is done by goniometer measurements which are introduced in Section 4.12.

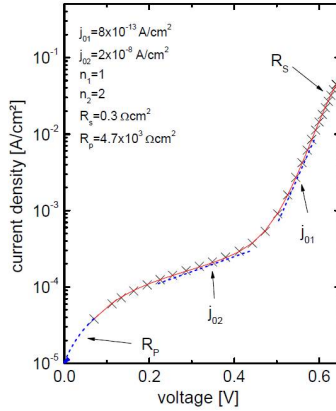


Figure 4.1.1: Dark IV-curve with two-diode fit. Labels show sections dominated by certain cell parameters [35]

4.1 I-V Curve

The most important characterization method for solar cells is the measurement of the I-V curve, which gives information about the most important cell parameters. There are two ways of measuring the I-V characteristics of a solar cell.

4.1.1 Dark I-V curve

Without illumination a solar cell can be described as a large flat diode. Therefore, I-V measurements in the dark delivers an I-V curve similar to the one given by a diode and can also be fitted according to the two-diode model.

In regions with low current change, the linearly plotted curve does not deliver enough details. Thus, current density is plotted semi-logarithmically against the voltage to increase the resolution.

The shape of the dark I-V curve is influenced by certain cell parameters, which can be determined from the graph of the section dominated by the following parameters:

- Between 0 and approximated 0.15 V the graph is dominated by

the parallel resistance R_P .

- For voltage values of 0.2 - 0.4 V the curve is most dependent on the second summand of equation 2.2. j_{02} can be determined. Only very rarely the ideality factor n_2 is close to 2.
- j_{01} is taken from the section between 0.4 - 0.6 V, if the ideality factor n_1 is close to 1.
- The last section of the dark I-V curve is dominated by the series resistance.

4.1.2 Illuminated I-V Curve

As solar cells are normally not operational in the dark but operate under illumination, their performance is determined from measuring the I-V curve under a normed light source.¹

Under irradiation the dark I-V curve is shifted by the photocurrent generated by the cell. The current is negative by convention but is often displayed at the positive axis. To measure the cell parameters the cell gets illuminated under a constant intensity of one sun (1000 Wm^{-2}) at 25 °C, which causes the current generation in the cell. Front and rear side of the solar cell are connected and the voltage between the contacts can be varied by a variable resistor. At zero resistance, the cell is short circuited and the voltage is zero. The measured current, generated by the cell itself at zero voltage is called *short circuit current density*, j_{SC} , and gives the maximum current density the cell can deliver. With increasing resistance, the current gets reduced and the voltage increases, due to the diode behavior of the solar cell. If the resistance is high enough to suppress current flow completely, the maximum voltage, called *open circuit voltage*, V_{OC} is delivered. Shortly before reaching the V_{OC} the power of the cell (product of current and voltage) reaches its maximum. This point is called

¹The light source commonly used are high pressure Xenon arc lamps. With filters installed it approximates the AM1.5G spectrum. The AM1.5G spectrum gives the standard spectrum used for comparing solar cell parameters independent of location. AM is shortage for air mass. The intensity and spectrum of the suns irradiation depends on the path length through the atmosphere which the light has to pass before hitting the solar cell. When the sun is directly overhead the air mass is 1. "G" stands for "global" and includes direct and diffuse radiation.

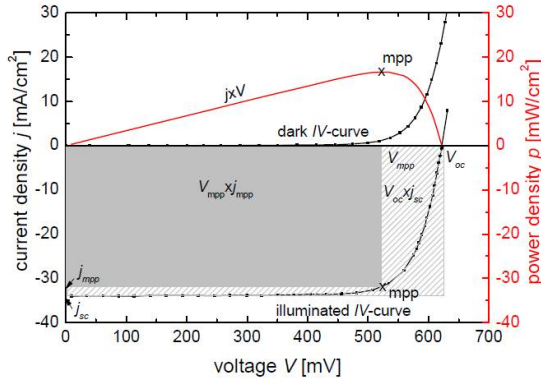


Figure 4.1.2: Dark and illuminated I-V curve and power density vs. voltage of a solar cell. Important I-V parameters are illustrated [35]

the *maximum power point*, *mpp*. To obtain the best possible performance of a cell, it is desirable to operate the cell around those current and voltage values. A plot of an I-V curve in dark and illuminated is given in Figure 4.1.2.

Another very important cell parameter is the *fill factor*, also illustrated in Figure 4.1.2. The fill factor, FF , is given by the largest rectangle which can be fitted between x-axis and I-V curve. For a solar cell without recombination and ohmic losses, the I-V curve would form an angle of 90° at the *mpp* at V_{OC} and j_{SC} and the fill factor would be 100% ². Numerically, the fill factor can be calculated by equation 4.1.

$$FF = \frac{j_{mpp} V_{mpp}}{j_{sc} V_{OC}} \quad (4.1)$$

By multiplying V_{OC} , j_{SC} and FF one can calculate the power of the solar cell. To get the most often used parameter for comparing solar cells, the *efficiency*, one has to compare the power of the cell with the incident irradiative power P_{Ph} :

²Auger recombination and radiative recombination can not be fully suppressed even in the purest material. This limits the fill factor to a maximum of 85 %.

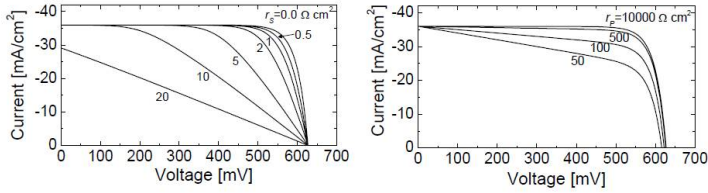


Figure 4.1.3: Influence of serial (left) and parallel (right) resistance on the shape of the illuminated IV-curve [35]

$$\eta = \frac{P_{mpp}}{P_{Ph}} = \frac{V_{OC} j_{SC} FF}{P_{Ph}} \quad (4.2)$$

The fill factor and, therefore, the shape of the illuminated IV curve is strongly influenced by the serial and the parallel resistance. An illustration of the dependence of the shape of the IV curve from both resistances is given in Figure 4.1.3.

To receive the same current in dark I-V curve measurements as the j_{SC} in illuminated curves, a higher voltage, V_{ex} than the open circuit voltage has to be applied, due to the higher potential difference caused by the series resistance. Thus, the series resistance can be determined from both IV curves by the following equation:

$$R_S = \frac{V_{Ex} - V_{OC}}{j_{SC}} \quad (4.3)$$

Illuminated IV curves have to be validated by measuring a calibrated reference cell to avoid irregularities in the measurement, for example, through an unsteady light source.

4.2 I_{SC} - V_{OC} characteristics - Suns V_{OC} measurement

I_{SC} - V_{OC} curves deliver IV curves under open circuit conditions (measuring V_{OC}) and short circuit conditions (j_{SC}), respectively. This makes the IV curve free of the influence of the series resistance.

An relatively easy way to measure the I_{SC} - V_{OC} curves are Suns V_{OC} measurements as proposed by Cuevas and Sinton [115]. The voltage

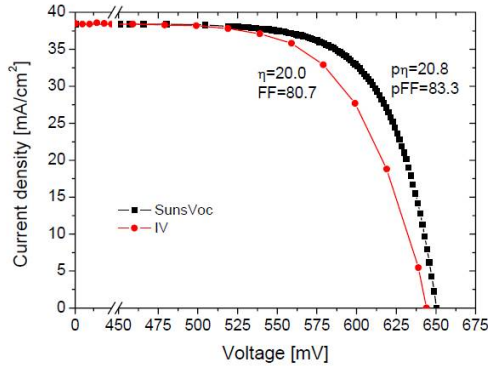


Figure 4.2.1: Comparison of IV- and $SunsV_{OC}$ measurement [1]

is measured under varying illumination intensity. Since the current is proportional to the light intensity, it can be measured by a separate calibrated reference solar cell. The measurement can be done without metallization as long as both sides (cell base and emitter) can be contacted.

Fill factor and efficiency determined from $SunsV_{OC}$ measurements are called *pseudo fill factor*, pFF , and *pseudo efficiency*, respectively. They give the upper limit for the measured cell performance since they are free of the serial resistance. Limitations from recombinations and shunts can be more easily detected and interpreted. By comparing $SunsV_{OC}$ and IV measurements, the series resistance R_S can be determined. Additionally, $SunsV_{OC}$ measurements are a helpful tool to determine the influence of processes, like tempering, on the cell performance, as they can be done without metallization and as long as front and rear side of the cell can be contacted. Also, degenerating effects, for example, caused by metallization with copper, can be easily observed.

4.3 Four point probe measurement

One of the most important characteristics of a solar cell is the series resistance. It is mainly influenced by the metallization and the met-

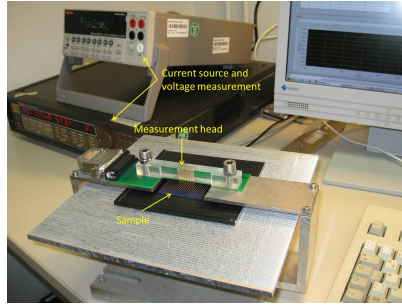


Figure 4.3.1: Photograph of 4-point probe measurement set-up

alization quality. An overview about the different parts which summarize to the series resistance is given in Figure 2.1.4. To evaluate the resistance of the metallization and the contact resistance between metal and emitter (or metal and ITO), the *four point probe measuring method* was used. This method uses two separated pairs of contact electrodes for applying the current and measuring the resulting voltage, respectively. In general, it would be possible to apply current and measure the voltage with the same set of electrodes. However, at the point of current induction, a transfer resistance occurs, which would falsify the voltage measurement.

4.3.1 Line resistance

Figure 4.3.1 shows the TLM measurement set-up. A TLM measurement head is shown. For line resistance measurements, a different measurement head with four measurement pins, which are arranged in a line, is used.

Individual lines were measured. The electrodes were applied with the same pressure on top of the metalized samples. A current source to induce the current was used and the voltage drop was measured with a digital multimeter (Keithley Instruments).

To be able to compare metallization lines of different geometry, the calculated resistance which is given by

$$R = \frac{U}{I} \quad (4.4)$$

has to be normalized with the length l and the cross section area A and is then given as the *specific resistance* ρ :

$$\rho = \frac{RA}{l} \quad (4.5)$$

In reality, the geometrical parameters are often difficult to measure. The length of the contact can be defined by the distance of the electrodes. But, the cross section area has to be measured separately. Even with modern 3D microscopes the measurement on textured wafers can be difficult. For very shallow metal layers which don't fully cover the pyramids of the texture, measurement is even impossible. In addition, only small sections of the metalized lines can be measured. Irregularities in the printed lines are easy to overlook. Thus, the evaluation of the cross section is always just a mean value of the measured area.

4.3.2 Contact resistance measurement

To measure the contact resistance between the metallization and the underlying emitter (or ITO, respectively) the *transfer line method*, TLM, was used. The TLM method was originally introduced by Shockley [116] and has been further refined by Widmann, Murrmann and Berger [117–120]. It was developed from the multiple contact, two-terminal method, which did not take the problem of current crowding³ into account. An illustration of the measurement setup is given in Figure 4.3.2.

The voltage given by the TLM method is given by equation 4.6:

$$V(x) = \frac{I\sqrt{R_{Sh}\rho_c}}{W} \frac{\cosh[(w_c - x)/L_T]}{\sinh(w_c/L_T)} \quad (4.6)$$

with I , the current flowing through the contacts, R_{Sh} , the sheet resistance, ρ_c , the specific contact resistance or contact resistivity, W , the contact width, w_c , the contact length and L_T , the transfer length. x gives the place of measurement on the contact with $x = 0$, the contact edge. The voltage is highest on the contact edge and drops

³Current crowding is the nonhomogenous distribution of the current density within a conductor or semiconductor especially under the contact formation points. The presence of the effect under contacts has been discovered by Kennedy and Murley [121].

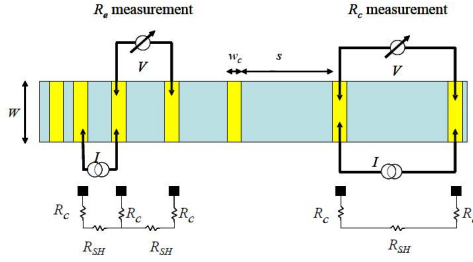


Figure 4.3.2: Illustration of the TLM measurement structure with the resistor network for the end contact resistance measurement (left) and the front contact resistance (right) [35]

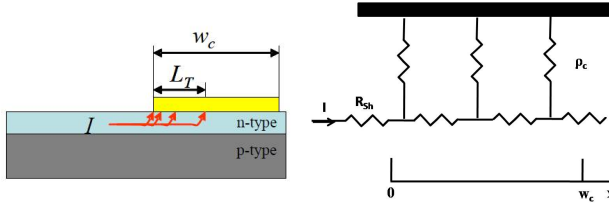


Figure 4.3.3: Illustration of transfer length (left) and contact resistance under the contact (right) ([35] and retraved from [122])

nearly exponentially with distance. The transfer length L_T is given as the distance where $V(x = L_T) = \frac{1}{e}V(x = 0)$. The transfer length is illustrated in Figure 4.3.3 and given by equation 4.7.

$$L_T = \sqrt{\frac{\rho_c}{R_{Sh}}} \quad (4.7)$$

The first simplification which is made, is the assumption that the current only flows one-dimensional through the emitter (or ITO, respectively) and that the sheet resistance R_{Sh} is constant over the whole contacted area as well as under the contact. The illustration of the transfer length shows, that the area underneath the contact has to be considered as areas of different contact resistances dependent on place x .

The contact resistivity or specific contact resistance ρ_c is independent on the contact geometry and can be calculated, if the effectively used contact area is known. If the current would be homogeneously distributed over the whole contact area, the resistivity could be easily calculated by weighing the contact resistance R_c with the contact area $w_c W$. As shown above, this is not necessarily the case, which is why calculation of the resistivity is more complicated and dependent on the transfer length L_T .

For good contacts the transfer length is in the range of $L_T = 1 \mu\text{m}$ and contact resistivity $\rho_c \leq 10^{-3} \Omega\text{cm}^{-2}$ [35]. For most contacts, the contact length is longer than $1 \mu\text{m}$, thus the active contact area is smaller than the geometrical area of the contact.

Two measurement structures can be realized by TLM. Measuring in a setup demonstrated in Figure 4.3.2 on the left-hand side enables to evaluate the contact end resistance and is also referred to as *contact end resistance test structure* (CER). A setup as given on the right-hand side gives the *contact front resistance test structure* (CFR). The CFR test structure gives the contact resistance R_c . In this case $x = 0$ and R_c is given by equation 4.8:

$$R_c = \frac{V}{I} = \frac{\sqrt{R_{Sh}\rho_c}}{W} \coth(w_c/L_T) = \frac{\rho_c}{L_T w_c} \coth(w_c/L_T) \quad (4.8)$$

Two cases can be considered to simplify equation 4.8:

1. $w_c \leq 0.5L_T \rightarrow \coth(w_c/L_T) \approx L_T/w_c \rightarrow R_c \approx \frac{\rho_c}{w_c W}$
2. $w_c \geq 1.5L_T \rightarrow \coth(w_c/L_T) \approx 1 \rightarrow R_c \approx \frac{\rho_c}{L_T W}$

For the first case, where the lateral length L_T is larger than the contact length w_c , the entire contact area $w_c W$ is used for the current transfer from the emitter (or ITO, respectively) to the contact and the contact resistance R_c is dependent on the contact geometry. This is important, since the contact resistance decreases strongly with increasing contact length w_c until $w_c = L_T$, which is illustrated in Figure 4.3.4.

As soon as the w_c exceeds L_T the contact resistance R_c approaches a constant value, which is described by case 2, when R_c is independent of w_c and the whole current enters the contact at the contact etch. However, the resistivity ρ_c is steadily increased, because it is weighted by the contact area, which increases with increasing contact length. The

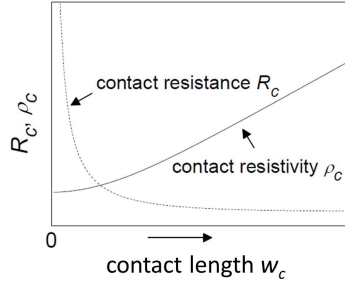


Figure 4.3.4: Illustration of relationship between contact length w_c and contact resistance and resistivity for a constant transfer length [35]

resistivity rises at an almost constant rate for small contact lengths due to the additional contact area, which is almost compensated by a more effective current transfer. As soon as $w_c \gg L_T$ the resistivity increases faster. Therefore, the contact length can be reduced until it is in the range of the transfer length, before the contact resistance, which is the limiting parameter for the solar cell, is increased [35, 122].

For the second case, when almost all the current enters at the edges of the contacted area, the current density is very high at such a small area, which can lead to degrading or even destroyed contacts after a sufficient time of operation [122].

For $x = w_c$ the measurement is done using the contact end resistance test structure and the *end resistance* R_e can be determined from equation 4.9:

$$R_e = \frac{V}{I} = \frac{\sqrt{R_{Sh}\rho_c}}{W} \frac{1}{\sinh(w_c/L_T)} = \frac{\rho_c}{L_T W} \frac{1}{\sinh(w_c/L_T)} \quad (4.9)$$

For short contacts, R_e is sensitive to the contact length and is, therefore, limited by the error in determining w_c .

The transfer length L_T which is necessary to calculate ρ_c can be calculated from measuring both, contact resistance R_c and R_e :

$$\frac{R_c}{R_e} = \cosh\left(\frac{w_c}{L_T}\right) \quad (4.10)$$

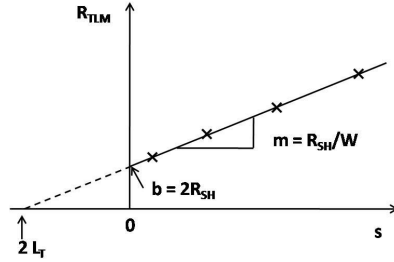


Figure 4.3.5: TLM-measurement plot with R_{TLM} is plotted against spacing s between contacts (retraced from [122])

Due to the various parameters, which influence the transfer length, a third value for description of the contact resistance, the *normalized contact resistance* $R_c * W$ can be used. It is the measured contact resistance multiplied with the contact width [37]. It is independent of the contact length and, therefore, useful for the comparison of similar contact structures. In addition, it is independent of the transfer length, thus, less error-prone than the contact resistivity ρ_c . The normalized contact resistance is used for discussion in this work. The contact resistance does not significantly contribute to the series resistance of silicon solar cells for values $< 1 \Omega\text{cm}$ [35].

To evaluate the different parameters from TLM measurements, the total resistance R_{TLM} is measured for various contact spacings and plotted versus the distance s (Figure 4.3.2). The applied current I has to overcome the contact resistance R_c twice ($2R_c$) and the emitter (or ITO, respectively) in between (R_{em}).

$$R_{TLM} = \frac{V_{i,i+1}}{I_{i,i+1}} = 2R_c + R_{em} = 2R_c + R_{Sh} \frac{s}{W} \approx \frac{R_{Sh}}{W}(s + 2L_T) \quad (4.11)$$

A measurement plot is illustrated in Figure 4.3.5.

Three parameters can be extracted from the plot:

1. The slope gives the sheet resistance R_{Sh} , if the contact width W is known.
2. The intercept at $s = 0$ leads to the contact resistance $2R_c$.

3. The intercept at $R_{TLM} = 0$ gives $-s = 2L_T$.

From these parameters the contact resistivity ρ_c can be calculated from equations 4.8 and 4.9.

However, the transfer length L_T is normally not extracted from the plot but rather calculated from measurements of contact and end resistance, when a setup shown in Figure 4.3.6 is used. Errors, which arise from this setup, can be minimized by calculating the transfer length rather than extracting it from the plot.

The shown TLM measurement setup in Figure 4.3.2 is often used and is advantageous over the setup shown in Figure 4.3.6. When the voltage is measured between contacts 1 and 4 (Figure 4.3.6) for example, the current flow can be perturbed by contacts 2 and 3. The effect of contacts 2 and 3 depend on the transfer length. If $w_c \ll L_T$, then the current does not preferably flow into the metal and contacts roughly don't influence the measurement. If $w_c \gg L_T$, then the current does flow into the contacts. In this case the contact can be thought of as two contacts joined by a metallic conductor. The shunting of the current by contacts 2 and 3 influence the measurement a lot. Therefore, the further developed structure of Figure 4.3.2 is preferred, but has to be produced separately. In practice, the structure shown in Figure 4.3.6 can be cut out of a fully processed solar cell wafer and is easier to realize.

To do a *current sweep* measurement a current is applied between two fingers of the TLM measurement structure and the corresponding voltage is measured. The current gets altered during the measurement to create a data set of current and corresponding voltage values. The form of the resulting graph gives information about the type of contact between the measured materials. A linear fit following the equation 4.4 indicates an ohmic contact, while a typical diode curve following equation 2.1 gives hint to a Schottky contact.

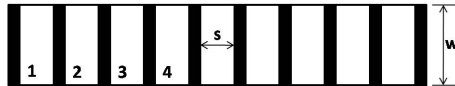


Figure 4.3.6: Illustration of simplified TLM measurement structure (retraced from [122])

4.4 Thermal gravimetric-differential scanning analysis - TG-DSC

Thermal gravimetric-differential scanning analysis is a combination of thermo-gravimetry (TG) and differential scanning analysis (DSC). It was used to study the reaction mechanism during contact formation on silicon solar cells (chapter 8) and the behavior of organics used in silver nanoparticle ink and paste formulations (chapter 5). The thermal gravimetric measurement is used to study mass changes of a sample against temperature and/or time. The sample is placed in a temperature stable crucible (e.g. platinum, aluminum (up to 630 °C) or ceramic), which is connected to a sensitive balance. The crucible is situated within a furnace which is heated up with a defined temperature ramp. The mass change is measured during the whole process. From mass changes, which occur during heating and/or cooling, one can reason the underlying reaction or change in state. Evaporation, combustion or chemical reactions between educts in the sample or oxidation or reduction can lead to a mass change. The furnace can be flooded with different gases (oxygen, nitrogen, argon, hydrogen, etc.). The information gained from a TG measurement are: mass changes, reaction temperature and reaction kinetics.

Additional information can be collected by differential scanning analysis measurements. The temperature difference of the sample against a reference (usually an empty crucible of the same material as the measuring crucible) is measured. The temperature signal is then calculated into a heat flux signal which is proportional to the temperature. The setup is the same as for TG measurements, except for the holder. The DSC measurement holder consists of two plates of which each is connected to a thermocouple. If the holder is placed on a balance a combined measurement of TG- and DSC signal against temperature and/or time is possible. During the measurement, both, the reference and the sample, change in temperature. If a reaction takes place, the temperature for the sample rises faster (exothermic reaction - “heat production”) or slower (endothermic reaction - “heat consumption”) compared to the reference. Exothermic changes can be measured, for example, of oxidation or recrystallization processes; endothermic changes occur, e.g., of evaporation or melting. The difference in the thermal voltage is measured from the thermocouples,

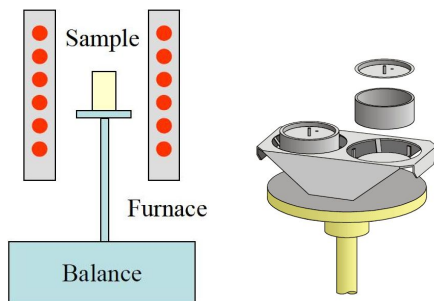


Figure 4.4.1: Schematic setup of a thermo-gravimetric (TG) measurement setup (left) and a DSC sample holder (right) [123]

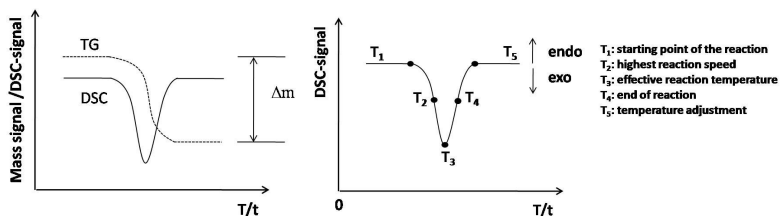


Figure 4.4.2: Schematic TG-DSC signals (left) and characteristic points in DSC signal (right) (retraced from [35])

calculated to heat flux, which can be plotted as a function of given temperature or time. A schematic illustration of a thermo-gravimetric (TG) measurement setup and a DSC holder are shown in Figure 4.4.1. Figure 4.4.2 shows the signals which are determined by a TG-DSC measurement and the information which can be drawn from a DSC signal.

In this work a STA 449 F3-Jupiter TG-DSC measurement tool by NETZSCH was used. The measurement setup was equipped with a high-speed furnace with air cooling and a platinum TG-DSC sensor. The samples were processed by an automated sample changer.

4.5 Determination of sintering temperature

The sintering temperature is not easy to determine. Sintering is a diffusion process (see Section 2.4.3) and is not detectable with conventional measuring methods like differential thermal calorimetry. Silver nanoparticles within sizes around 20 to 50 nm appear copper colored or golden, when placed on a silicon nitride surface. During sintering the color changes noticeably from copper or golden to bright white. The change is very fast and easy to detect. A heating device (Linkam TS 1500⁴), with precise temperature control was used and sintering temperature was estimated optically. The particles were placed drop wise on a silicon nitride covered wafer and were heated up with a rate of 20 °C/min. Note that all sintering temperatures given below are estimations from this color change during heating and are not more precise than in a range of +/- 10 °C.

4.6 Cross section preparation

A cross section allows to visually evaluate the contact formation between metal and semiconductor (or ITO, respectively) and to study the contact itself.

Within this work, an IM4000 ion beam miller (Hitachi) was used to produce smooth cross sections without the necessity of resin embedding and without material smearing due to mechanical abrasion.

The sample is placed in an evacuation chamber and an argon ion beam which is accelerated by an electric field in vacuum, is used to mill the surface of the sample. The ions collide with the surface atoms and release them from the solid.

4.7 SEM/EDX and FIB

A very important characterization method for this work was the *scanning electron microscope* (SEM). Electrons are accelerated from a cathode under high voltage onto the sample. They interact with the

⁴A specimen holder built in a furnace. The device is illustrated in the appendix. With this setup, temperature ramps up to 1500 °C can be conducted.

surface and - depending on the voltage - also with the matter to a certain depth. The reflected electrons (backscattered electrons) and the electrons which were released from the matter (secondary electrons) can be detected. A software calculates an image of the surface. The electron beam is moved over the sample (scanned) by a set of electronic lenses. The method is, in general, similar to an optical microscope but with the wavelength of the electrons used to scan or reflect the surface, respectively, much higher resolutions can be achieved.

Electrons can interact with the matter of the sample in a way that electrons from the inner shells of the atoms are released. These are replaced by outer shell electrons. The energy of the X-ray radiation which is released by this process can be detected and is characteristic for each element. The detection method for characterizing elements this way is called *energy dispersive X-ray analysis* (EDX). It allows for the spatial determination of the elements at or closely below the sample surface.

The focused ion beam (FIB) equals basically a cross section miller system but with much higher resolutions. The ion beam is focused on the surface and very small areas can be milled with the ions. Cuts of few nanometers can be milled into the sample. The FIB is combined in an SEM microscope and SEM images can be taken after each milling period of which the resolution can be set. With this method several places at the sample can be characterized without the need to make a new cross section polish after each imaging.

With SEM, visual determination in the submicrometer range can be made and especially the contact formation between metal and semiconductor can be determined in detail.

Within this work the SEM SU 70 from HITACHI was used. An EDX detector from EDAX was used. The FIB used is an Auriga 60 from ZEISS equipped with a BRUKER EDX detector.

4.8 Confocal microscope

The microscope used in this work was the LEXT confocal microscope (Olympus). A confocal microscope allows the evaluation of three dimensional images of a surface, calculated by a software. The technique is based on the reflection of light from the sample surface while changing the vertical distance between sample and light sensor. The LEXT

microscope uses a laser with a wavelength of $\lambda = 405$ nm, which allows for very high resolutions of the image. A second image is measured with white light which allows a color image of the surface, which can also be allocated with the laser image.

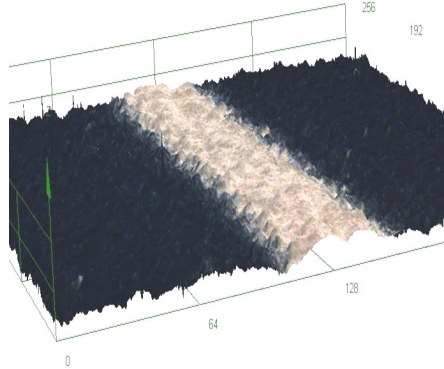


Figure 4.8.1: 3D image taken with LEXT confocal microscope of an aerosol jet printed contact

The software allows to evaluate several properties of the surface, like the surface roughness. It also allows “stitching” of several images, to increase the image area. Also, a division of the 3D image into multiple profiles and a cross section area measurement are possible. The calculation of a mean cross section area of 1000 single cross sections is possible.

However, the exact determination of the surface is not trivial especially for textured solar cell surfaces. The pyramidal surface structure complicates the calculation of the exact surface height and thus, cross section area calculations always imply some uncertainty.

A 3D image taken with the LEXT microscope of an aerosol jet printed contact is shown in Figure 4.8.1.

4.9 Electroluminescenz measurement

Electroluminescenz (EL) uses the property of a semiconductor to work as a light emitting device (LED) if external voltage is applied: elec-

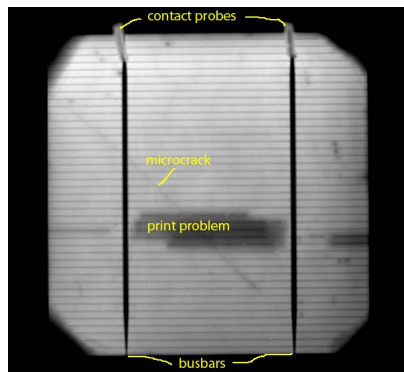


Figure 4.9.1: EL image of a silicon solar cell showing microcrack and region of poor metallization [25]

trons recombine at the p/n-junction partially by illumination of light. This phenomenon is called *electroluminescenz*. The light illuminated by a silicon solar cell has a wavelength in the infrared region and can only be detected by CCD cameras or special detectors.

The emitted light intensity is proportional to the applied voltage and the local voltage within the solar cell. Therefore, inactive cell regions, for example, non-contacted regions or cracks within the cell appear dark in the EL image. A cell or even a module can be measured within seconds and defects can be detected locally. An example for an electroluminescenz image is given in Figure 4.9.1.

4.10 Cyclic voltammetry

A commonly used experiment to characterize electrochemical systems consists of potential sweeps and the recording of the current response. Transfer processes which occur at different potentials can be recognized at the current. The electrochemical system can be characterized over a wide range of potential within a short time. The potential can be scanned only one directional. The method is known as *linear potential sweep* or the measurement can also be done with the corresponding backward sweep which results in the *cyclic voltammetry* (CV) measurement. Processes which occur within the system and the

counter processes can be analyzed.

The method depends on the electrochemical system, the potential range and the speed of the sweep and resting times (e.g. at the open circuit voltage). More information about the method is given in [106].

4.11 Tape test

The tape test is a rather simple test to evaluate the quality of adhesion. It is very imprecise and can only be used for first qualitative determinations. An adhesive tape (e.g. TESA) is pressed on the metallization and the substrate surrounding. The substrate is fixed onto a stable surface (e.g. with a ruler) to avoid wafer breakage. The tape is then peeled off the surface and the amount of teared metallization roughly estimated. If no metal sticks to the tape, adhesion quality is adequate for further characterization. For exact determination of the adhesion strength, quantitative methods have to be used.

A more quantitative test according to DIN EN 61189-2 includes soldering of a solderable strip onto the plated contact and pull-off of the strip with a force meter. For solar cell application a minimum adhesion of 1 N/mm has to be reached to fulfill industrial demands

4.12 Goniometer measurements

Goniometer measurements were done with a KRÜSS EasyDrop DSA100. Contact angle measurements can be done to investigate the behavior of a surface against a certain liquid or liquid system and/or to determine the surface energy. To determine the surface energy of a surface, the contact angle of several liquid drops, sitting on the surface are measured with a camera. The measurement of the contact angle has to be done within 10 seconds after setting the drop onto the surface. Otherwise gravitation and liquid evaporation can influence the measurement.

5 Nanoparticle based Metallization on ITO

*In this chapter, metallization on ITO with inks and pastes based on silver nanoparticles is presented. The suitability of silver nanoparticles for low temperature metallization and the contact properties to ITO are discussed in detail. After a short introduction 5.1 the experiments discussed in this chapter are described in Section 5.2. The synthesis of silver nanoparticles with low sintering temperatures is addressed in Section 5.2.1. The effects of nanoparticle sintering are described in Section 5.3.2. The importance of the capping agent will be highlighted. Section 5.3.3 discusses the results of printing experiments. The effect of chemical sintering and tempering on silver nanoparticles in comparison to thermal sintering is focused on in Section 5.3.4. It is shown that chemical sintering can significantly lower the necessary tempering temperature and mechanically stabilizes the silver layer to a certain extent. The electrical results for line resistivity and contact resistivity to ITO are discussed in Section 5.3.5 and Section 5.3.6, respectively. For inks, line resistivities of only $\rho_{spez.} = 2.3 \cdot 10^{-8} \Omega\text{m}$ and a normalized contact resistance of $R_c * W = 0.166 \Omega\text{cm}$ were measured. For pastes, very good values for the line resistivity ($\rho_{spez.} = 3.16 \cdot 10^{-8} \Omega\text{m}$) and the normalized contact resistances ($R_c * W = 0.068 \Omega\text{cm}$) were measured. The alternative approach of chemical sintering with in-built chemical sintering agents is described and discussed in Section 5.3.7. Section 5.4 gives a short summary of the chapter.*

5.1 Introduction

Besides the common industrial solar cell concepts which are processed at high temperatures ($> 800 \text{ }^\circ\text{C}$), alternative and new cell concepts are being developed. Some of those cell designs like hetero junction with intrinsic thin layer (HIT) solar cells and organic solar cells are sen-

sitive against high processing temperatures. The substrate of organic solar cells is usually a polymer like polyethylene terephthalate (PET), which are not stable against high temperatures. HIT cells contain amorphous silicon which degrades $> 200 - 250$ °C (also depending on the duration of heat exposure) and loses its good passivation properties [93]. In addition, they require a full size area metallization to collect the charge carriers of the active cell areas, due to short mean free paths of the charge carriers in the amorphous silicon. However, a full area metallization with a metal on the front side is not possible, due to the intransparency of metals. For this reason, these cell designs have to be metalized with a full area *transparent conductive oxide*, a TCO.

The most widely used TCO is ITO (Indium Tin Oxide). The TCO is contacted with a metal grid to collect the energy and allows soldering of the single cells. Most important for the metal grid application is to avoid high temperatures as normally used during contact formation of standard silicon solar cells. To avoid high temperatures, two metallization techniques are mainly being used today.

Photolithography is the primary metallization technique used on the lab scale: very narrow and precise metallization grids can be applied. However, the technique is complicated and expensive and is not reasonable for mass production [17] (see also Section 3.4).

Industrially, polymer based silver pastes are being screen printed on the cells. These pastes contain a high amount of silver particles or flakes. The high silver content, which is necessary to gain good conductivities, is the reason for high silver consumption and, thus, high costs [17]. The silver amount used in polymer pastes is very high (70 - 90 %) [8, 9] compared to the low conductivity [62]. The best polymer paste reaches specific conductivity values of $\rho_{spec.} = 10 * 10^{-8} - 15 * 10^{-8} \Omega * m$, which is still 4 to 6 times higher compared to high temperature firing pastes and even 10 times higher than bulk silver (specific conductivity of bulk silver $\rho_{spec.} = 1,58 * 10^{-8} \Omega * m$) [5, 112]. Furthermore, screen printing is a contact metallization technique, which can cause wafer breakage.

A crucial factor for the introduction of a new cell concept is the industrial feasibility and the production costs. Therefore, an alternative metallization technique for these new cell designs is necessary.

One possibility for a new metallization technique could be based on silver nanoparticles. Nanoparticles are able to be sintered at much

lower temperatures (< 200 °C) than the melting temperature of the corresponding bulk material [23]. The sintering allows higher conductivities than contact formation between single particles through simply touching. In addition, nanoparticles can be stabilized in liquids and formulated to an ink, which can be printed contactless via ink jet or aerosol jet printing [22]. Ink jet and aerosol jet printing are low cost and fast printing techniques, which make very narrow line widths of $10\ \mu\text{m}$ (aerosol jet [19]) and $< 35\ \mu\text{m}$ (ink jet [20]) possible.

The silver nanoparticles have to be stabilized via “capping agents”. These capping agents are organics, mostly polymers, which cover the surface of the silver and form an insulating layer between the metal particles. To overcome this limitation the silver patterns are getting cured after printing. This is most often done thermally [16, 65, 76–78] but requires temperatures as high as at least 200 °C and quite long sintering times of around $30 - 60$ min. For the application on temperature sensitive solar cell concepts like HIT solar cells, this temperature is close to the limit but still acceptable [93], if curing times are short. Other low sintering or curing techniques are electrical sintering [56], plasma sintering [59], microwave sintering [57] and laser sintering [55] of the printed patterns. However, the achievable conductivity of all these techniques is still too poor for industrial application on solar cells.

Another low-temperature sintering technique, which can be even done at room temperature, is chemical sintering invented by Magdassi et al. [60, 83]. The sintering of the particles is triggered by substitution of the capping agent by smaller particles, which leads to coalition and sintering of the particles.

Ink formulations based on metal nanoparticles are already commercially available, however, in general those inks are meant for application for printed electronics based on polymeric films. The amount of current that has to be transported is lower than for solar cells. In addition, these ink formulations do not consider the demands on contact resistance to the substrate [55–59, 81, 85].

Within this chapter the potential of silver nanoparticles as alternative material for metallization of temperature sensitive cell concepts, especially on ITO, is being investigated.

5.2 Experimental

Specifications of used chemicals:

Silver acetate: Acros organics, 99% pure

1-Dodecylamine, 1-heptylamine: ABCR, 98%

Phenyldiazine: ABCR, 97%

Ethyl cellulose: Sigma-Aldrich, 300 cP in toluene/ethanol (80/20), 48% ethoxyl

Hydroxy ethyl cellulose: Sigma-Aldrich, average $M_w \sim 90000$ mol

Gluten: organic market, food-grade

Ethylene glycole: Sigma-Aldrich, anhydrous 99.8%

Acetone: Applichem, ACS ISO

Ethanol: Rectapur, 90%, denatured with methanole GPR

Isopropanole: Kraft, Bernd, for analysis

Toluene, Sigma-Aldrich, ACS reagent, >99.5%

5.2.1 Nanoparticle characterization

Synthesis description

Silver nanoparticles were synthesized according to the procedures published by Li [124] and Peng [125]. The basic synthesis described by Li is as follows:

A mixture of silver acetate (AgAc) (0.17 g, 1 mmol) and 1-dodecylamine (DA) (2.41 g, 10 mmol) in toluene (40 ml) was first heated at 60 °C until silver acetate was dissolved (about 5 min). To the resulting solution a solution of phenylhydrazine (PH) (0.11 g, 1 mmol) in toluene (10 ml) was added drop wise (rate 1 ml/min). The resulting reaction mixture was stirred at 60 °C for 1 h before cooling down to room temperature. Subsequently, acetone (10 ml) was added to the reaction mixture to destroy excess phenylhydrazine. Afterwards, the solvent was removed with a rotary evaporator (bath temperature ≤ 50 °C). The resulting concentrated reaction mixture was added to a stirring ethanol/acetone mixture (50 ml/50 ml) to precipitate the crude silver nanoparticle product. The crude silver nanoparticles were isolated by centrifugation, washed twice with acetone (50 ml each), and vacuum-dried at room temperature to receive a black solid.

Several parameters were varied following the procedure by Li in order to improve nanoparticle quality and stability. The variations

Table 5.2.1: Nanoparticle synthesis: Varied parameters

Varied parameter	Range of parameter variation
$n(\text{AgAc})/n(\text{DA})$	0.1, 0.2, 0.5
$n(\text{AgAc})/n(\text{PH})$	0.2, 1.0, 2.0
Reaction temperature [$^{\circ}\text{C}$]	30, 40, 60
Drop rate of PH addition [ml/min]	0.5, 1.0, all at once
Capping agent	1-dodecylamine, 1-heptylamine
$c(\text{AgAc})$ [mol/L] ¹	0.1, 0.2
Doubling the whole synthesis volume	

done can be seen in Table 5.2.1.

The most important difference of Peng's synthesis in comparison to the one described by Li is the sequence of addition of the reducing agent phenylhydrazine. Peng adds the silver acetate to the phenylhydrazine instead the other way around as described by Li.

In further experiments, the synthesis described by Li was altered according to the results of Peng and the results gained by the experiments of this work. The final synthesis procedure for silver nanoparticles as used in the ink formulations was as follows:

1-Dodecylamine (1.85 g, 10 mmol) was dissolved in toluene (30 ml) under stirring at room temperature. Silver acetate (0.85 g, 5 mmol) was added and further stirred until complete dissolution. Phenylhydrazine (0.5 ml, 5 mmol) was dissolved in toluene (100 ml) at room temperature. The solution of 1-dodecylamine and silver acetate was added quickly to the solution of phenylhydrazine under stirring and left stirring for 15 minutes at room temperature. Acetone (10 ml) was added to destroy excess phenylhydrazine. Subsequently, the solvent was removed with a rotary evaporator (bath temperature ≤ 50 $^{\circ}\text{C}$). The resulting concentrated reaction mixture was added to a stirring ethanol/acetone mixture (50 ml/50 ml) to precipitate the crude silver

nanoparticle product. The crude silver nanoparticles were isolated by centrifugation, washed twice with acetone (50 ml each), and vacuum-dried at room temperature to receive a black solid.

Sedimentation

Synthesized and commercially available PAA-capped particles (product “P02” from METALOR[®], average particle size 20-50 nm) were tested for sedimentation behavior.

Particle suspensions of either 1-dodecylamine or 1-heptylamine capped particles of either 20 wt% silver particles or 50 wt% silver particles in toluene or isopropanole were mixed, sonicated for 15 min at room temperature and left standing for sedimentation for 24 hours.

Particle suspensions of PAA capped particles of 20 wt% or 50 wt% silver particles, respectively, and 1 $\mu\text{l/g}_{\text{Ag-particles}}$ NH_4OH in water/ethylene glycol (50/50) were mixed, sonicated for 15 min at room temperature and left standing for sedimentation for 24 hours.

The overlaying solvent or suspension was decanted and the sediments were dried on a hot plate. The mass of the sediments were evaluated.

Characterization

Particle size, dispersity and agglomeration behavior were investigated by scanning electron microscopy (SEM).

5.2.2 Effects on particle sintering

Effect of size

Particles of different size but with the same capping agent synthesized as described in Section 5.2.1 were used. A dispersion of silver nanoparticles in isopropanole was sonicated for 15 min.

The sintering temperature was determined with a heating device (Linkam TS 1500²). The particles were placed drop wise on a silicon nitride covered wafer, dried slowly on a hot plate at 50 °C for 5 min and were then heated up in the heating device with 20 °C/min. Unsintered

²A specimen holder built in a furnace. The device is illustrated in the appendix. With this setup, temperature ramps up to 1500 °C can be conducted.

Table 5.2.2: Details of silver nanoparticles investigated in this work

Particle No.	Ø Particle size [nm]	Capping agent
1	20-50	PVP
2	~20	PAA
3	10-50	1-dodecylamine

particles appear copper or golden colored. Sintered particles change to a silver-white color. Note that all sintering temperatures given below are estimations from this color change during heating and are not more precise than in a range of ± 10 °C.

TG-DSC characterization was done using a STA 449 F3-Jupiter TG-DSC measurement tool by NETZSCH. Aluminum crucibles with open lid were used. Heating rate was 5 °C/min. Temperature and calorimetric corrections specific for each TG-DSC setup were used. The measurement chamber was flooded with compressed air with a gas flow rate of 50 ml/min. The balance was protected by a nitrogen gas flow of 20 ml/min. Weight determination was done just before the measurement.

Effect of capping agent

To investigate the effect of capping agents, different silver nanoparticles were chemically sintered. Details on the used particles and capping agents are given in Table 5.2.2.

Particles capped with 1-dodecylamine (particle 3) were synthesized according to the following procedure (see also Section 5.2.1).

1-Dodecylamine (1.85 g, 10 mmol) was dissolved in toluene (30 ml) under stirring at room temperature. Silver acetate (0.85 g, 5 mmol) was added and further stirred until complete dissolution. Phenylhydrazine (0.5 ml, 5 mmol) was dissolved in toluene (100 ml) at room temperature. The solution of 1-dodecylamine and silver acetate was added quickly to the solution of phenylhydrazine under stirring and left stirring for 15 minutes at room temperature. Acetone (10 ml) was added to destroy excess phenylhydrazine. Subsequently, the solvent was removed with a rotary evaporator (bath temperature ≤ 50 °C). The resulting concentrated reaction mixture was added to a stirring ethanol/acetone mixture (50 ml/50 ml) to precipitate the crude silver

nanoparticle product. The crude silver nanoparticles were isolated by centrifugation, washed twice with acetone (50 ml each), and vacuum-dried at room temperature to receive a black solid.

Particles 1 and 2 were purchased from Cabot and Metalor, respectively (product from Cabot with PVP capped particles from ink CCl300, product P02³ from Metalor[®] with PAA capped particles.).

Suspensions of 20 wt% PAA capped silver nanoparticles in water and NH₄OH (1 µl/g_{Ag particles}) and 20 wt% DA capped silver nanoparticles in isopropanole were sonicated for 15 min and dropped on a SiN_x coated silicon wafer. The samples were dried on a hot plate at 100 °C for 5 min. PVP capped particles were already suspended by Cabot and also dried at 150 °C for 5 min.

Particle samples were then chemically sintered according to Magdassi et al. [60] by placing the samples over concentrated HCl within a distance of 2 cm and left in the HCl vapor for 10 sec according to Magdassi et al. [60]. After chemical sintering the samples were tempered on a hot plate at 200 °C for 15 min.

Particles were characterized via SEM imaging before and after chemical sintering.

TG-DSC characterization was done using a STA 449 F3-Jupiter TG-DSC measurement tool by NETZSCH. Aluminum crucibles with open lid were used. Heating rate was 5 °C/min. Temperature and calorimetric corrections specific for each TG-DSC setup were used. The measurement chamber was flooded with compressed air with a gas flow rate of 50 ml/min. The balance was protected by a nitrogen gas flow of 20 ml/min. Weight determination was done just before the measurement. Samples tested were products P02 (PAA capped) and D02 (PVP capped) from METALOR.

Effect of additives

Comparison of some common additives used in inks and pastes was done to investigate the impact of their effect by mixing suspensions of 20 wt% PAA capped silver nanoparticles (see Section 5.2.2) and 1 µl/g_{Ag-particle} NH₄OH in water/ethylene glycol (50/50) and adding

³The product P02 is no longer available from Metalor. In cooperation with this work, the product has been further developed and is now available as "Ag P04".

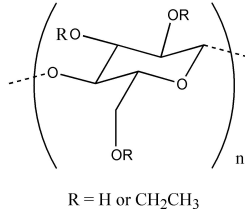


Figure 5.2.1: Chemical structure of (hydroxy)ethyl cellulose

1-3 wt% of the additive (see Table 5.2.3) according to the manufacturer's instructions. For better solubility of ethyl cellulose in the suspension, a solvent mixture of terpineol/ethylene glycol (50/50) instead of water/ethylene glycol was used.

All additives are based on different polymers (see Table 5.2.3).

The suspensions were dropped on SiN_x coated silicon wafers and dried at 100-150 °C for 5 min on a hot plate.

After drying particles were chemically sintered according to Magdassi et al. [60] by placing the samples over concentrated HCl within a distance of 2 cm and left in the HCl vapor for 10 s. After chemical sintering the samples were tempered on a hot plate at 200 °C for 15 min.

Samples were characterized by SEM imaging.

Table 5.2.3: Details of additives investigated in this study

Additive	wt%	Functional group	Kind of additive
Byk 4510	2.5	COOH	Adhesion promoter
Byk ES80	1	OH, COOH	Electrical conductive
Ethyl cellulose	3	OR	Binder
Hydroxyethyl cellulose	2	OH, OR	Binder
Gluten ⁴ (no used commonly)	1	N, O	Binder

5.2.3 Ink and paste printing

Nanoparticle inks

Inks were formulated according to the following procedures:

- PAA capped particles (P02 from METALOR[®], average particle size 20-50 nm): 20 wt% silver nanoparticles were suspended in 80 wt% of a solution of deionized water/ethylene glycol (50/50). 50 $\mu\text{l}/1\text{g}_{\text{silver particles}}$ of concentrated ammonia were added.
- Amine capped particles: 20 wt% amine capped particles were suspended in 80 wt% isopropanole.

The test inks were printed on planar silicon wafers and silicon wafers with alkaline etched random pyramid texture with a 70 nm thick PECVD⁵ SiN_x⁶ ARC⁷, respectively. In addition, multi-crystalline silicon wafers with acidic texture and PECVD SiN_x anti-reflection coating were used.

Ink jet printing was done using a DIMATIX DMP 2831 drop-on-demand printer with piezo ink jet cartridge. The chuck was heated to 60 °C. A cartridge with 10 pl nozzle size was used. Due to uneven print impression, only 4 out of 16 nozzles were used for printing. The drop spacing was set to 50 μm and 50 μm line width. To gain measurable line heights of around 1 μm , 10 layers were printed.

Aerosol jet printing was done with a M3D system from OPTOMECH INC. Gas flow has to be adjusted to the ink for each printing process. The chuck was heated to 120 °C and a print head with 8 nozzles and 150 μm nozzle size was used. The number of printing layers is also dependent on the gas flow settings and ink behavior. Within a batch the number of layers was chosen in a way, that a closed metallization finger could be observed under the confocal microscope.

The inks were dried at 100-150 °C for 5 min on a hot plate. After drying, the samples were placed over concentrated HCl within a distance of 2 cm and left in the HCl vapor for 10 sec according to Magdassi et al. [60].

Characterization was done by SEM and confocal microscope (LEXT) imaging.

⁵Plasma-enhanced chemical vapor deposition

⁶Silicon nitride

⁷Anti-reflection coating

Adhesion testing was done with the tape test.

Nanoparticle pastes

The screen printing paste was formulated from 75 wt% PAA capped silver nanoparticles (P02 from METALOR[®], average particle size 20-50 nm), 2 wt% hydroxy ethyl cellulose and 23 wt% of solvent (water/ethylene glycol = 50/50) and 50 $\mu\text{l}/\text{g}_{\text{Ag particles}}$ NH_4OH . The paste was homogenized in a 3-roller mill for 5 times.

The paste was screen printed on silicon wafers with alkaline etched random pyramid texture with a 70 nm thick PECVD SiN_x anti-reflection coating.

Screen printing was done by hand printing. The screen characteristics were: openings for the fingers = 100 μm , finger spacing $d = 2$ mm, mesh/inch = 280 in^{-1} , thread size 0.032 mm.

The pastes were dried at 100-150 $^\circ\text{C}$ for 5 min on a hot plate. After drying, the samples were placed over concentrated HCl within a distance of 2 cm and left in the HCl vapor for 10 s according to Magdassi et al. [60].

Characterization was done by SEM and confocal microscope (LEXT) imaging.

Adhesion testing was done with the tape test.

5.2.4 Sintering

Nanoparticle inks

The nanoparticle inks were formulated according to the following procedure.

20 wt% PAA capped silver nanoparticles (P02 from METALOR[®], average particle size 20-50 nm) were suspended in 80 wt% of a solution of deionized water/ethylene glycol (50/50). 50 $\mu\text{l}/\text{g}_{\text{Ag particles}}$ of concentrated ammonia was added.

The test inks were printed on silicon wafers with alkaline etched random pyramid texture with a 70 nm thick PECVD SiN_x anti-reflection coating.

Ink jet printing was done using a Dimatix DMP 2831 drop-on-demand printer with piezo ink jet cartridge. The chuck was heated to 60 $^\circ\text{C}$. A cartridge with 10 pl nozzle size was used. Due to uneven print impression, only 4 out of 16 nozzles were used for printing.

The drop spacing was set to 50 μm and 50 μm line width. To gain measurable line heights of around 1 μm , 10 layers were printed.

Aerosol jet printing was done with a M3D system from OPTOMECH INC. Gas flow has to be adjusted to the ink for each printing process. The chuck was heated to 120 $^{\circ}\text{C}$ and a print head with 8 nozzles and 150 μm nozzle size was used. The number of printing layers is also dependent on the gas flow settings and ink behavior. Within a batch the number of layers was chosen in a way, that a closed metallization finger could be observed under the confocal microscope.

The inks were dried at 100-150 $^{\circ}\text{C}$ for 5 min on a hot plate. The samples were divided into two groups of which one group was chemically sintered and tempered and the second group was thermally sintered. The two groups were further subdivided into two groups. One subgroup was tempered for 10 s and the second subgroup was tempered for 15 min on a hot plate.

For chemical sintering, samples were placed over concentrated HCl within a distance of 2 cm and left in the HCl vapor for 10 s according to Magdassi et al. [60]. After chemical sintering, samples were tempered on a hot plate. Tempering was done at temperatures of 150 $^{\circ}\text{C}$, 200 $^{\circ}\text{C}$, 250 $^{\circ}\text{C}$, 300 $^{\circ}\text{C}$, 350 $^{\circ}\text{C}$ and 400 $^{\circ}\text{C}$ for 10 s and 15 min, respectively.

Thermal sintering was done at temperatures of 150 $^{\circ}\text{C}$, 200 $^{\circ}\text{C}$, 250 $^{\circ}\text{C}$, 300 $^{\circ}\text{C}$, 350 $^{\circ}\text{C}$ and 400 $^{\circ}\text{C}$ on a hot plate for 10 s and 15 min, respectively.

Characterization was done by SEM imaging.

Nanoparticle pastes

Screen printing paste 1 was formulated from 75 wt% PAA capped silver nanoparticles (P02 from METALOR[®], average particle size 20-50 nm), 2 wt% ethyl cellulose and 23 wt% of solvent (terpineol/ethylene glycol = 50/50) and 50 $\mu\text{l}/\text{g}_{\text{Ag particles}}$ NH_4OH . The paste was homogenized in a 3-roller mill for 5 times.

Screen printing paste 2 was formulated from 75 wt% PAA capped silver nanoparticles, 2 wt% hydroxy ethyl cellulose and 23 wt% of solvent (water/ethylene glycol = 50/50) and

50 $\mu\text{l}/\text{g}_{\text{Ag particles}}$ NH_4OH . The paste was homogenized in a 3-roller mill for 5 times.

The pastes were screen printed on silicon wafers with alkaline etched random pyramid texture with a 70 nm thick PECVD SiN_x anti-

reflection coating.

Screen printing was done by hand printing. The screen characteristics were: openings for the fingers = 100 μm , finger spacing $d = 2$ mm, mesh/inch = 280 in^{-1} , thread size 0.032 mm.

The pastes were dried at 100-150 $^{\circ}\text{C}$ for 5 min on a hot plate.

The samples of paste 1 were chemically sintered and tempered at 200 $^{\circ}\text{C}$ for 15 min.

The samples of paste 2 were divided into two groups of which one group was chemically sintered tempered and the second group was thermally sintered. The two groups were further subdivided into two groups. One subgroup was tempered for 10 s and the second subgroup was tempered for 15 min on a hot plate.

For chemical sintering, samples were placed over concentrated HCl within a distance of 2 cm and left in the HCl vapor for 10 s according to Magdassi et al. [60]. After chemical sintering, samples were tempered on a hot plate. Tempering was done at temperatures of 150 $^{\circ}\text{C}$, 200 $^{\circ}\text{C}$, 250 $^{\circ}\text{C}$, 300 $^{\circ}\text{C}$, 350 $^{\circ}\text{C}$ and 400 $^{\circ}\text{C}$ for 10 s and 15 min, respectively.

Thermal sintering was done at temperatures of 150 $^{\circ}\text{C}$, 200 $^{\circ}\text{C}$, 250 $^{\circ}\text{C}$, 300 $^{\circ}\text{C}$, 350 $^{\circ}\text{C}$ and 400 $^{\circ}\text{C}$ on a hot plate for 10 s and 15 min, respectively.

Characterization was done by SEM imaging.

TG-DSC characterization was done using a STA 449 F3-Jupiter TG-DSC measurement tool by NETZSCH. Aluminum crucibles with open lid were used. Heating rate was 5 $^{\circ}\text{C}/\text{min}$. Temperature and calorimetric corrections specific for each TG-DSC setup were used. The measurement chamber was flooded with compressed air with a gas flow rate of 50 ml/min. The balance was protected by a nitrogen gas flow of 20 ml/min. Weight determination was done just before the measurement.

5.2.5 Line resistivity

Nanoparticle inks

The nanoparticle inks were formulated according to the following procedure.

20 wt% PAA capped silver nanoparticles (P02 from METALOR[®], average particle size 20-50 nm) were suspended in 80 wt% of a solu-

tion of deionized water/ethylene glycol (50/50). 50 μl /1g_{Ag} particles of concentrated ammonia had been added.

The test inks were deposited on silicon wafers with alkaline etched random pyramid texture with a 70 nm thick PECVD SiN_x anti-reflection coating. In addition, multi-crystalline silicon wafers with acidic texture and PECVD SiN_x anti-reflection coating were used.

Ink jet printing was done using a Dimatix DMP 2831 drop-on-demand printer with piezo ink jet cartridge. The chuck was heated to 60 °C. A cartridge with 10 pl nozzle size was used. Due to uneven print impression, only 4 out of 16 nozzles were used for printing. The drop spacing was set to 50 μm and 50 μm line width. To gain measurable line heights of around 1 μm , 10 layers were printed.

Aerosol jet printing was done with a M3D system from OPTOMECH INC. Gas flow has to be adjusted to the ink for each printing process. The chuck was heated to 120 °C and a print head with 8 nozzles and 150 μm nozzle size was used. The number of printing layers is also dependent on the gas flow settings and ink behavior. Within a batch the number of layers was chosen in a way, that a closed metallization finger could be observed under the confocal microscope.

The inks were dried at 100-150 °C for 5 min on a hot plate. The samples were divided into two groups of which one group was chemically sintered and tempered and the second group was thermally sintered. The two groups were further subdivided into two groups. One subgroup was tempered for 10 s and the second subgroup was tempered for 15 min.

For chemical sintering, samples were placed over concentrated HCl within a distance of 2 cm and left in the HCl vapor for 10 s according to Magdassi et al. [60]. After chemical sintering, samples were tempered on a hot plate. Tempering was done at temperatures of 150 °C, 200 °C, 250 °C, 300 °C, 350 °C and 400 °C for 10 s and 15 min, respectively.

Thermal sintering was done at temperatures of 150 °C, 200 °C, 250 °C, 300 °C, 350 °C and 400 °C on a hot plate for 10 s and 15 min, respectively.

The line width and height of printed silver metallization was measured using the confocal laser microscope LEXT and SEM imaging. Each finger was measured separately to ensure exact resistivity calculation.

The lateral resistance was measured by a transfer length method (TLM) measurement setup. A linear measurement head was used.

The applied current was set to $I = 10$ mA.

Nanoparticle pastes

Screen printing paste 1 was formulated from 75 wt% PAA capped silver nanoparticles (P02 from METALOR[®], average particle size 20-50 nm), 2 wt% hydroxy ethyl cellulose and 23 wt% of solvent (water/ethylene glycol = 50/50) and 50 $\mu\text{l}/\text{g}_{\text{Ag particles}}$ NH_4OH . The paste was homogenized in a roller for 5 times.

Screen printing paste 2 was formulated from 75 wt% PAA capped silver nanoparticles, 2 wt% ethyl cellulose and 23 wt% of solvent (terpineol/ethylene glycol = 50/50) and

50 $\mu\text{l}/\text{g}_{\text{Ag particles}}$ NH_4OH . The paste was homogenized in a roller for 5 times.

The pastes were deposited on multi-crystalline silicon wafers with acidic texture and PECVD SiN_x anti-reflection coating.

Screen printing was done by hand printing. The screen openings of fingers were 100 μm , finger spacing $d = 2$ mm mesh/inch = 280 in^{-1} , thread size 0.032 mm.

The pastes were dried at 100-150 $^\circ\text{C}$ for 5 min on a hot plate. The samples were divided into two groups of which one group was chemically sintered and tempered and the second group was thermally sintered. The two groups were further subdivided into two groups. One subgroup was tempered or sintered for 10 s and the second subgroup was tempered or sintered for 15 min.

For chemical sintering, samples were placed over concentrated HCl within a distance of 2 cm and left in the HCl vapor for 10 s according to Magdassi et al. [60]. After chemical sintering, samples were tempered on a hot plate. Tempering was done at temperatures of 150 $^\circ\text{C}$, 200 $^\circ\text{C}$, 250 $^\circ\text{C}$, 300 $^\circ\text{C}$, 350 $^\circ\text{C}$ and 400 $^\circ\text{C}$ for 10 s and 15 min, respectively.

Thermal sintering was done at temperatures of 150 $^\circ\text{C}$, 200 $^\circ\text{C}$, 250 $^\circ\text{C}$, 300 $^\circ\text{C}$, 350 $^\circ\text{C}$ and 400 $^\circ\text{C}$ on a hot plate for 10 s and 15 min, respectively.

The line width and height of printed silver metallization was measured using the confocal laser microscope LEXT. Each finger was measured separately to ensure exact resistivity calculation.

The lateral resistance was measured by a TLM measurement setup. A linear measurement head was used. The applied current was set to $I = 10$ mA.

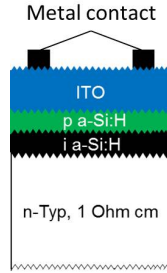


Figure 5.2.2: Illustration of sample structure with random pyramid texture for contact resistance measurements

5.2.6 Contact formation to ITO

Nanoparticle inks

The nanoparticle inks were formulated according to the following procedure.

20 wt% PAA capped silver nanoparticles (P02 from METALOR[®], average particle size 20-50 nm) were suspended in 80 wt% of a solution of deionized water/ethylene glycol (50/50). 50 $\mu\text{l}/1\text{g}_{\text{Ag}}$ particles of concentrated ammonia had been added.

The test inks were printed with the aerosol jet printer on ITO coated test substrates. ITO was applied via sputtering.

The substrates structure is illustrated in Figure 5.2.2. Here the textured substrate is illustrated. For ink deposition planar substrates were used. Wafer material was n-type mono crystalline FZ (float zone) silicon with a sheet resistance of 0.8-1.2 Ωcm .

For sputtering an OXFORD cluster tool with argon plasma was used.

The ITO chamber was equipped with an $\text{In}_2\text{O}_3/\text{SnO}_2$ (90/10 wt%) target. Gases like oxygen and argon can be fed separately. ITO coating thickness was 70 nm. An oxygen flow of 0.7 sccm was used.

Amorphous silicon was sputtered with silane and hydrogen gas. For p-type doped a-Si B_2H_6 gas was additionally added. A-Si thicknesses were 1 nm for a-Si(i) and 10 nm for a-Si(p), respectively.

ITO growth and properties are dependent on the substrate, which is why a silicon wafer was used instead of a cheaper glass substrate.

Aerosol jet printing was done with a M3D system from OPTOMECH INC. Gas flow has to be adjusted to the ink for each printing process. The chuck was heated to 120 °C and a print head with 8 nozzles and 150 µm nozzle size was used. Number of printing layers is also dependent on the gas flow settings and ink behavior. Within a batch the number of layers was chosen in a way, that a closed metallization finger could be observed under the confocal microscope.

The inks were dried at 100-150 °C for 5 min on a hot plate. After drying, the samples were placed over concentrated HCl within a distance of 2 cm and left in the HCl vapor for 10 s according to Magdassi et al. [60].

After chemical sintering in HCl vapor, tempering was done at temperatures of 200 °C and 300 °C on a hot plate for 15 min, respectively.

The line width and height of printed silver metallization was measured using the confocal laser microscope LEXT. Each finger was measured separately to ensure exact resistivity calculation.

The contact resistance was measured by a TLM measurement setup. Contact resistance was determined measuring eight silver lines. The applied current was set to $I = 10$ mA.

The sheet resistance R_{Sh} was determined with the 4-point probe measurement setup from NAPSON CORPORATION, setup RT-3000/RG-100, 4PP Resistance Measuring System.

Nanoparticle pastes

Screen printing paste 1 was formulated from 75 wt% PAA capped silver nanoparticles (P02 from METALOR[®], average particle size 20-50 nm) (aged batch), 2 wt% hydroxy ethyl cellulose and 23 wt% of solvent (water/ethylene glycol = 50/50) and 50 µl/g_{Ag particles} NH₄OH. The paste was homogenized in a roller for 5 times.

Screen printing paste 2 was formulated from 75 wt% PAA capped silver nanoparticles (P02 from METALOR[®], average particle size 20-50 nm) (new batch), 2 wt% hydroxy ethyl cellulose and 23 wt% of solvent (water/ethylene glycol = 50/50) and 50 µl/g_{Ag particles} NH₄OH. The paste was homogenized in a roller for 5 times.

Screen printing paste 3 was formulated from 75 wt% PAA capped silver nanoparticles, 2 wt% ethyl cellulose and 23 wt% of solvent (terpineol/ethylene glycol = 50/50) and 50 µl/g_{Ag particles} NH₄OH. The paste was homogenized in a 3-roller mill for 5 times.

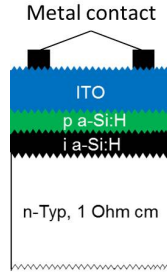


Figure 5.2.3: Illustration of sample structure with random pyramid texture for contact resistance measurements

The pastes were screen printed on ITO coated test substrates.

The substrates structure is illustrated in Figure 5.2.3. Here the textured substrate is illustrated. Pastes 1 and 2 were also deposited on planar substrates. Wafer material was n-type mono crystalline FZ silicon with a sheet resistance of 0.8-1.2 Ωcm .

For sputtering an OXFORD cluster tool with argon plasma was used.

The ITO chamber was equipped with an $\text{In}_2\text{O}_3/\text{SnO}_2$ (90/10 wt%) target. Gases like oxygen and argon can be fed separately. ITO coating thickness was 70 nm. An oxygen flow of 0.7 sccm was used.

Amorphous silicon was sputtered with silane and hydrogen gas. For p-type doped a-Si B_2H_6 gas was additionally added. A-Si thicknesses were 1 nm for a-Si(i) and 10 nm for a-Si(p), respectively.

ITO growth and properties are dependent on the substrate, which is why this kind of substrate was used.

Screen printing was done by hand printing. The screen characteristics were: openings for the fingers = 100 μm , finger spacing $d = 2$ mm, mesh/inch = 280 in^{-1} , thread size 0.032 mm.

The pastes were dried at 100-150 $^\circ\text{C}$ for 5 min on a hot plate. After drying, the samples were placed over concentrated HCl within a distance of 2 cm and left in the HCl vapor for 10 s according to Magdassi et al. [60].

After chemical sintering in HCl vapor, tempering was done at temperatures between 200 $^\circ\text{C}$ on a hot plate 15 min.

For current sweep measurements, paste 1 was used.

The line width and height of printed silver metallization was measured using the confocal laser microscope LEXT. Each finger was measured separately to ensure exact resistivity calculation.

The contact resistance was measured by a TLM measurement setup. Contact resistance was determined measuring eight silver lines. The applied current was set to $I = 10$ mA.

Current sweep measurements were done using paste 1 on a planar ITO coated substrate. A TLM measurement setup was used. Applied current was set to $I = -10$ mA to $I = 10$ mA. and measuring steps were 1 mA.

The sheet resistance R_{Sh} was determined with the 4-point probe measurement setup from NAPSON CORPORATION, setup RT-3000/RG-100, 4PP Resistance Measuring System.

5.2.7 Chemical sintering with in-built chemical sintering agent

The in-built sintering process was tested with several chlorine containing salts like NaCl, KCl, NH_4Cl and diluted hydrochloric acid. The basic inks with PAA capped nanoparticles were formulated as described in Section 5.2.3 and several amounts of salt were added to the preformulated inks. An additional variation was the silver nanoparticle concentration which was 20 wt% and 50 wt%, respectively. From Grouchko's work [79] follows that an initial salt concentration of 200 mmol/l is necessary to gain effective sintering of printed metal layers. The tested salt concentrations are listed in Table 5.2.4:

The inks were dropped on SiN_x coated silicon wafers and tried at 100 °C for 5 min on a hot plate.

Samples were characterized optically by sight and by SEM imaging.

Table 5.2.4: Salt concentrations in PAA capped nanoparticle silver inks

$c(\text{NaCl})$ [mmol/l]	$c(\text{NH}_4\text{Cl})$ [mmol/l]	$c(\text{KCl})$ [mmol/l]	$c(\text{HCl})$ [mmol/l]
75			
100	100	100	100
150	150	150	150
200	200	200	200
250			
300			

5.3 Results and discussion

5.3.1 Nanoparticle synthesis and characterization

Synthesis

The particle synthesis described by Li gave polydisperse particles with a diameter range of 40-90 nm as shown in Figure 5.3.1.

To increase the quality of the silver particles, which means decreasing size and dispersity of the silver particles, several parameters of the synthesis were varied as described in Section 5.2. When analyzing the particle quality, one has to take into account that size determination from SEM images is not too precise for the given particle sizes. Due to the resolution limit of the SEM and measurement errors the particle size determination is only no more accurate than ± 5 nm and becomes less precise with decreasing particle size. Therefore, effects on particle quality, which are within a size variation of ± 5 nm and which might occur from the synthesis parameter variation, could not be detected.

The variation of the proportion of silver acetate to 1-dodecylamine ($n(\text{AgAc})/n(\text{DA})$) (metal precursor to capping agent ratio) has only minor influence on the particle quality as shown in Figure 5.3.2. The particle size decreased slightly with decreasing amount of capping agent. Silver acetate was no longer soluble when a proportion of $n(\text{AgAc})/n(\text{DA}) = 0.5$ was used.

The variation of the ratio of metal precursor to reducing agent $n(\text{AgAc})/n(\text{PH})$ had a small effect on the particle size distribution

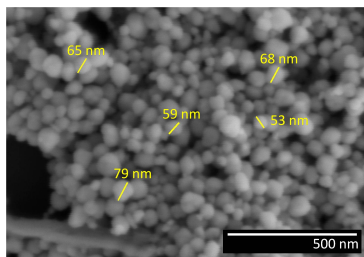


Figure 5.3.1: SEM image of silver nanoparticles synthesized according to Li [124]

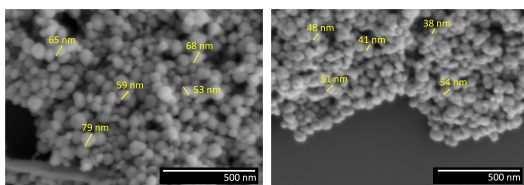


Figure 5.3.2: SEM images of particles synthesized according to Li [124] with different $n(\text{AgAc})/n(\text{DA})$ proportions
Left: $n(\text{AgAc})/n(\text{DA}) = 0.1$, Particle size: 30-90 nm
Right: $n(\text{AgAc})/n(\text{DA}) = 0.2$, Particle size: 25-85 nm

which is shown in Figure 5.3.3 (note different scales!). The particle distribution decreases with increasing amount of reducing agent.

Since the volume of solvent in which the reducing agent was dissolved was kept constant, the amount of phenylhydrazine which has been added to the silver solution per drop rose. With the first drops, more silver nuclei were formed which lead to smaller particles at the end of the reaction.

The reaction temperature should also have an effect on the particle size. Higher reaction temperatures increase the reaction rate, which means a faster reduction process, which benefits smaller particles and a narrow size distribution. However, a high reaction rate also conditions an earlier start of Ostwald ripening, which causes dissolving of small particles in favor of larger particles, therefore, causing bigger

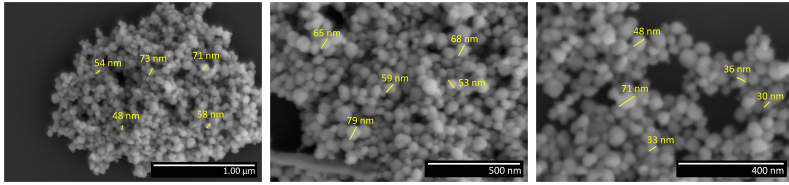


Figure 5.3.3: SEM images of particles synthesized according to Li [124] with different $n(\text{AgAc})/n(\text{PH})$ proportions. Left: $n(\text{AgAc})/n(\text{PA}) = 2.0$, Particle size: 30-100 nm Middle: $n(\text{AgAc})/n(\text{PH}) = 1.0$, Particle size: 30-90 nm Right: $n(\text{AgAc})/n(\text{PH}) = 0.2$; Particle size: 20-80 nm

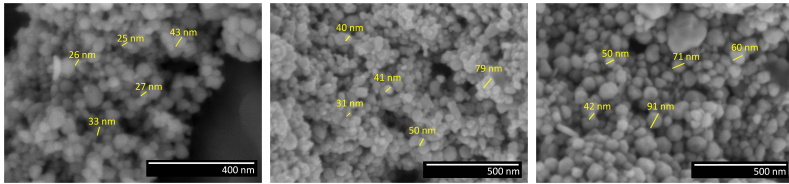


Figure 5.3.4: SEM images of particles synthesized according to Li [124] synthesized at different reaction temperatures. Left: $T = 30\text{ }^{\circ}\text{C}$, Particle size: 10-70 nm Middle: $T = 40\text{ }^{\circ}\text{C}$, Particle size: 20-90 nm Right: $T = 60\text{ }^{\circ}\text{C}$; Particle size: 30-100 nm

particle sizes. For very fast reactions, such as the reduction of silver acetate with phenylhydrazine, the reaction process is difficult to control. Thus, bigger particles are expected for higher reaction temperatures. This can be confirmed by the experiments shown in Figure 5.3.4 (note different scales!).

Beside the reaction temperature, the rate of addition of the reducing agent has a significant effect on the particle size and distribution.

Silver is an easy reducible metal. The energy barrier which has to be overcome to trigger the reduction of a silver salt is very low. Therefore, the reaction rate is very high and difficult to control. To get small particles the nucleation process should be very short and the overall reaction time at low reaction temperatures should also be

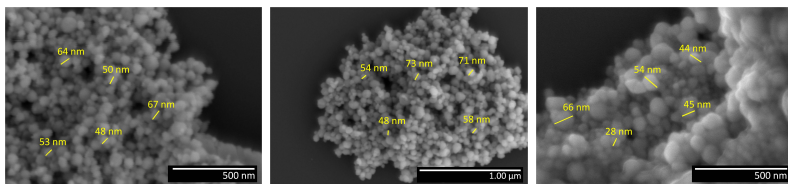


Figure 5.3.5: SEM images of particles synthesized according to Li [124] with different reducing agent drop rates. Left: Drop rate = 0.5 ml/min, Particle size: 20-100 nm Middle: Drop rate = 1.0 ml/min, Particle size: 30-100 nm Right: Addition at once; Particle size: 15-60 nm

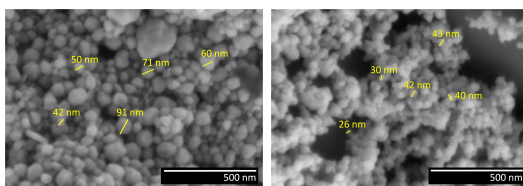


Figure 5.3.6: SEM images of particles synthesized according to Li [124] with different capping agents. Left: 1-Dodecylamine, Particle size: 30-100 nm Right: 1-Heptylamine; Particle size: 20-80 nm

quite short to avoid Ostwald ripening. Therefore, smaller particles and a narrower particle distribution can be expected when increasing the drop rate for the addition of the reducing agent. This can be seen in Figure 5.3.5 (note different scales!). Quite low drop rates of 0.5 ml/min and 1 ml/min gave particles with sizes of 20-100 nm and 30-100 nm. With addition of phenylhydrazine at once particle sizes of 15-60 nm could be achieved.

The capping agent is crucial for the stabilization of the particles during synthesis, for storage and also stabilization in solutions or dispersions. During the synthesis, the capping agent has significant influence on the particle size. Besides 1-dodecylamine also 1-heptylamine was used. With 1-heptylamine smaller particle sizes were reached compared to 1-dodecylamine as shown in Figure 5.3.6.

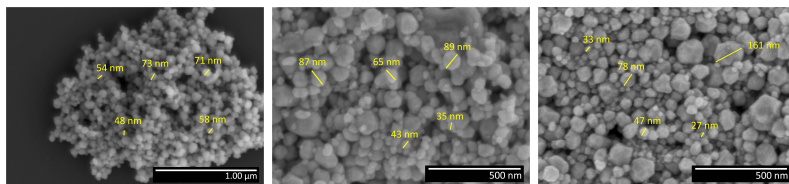


Figure 5.3.7: SEM images of particles synthesized according to Li [124] with higher concentration and doubled synthesis volume. Left: Original synthesis as described by Li, Particle size: 30-100 nm Middle: Double concentration, Particle size: 20-100 nm Right: Double synthesis volume; Particle size: 20-150 nm

For the formulation of inks and pastes high amounts of silver nanoparticles were to be synthesized. Therefore, it was tried to double the concentration of synthesis and to double the volume of the whole synthesis. For the reaction described by Li [126] both variations gave bigger particles and higher size distributions as seen in Figure 5.3.7 (note different scales!).

These variations show that the most effective ways to reduce particle size and distributions for this synthesis are the reduction of the reaction temperature and the increase of addition rate of the reducing agent.

Peng [125] also described nanoparticle synthesis strategies for noble metals. He further lowered the reduction temperature to room temperature and added the silver acetate to the reducing agent instead the other way around. He also varied the reducing agent and used a combination of boranes and hydrazines for the reduction. In this work, the combination of both synthesis descriptions from Li using phenylhydrazine and Peng adding the metal precursor to the reducing agent at room temperature was combined as described in Section 5.2. Small particles with relative narrow size distribution in the range of 20-50 nm could be synthesized as shown in Figure 5.3.8.

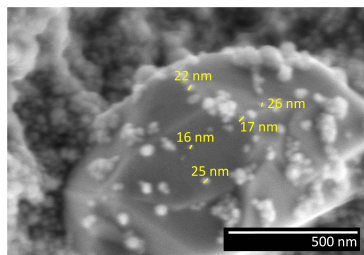


Figure 5.3.8: SEM images of particles synthesized according to Li [124] and Peng [125] Particle size: 20-50 nm

Sedimentation

For the 1-dodecylamine and 1-heptylamine capped silver nanoparticle suspension, no mass determination for the sedimented particles were determined: the particles were almost completely sedimented in case of 1-dodecylamine capped particles and completely sedimented for 1-heptylamine capped silver particles. The choice of solvent did not significantly influence sedimentation behavior.

The amine ligands are not able to stabilize the silver particles. The particles have a very high density, which makes stabilization within a liquid medium difficult.

However, the particles were stable during storage as powder. No particle growth could be detected after several month of storing under ambient conditions.

Results for the PAA capped particles were changing depending on the batch and age of the samples. Older samples, stored as powder under ambient conditions, sedimented faster than fresh samples. During storage particle growth occurred (see also Section 5.3.2 below). New particles were in the range of 20 nm with low distribution. The sedimentation behavior stagnated when particles reached a size around ~ 50 nm.

For low particle concentrations of 20 wt% fresh particles sedimented after 24 h to 0-10 %. For higher concentrations sedimentation was faster and around 20-30 wt% sedimented.

Aged particles sedimented much faster. For particle concentrations of 20 wt%, 25-35 wt% of the silver particles sedimentated after 24 h..

The exact sedimentation mass for 50 wt% suspensions was not determined because sedimentation seemed already very high. Apparently ≥ 50 % of the particles were sedimented.

According to these results, inks containing 1-heptylamine capped silver nanoparticles were not formulated. The synthesis of these nanoparticles was stopped after several sedimentation tests.

Due to very bad printing results caused by nozzle clogging, inks containing 1-dodecylamine capped particles were no longer formulated after several printing experiments. The fast clogging of the nozzles was also favored by the very high vapor pressure of the solvent.

For further experiments, only PAA capped particles were used. In addition to the the better sedimentation results, it was not possible to synthesize the required amount of 1-dodecylamine capped particles for ink and paste formulations in the lab.

Poly acrylic acid is water soluble and contains carboxyl groups which get deprotonated in basic solutions. PAA is a so called electrostatic capping agent (see also chapter 2.4.3).

A drawback of the used particles is a very short shelf life when stored as powder under ambient conditions. Particle growth appears within a very short time (days to 2-3 weeks after synthesis). This causes lower stability in solution as well as worse sintering ability, which will be discussed in more detail later in this chapter (Figure 5.3.15). Our supplier enhanced the particle synthesis and particles are now much more stable for storage and in solution. However, experiments described in the following sections were done with the first generation of the particles.

5.3.2 Influences on particle sintering

Influence of size

As already describe in Section 2.4 according to Buffat [23] the melting temperature of metal nanoparticles is strongly dependent on the size of the nanoparticles.

The reason for the decrease of the melting temperature of uncoated or uncapped nanoparticles is the increase of surface to volume ratio with decreasing particles size. Buffat used particles from condensated gold vapor [23]. The surface of those particles is not influenced by capping agents, which are used for the formation and stabilization of

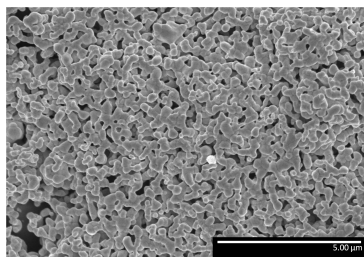


Figure 5.3.9: Sintered 1-heptylamine capped silver nanoparticles

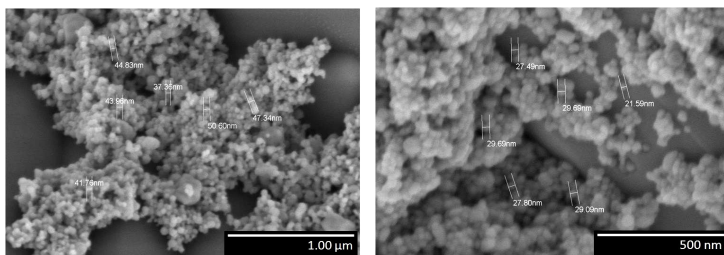


Figure 5.3.10: SEM images of nanoparticles of different sizes and sintering temperatures. Left: Particle size \sim 20-70 nm, capped with 1-heptylamine, sintering temperature \sim 130 °C. Right: Particle size \sim 20 – 30 nm, capped with 1-dodecylamine, sintering temperature \sim 200 °C (note the different scales).

nanoparticles by wet chemical synthesis. In addition, capping agents are obligatory for the stabilization of the particles in solutions or even dispersions.

According to the experiments in this work, for particles within a certain size range (here 10-100 nm), the diameter of the particles alone is not the crucial influencing factor for the sinter or melting temperature, respectively. An example for sintered particles is shown in Figure 5.3.9.

Table 5.3.1 gives a list of some particles with capping agent (CA), sizes and sintering temperature. Figure 5.3.10 shows particles capped with 1-dodecylamine (DA) and 1-heptylamine (HA), respectively.

Table 5.3.1: Particle sizes and sintering temperatures

Particle Nr.	Capping Agent	n(AgAc)/n(CA)	Size [nm]	Sintering temperature [°C]
1	DA	1/2	30-40	120
2	DA	1/5	20-70	130
3	DA	1/5	15-60	150
4	DA	1/5	20-90	150
5	DA	1/5	30-150	150
6	DA	1/2	20-30	200
7	HA	1/5	-	unstable at RT
8	HA	1/5	20-80	120
9	HA	1/10	20-50	130
10	HA	1/10	20-80	160

Although the mean diameter of the particles in Figure 5.3.10 does only differ within very narrow ranges, quite large differences in sintering temperatures could be measured. The bigger particles even sintered at lower temperatures than the smaller particles.

Table 5.3.1 shows that within the groups of the same capping agent (particles 2-5 and 9 and 10), the smaller particles tend to have lower sintering temperatures, which is in agreement with the findings of Buffat [23]. When comparing particles 8 and 10, it seems that an increasing amount of capping agent on the surface of the particles also increases the sintering temperature. Some particles were even unstable at room temperature and were partially sintered together which was the case for particle 7 in Table 5.3.1. Particles 7 and 8 have been synthesized following the same synthesis description. Particle 7 was unstable at room temperature whereas particle 8 was more stable but had a low sintering temperature. The preparation of the particles has to be carefully controlled. Very small differences in synthesis can already have influence on the particle stability.

The results in Table 5.3.1 show, that the capping agent itself as well as the amount of capping agent have a big influence on the sintering temperature. The influence of the particle size is subordinated to the effect of particle size.

The effect of the capping agent on the sintering behavior of silver

nanoparticles is quite high and will be analyzed and discussed in detail in the following Section.

Effect of capping agents

The sintering of silver nanoparticles is strongly dependent on the nature of the capping agent used to stabilize the particles during synthesis and ink formulation.

The capping agent has to diffuse from the metal surface to enable sintering of the nanoparticles. The TG-DSC measurements of PVP and PAA capped silver nanoparticles are shown in Figure 5.3.11⁸.

The measurements demonstrate that relatively high temperatures are necessary to eliminate the polymeric capping agents from the silver surface, which is necessary to trigger particle sintering. The main reactions can be observed at $T_{on, PAA} = 225$ °C and $T_{on, PVP} = 295$ °C. The so called *onset temperature* (T_{on}), which gives the starting temperature of a reaction, is calculated from the intersection of two regression lines, thus, it can vary around ± 5 °C.

The reactions are exothermic and show that the the capping agent does not evaporate from the silver surface, but is oxidized and “burned” from the particle surface. The mass loss could be determined to be $\Delta m(\text{PAA}) = -2.1\%$ and $\Delta m(\text{PVP}) = -3.72\%$, which is likely to correlate with the amount of capping agent attached to the particle surface.

Effective nanoparticle sintering cannot occur at lower temperatures, because the particle surface is still protected by the polymers. However, to ensure good stabilization against agglomeration, early sintering and precipitation of high concentrated dispersions, polymeric capping agents are necessary.

For sintering methods which use the thermal effect indirectly like microwave sintering, photonic or electrical sintering, this effect might not be detectable because the temperatures reached at the surfaces of the particles are very high.

Chemical sintering (described in Section 2.4.5) provides the possibility to make use of polymeric stabilizers and sintering at low temperatures, because the polymers do not have to be evaporated or decomposed by heat to be released from the particle surface. Nevertheless,

⁸Onset temperatures not marked for better readability

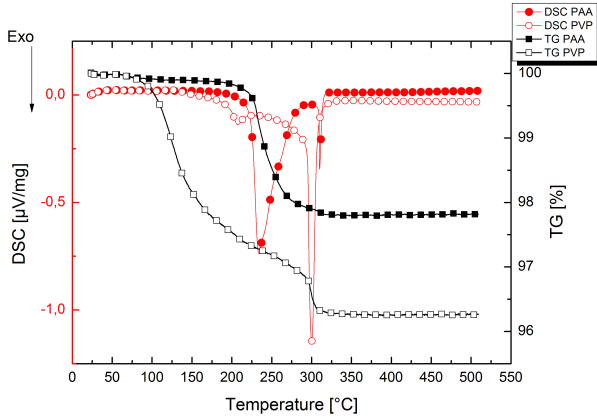


Figure 5.3.11: TG-DSC measurement of PAA and PVP capped silver nanoparticles, respectively

the chemical nature of the capping agents has a significant influence on chemical sintering which is investigated and discussed within this chapter.

Three factors, dependent on the capping agent, mainly influence the sintering behavior of the nanoparticles:

1. Chain length and branching factor
2. Functional group (anchor group)
3. Amount of capping agent protecting the particle

One of the capping agents used in this work is PVP. PVP contains oxygen as well as nitrogen as potential anchor group. Wang et al. [71] has shown that silver is mainly coordinated by the nitrogen atom as long as steric hindrance by particle size itself is not a factor. This is the case for particles until a size of 50 nm. Wang explains the preferred coordination to silver by nitrogen with the lower electron affinity of nitrogen compared to oxygen [71]: nitrogen is a better electron donor than oxygen. The postulated reactions are given in Figure 5.3.12.

Figure 5.3.13 shows SEM images of the particles described in Section 5.2 before and after chemical sintering. The formation of sintering

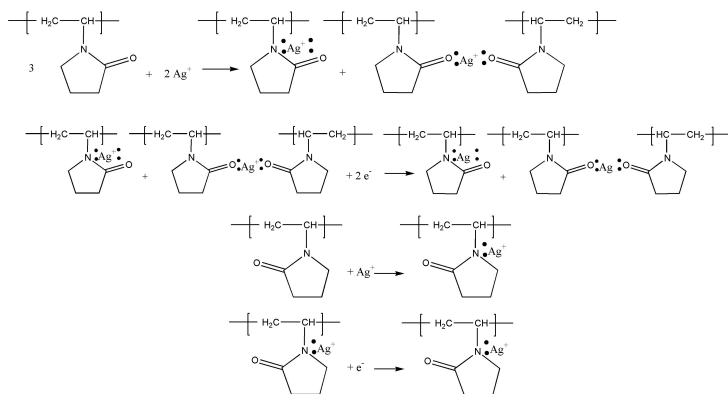


Figure 5.3.12: Possible reactions path for nanoparticle formation stabilized with PVP (retraced from [71])

necks indicates successful sintering and electrical effective connection between the particles (see also Figure 5.3.9).

1. Chain length

Particles which are capped with PVP (1) do not show any significant neck formation whereas particles stabilized with 1-dodecylamine (2) show the typical sintering necks. Bulky polymer stabilizers provide not only a good protection against agglomeration, but also against smaller particles (here chloride anions) to reach the metal surface as can be concluded from the comparison of particles 1 and 2. The functional group in both cases contains nitrogen, but the polymeric organic group of particle 1 provides a far better steric hindrance.

2. Functional group (anchor group)

Even more sintering necks and less visible grain boundaries are observed for particles capped with PAA. The comparison of particle 2 and 3 indicates that the better sintering of particle 3 is due to the affinity of the carboxyl anchor group which is much weaker to the silver surface compared to the amine group. This is in accordance to the order of the relative stability of silver – nonmetal element bond. Nitrogen forms a more stable bond to

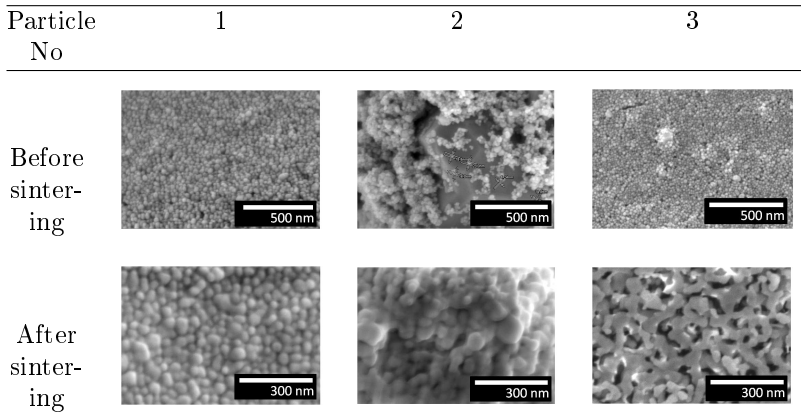


Figure 5.3.13: SEM images of particles with different capping agents before and after chemically sintering. Order according to Table 5.2.2

the silver surface than oxygen ($N > O$) as has been described in [127]. This means that capping agents with functional groups including nitrogen adsorb more strongly to the silver surface than agents with functional groups including oxygen as coordinator. Substitution of the nitrogen anchor group is, thus, more difficult and, therefore, the chemical sintering of the particles is hindered.

The effect of the anchor group is even higher than the steric effect of polymers. This can be argued from comparison of sintering efficiency of particles 1 and 3. Both particles are capped with polymers but particle 3 is capped by a polymer having a carboxyl group as anchor group and shows nice sintering results whereas particle 1 is capped by a polymer with nitrogen as anchor group and shows no effective sintering.

3. Amount of capping agent per particle

Besides the type of capping agent, also the amount of agent protecting the particles from agglomeration is important. If the amount of agent is too low, particle sintering starting already at room temperature or particle growth during storage can occur

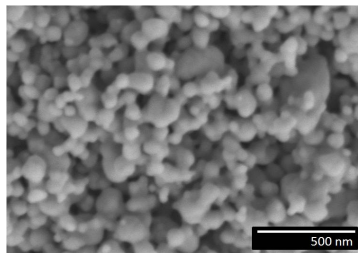


Figure 5.3.14: Silver particles capped with 1-heptylamine unstable at room temperature

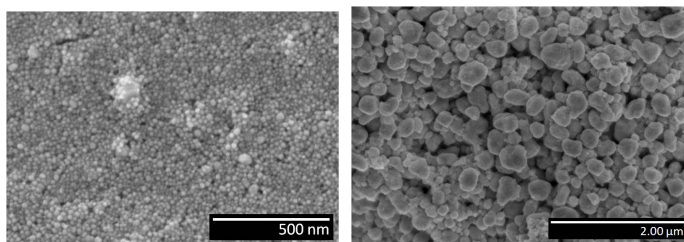


Figure 5.3.15: SEM images of PAA capped silver nanoparticles. Left: 1 week after preparation Right: 3 weeks after preparation and storage under ambient condition

as shown in Figures 5.3.14 and 5.3.15. The small amount of capping agent resulted in poorly protected particles: silver surfaces of two neighboring particles came into direct contact and the sintering process started without additional energy supply. This effect can also lead to particle growth during storage as shown in Figure 5.3.15.

Effect of additives

Besides stabilized nanoparticles and solvents, inks and pastes generally contain additives to adjust, for example, surface tension, viscosity, adhesion to substrate and so on. Those additives mix homogeneously within the suspension and potentially cover the particles. After evaporation of the solvent, they remain in the metal grid and, thus, may

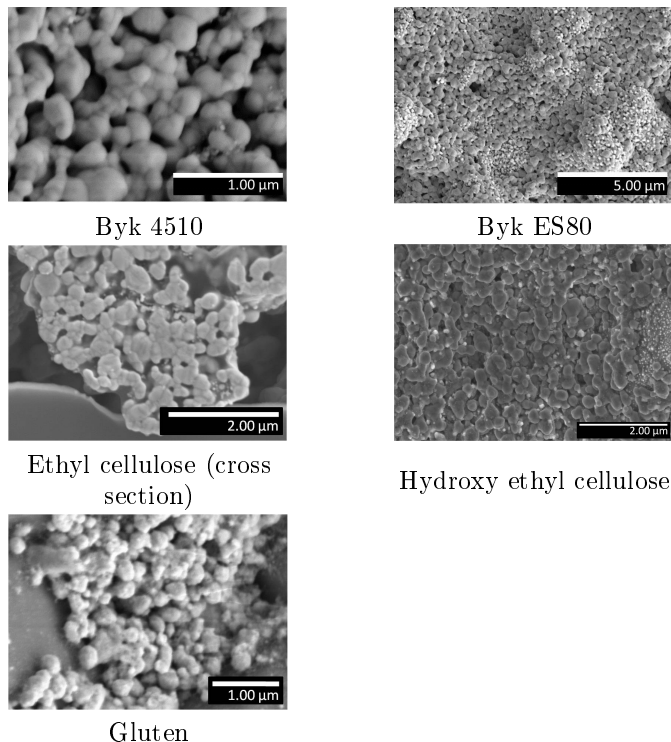


Figure 5.3.16: SEM pictures of inks with different additives (see Table 5.2.3) after drying, chemical sintering in HCl vapor and tempering at 200 °C for 15 min

hinder or prevent sintering.

The results for the chemical sintering of inks containing different additives are shown in Figure 5.3.16.

The influence of additives on the chemical sintering process is less significant than the influence of stabilizing agents. However, the mechanism is the same. Additives only containing oxygen as potential coordination group do not influence the chemical sintering process significantly. If nitrogen containing functional groups are involved, as in the protein gluten, the sintering process is hindered even at tempering temperatures of 200 °C.

The steric structure of the polymers may also have an influence on this result. Except for the used ethyl cellulose and hydroxy ethyl cellulose the author has no information about the molecular weight of the tested additives, which is why the influence of the chain length and degree of branching can not be analyzed any further.

As can be seen from the sample containing ethyl cellulose and hydroxy ethyl cellulose the miscibility of the particles, which is mainly defined by the surrounding capping agent, with the additive and the solvent is also important regarding the quality of the finished metal grid. In case the miscibility of capping agent, solvent and additive is rather low which is the case for the capping agent PAA and terpineol and PAA and the binder ethyl cellulose, particle “clusters” are formed, which sinter, but form large caves between the clusters. Hydroxy ethyl cellulose on the other hand, is miscible with PAA and the solvent and, therefore, a uniform sintered metal layer can be formed.

Different amounts of additives within the narrow limits recommended by the manufacturer (up to 5 wt%) were also investigated but showed no difference to the results displayed here. Nevertheless, much higher amounts than used in this work could still have impact on the process.

5.3.3 Printing results

Ink jet printing

A photograph and a microscope image of the ink jet samples and printed fingers from the ink containing PAA capped particles is shown in Figure 5.3.17. An SEM picture of a cross section is given in Figure 5.3.18.

The printed fingers showed little ink bleeding and uniform shape. Due to good wettability of the hydrophilic SiN_x surface of the substrate, the ink spread over the surface. This effect is intensified by the capillary effect which is caused by the alkaline etched random pyramid texture. Thus, the printed fingers were quite broad (0.8 mm in average) and thin. Narrower lines should be possible by heating the substrate up to at least 100 °C. The chuck of the used ink jet printer system can only be heated up to 60 °C.

Due to the surface texture of the substrates, the line height could not be measured with the confocal microscope. SEM measurements on cross sections show, that line height varies from 100 nm to 3 μm . To

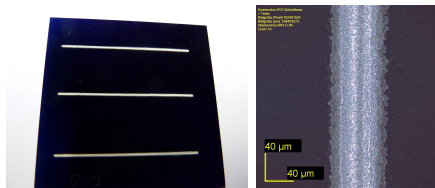


Figure 5.3.17: Left: Photograph of ink jet printed sample. Right: Microscope image of ink jet printed line (magnification 5x)

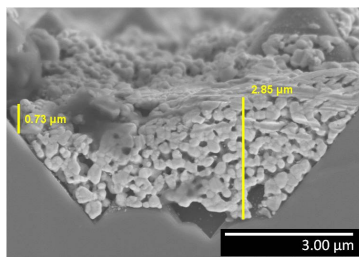


Figure 5.3.18: SEM image of cross section of ink jet printed and chemically sintered metal finger

consider also line interruptions due to only partially covered pyramids, the mean height of the lines was estimated to be 1 μm. This value was also used in resistivity calculations given in Section 5.3.5.

Ink jet printing with PAA capped particles was also difficult due to heavily fluctuating nanoparticle qualities. When the quality was low, particle aggregation was very fast. As a result, clogging of the ink jet nozzles occurred and printing was no longer possible.

Adhesion to alkaline etched random pyramid textured surfaces was low.

The inks with 1-dodecylamine capped nanoparticles were not stable enough to be printed and led to rapid nozzle clogging.

Due to the relatively low amount of ink application, ink jet printing is only practical for seed-layer metallization.

Aerosol jet printing

Due to problems regarding nozzle clogging and control of line width, aerosol jet printing was used as alternative to ink jet printing. The demands for aerosol jet printing on the ink formulation are far less restrictive than for ink jet printing as already explained in Section 3.2.2. In addition, the chuck of the aerosol jet printer can be heated up to 200 °C. Results of aerosol jet printed metallization fingers for the ink with PAA particles are shown in Figures 5.3.19 and 5.3.20.

Line widths down to 30 μm could be achieved.

The acidic texture of multicrystalline silicon wafers is much shallower than the alkaline texture with random pyramids on monocrystalline silicon wafers. The use of those wafers enabled automated measuring of the cross section area with the confocal microscope software.

The nozzles of the print head are clued by hand and can differ in alignment. In addition, although clogging of the nozzles is a lot easier for ink jet printing, this can occur with aerosol jet print head nozzles as well. This can cause very irregular printing results even on the same wafer, which is demonstrated with the microscope images in Figure 5.3.20.

The inks with 1-dodecylamine capped nanoparticles could not be printed by aerosol jet printing due to the rapid evaporation of the solvent, which led to a dry particle stream to the sample surface.

Adhesion to the multicrystalline wafer surfaces was poor.

Due to relatively low output several layers of printing are necessary to achieve adequate line heights. Thus, aerosol jet printing, similar to ink jet printing, is only practical for seed-layer metallization.

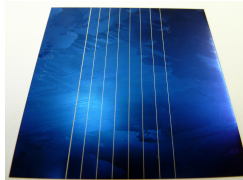


Figure 5.3.19: Photograph of aerosol jet printed metallization fingers on acidic etched multicrystalline silicon wafer coated with SiN_x

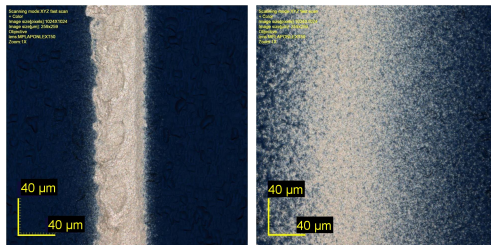


Figure 5.3.20: Microscope images of aerosol jet printed metallization fingers on the same wafer. Left: Uniform printed finger with little overspray. Right: Heavy overspray caused by partially clogged nozzle

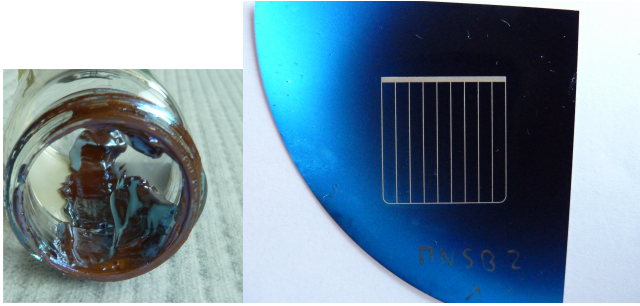


Figure 5.3.21: Picture of silver nanoparticle paste with hydroxy ethyl cellulose (left) and hand screen printed grid on a monocrystalline wafer with random pyramid texture (right)

Screen printing

The demands on screen printing pastes to reach ideal aspect ratios with narrow line widths are high. Due to the high viscosity of the pastes and the thixotropic properties, screen printing pastes can be used for seed-layer and thick film metallization. A photograph of a screen printing paste with PAA capped silver nanoparticles and hydroxy ethyl cellulose and a screen printed metal grid on a monocrystalline wafer with random pyramid texture is shown in Figure 5.3.21.

A microscope image (Figure 5.3.22) of one of the screen printed fingers shows a good aspect ratio of 0.22. The measurement was done over the whole image width and is, therefore, a mean value for the measured part of the finger.

Aspect ratios between 0.15 to 0.3 could be achieved. Normally, screen printing reaches aspect ratios around 0.2. Higher aspect ratios >0.3 can be considered as very good [128].

In general, screens used for solar cell metallization are adjusted to organic solvent based screen printing pastes. Because the formulated nanoparticle pastes were based on water, the used screens were much more easier clogged than usual and quite hard to clean from nanoparticle paste. The pastes used for the experiments only included ethyl cellulose or hydroxy ethyl cellulose, respectively, to adjust rheology without any further additives. Good printing results with average

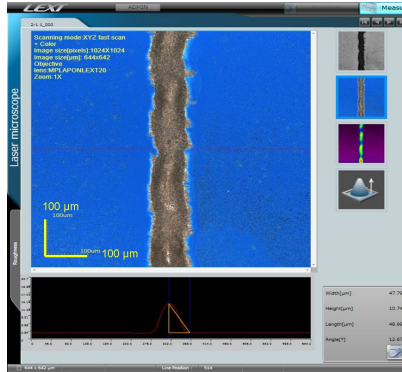


Figure 5.3.22: Microscope measurement of screen printed metallization finger (magnification 20x); finger height: 10.7 μm , width: 95.6 μm

aspect ratios could already be achieved even without adjusting the rheology of the paste. Even better printing results can be expected by addition of proper rheology and print additives.

The adhesion to the substrate was tested by tape testing and showed good results as non of the silver fingers stucked to the tape.

5.3.4 Sintering results

The sintering results of inks and pastes only chemically sintered, only thermally sintered and chemically sintered and tempered were examined qualitatively and characterized by SEM imaging. Screen printing pastes additionally contain ethyl cellulose or hydroxy ethyl cellulose and are, thus, examined and compared to the binder free formulation of the inks.

Silver nanoparticle inks

First the sintering development of the nanoparticles within the ink formulation will be analyzed.

In Figure 5.3.23 SEM images of differently treated metallization samples are shown. The quality of the used particles was quite low:

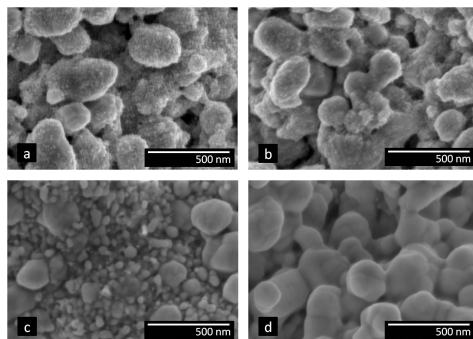


Figure 5.3.23: SEM images of differently treated nanoparticles in ink formulation;

- a) Dried particles
- b) Particles thermally treated at 200 °C for 15 min
- c) Particles treated with HCl vapor
- d) Particles treated with HCl vapor and tempered at 200 °C for 15 min

the size distribution of the particles was high and a lot of the particles formed already large agglomerates > 100 nm.

On the surface of the agglomerates, small particles are visible (Figure 5.3.23 a). It can be seen that temperature treatment at 200 °C is only effective, if chemical sintering has been done in advanced (compare 5.3.23 b) to d)). The small particles at the surface of the agglomerates are still present, as long as the ink was only heat treated at 200 °C (Figure 5.3.23 b).

In this case, remains of organics (presumably of the capping agent) are still present on the silver particle surface, which prevents sintering of the particles (Figure B.1.3 in the appendix B.1.1). When treated with HCl vapor the organic is removed from the surface: the agglomerates broke up and small single particles formed sintering necks (Figure 5.3.23 c). Additional tempering of the particles at 200 °C after treatment with HCl vapor led to further growth of particles and sintering necks between them (Figure 5.3.23 d).

In Figures 5.3.24 particles chemically sintered and tempered at different temperatures and different tempering times are shown while Figure 5.3.25 displays particles thermally sintered at different tem-

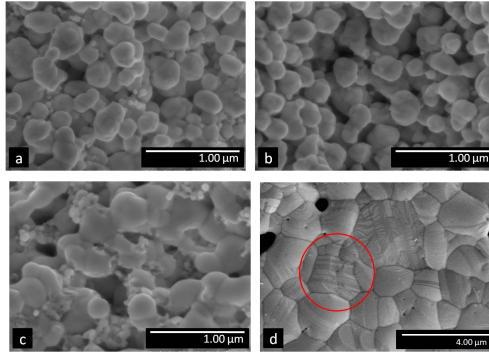


Figure 5.3.24: SEM images of chemically sintered and tempered silver nanoparticle inks at different temperatures (note different scales!)

From left to right: a) 200 °C, 10 sec; b) 200 °C, 15 min; c) 300 °C, 15 min; d) 400 °C, 10 s, Marking: Grain with several crystal planes

peratures and tempering times.

By heating the particles at higher temperatures, sintering necks grow and a more and more dense layer of silver is developed. At 200 °C small particles disappear and sintering necks developed independent of tempering time (Figure 5.3.24 a and b, cp. Figure 5.3.23). Particle necks are still present at 300 °C (5.3.24 c). At 400 °C (Figure 5.3.24) grain boundaries could be observed, but necks between particles are almost vanished. Even different crystal planes could be observed. Grain sizes > 500 nm can be measured.

During the chemical sintering process with HCl vapor, chlorine ions get transported to the surface of the silver nanoparticles. The ions substitute the protecting organic capping agents from the particle surface. The particles are now able to contact which triggers particle sintering even at room temperature [83]. The initial sintering takes place until the surface tension has reached equilibrium with grain boundary formation energy. For further sintering, more energy is needed [129]. Thus, higher temperatures and longer tempering times provide enough energy for solid state diffusion, which results in denser and more compact silver layers, which is demonstrated by the



Figure 5.3.25: SEM images of thermally sintered silver nanoparticle inks at different temperatures; From left to right: a) 200 °C, 10 s; b) 200 °C, 15 min; c) 300 °C, 15 min; d) 400 °C 10 s

results.

The sintering process is very rapid at 300 °C. A tempering time of only 10 s is sufficient to reach shown states of sintering (Figure 5.3.24 b). Longer tempering times can lead to a denser packing (Figure 5.3.24 c) but do also increase the tension within the silver layer which led to failures of adhesion to the substrate. This can be seen from the silver layers tempered at 400 °C: the tension within the silver layer led to breakage of the metallization layer and to adhesion failure to the substrate. The stress occurs due to the different thermal expansion coefficients of the silver layer ($\alpha(\text{Ag}) = 18.9 \cdot 10^{-6} / ^\circ\text{C}$ [130]) and the substrate Si and SiN_x ($\alpha(\text{Si}) = 4.68 \cdot 10^{-6} / ^\circ\text{C}$ [130], $\alpha(\text{SiN}_x) = 3.3 \cdot 10^{-6} / ^\circ\text{C}$ [131]), respectively. During the heating process, silver with a bigger thermal expansion coefficient expands more than Si and SiN_x . However, due to the adhesion of the silver layer to the substrate, the expansion of silver is restricted by the substrate, which causes a tension within the silver layer. The tension exceeds the elastic limit of the silver layer, which leads to the fraction of the layer and also to adhesion failure to the substrate [132]. The layer peels of the substrate.

Figure 5.3.25 shows that effective *thermal* sintering starts at tem-

peratures > 200 °C. At 200 °C there are still very small particles visible at the surface of large agglomerates independent of the sintering time (see Figure 5.3.25 a and also Figure 5.3.23 b). This is not the case for particles which were chemically sintered.

The SEM measurement results for chemical sintering combined with tempering at 300 °C (15 min) and thermal sintering at 300 °C (15 min) are comparable as can be seen from Figures 5.3.24 c and 5.3.25 b and c. However, samples thermally sintered at temperatures ≥ 300 °C were mechanically unstable and broke most of the time. Samples which were chemically sintered first were mechanically much more stable. The sintering necks stabilize the silver layer to a certain extent.

The initial sintering is triggered by removal of the protecting organic capping agent surrounding the silver nanoparticles. The removal of the organics can also be done thermally. However, this means the capping agent has to be either decomposed or evaporated, which requires higher temperatures, depending on the capping agent. The results demonstrate, that in our case, temperatures >200 °C are required to remove the capping agent and start sintering. Above the critical temperature (removal of the capping agent) the sintering results for thermal and chemical sintering with additional tempering are comparable.

These results show that chemical sintering is a good alternative to thermal long time sintering at temperatures below 300 °C and can even be advantageous for sintering at 300 °C.

Silver nanoparticle pastes

Binders in pastes are most often polymers (or inorganic glass compositions as used in high temperature pastes). Polymers have high boiling and decomposition temperatures, respectively. Ethyl cellulose (EC) and hydroxy ethyl cellulose (HEC) decompose above 200 °C as can be seen from TG-DSC measurement of hydroxy ethyl cellulose shown in Figure 5.3.26. Thus, it was investigated, if a binder prevents chemical and/or thermal sintering.

As can be seen from Figure 5.3.26, a first reaction of hydroxyethyl cellulose occurs at $T_{on,1} = 192$ °C while the main oxidative “burn-out” starts at $T_{on,2} = 246$ °C (exothermic). The mass loss indicates that the burn-out is not completed at $T = 500$ °C. 20 % of the initial mass are still present. The burn-out is most effective at temperatures

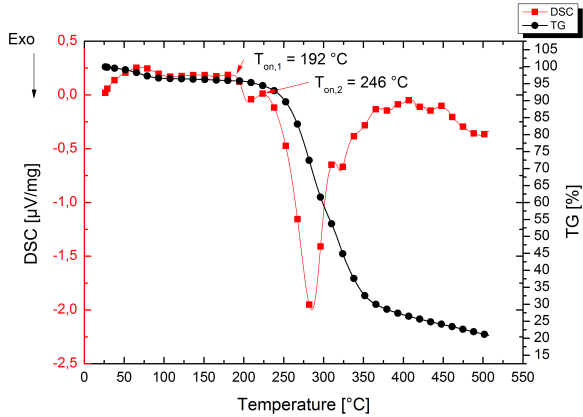


Figure 5.3.26: TG-DSC measurement of hydroxy ethyl cellulose. Onset temperatures are marked. Main decomposition reaction starts at onset temperature $T_{on,2}$

between $T_{on,2} = 246\text{ °C}$ and approximately $T = 375\text{ °C}$. This is important regarding tempering or sintering temperature and time for the processing of pastes based on silver nanoparticles.

Ethyl cellulose shows four reaction temperatures: $T_{on,1} = 181\text{ °C}$, $T_{on,2} = 310\text{ °C}$,

$T_{on,3} = 336\text{ °C}$ and $T_{on,4} = 427\text{ °C}$. The main burn-out occurs between $T_{on,2}$ and $T_{on,3}$ and shows that removal of EC needs higher temperatures than the removal of HEC from a silver nanoparticle paste. However, the burn-out is almost completed after the last reaction starting at $T_{on,4}$. The TG-DSC measurement of EC is shown in the appendix in Figure B.1.1.

First ethyl cellulose⁹ as a non-toxic binder was used. Ethyl cellulose is soluble in organic solvents like ethylene glycol and terpineol (a commonly used solvent in paste formulation), but not in water. Thus, the paste was formulated with a solvent mixture of terpineol/ethylene glycol (50/50).

For paste 1 chemical sintering could be observed but was less effec-

⁹Ethyl cellulose is a standard binder for paste formulations.

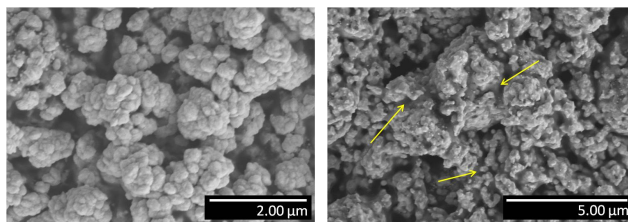


Figure 5.3.27: SEM images of chemically sintered silver nanoparticle paste with ethyl cellulose. Left: Cluster formation, Right: Ethyl cellulose residues (markings) between particles (note different scale!)

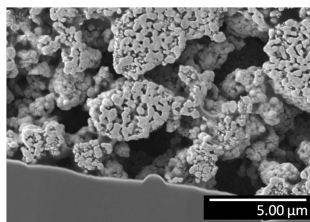


Figure 5.3.28: SEM image of cross section of chemically sintered silver nanoparticle paste with ethyl cellulose

tive than without binder. The binder glues the particles together and hinders sintering. This can be seen from the SEM image in Figure 5.3.27. Also the paste appeared smooth and homogenous after mixing in the 3-roller mill, it seems that poor miscibility of ethyl cellulose with the capping agent of the silver nanoparticles (which is soluble in water) and/or the miscibility of the particles in terpineol leads to cluster formation of silver nanoparticles and large pores and holes between those clusters (Figure 5.3.28). The immiscibility of the binder has further effects on the contact resistance to the substrate which will be discussed in chapter 5.3.5.

Based on these results, the impact of the miscibility of the binder with the capping agent of the particles and influence on chemical sintering should be tested. Hydroxy ethyl cellulose has similar properties as ethyl cellulose regarding rheological characteristics, but is soluble

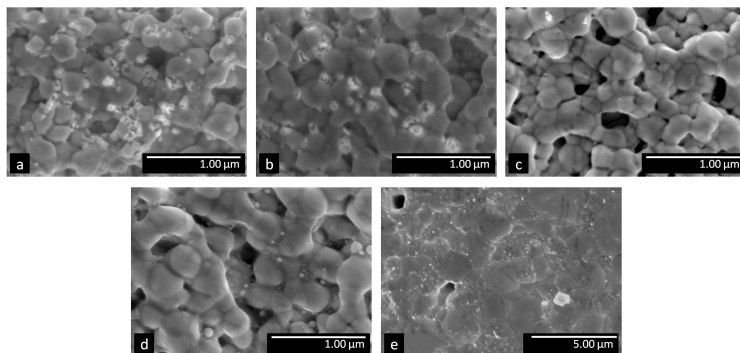


Figure 5.3.29: SEM images of chemically sintered and tempered silver nanoparticle pastes with hydroxy ethyl cellulose at different temperatures (note different scales!)

Top row: a) 200 °C, 15 min; b) 300 °C, 10 s; c) 300 °C, 15 min; Bottom row: d) 400 °C, 10 s; e) 400 °C, 15 min

in water. However, hydroxy ethyl cellulose is toxic.

Hydroxy ethyl cellulose gives much better results regarding chemical sintering behavior than ethyl cellulose (Figure 5.3.30). Chemical sintering is slightly hindered compared to inks without binder but is still effective. Tempering starting at 200 °C gives already good sintering results, which is shown in Figure 5.3.29 (Paste 2 group 1).

The binder makes detection of sintering necks difficult, thus, the optical difference of tempering at 200 °C for 15 min and a 10 s cure at 300 °C is only minimal. Still, much organic binder can be seen at the particle etches. This is also the case for tempering at 400 °C for 10 s. However, for tempering for 15 min and temperatures ≥ 300 °C hydroxy ethyl cellulose does decompose and the particles are able to form more uniform layers.

Cluster formation as was observed with ethyl cellulose did not appear. The printed pastes appeared uniform with less holes or even caves within the layer as shown in Figure 5.3.30.

These results show the importance of the miscibility of the ink components especially with the capping agent of the particles.

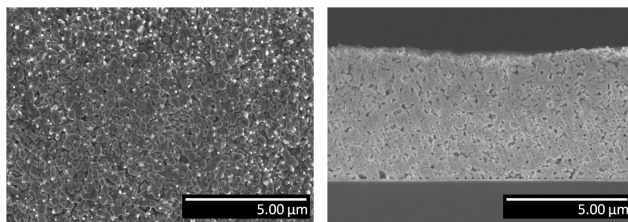


Figure 5.3.30: SEM images of silver nanoparticle paste with hydroxy ethyl cellulose chemically sintered and tempered at 200 °C (15 min) (left) and cross section (right)

Observation of samples of paste 2 group 2, which were thermally sintered, shows that thermal sintering effectively starts at temperatures ≥ 250 °C for 15 min. This is in good agreement with the TG_DSC measurements, where effective burn-out of HEC is visible at 246 °C. The results at 300 °C for 1 min and 400 °C are again comparable with the chemical sintering combined with tempering process (see Figure 5.3.31).

The paste metal layers were mechanically more stable than the ink samples even for higher temperatures. However, samples sintered at 400 °C showed bad adhesion to the substrate as well. The comparison of chemical sintered samples with tempered ones demonstrates that chemical sintering enhances the mechanical stability against thermal layer tensions to a certain extent.

A comparison of the chemically sintered and tempered inks (Figure 5.3.24) and pastes (Figure 5.3.29) shows, that the addition of a good miscible binder like hydroxy ethyl cellulose does hinder sintering as long as the organics are not burned from the paste. Higher tempering temperatures or longer tempering times are necessary to reach the same quality of sintering as for binder free inks. However, comparing the sintering result of the ink at 300 °C for 15 min and the corresponding paste samples, it seems, that the silver layer formed by the paste formulation is denser than the ink sample. The binder keeps the particles more densely packed, whereas the ink spreads out on the sample. The particles take more distance from each other, which leads to a silver layer which is not as dense compared with the one formed by the paste.

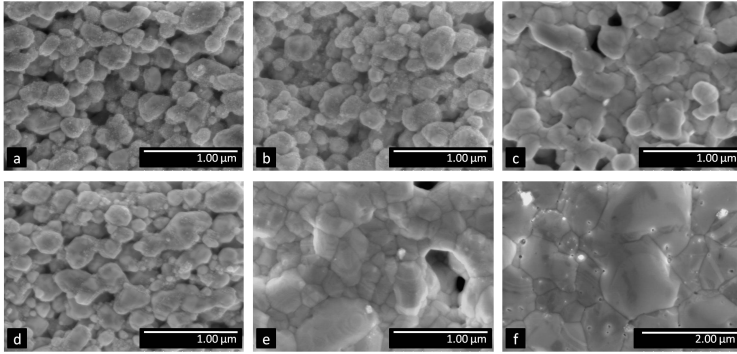


Figure 5.3.31: SEM images of thermally sintered silver nanoparticle pastes with hydroxy ethyl cellulose at different temperatures (note different scales!)

Top row: a) 200 °C, 15 min; b) 250 °C, 10 s; c) 250 °C, 15 min; Bottom row: d) 300 °C, 10 s; e) 300 °C, 15 min, f) 400 °C, 15 min

5.3.5 Line resistivity of silver nanoparticle inks and pastes

Line resistivity of ink jet and aerosol jet printed seed layers

The seed layers were printed by ink jet or aerosol jet as described in Section 5.2.

Line resistivities of seed layers based on the ink formulation described above are shown in Figure 5.3.32.

The samples were chemically sintered and tempered for 15 minutes and 10 seconds, respectively.

Pure chemical sintering shows a large distribution of the resulting resistivities. This uncertainty can be significantly lowered by tempering the pre-sintered nanoparticles as shown in Figure 5.3.32.

Post tempering at 100-150 °C can already significantly reduce the value distribution.

Best conductivities were reached in the temperature range between 200 °C and 400 °C. The median values for a post tempering of 15 min lay closely together for tempering temperatures of 250 °C, 300 °C and

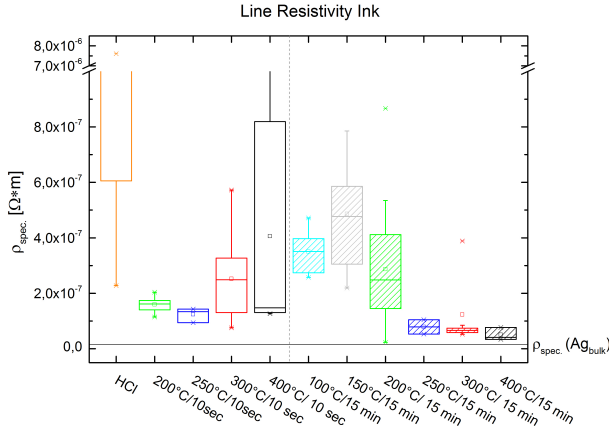


Figure 5.3.32: Line resistivities of ink jet and aerosol jet printed seed layers: Samples were chemically sintered with HCl prior to tempering at different temperatures. Silver bulk resistivity is marked

400 °C: $\rho(250\text{ °C}) = 7.86 \times 10^{-8}\ \Omega\text{m}$, $\rho(300\text{ °C}) = 6.6 \times 10^{-8}\ \Omega\text{m}$ and $\rho(400\text{ °C}) = 4.08 \times 10^{-8}\ \Omega\text{m}$. The absolute resistivity values drop with increasing tempering temperature, but starting from 250 °C the decrease is low proportional to the increase of the temperature. The lowest absolute value measured was $\rho = 2.30 \times 10^{-8}\ \Omega\text{m}$ for a sample tempered at 200 °C for 15 min (median $\rho(200\text{ °C}) = 2,48 \times 10^{-7}\ \Omega\text{m}$). These very low resistivity values are very close to the silver bulk resistivity of $\rho = 1.58 \times 10^{-8}\ \Omega\text{m}$. Commercially available inks, which are usually thermally sintered, only reach those values after 30 min of thermal sintering [80]. Chemical sintering alone obtains values five times of the conductivity of bulk silver [83].

Within the temperature range of 200-400 °C longer tempering times (15 minutes compared to 10 seconds) give slightly better results regarding absolute values as well as result distribution than short term tempering. The median resistivities measured are $\rho(200\text{ °C}) = 1.62 \times 10^{-7}\ \Omega\text{m}$, $\rho(250\text{ °C}) = 1.34 \times 10^{-7}\ \Omega\text{m}$, $\rho(300\text{ °C}) = 2.49 \times 10^{-7}\ \Omega\text{m}$ and $\rho = 1.48 \times 10^{-7}\ \Omega\text{m}$.

The drop of resistivity as well as the better resistivity values for longer sintering time is in good agreement with the sintering theory for metal nanoparticles: higher temperatures and longer tempering times provide enough energy for solid state diffusion which results in denser and more compact silver layers and, thus, in lower resistances. This was already shown in Figures 5.3.24 and 5.3.25.

However, longer tempering as well as high temperatures ($> 250\text{ }^{\circ}\text{C}$) increase thermal stress within the metal layers, which causes cracks within the layer and adhesion failure to the substrate. This can particularly be seen at the high value distribution and low amount of values for samples tempered at $300\text{ }^{\circ}\text{C}$ and $400\text{ }^{\circ}\text{C}$, respectively. The layer peels of the substrate. Thus, $300\text{ }^{\circ}\text{C}$ is critical and $400\text{ }^{\circ}\text{C}$ not suitable for tempering nanoparticle based silver layers.

In order to interpretate the results, it has to be taken into account that due to measurement failures the results were overestimated. When textured substrates were used, the adhesion to the surface was high enough to withstand the pressure caused by the measurement needles. However, the tips of the texture pyramids caused interruptions of the printed silver layer. That means that the effective line geometry used to calculate the resistivity is even smaller than the measured one.

When using plane substrates or the multi-crystalline substrates the adhesion of the silver lines to the substrate was very low. Contacting the lines with the measurement needles often damaged the silver layer which increased the measured line resistance.

The low mechanical strength of the silver layers led to an overestimation of the measured resistances. This means, that actual possible resistivities for silver layers formed by nanoparticle sintering are even lower than the values shown here.

The values are likely to be further improvable if silver particles of higher quality are used. As one can see from SEM images already shown in previous Sections, size distribution of the used nanoparticles was quite wide. The author assumes that the ideal tempering temperature can be further lowered by using particles with narrower size distribution. Monodispers nanoparticles with a good stability within the ink formulation could form a closed packing, and a dense silver layer could be formed. However, particle movement within the ink and after deposition on the sample has to be high, to enable self organization of the particles. A smaller size distribution would also lead

to a more consistent sintering of the single particles both for chemical sintering and tempering and thermally sintering.

Experiments were also done for thermal sintering. The values measured were compared to chemical sintering and tempering and are shown in Figure 5.3.33.

A small trend towards better conductivity values for chemical sintering towards thermal sintering can be seen from the results. These results are also supported by the optical measurements shown in Figures 5.3.24 and 5.3.25.

Most of the measurements were unfeasible. Mechanical stability of thermally sintered silver samples was not high enough for reliable measurements. The initial neck formation which is provided by chemical sintering stabilizes the conductive layer against early abrasion of the nanoparticles, which is another advantage of chemical sintering compared to thermal sintering.

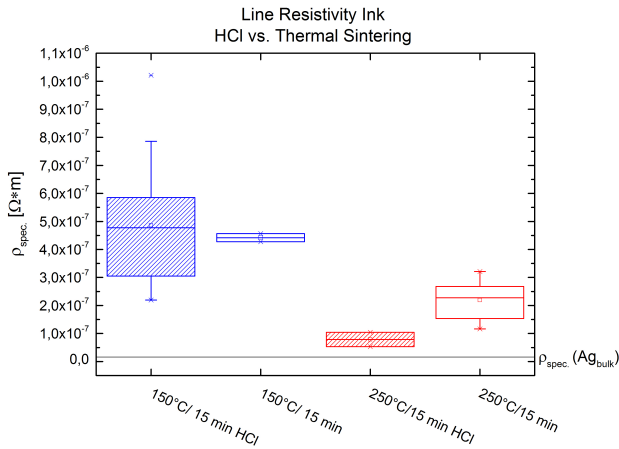


Figure 5.3.33: Comparison of line resistivities of silver nanoparticle ink layers chemically sintered and tempered and thermally sintered, respectively

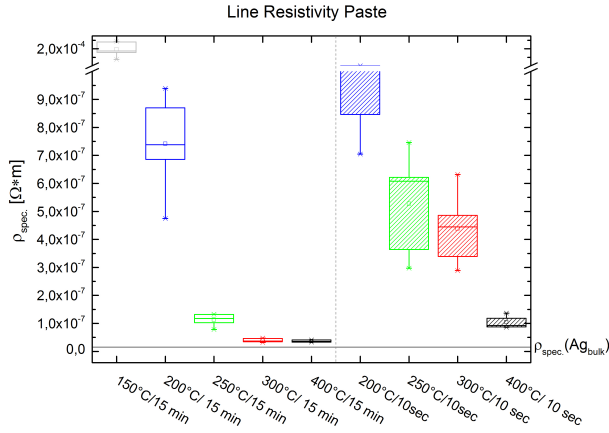


Figure 5.3.34: Line resistivities of screen printed metallization: Samples were chemically sintered with HCl prior to tempering at different temperatures. Silver bulk resistivity is marked

Line resistivity of screen printed metallization layers

The predominant printing technique is still screen printing with low temperature polymer pastes. For better comparability also screen printable pastes were formulated. In contrast to the very simple ink formulations used in this work, metallization pastes contain hydroxy ethyl cellulose to provide the rheology needed for screen printing. The specific line resistivity results for screen printed nanoparticle pastes chemically sintered and tempered are given in Figure 5.3.34.

Good line resistivities could be reached for samples tempered for 15 min at temperatures ≥ 250 °C. The resistivity drop between 250 °C and 400 °C is low proportional to the increase of temperature. Best results were obtained at temperatures at 300 °C: $\rho = 3.7 \times 10^{-8}$ Ωm median and $\rho = 3.16 \times 10^{-8}$ Ωm absolute. Even at 250 °C very good line resistivity values of $\rho = 1.18 \times 10^{-7}$ Ωm median were obtained.

The very low resistivity values are very close to the silver bulk resistivity of $\rho = 1.58 \times 10^{-8}$ Ωm . Commercially available polymer pastes, which are used for the metallization of temperature sensitive cells to-

day, only reach values of $\rho = 1 * 10^{-7} \Omega\text{m}$ at tempering temperatures $\leq 220 \text{ }^\circ\text{C}$ [62].

The resistivities reached for sintering times of only 10 s were higher compared to a longer sintering time of 15 min. Also the value distribution was higher.

The results are in good agreement with the optically observed sintering results described above: longer sintering times are necessary to get rid of the binder and enable a better particle sintering (Section 5.3.4).

A minimal tempering temperature of $150 \text{ }^\circ\text{C}$ is necessary to cast out organic residues.

The mechanical stability of the silver layers was good up to $250 \text{ }^\circ\text{C}$: the silver layers showed no cracks and adhered to the substrate. The adhesion to the substrate decreased for samples tempered at $300 \text{ }^\circ\text{C}$ and almost failed completely for samples tempered at $400 \text{ }^\circ\text{C}$. At this temperature the silver layer itself was not stable anymore: cracks within the layer were visible and the layer peeled off the substrate.

Thermal sintering and chemical sintering and tempering were also compared for screen printed silver nanoparticle layers.

Optical observation shows that the samples which were initially treated with HCl vapor are silver white while samples without chemical sintering stay gray as shown in Figure 5.3.35. The color change is related to the degree of sintering and organic residues in the paste. The effect is observable for temperatures up to $300 \text{ }^\circ\text{C}$. At this temperature, both samples appear silver white. Specific line resistivity results are given in Figure 5.3.36.

Thermal sintering gave no measurable results for sintering temperatures $\leq 250 \text{ }^\circ\text{C}$. For very short sintering times of 10 s measurements were not possible. With initial chemical sintering measurements were already possible starting at $150 \text{ }^\circ\text{C}$. The hydroxy groups in the binder HEC are substituted by Cl-groups during HCl evaporation. The Cl-groups coordinate more effectively to the silver particle surface, which delays the diffusion of the polymer between the particles. Chemical sintering is still effective as the impact on the capping agent through HCl vapor is higher. Otherwise resistivity measurement would not be possible for tempering temperatures of $150 \text{ }^\circ\text{C}$.

When comparing thermal sintering and chemical sintering with tempering it strikes out, that the values for thermal sintering and chemical

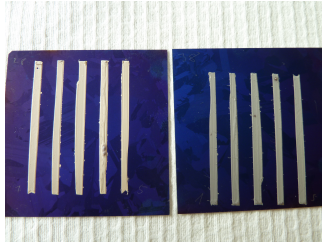


Figure 5.3.35: Photograph of screen printed silver nanoparticle layers after processing. Left: Chemical sintering with post tempering at 200 °C for 10 s. Right: Thermal sintering at 200 °C for 10 s.

sintering and tempering for 15 min were similar, whereas the values for a cure of 10 s were much higher for the thermally sintered samples. This effect is caused by the time the organics need to be removed from the particle surface.

For temperatures ≥ 250 °C thermal sintering seems to give slightly better resistivities than chemical sintering and tempering. The median value for thermal tempering at 250 °C is $\rho_{spec.} = 5.54 \cdot 10^{-8}$ Ωm . The values for 300 °C and 400 °C are comparable within the measurement failure ranges.

As has already been discussed in Section 5.3.4, decomposition of HEC takes place at 246 °C. In Figure 5.3.31 it could be seen that almost all organics were burned out from the silver layer after 15 min at 250 °C, and none could be seen in layers sintered at 300 °C. The organics should have no further impact on the conduction quality of the silver layers for longer sintering times, which is confirmed by the measurements: the difference between the values resulting from both sintering processes is small and is within measurement failure ranges.

These results show that chemical sintering can significantly lower the tempering temperature for metallization pastes based on silver nanoparticles even below the decomposition temperature of the binding organics. The process enables conductivity when thermal sintering does not deliver conductive silver layers.

The line resistivity of pastes containing ethyl cellulose (EC) and hydroxyethyl cellulose (HEC) were compared. Results for samples

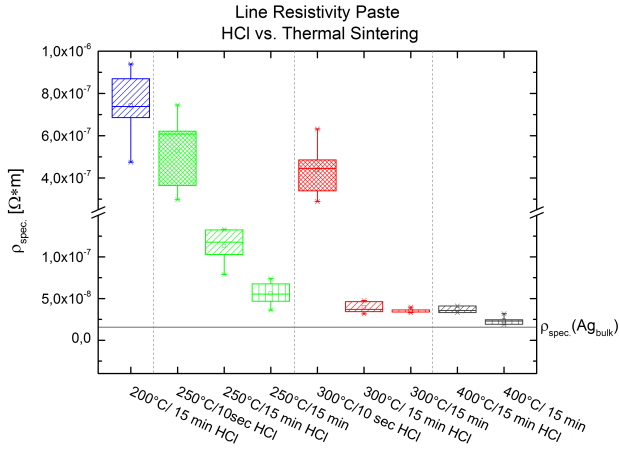


Figure 5.3.36: Comparison of line resistivities of silver nanoparticle screen printed layers chemically sintered and tempered and thermally sintered, respectively

chemically sintered and tempered at 200 °C for 15 min are shown in Figure 5.3.37.

Figure 5.3.37 shows a higher distribution of the measurement values of the silver layers containing ethyl cellulose than layers printed from a paste containing hydroxyethyl cellulose. Considering measurement failures the specific line resistance of pastes using ethyl cellulose or hydroxy ethyl cellulose as binder are comparable.

As has already been shown in Section 5.3.4 the additives have to be miscible especially with the capping agent of the particles and the solvent system used. Immiscible or bad miscibility of one of the components results in formation of agglomerates and large caves in between. Regarding the results, cave formation as shown in Figure 5.3.28 does not significantly influence the specific line resistance.

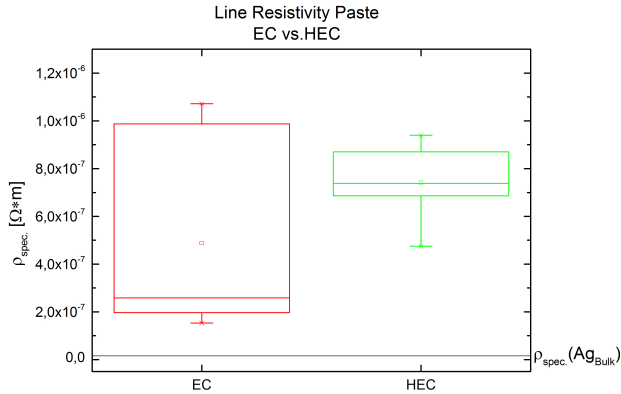


Figure 5.3.37: Comparison of line resistivities of silver nanoparticle pastes with EC and HEC, respectively

Line resistivity comparison of paste and ink

Some values for the comparison of the line resistivity values from nanoparticle ink and paste formulation are given in Figure 5.3.38. The samples were chemically sintered and tempered. Results for 400 °C are not shown, due to abrasion and disruption effects already discussed above.

For tempering temperatures below ≤ 200 °C ink formulations without non-decomposable organics show better conductivities than the corresponding paste formulation. At temperatures ≥ 250 °C, which means above the decomposition temperature of the binder HEC, the resistivity values differ only slightly and within measurement failure ranges.

When comparing Figures 5.3.32 and 5.3.34 one can see the same trends for the resistivity of the silver layers formed by the paste formulation as for the ink formulations. The resistivity and the distribution of the values drop fast with increasing temperature. A difference of ink and paste can be seen from the absolute values of the used tempering temperature: the paste samples have to be tempered at higher temperatures to reach comparable resistivity values and distri-

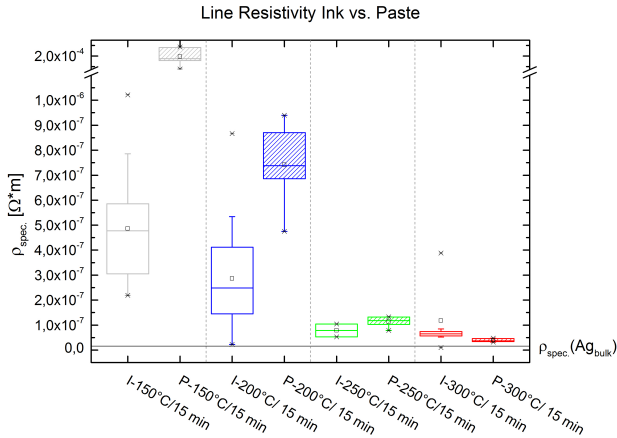


Figure 5.3.38: Comparison of line resistivities of silver nanoparticle ink and paste (chemical sintering and tempering)

butions as the inks. As soon as decomposition of the organics starts (in this case at 250 °C) no significant difference between ink and paste conductivities could be measured.

Another difference occurs when comparing the trends for a tempering/sintering of 10 s (Figures 5.3.32 and 5.3.34). The values for the paste samples are a lot higher and do not drop as fast as the values for the ink. This effect has already been explained above: organics do not have enough time to decompose and evaporate from the paste formulation, which is why the sintering of the particles in the paste is not developed as far as in the inks.

At temperatures ≥ 300 °C the paste benefits from the organic binder: mechanical stability of the silver layers is higher compared to the layers formed from the ink. Also, the adhesion to the substrate is improved. However, this effect is only relevant within a narrow temperature range. As soon as organic decomposition and burn out is finished, thermal stress within the metal layer and between metal and substrate also occurs for silver layers from paste formulations.

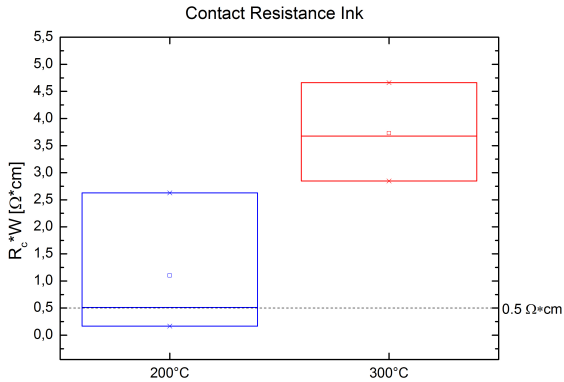


Figure 5.3.39: Normalized contact resistance of silver nanoparticle ink to ITO

5.3.6 Contact formation to ITO

ITO growth and morphology strongly influence the ITO quality and thus, conductivity, contact resistance and adhesion. The growth of ITO in turn, depends strongly on the substrate it is grown on [133]. To make sure that ITO morphology is the same as on real HIT solar cells, samples as illustrated in Figure 5.2.2 were used. Additional to samples with alkaline etched random pyramid texture also planar samples were used. Planar wafers provide the advantage of smoother printing results and in case of seed-layer printing, silver lines are not interrupted by pyramids. Advantage of textured surfaces is a higher adhesion of the silver lines to the substrate due to the increased surface roughness [134].

Contact resistance of nanoparticle inks to ITO

Figure 5.3.39 shows the normalized contact resistance ($R_c * W$) for the silver nanoparticle inks chemically sintered and tempered.

The normalized contact resistance is significantly lower for the ink tempered at 200 °C than at 300 °C. The median for the normalized

contact resistance for samples sintered at 200 °C was $R_c * W = 0.513 \Omega\text{cm}$ with the best value $R_c * W = 0.166 \Omega\text{cm}$ and an average measurement error of $R_c * W = 0.4 \Omega\text{cm}$. For 300 °C tempering temperature the median for the normalized contact resistance was $R_c * W = 3.68 \Omega\text{cm}$ and an average measurement error of $R_c * W = 0.468 \Omega\text{cm}$. Sheet resistances for ITO were $R_{Sh,200^\circ\text{C}} = 143,25 \Omega/\text{sq}$ and $R_{Sh,300^\circ\text{C}} = 28,49 \Omega/\text{sq}$, respectively.

The contact resistance does not significantly contribute to the series resistance for values $R_c * W < 0.5 \Omega\text{cm}$ [35]. Typical values for screen printed polymer pastes are between $R_c * W < 0.3\text{-}0.5 \Omega\text{cm}$ [135, 136].

Thermal effects like strain or evaporation of organics and the solvent from the ink could lead to a weaker contact between metal and ITO and would cause higher contact resistances for higher tempering temperatures. The effect of lower adhesion to the substrate has already been discussed in Section 5.3.5.

The sheet resistance of the ITO layer influences the contact resistance. The interpretation of TLM measurement results have to be treated with care. One problem of the method is the extrapolation of the measured data, which can lead to errors. The error which is made by the interpolation can be minimized by using only data where the coefficient of determination is close to $R^2 = 1$. Data shown here fulfill this requirement.

During the measurement, a current flows laterally around the contacts which also influences the measurement values. This effect is quite strong for highly conductive ITO. In addition, the sheet resistance of the semiconductor or ITO, respectively, corrupts the measured data. For ITO, this is a problem in particular because sputtered ITO layers are microcrystalline and the sheet resistance can differ widely throughout the whole layer.

Contact resistivity values are not shown because they are dependent on the transfer length, which is even more falsified by errors than the contact resistance measurement itself.

As has been discussed in Chapter 4.3, a large number of samples has to be measured to collect big statistics and counter balance the mentioned effects.

Within this work, sample numbers were limited, thus statistics were rather small. The interpretation of trends for the contact formation of the nanoparticle inks to ITO must, therefore, be treated carefully. This has also be in mind for interpretation of following contact resis-

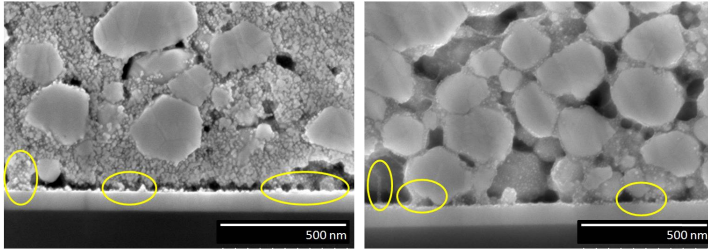


Figure 5.3.40: Cross section SEM images of contact resistance measurement samples containing particles of different qualities. Left: Paste 1 right: Paste 2

tance results.

Contact resistance of nanoparticle pastes to ITO

Samples of screen printing pastes were also measured. Cross sections of fully processed paste 1 and paste 2 are shown in Figure 5.3.40. The normalized contact resistances are shown in Figure 5.3.41.

Particles from paste 2 were freshly prepared one week before paste formulation, particles from paste 1 were from an older, and apparently higher quality batch. As can be seen from Figure 5.3.41 paste 1 shows better contact resistance values than paste 2 independent of the substrate surface. The median normalized contact resistance for paste 1 on a planar wafer was $R_c * W = 0.5 \Omega\text{cm}$ with an average error of $\Delta R_c * W = 0.1 \Omega\text{cm}$ and $R_c * W = 0.695 \Omega\text{cm}$ with an average error of $\Delta R_c * W = 0.311 \Omega\text{cm}$ on a textured surface. The lowest value measured was $\Delta R_c * W = 0.068 \Omega\text{cm}$. The median normalized contact resistance for paste 2 on a planar wafer was $R_c * W = 4.56 \Omega\text{cm}$ with an average error of $\Delta R_c * W = 0.8 \Omega\text{cm}$ and $R_c * W = 1.82 \Omega\text{cm}$ with an average error of $\Delta R_c * W = 0.5 \Omega\text{cm}$ on a textured surface. The sheet resistance of all ITO layers were comparable and had a value between $R_{Sh} = 60\text{-}80 \Omega/\text{sq}$

The cross sections (Figure 5.3.40) of the samples show, that paste 1 consists mostly of well sintered small particles. Although there seems to be a wide gap between the particles and the ITO, a closer look shows, that small particles are covering the ITO surface which are

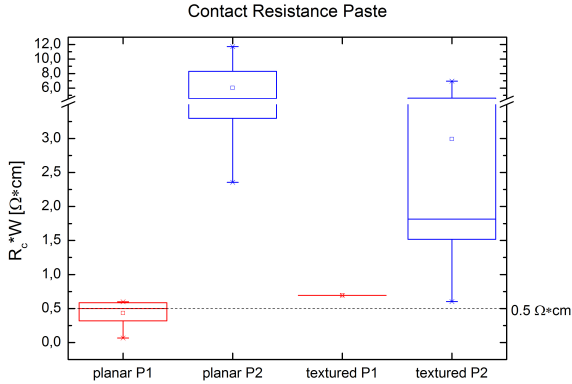


Figure 5.3.41: Normalized contact resistance of silver nanoparticle pastes with hydroxy ethyl cellulose to ITO with particles from two batches on planar and textured wafers

partially connected to the overlying bulk. In contrast, the interface between paste 2 and ITO seems to be more or less covered with a polymer (hydroxy ethyl cellulose in this case). Although this polymer film is very thin, it is still thick enough to slightly deteriorate the contact quality.

The texture of the surface has no measurable impact on the contact resistance.

The experiment shows, that the particle quality has a high impact on the contact formation. This observation could not be made for the line resistivity. By formulating inks and pastes for contact formation to solar cells, the choice of the components has to be more carefully adapted to the demands of contact formation compared to line resistivity.

In Chapter 5.3.4 it has already been mentioned that the components of the paste containing ethyl cellulose do not effectively mix and thus, big clumps with wide caves in between are formed. To evaluate the impact of the different organics on the contact formation, pastes con-

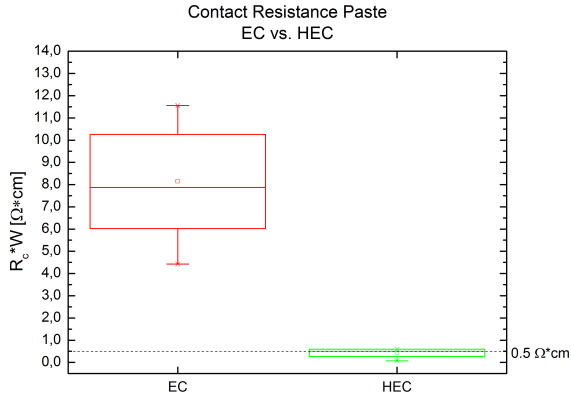


Figure 5.3.42: Normalized contact resistance of silver nanoparticle pastes with ethyl cellulose (EC) and hydroxy ethyl cellulose (HEC) to ITO

taining ethyl cellulose or hydroxy ethyl cellulose were investigated. The results are shown in Figure 5.3.42.

The normalized contact resistance for the paste containing EC was $R_c * W = 7.87 \Omega\text{m}$ median with an average measurement error of $R_c * W = 0.99 \Omega\text{m}$. For the paste with HEC the values were $R_c * W = 0.5 \Omega\text{cm}$ for the median normalized contact resistance with an average error of $\Delta R_c * W = 0.1 \Omega\text{cm}$. The sheet resistance for all substrates was between values of $R_{Sh} = 20\text{-}30 \Omega/\text{sq}$.

The contact formation of pastes formulated with ethyl cellulose is worse compared to pastes with hydroxy ethyl cellulose as shown. This is interesting because the line resistivity is not influenced or even better for the pastes containing ethyl cellulose according to the results shown in Section 5.3.41. This indicates that the contact formation is more sensitive to particle quality and organic influences than the line resistivity.

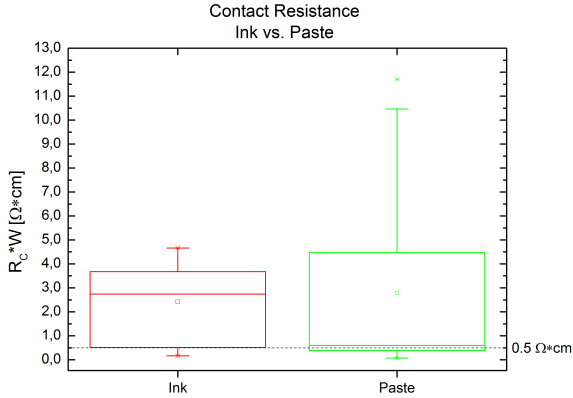


Figure 5.3.43: Normalized contact resistance of silver nanoparticle paste and ink to ITO

Contact resistance comparison of paste and ink

The contact resistance of the HEC paste 1 and the ink to a planar ITO coated substrate were compared. The results are shown in Figure 5.3.43.

The median value for the normalized contact resistance of the HEC paste is $R_c * W = 0.6 \Omega\text{cm}$ with an average error of $\Delta R_c * W = 0.1 \Omega\text{cm}$ and $R_c * W = 2.74 \Omega\text{cm}$ with the best value $R_c * W = 0.166 \Omega\text{cm}$ and an average measurement error of $R_c * W = 0.4 \Omega\text{cm}$ for the ink samples tempered at 200°C . Regarding contact formation, both metallization processes show good results. However, the paste already includes a binder which also serves as adhesion promoter. This improves the contact quality significantly. Regarding contact stability, a silver particle paste is favorable compared to the simply silver particle ink. To obtain similar results for inks, the addition of an adhesion promoter is necessary.

Type of contact

ITO is a degenerated n-doped semiconductor with the Fermi level situated within the conduction band. Therefore, ITO is often treated as a metal.

In fact, the Fermi level of the bulk material and the Fermi level of the surface, which is of importance for the contact formation, have to be considered separately. The surface of ITO could be treated as metallic not because of electrons inside the conduction band but because of metallic surface states [137]. The ITO work function can be manipulated by surface treatment, which is a result of the Fermi level of the surface being lowered inside the forbidden band gap [138]. If ITO is treated with oxygen (e.g. UV ozone treatment, O₂ plasma, etc.) the Sn-donor complexes are saturated and the Fermi level drops in energy. Thus, the work function increases at the surface [139, 140]. As a consequence ITO can not necessarily be considered and treated as a metal regarding electrical surface characteristics.

The effect of oxygen treatment is only effective for a very short time (several minutes to one hour). The mobility of oxygen atoms within the ITO lattice is very high, which is probably caused by the bixbyite structure [138, 140].

Regarding contact formation to a metal, ITO can be considered as a semiconductor or a metal.

In case ITO has to be treated as a semiconductor, the contact formation quality could be dependent on the ITO surface treatment before the metallization. Gassenbauer et al. observed that the concentration of tin within the surface layers might be the reason for the observed change of Fermi level [140]. Further evidence of the importance of the ITO surface to contact formation is given by Barraud et al. who observed very poor contact resistances to silver for high conductive, high transparent hydrogen-doped In₂O₃ (In₂O₃:H) [94]. The fact that manipulating the ITO surface is already in use to adapt the work function to fit whole injection properties to organic conductors [138] implies, that work function plays an important role in contact formation.

However, if ITO is a semiconductor with a high density of surface states the formation of an ohmic contact instead of a Schottky contact is possible (see Section 2.2.2).

Which kind of contact is formed can be measured by current sweep measurements with TLM on metalized ITO contacts as was done for

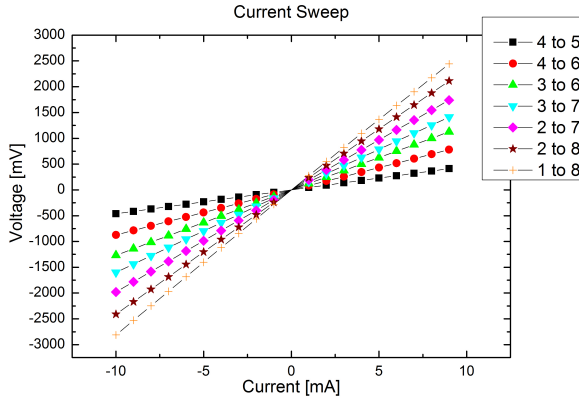


Figure 5.3.44: Current sweep of TLM measurements of silver nanoparticle paste on ITO

samples of ITO layers metalized with a silver nanoparticle paste with HEC. The measurements are shown in Figure 5.3.44.

The linear progress of the measurements according to equation 4.4 imply an ohmic contact between the metallization paste and ITO. This implies that contact formation to ITO is controlled by a high number of metallic surface states as postulated by Gassenbauer et al.

5.3.7 Chemical sintering with in-built chemical sintering agent

The HCl vapor chemical sintering is an effective way of sintering silver nanoparticles even at room temperature in a very short time and reaching good conductivity values with post tempering. However, HCl is a quite aggressive chemical and ITO in particular is sensitive against acids. ITO can be completely removed from a surface if the layer quality is bad or if the layer is exposed to the acid vapor for a longer time (around 60 seconds). In addition, the vapor exposure is an additional processing step, which makes the manufacturing process for the solar cells more expensive.

Grouchko et al. suggested an in-built mechanism for the chemical

Table 5.3.2: Sinter salt results of NaCl (particle concentration 20 wt%)

c(NaCl) [mmol/l]	Ink stability	Appearance	Sintering effect
75	stable	orange brown	few sinter islands
100	stable	orange brown	sinter islands
150	sedimentation after 1 d	gray after 1 d	many sinter islands
200	sedimentation after 2 h	dark brown	sinter islands and agglomerated particles
250	sedimentation	dark brown	few sinter island high degree of agglomeration
300	sedimentaion	Grey	mainly agglomerated particles

sintering of metal nanoparticle inks [79]. He suggested to insert the chemical sintering agent (in this case chlorine ions) into the ink in terms of an inorganic salt [79]. According to Grouchko et al., the salt concentration is kept very low to avoid early triggering of the sintering process, which keeps the ink stable during storage. After printing, the solvent evaporates and the salt concentration within the printed layer rises. When a certain concentration limit is exceeded, the chemical sintering process starts and the metal nanoparticles agglomerate and sinter. This way a good shelf life for the metallization ink could be reached, and the additional aggressive HCl vapor process step could be avoided.

This approach was tested with several chlorine salts as described in Section 5.2.

The results for NaCl as sinter salt are shown below.

SEM images show the sintering effect of the dried inks on a silicon substrate (Figures 5.3.45 and 5.3.46).

As expected, the results shown in Table 5.3.2 demonstrate that the stability of the inks decreased with increasing salt concentration. Only the inks with a salt concentration of 75 mmol/l and 100 mmol/l

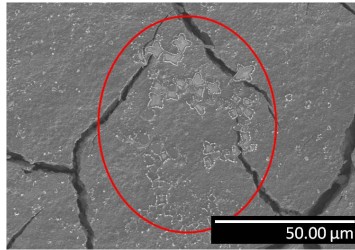


Figure 5.3.45: SEM image of NaCl in-built chemical sintering ink: sinter islands are marked ($c(\text{NaCl}) = 100 \text{ mmol/l}$, silver particle concentration 20 wt%)

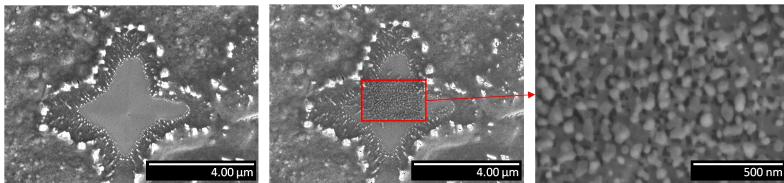


Figure 5.3.46: SEM image of sintering island before (left) and after (middle/right) electron beam exposure ($c(\text{NaCl}) = 100 \text{ mmol/l}$)

showed a good shelf life. The inks containing 150 mmol/l of NaCl started to agglomerated after 24 h and inks with the highest salt concentration of 300 mmol/l turned gray almost instantly, which indicates the agglomeration and growth of the nanoparticles within the ink.

Small areas of sintered particles can be found throughout the sample (Figure 5.3.45). These areas will be called *sinter islands* in the following. Most of these islands are star shaped but can also be shaped as a circle or squares.

The sinter islands seem to be covered with an organic residue (probably a layer of capping agent which has diffused from the silver surface). The residue is burned off by the electron beam at higher magnifications, which is shown in Figure 5.3.46. Under the organic residues the particles are sintered. Outside the sinter islands no sintering could be detected.

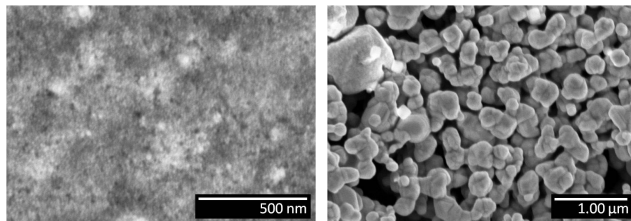


Figure 5.3.47: SEM images of unsintered nanoparticles outside of sinter islands ($c(\text{NaCl}) = 100 \text{ mmol/l}$; left) and agglomerated particles ($c(\text{NaCl}) = 300 \text{ mmol/l}$; right)

The number of sinter islands increases with increasing initial salt concentration. However, starting from 150 mmol/l salt concentration, particle size also rises as shown in Figure 5.3.47.

Inks with $50 \text{ wt}\%$ silver particle concentration show similar effects but particle agglomeration appears faster and the ink layers are more densely packed compared to the layers formed from inks with $20 \text{ wt}\%$ silver particles.

The results for KCl as sintering agent are shown in Table 5.3.3.

KCl was less effective regarding the formation of sintering islands than NaCl. Sintering could only be observed within isolated areas of sinter islands but not throughout the whole silver layer. In case of KCl, bigger agglomerated particles were formed instead of sinter islands. $50 \text{ wt}\%$ silver particle inks behaved similar to NaCl inks.

Table 5.3.3: Sinter salt results of KCl (Particle concentration 20 wt%)

$c(\text{KCl})$ [mmol/l]	Ink stability	Appearance	Sintering effect
100	stable	orange brown	few sinter islands
150	sedimentation after 1 d	dark brown after 1 d	slightly more sinter islands and bigger agglomerated particles
200	sedimentation after 12 h	dark brown after 12 h	sinter islands and big agglomerated particles

Table 5.3.4: Sinter salt results of HCl (Particle concentration 20 wt%)

$c(\text{HCl})$ [mmol/l]	Ink stability	Appearance	Sintering effect
100	stable	orange brown	no visible sintering
150	stable	orange brown	no visible sintering but agglomerated particles
200	stable	orange brown	no visible sintering but agglomerated particles

Results for diluted HCl are summarized in Table 5.3.4

Diluted hydrochloric acid did not show any effective particle sintering but particle agglomeration starting from 150 mM HCl concentration.

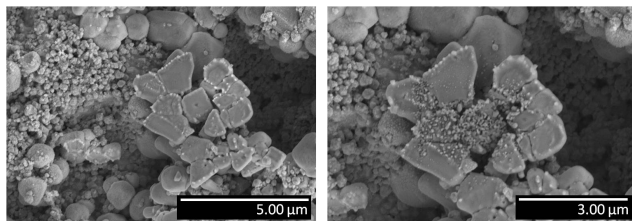
The results for NH_4Cl are summarized in Table 5.3.5 and Figures 5.3.48 and 5.3.49.

For sintering with NH_4Cl besides big agglomerated particles, also big sinter islands or *sinter cubes* can be found (Figure 5.3.48).

However, NH_4Cl showed more effective sintering compared to NaCl . Here particle sintering could also be observed outside of sintering is-

Table 5.3.5: Sinter salt results of NH_4Cl (Particle concentration 20 wt%)

$c(\text{NH}_4\text{Cl})$ [mmol/l]	Ink stability	Appearance	Sintering effect
100	stable	orange brown	sinter islands
150	sedimentation	Grey	sinter islands, sintered and agglomerated particles
200	sedimentation	Grey	sinter islands and agglomerated particles

Figure 5.3.48: SEM images of sinter cubes before (left) and after (right) electron beam exposure ($c(\text{NH}_4\text{Cl}) = 200$ mmol/l)

lands for a salt concentration of $c(\text{NH}_4\text{Cl}) = 100$ mmol/l and a silver nanoparticle concentration of 20 wt%. At higher silver nanoparticle concentrations (50 wt%), no sintering but particle agglomeration could be observed similar to the behavior of inks mixed with NaCl or KCl, respectively (Figure 5.3.49). For higher salt concentrations ($c(\text{NH}_4\text{Cl}) \geq 150$ mmol/l) particle sintering was suppressed by particle agglomeration.

The appearance of a stable and unstable ink is shown in Figure 5.3.50.

Early particle agglomeration could easily be observed optically by a color change of the inks from dark orange brown to gray. The particles are already destabilized due to a high concentration of chlorine ions within the ink. The silver particles agglomerate and grow together,

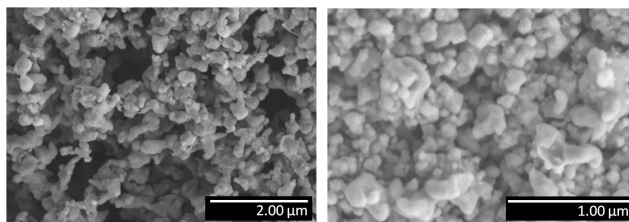


Figure 5.3.49: SEM images of nanoparticle sintering with NH_4Cl ($c(\text{NH}_4\text{Cl}) = 100 \text{ mmol/l}$) ink 20 wt% silver nanoparticle ink (left) and particle agglomeration in 50 wt% silver nanoparticle ink (right)

which causes the change in color.



Figure 5.3.50: Photograph of inks including NH_4Cl one week after preparation: left-hand side: 100 mmol/l; right-hand side 200 mmol/l

The effect of sinter island formation instead of equal sintering of the whole area could be explained by diffusion time of the sintering agent, which are chlorine ions in this case. The evaporation of the solvent is too fast (even at room temperature) for the ions to spread evenly between the PAA capped silver nanoparticles. This suggestion is supported by the fact, that inks with lower silver nanoparticle concentrations are sintered more effectively throughout the whole silver layer than inks with higher silver concentrations. Due to the presents of NH_4OH , NH_4Cl is chemically more related to the ink components within the formulation than NaCl and KCl , respectively. That means

better miscibility of all ink components and, therefore, better diffusion within the dispersion.

Nevertheless, chemical sintering by an in-built sintering agent in terms of salts is less effective than chemical sintering via HCl vapor exposure. The formulation of in-built chemical sintering inks is complicated regarding shelf life of the inks and limited to a certain amount of silver nanoparticle concentration which is disadvantageous for metallization inks, which should contain as much conductive material as possible.

5.4 Summary

In this chapter, the sintering of wet-chemically synthesized silver nanoparticles was examined. To obtain small uniform silver nanoparticles the reaction temperature has to be low and the addition of reducing agent has to be kept as short as possible to enable fast nucleation and uniform particle growth.

The parameters which have an effect on chemical sintering were investigated in detail. These results frame the basic requirements necessary for the formulation of metallization inks and pastes based on silver nanoparticles. It was shown that the choice of the capping agent has a higher influence on the sintering behavior of the investigated particles than the particle size. Additives show the same trends in effects on the particle sintering as the capping agent, but the effect is less significant than of the capping agent.

The effect of additional tempering on chemically sintered silver nanoparticles was investigated and compared to the results produced by thermal sintering. Prior chemical sintering lowers the temperature of the subsequently thermal treatment of the silver layers compared to thermal sintering.

Silver nanoparticle inks reach the lowest resistivity possible after very short tempering periods of only 10 s. Pastes need longer tempering in order to compensate long diffusion times of polymeric binders in the paste formulation (here 15 min).

The miscibility of the different ink and paste components must fit. Poor miscibility leads to cluster and cave formation within the silver layer, which has a high impact especially on the contact formation. Chemical sintering stabilizes the resulting silver layer against thermal

stress to a certain extent.

As a result, for a simple ink formulation, line resistivities down to $\rho = 2.30 \cdot 10^{-8} \Omega\text{m}$ for a sample tempered at 200 °C for 15 min could be obtained. This compares to only 1.5 times the resistivity of bulk silver. Commercially available inks reach comparable values after 30 min of thermal sintering [80]. Chemical sintering alone obtains values five times the conductivity of bulk silver [83]. By post annealing at 250 °C for 15 min a median resistivity of $\rho = 7,86 \cdot 10^{-8} \Omega\text{m}$ was measured.

For pastes containing hydroxyethyl cellulose as binder, the best results were obtained at 300 °C: $\rho = 3.7 \cdot 10^{-8} \Omega\text{m}$ median and $\rho = 3.16 \cdot 10^{-8} \Omega\text{m}$ absolute, which compares to twice the resistivity of bulk silver. Commercially available polymer pastes, which are used for the metallization of temperature sensitive cells today, obtain values of $\rho = 1 \cdot 10^{-7} \Omega\text{m}$ at tempering temperatures ≤ 220 °C [62]. Even at 250 °C very good line resistivity values of $\rho = 1.18 \cdot 10^{-7} \Omega\text{m}$ median were obtained.

The contact formation to ITO was measured and good values $< R_c * W = 0.5 \Omega\text{cm}$ were obtained: $R_c * W = 0.166 \Omega\text{cm}$ for inks and $R_c * W = 0.068 \Omega\text{cm}$ for pastes applied to ITO. Typical values for screen printed polymer pastes are between $R_c * W < 0.3\text{-}0.5 \Omega\text{cm}$ [135, 136].

Besides the chemical sintering with HCl vapor, the in-built chemical agent sintering process was tested with different chlorine salts as sintering agents. Although the process led to locally sintered areas, a layer wide effective sintering of the single nanoparticles could not be obtained. Thus, the process is not suitable for metallization with silver nanoparticles.

The results demonstrate that metallization based on silver nanoparticles is a promising alternative for low temperature metallization on ITO and mass production.

Inks formulated with silver nanoparticles can be used for the contactless seed-layer metallization via ink jet or aerosol jet printing. The requirements, which have to be fulfilled by additives to obtain stable ink formulations with good adhesion to the substrate were compiled. Very low resistivities could be achieved by short processing times with chemical sintering (10 s to 15 min), while thermal sintering needs at least 30 min to obtain comparable values [80]. A good contact to ITO with low contact resistance can also be formed.

Pastes can be formulated and processed as described. With chemi-

cal sintering and post tempering very, low resistivities can be reached at temperatures between 250-300 °C. Such low values can not be reach by polymeric silver pastes [62].

6 Influence of Sample Surface on Metallization

In this chapter the surface properties of ITO with regard to the latter's behavior with solvents is discussed. After a short introduction in Section 6.1, the experiments are described in Section 6.2. Goniometer measurements were used to examine the ITO's surface properties and its development when stored in air. A rapid change in surface properties regarding its behaviour against liquids could be observed. The change in the surface properties of ITO may also have an influence on the adhesion of metals on ITO as well as on the contact resistance to the metallization. The discussion of the results is given in Section 6.3. The chapter is then summarized in Section 6.4.

6.1 Introduction

ITO is often used as contact material for new and alternative solar cell designs, which require a full area and, thus, transparent metallization on the front side. To extract the current from the cell, ITO has to be contacted by a metal. Cell designs, which require ITO as contact material, are often temperature sensitive which is why conventional metallization requiring high temperature processes can not be used. In Chapter 5 inks and pastes based on silver nanoparticles were introduced as an alternative to the cost intensive sputtering or evaporation of metals through a photolithographic mask. A proper paste and ink formulation is complicated and, especially in the case of inks, depends strongly on the surface properties of the substrate. The ink formulation has to be adjusted to the properties of the substrate surface in order to gain optimal printing results and avoid bleeding effects or repulsion of the ink. Adhesion as well as contact formation are both influenced by surface properties, too. It will be shown that ITO changes its surface properties within only a few hours after deposition. The

behavior of the ITO surface coating on planar and alkaline textured wafers towards liquids is analyzed and discussed in this chapter. In addition, since photolithographic (PL) structuring and evaporation of metal is still a standard metallization technique for ITO covered solar cells, the influence of the chemicals used for the PL process is analyzed as well. Lastly, the influence of the surface properties on adhesion and contact resistance against evaporated metals is investigated.

6.2 Experimental

Specifications of used chemicals:

Diodmethane: ABCR, 99% stabilized with copper

6.2.1 Contact angle measurements on ITO

Substrate

Alkaline textured (alkaline etched random pyramid texture) and planar mono crystalline silicon wafers coated with sputtered ITO were used.

For sputtering an OXFORD cluster tool with argon plasma was used.

The ITO chamber was equipped with an $\text{In}_2\text{O}_3/\text{SnO}_2$ (90/10 wt%) target. Gases such as oxygen and argon can be fed separately. ITO coating thickness was 70 nm. An oxygen flow of 0.7 sccm was used.

Measurements of the substrate surfaces were repeatedly done right after preparation and again after a few hours to several days. In the mean time, samples were stored under ambient conditions.

Ozone cleaning

A UV excimer¹ was used for the ozone cleaning process.

Samples were placed under the UV excimer at a distance of 1 cm. Radiation was on for one minute.

¹With an UV excimer O_2 - and O_3 molecules can be splitted at certain wavelengths. The molecules are splitted into oxygen atoms and oxygen molecules, respectively. Wavelengths of excimer: 184 nm (O_2 splitting) and 253 nm (ozone splitting) [141]

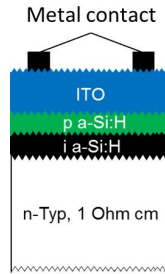


Figure 6.2.1: Illustration of sample structure with random pyramid texture for contact resistance measurements

Contact angle measurement

Contact angle measurements were done with a KRÜSS EasyDrop DSA 100 goniometer. The sessile drop mode was used. Contact angles were measured within 10 s after drop application to the substrate. Of each liquid, 10 measurements were taken. Deionized water was used as the polar solvent and diiodmethan (DIM) as the non-polar solvent.

The contact angle measurement was intentionally carried out at different areas of the sample so as to avoid false measurements due to surface manipulation by measurement liquids.

Surface energy calculation

Surface energy was calculated from average values of contact angle measurements. The method of Owens, Wendt, Rabel and Kaelble (cp. Section 2.7) was used for calculations.

6.2.2 Influence of surface properties on metallization characteristics

Sample preparation

As substrate, planar n-type mono crystalline FZ silicon wafers with a sheet resistance of 0.8-1.2 Ωcm were used. The wafers were coated with a-Si and ITO. The substrate structure is illustrated in Figure 6.2.1.

For sputtering, an OXFORD cluster tool with argon plasma was used.

The ITO chamber was equipped with an $\text{In}_2\text{O}_3/\text{SnO}_2$ (90/10 wt%) target. Gases such as oxygen and argon can be fed separately. ITO coating thickness was 70 nm. An oxygen flow of 0.7 sccm was used.

Amorphous silicon was sputtered with silane and hydrogen gas. For p-type doped a-Si, B_2H_6 gas was additionally added. A-Si thicknesses were 1 nm for a-Si(i) and 10 nm for a-Si(p), respectively.

The preparation was identical for all substrates, including ITO application. Afterwards the samples were separated in two groups. The process flow of the experiment is shown in Figure 6.2.2.

The contact angle of deionized water on samples of wafer group 1 was measured right after ITO application. Afterwards the samples were further divided into groups 1a and 1b.

A process used for photolithographic structuring was used on samples of group 1a. The whole sample surface was treated. After lift-off (removal of photolithographic chemicals) the contact angle of water was measured again. Afterwards, the group was further split. One part was metalized via evaporation through a shadow mask with Ag (5 μm thickness), the second grid was metalized with a TiPdAg (50 nm/50 nm/5000 nm thickness) stack.

For group 1b, treatment with photolithographic chemicals was skipped.

Samples of group 2 were stored under ambient conditions for seven days after ITO preparation. The contact angle of deionized water was measured. Further process flow was similar to group 1.

Each group was characterized by measuring the contact angle, the adhesion (qualitatively) by tape test and the contact resistance of the metal to ITO by TLM measurement. Figure 6.2.2 shows the process flow of the experiment.

Contact angle measurement

Contact angle measurement was done with a KRÜSS EasyDrop DSA100 goniometer. The sessile drop mode was used. Contact angles were measured within 10 s after drop application to the substrate. Of each liquid 10 measurements were taken. Deionized water was used.

The contact angle measurement was intentionally carried out at different areas of the sample so as to avoid false measurements due to surface manipulation by measurement liquids.

Measurements were additionally done on evaporated silver and titanium one week after evaporation. The samples were stored in air.

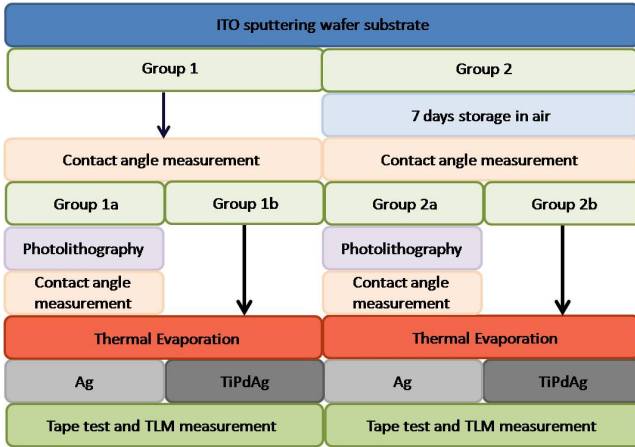


Figure 6.2.2: Process flow of experiment

Surface energy calculation

Surface energy was calculated from average values of contact angle measurements. For calculations, the method of Owens, Wendt, Rabel and Kaelble was used.

Contact resistance measurement

The contact resistance was measured with a TLM measurement setup. Contact resistivity was determined by measuring eight silver lines. The applied current was set to $I = 10$ mA.

Geometry was given by the geometry of the shadow mask.

Adhesion measurement

Adhesion was measured with a tape test.

The tape was applied to the metal grid and removed parallel and perpendicular to the metal fingers. An illustration is given in Figure 6.2.3.

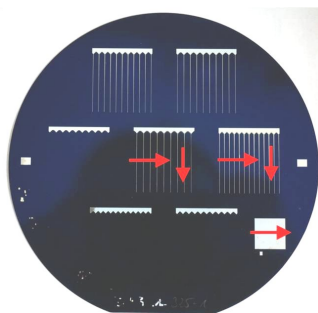


Figure 6.2.3: Photograph of experiment sample. Arrows mark pulling direction of adhesive tape.

6.3 Results and discussion

6.3.1 Solvents on ITO surface

Figures 6.3.1 and 6.3.3 show pictures of measured water and DIM drops directly after ITO deposition and after several days on alkaline textured and planar wafers, respectively.

It can be seen from Figures 6.3.2 and 6.3.4 that the contact angles of water and DIM change dramatically within only one day of storage in air.

The contact angle from water rises from 0° (total spreading on the surface not shown; measurement impossible) to almost 100° on a textured surface. A surface is considered hydrophobic when the contact angle value is around 90° . At even higher values the surface is called super hydrophobic [142]. As can be seen from Figure 6.3.2, the polar part of the surface energy drops dramatically in particular. Thus, the surface energy of ITO also drops. Similar observations can be made on planar surfaces.

It is assumed that ITO adsorbs organic and inorganic molecules from the air to lower its surface energy. The adsorption is very fast and the residues cause a dramatic drop in hydrophilicity and, thus, surface energy.

The standard cleaning procedure for silicon wafers can not be used for ITO because it involves an HCl dip amongst others and ITO is not stable against acids. However, ozone is able to clean surfaces

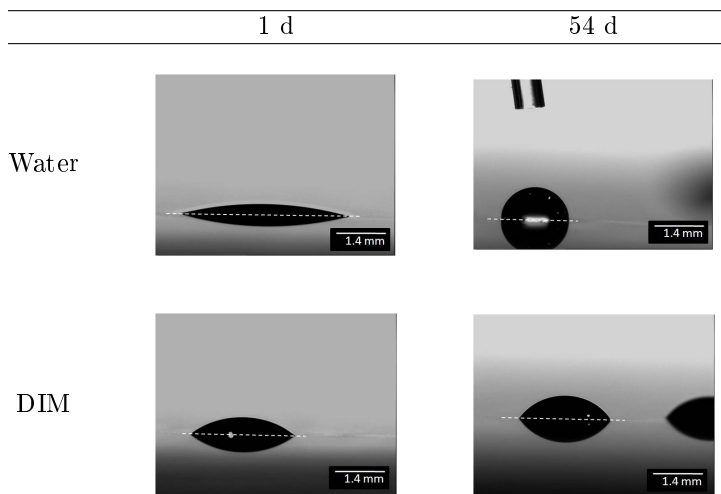


Figure 6.3.1: Goniometer pictures of water drops (top) and DIM drops (down) on alkaline textured Si surfaces with ITO

from organic adsorptions. Therefore, it was tested whether a UV-ozone treatment could “reset” the mechanical surface properties of the ITO surface. After cleaning the previously aged samples, goniometer measurements were done. After an additional aging step under ambient conditions, measurements were repeated for a third time.

The surface of ITO was again completely hydrophilic and contact angles could not be measured right after cleaning. The further development of the contact angle for the aged samples was the same as for freshly prepared samples, which were stored in air: the contact angles rose quickly again.

The high wettability of the surface by water means a wide spreading of aqueous metallization inks on freshly prepared cells if no proper additives are added to the ink to prevent the spreading. A solution to this problem could be to simply use solvent based inks. However, the metallization inks used on ITO contain low temperature curing silver nanoparticles, which are best stabilized in aqueous solutions. This has been discussed already in Chapter 2.4.3 and 5. Another choice could be to store the samples under inert gas, but the influence of the inert

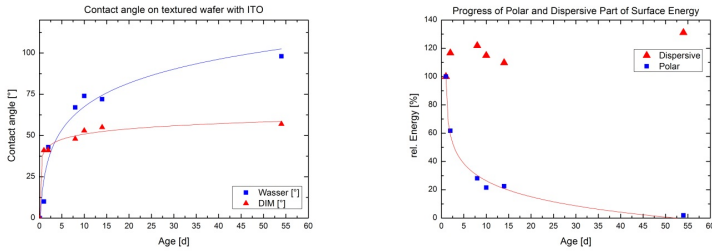


Figure 6.3.2: Development of contact angle (left) and polar and dispersive part of surface energy (right) on alkaline textured surface with ITO metallization

atmosphere on the ITO surface has not been examined so far.

An alternative would be to let the ITO surface age until the ink and substrate surface properties match.

The surface energy plays an important role with regard to the adhesion and wettability: higher surface energy should also cause higher wettability and thus adhesion (Section 2.7) [142]. In addition, the interdependency between ITO and the metal surface, which might also lead to better electrical contact between the materials, should improve with higher surface energy. This question will be discussed in the next Section.

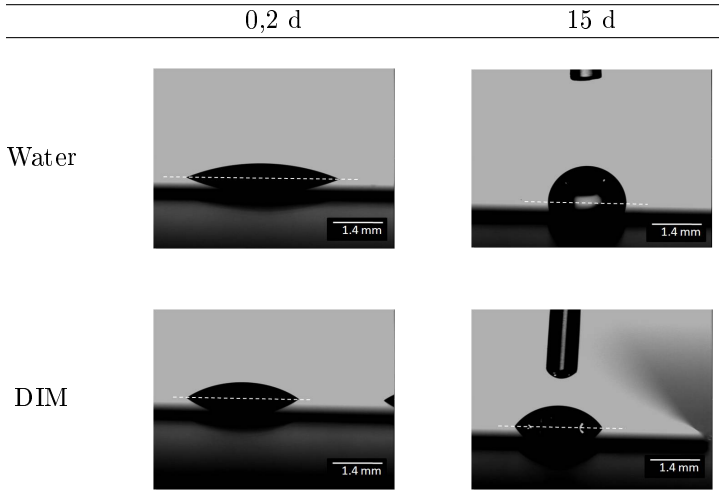


Figure 6.3.3: Goniometer pictures of water drops (top) and DIM drops (down) on planar Si surfaces with ITO

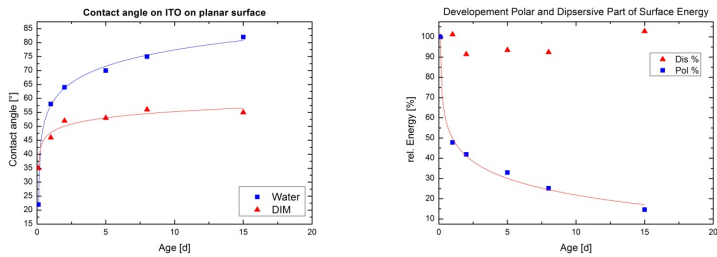


Figure 6.3.4: Development of contact angle (left) and polar and dispersive part of surface energy (right) on a planar surface with ITO metallization

6.3.2 Influence of surface properties on metallization characteristics

Figure 6.3.5 shows the development of the contact angle of water on ITO when stored in air.

The progress is as already expected from previous experiments: the contact angle rises with the age of the ITO. In Figure 6.3.6 the contact angle of water on the ITO surface is shown in dependence of the surface treatment.

As expected, the measurement liquids develop bigger contact angles on the ITO surface for the samples stored in air for seven days than on the freshly prepared samples.

The photolithographic treatment of the ITO surface does influence the surface properties, causing the ITO surface to be more hydrophobic compared to the freshly prepared samples, but less hydrophobic than the aged samples. In addition, the chemicals seem to be able to slightly clean the surface from adsorptions from the atmosphere again: the contact angles for the aged samples which were also treated with chemicals are smaller than those for the non-treated ones.

The results of the TLM measurements and the tape tests are given in Table 6.3.1.

First the results of the tape test will be discussed.

As can be seen from Table 6.3.1, all sample metalized with a TiPdAg stack passed the adhesion test. This was expected as titanium (aside from chromium) is used as an adhesion promoter for solar cell metallization via evaporation (Section 3.4). The high adhesion of titanium to ITO is likely caused by a thin TiO_2 layer at the boundary surface between the substrate and titanium. Due to their electronegativity and polarization, oxides can develop electrostatic attraction in addition to Van der Waals forces and, thus, adhere better to surfaces also containing polarized atoms such as SiO_2 (oxygen) or oxides such as ITO. The barrier height of titanium to silicon is quite low, which results in low contact resistivities [27]. The TiO_2 layer is still thin enough to not influence the contact formation, significantly.

The adhesion of silver to ITO is worse than that of titanium. Silver adheres to freshly prepared ITO surfaces when the surface energy is still high (low contact angle) but becomes significantly worse when ITO ages.

Silver does not develop an oxide layer on the boundary surface,

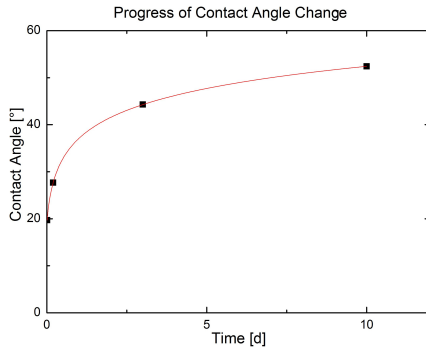


Figure 6.3.5: Contact angle change of water on untreated ITO surface aged in air

thus the adhesion is almost exclusively caused by dispersive energies. The adhesion results do not exactly correlate with the contact angle measurements. The adhesion to the pure ITO surface, which is 7 days old, is still better than the adherence to the aged surface additionally treated with photolithographic chemicals. If adhesion correlates with surface energy and contact angle, respectively, according to Figure 6.3.6, the result should be the other way around, because the contact angle of the PL treated sample is smaller than that of the non-treated sample. However, one has to take into account that a tape test is not very accurate.

Contact angle measurements and surface energy calculations with the polar and dispersive part of silver and titanium or silver and titanium oxide, respectively, (titanium develops a thin oxide layer if stored in air) also show a better analogy between ITO and titanium (TiO_2) than between freshly prepared ITO and silver, as demonstrated in Figure 6.3.7. This reassures the results of the measurements regarding the adhesion properties between ITO and the metals.

The surface energies are given with σ_s , representing the surface energy, σ_s^D the dispersive part of the surface energy and σ_s^P the polar part of the surface energy.

The polar part of the surface energy of titanium ($\sigma_s^P(\text{Ti}) = 4.63 \text{ mN/m}$)

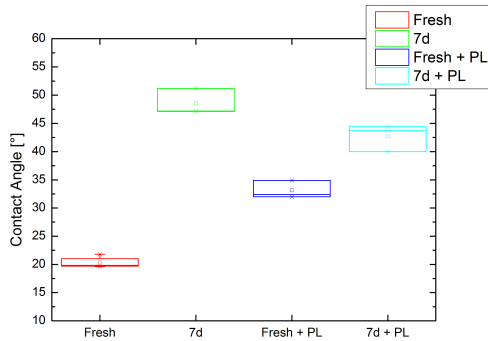


Figure 6.3.6: Contact angles of water after different surface treatment of ITO according to process flow in Figure 6.2.2

is higher than that of silver ($\sigma_s^P(\text{Ag}) = 1.61 \text{ mN/m}$), which can be explained by a thin TiO_2 layer at the surface. Therefore, titanium is able to interact with the ITO surface even by polar energies.

If the adherence were only to be influenced by interfacial tension characteristics, silver should show good adherence to ITO, which was stored in air. The dispersive and polar part of the surface energy almost match. However, the experiment shows that this is not the case.

One reason could be the overall smaller surface energy of ITO, which according to equation 2.15 also leads to a smaller value for the work of adhesion. A second reason is the contamination of the ITO surface by organic residues. Organic molecules build a barrier between the metal and the ITO surface which lowers the adhesive forces. Polar interactions reach higher values, which is why the TiPdAg stack still shows good adherence to ITO. Silver almost only interacts through dispersive forces and, thus, adherence is weakened.

More factors play an important role regarding adhesion and further research has to be done on this topic.

However, it can be concluded from the results that silver shows a better adherence to a new ITO surface than it does to an older surface. This influences ink formulation and the time of metal application.

Table 6.3.1: TLM and tape test results of evaporated Ag and TiPdAg metallization on differently treated ITO surfaces. Tape test rating: OK = no metal on tape; poor = some metal on tape; failed = complete adhesion failure

ITO treatment	$R_c W$ [Ωcm]	R_{sh} [Ω/sq]	Tape test
fresh + TiPdAg	22.945	27.988	OK
fresh + PL + TiPdAg	14.657	22.458	OK
fresh + Ag	14.342	24.279	wafer breakage
fresh + PL + Ag	13.891	10.331	OK
7d + TiPdAg	16.866	30.547	OK
7d + PL + TiPdAg	9.302	21.372	OK
7d + Ag	17.737	26.427	poor
7d + PL + Ag	9.402	21.338	failed

The TLM measurements show no significant trend regarding the contact formation quality.

It was assumed that the surface energy of ITO could also influence the contact formation between ITO and a metal. From the results shown above (Table 6.3.1) such a correlation can not be seen. All values are within the measurement error margin, especially considering the uncertainty of TLM measurements in general. One might say that a tendency for better contact formation towards aged ITO surfaces can be seen, but statistics are too small to be sure about that.

However the values for the normalized contact resistance of the 7 day old samples treated with PL stick out. Both values - and this is the case for Ag as well as for TiPdAg metallization - are lower than the values of all other samples. One has to take into account that the PL treatment also includes thermal curing steps which are known to influence the properties of ITO². In addition, the chemicals used during the PL process might also have an effect on the surface

²Due to recrystallization crystal defect curing occurs which causes a drop of the sheet resistivity

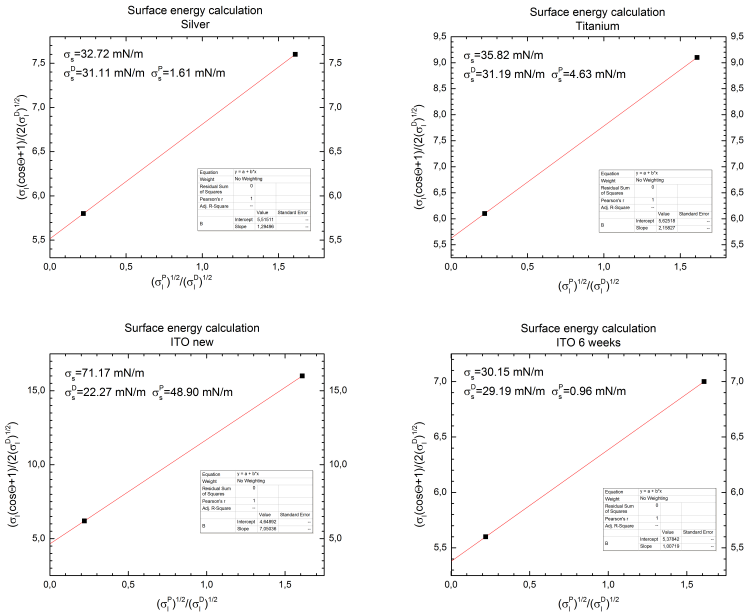


Figure 6.3.7: Surface energy calculations of silver (top, left), titanium (top, right) and ITO after deposition (bottom, left) and six weeks after preparation (bottom, right). The surface energies are given within the graphs.

of ITO, which can have electrical properties different from the bulk, as has already been discussed in Chapter 5.3.6. Further research on this topic is necessary.

6.4 Chapter Summary

In this chapter the surface behaviour of ITO towards liquids were analyzed with goniometer measurements. It was shown that ITO has a highly active surface with a very high surface energy right after deposition. This is expressed by a very hydrophilic surface and rapid decrease of the hydrophilicity within a few hours when stored in air. Non polar solvents also develop higher contact angles within a very short

time, but the effect is less pronounced compared to polar solvents like water.

To lower this energy, ITO adsorbs molecules from the environment. A UV radiation treatment cleans the surface from adsorbents by oxidating the latter and “resets” the mechanical surface properties of ITO back to hydrophilic. These results have an influence on the choice of ink formulation to be used for metallization. The results also influence the timescale of ITO storage in air after deposition.

The influence of the surface energy of ITO on adhesion and contact formation with silver and TiPdAg stack were investigated.

The adhesion of TiPdAg stacks to ITO are not influenced by the age of the ITO layer. Silver adherence becomes worse with age of ITO and th correlated drop of the surface energy. This results have also influence on the metal ink formulation and time of metal application.

The contact formation represented by the contact resistance measurements seem not to be significantly influenced by the surface energy of ITO.

7 Seed-and-Plate on ITO

In this chapter plating on metal seed-layers evaporated on a HIT cell is discussed. It is shown that selective plating on the metal seed-layer on conductive ITO is possible without further protection of the ITO layer. After a short introduction in Section 7.1, the experiments done are described in Section 7.2. Results and discussion are given in Section 7.3. Section 7.4 summarizes the chapter.

7.1 Introduction

As has already been explained in Section 3.4, contacting the ITO layer used for certain cell designs are either expensive or not yet really satisfying. At least, improvements are possible.

As shown in Chapter 5 nanoparticle inks are suitable as a contact material for ITO as they can be processed at low temperatures and show good conductivity as well as contact resistance to ITO. The seed-and-plate approach enables to separate the contact formation from the lateral conductivity and, thus, the optimization of both metal layers independently. In addition, ITO is a diffusion barrier for copper [111]. This allows the usage of copper as a metal for the lateral current transport, which reduces silver consumption significantly and, thus, production costs.

A special challenge for plating on a seed-layer applied on ITO is the high conductivity of ITO itself. Metals can be deposited not only on the metal seed-layer but also on the ITO surface. It would be possible to simply protect the ITO layer against metallization by applying a plating resist. However, this necessitates at least two additional process steps, which would raise the overall production costs.

Within this chapter electrochemical metal deposition on a metal seed-layer on ITO without protection of ITO is analyzed to evaluate a process for selective metal deposition on the seed-layer.

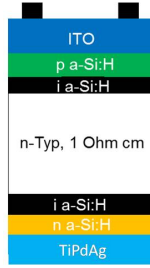


Figure 7.2.1: Illustration of the cell structure of the HIT solar cell

7.2 Experimental

7.2.1 Selective copper plating on HIT solar cells with TiPdAg seed-layer

To guarantee good contact formation to ITO and good line resistance within the seed-layer, cell samples with a thermally evaporated seed-layer of a TiPdAg stack (50 nm/50 nm/100 nm) were used.

Substrate

As substrate planar n-type mono crystalline FZ silicon wafers with a sheet resistance of 0.8-1.2 Ωcm were used.

For sputtering an OXFORD cluster tool with argon plasma was used.

The ITO chamber was equipped with an $\text{In}_2\text{O}_3/\text{SnO}_2$ (90/10 wt%) target. Gases such as oxygen and argon could be fed separately. ITO coating thickness was 70 nm. An oxygen flow of 0.7 sccm was used.

Amorphous silicon was sputtered with silane and hydrogen gas. For p-type doped a-Si, B_2H_6 gas was added and for n-type doped a-Si, PH_3 gas was added.

For the emitter 15 nm a-Si(i) and 17 nm a-Si(p) layers were applied. The BSF consisted of 7 nm a-Si(i) and 15 nm a-Si(n).

The metal front grid consisted of a TiPdAg stack (50 nm/50 nm/100 nm) and the back contact of TiPdAg (50 nm/50 nm/1000 nm).

The cell structure is illustrated in Figure 7.2.1.

Seven cells 2x2 cm in size were arranged on one wafer. The cells were cut out with a dicing saw before plating.

Plating

The cells were contacted at the back-side for Cu-plating onto the seed-layers. To avoid Cu deposition on the open cell edges and the back side, edges and back were protected with a plating resist. The contacted part of the back was left open and was not dipped into the electrolyte.

A current of 1, 5 and 10 mA was applied, respectively, and the resulting voltage was measured to control deposition. Plating time was 30 min.

Ozone cleaning of ITO surface

A UV excimer was used for the cleaning process of ITO.

Samples were placed under the UV excimer at a distance of 1 cm. Radiation time was one minute.

7.2.2 Cyclovoltammetric measurements on ITO

Substrate

Two groups of ITO samples were measured. The substrate structure was the same as described in Section 6.2. The samples of group 1 were stored in air for several days; samples of group 2 were ozone cleaned with UV radiation for 1 min (see description above).

Cyclovoltammetric measurement

The reduction potential of copper on ITO surfaces was determined by cyclovoltammetric (CV) measurements using a VSP multipotentiostat (biologic). The measurement apparatus was assembled in a metal case acting as a Faraday cage to eliminate disturbing electrical signals from the environment.

A commercially available copper electrolyte was used. As anode, a copper electrode was used. The ITO area measured was defined by size and kept constant for all measurements. A potential scan rate of $dE/dt = 20 \text{ mVs}^{-1}$ was applied within the potential limits of $E = -1 \dots 1.5 \text{ V}$ between the anode and ITO. The measurement was started, reaching to negative potentials.

Characterization

Characterization was done optically and with SEM imaging and EDX analysis.

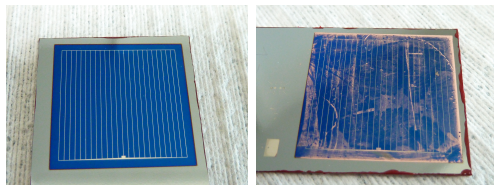


Figure 7.3.1: Cell before plating with copper (left) and after plating at 1 mA for 30 min (right)

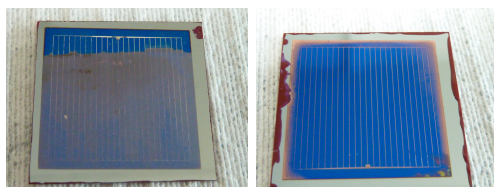


Figure 7.3.2: Left: Cell after copper plating with 10 mA applied current (upper part not dipped into electrolyte). Right: HIT cell with copper metallization on seed-layer after UV-ozone cleaning for 1 min (plating with 1 mA applied current for 30 min)

7.3 Results and discussion

7.3.1 Plating results

Figure 7.3.1 shows a test cell before plating and a copper plated cell without cleaning with ozone before. Plating was done with an applied current of 1 mA.

The blue area of the cell is coated with ITO and forms the active cell area. The white-silver stripes form the evaporated seed-layer metal grid.

The photograph 7.3.1 shows, that copper was not only deposited on the metal seed-layer but also on the open ITO surface. With increasing applied current, the amount of copper deposited on ITO even increases as illustrated in Figure 7.3.2. The shown cell was plated at 10 mA. A thin copper film is deposited over the whole area of the solar cell.

However, as visible in Figure 7.3.1, at lower application current,

the copper is not equally deposited over the whole surface but seems to follow a pattern resulting from inhomogeneities maybe caused by scratches or impurities (e.g. dust, organic deposits) on the ITO surface. The impurities acting as seed crystals could have caused an electrical surge at those areas and, thus, lead to copper plating on ITO. The cell edge which represents a position of high field density is also predominantly plated.

Therefore, it was assumed that a cleaning step prior to plating could solve the problem if the impurities were in fact caused by organic deposits. The standard cleaning process for silicon solar cells involves an HCl dip, which removes most of the impurities from the surface. However, ITO is not stable against acids, thus, this process could not be used. Instead, the organics were burned off by ozone generated under an UV excimer. It was shown in Chapter 6.3.1 that cleaned ITO surfaces, aged in air and with a hydrophobic surface could be “reset” to a hydrophilic surface behavior. The contact angle for those surfaces was too small to be measured.

In a second experiment the cells were ozone cleaned for one minute via UV radiation prior to plating. Time between cleaning and plating was less than 1 hour.

A photograph of a cleaned cell after copper plating with an applied current of 1 mA is shown in Figure 7.3.2 on the right-hand side. The photograph shows that copper was almost exclusively deposited on the metal seed-layer. Only the edges of the cell are also covered with copper.

Figure 7.3.3 shows an SEM image of copper deposited on the metal seed-layer at the edge of a finger ending in the busbar.

The SEM characterization shows that there are also small areas on the seed-layer which were not fully covered with copper and that the ITO surface is almost completely free of copper seeds.

As UV-ozone cleaning is able to remove organic impurities from the surface, it is unlikely that the surface was totally free of inorganic impurities. Therefore, it is likely that an additional reason for the selective plating of the metal seed-layer on ITO exists.

The value for the electron work function of copper lies between $\varepsilon_M = 4.48\text{-}5.1$ eV [143]. The work function of the electrolyte is even higher. ITO is a semiconductor and its work function varies with its doping level. On average, the work function can be estimated to be around $\varepsilon_{SE} = 3.5$ eV but never higher than $\varepsilon_{SE} = 4$ eV [139].

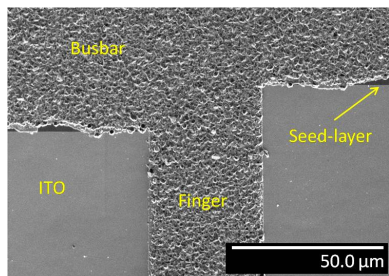


Figure 7.3.3: SEM image of copper plated finger and busbar on HIT cell with seed-layer metallization after cleaning

The work function of the semiconductor is lower than that of the metal species in the electrolyte. Thus, one could say that a kind of Schottky contact is formed between the ITO surface and the electrolyte. Electrons diffuse from the semiconductor (ITO) into the metal (copper electrolyte) until the Fermi levels equalize. Without further application of an external voltage, no further electron diffusion can occur and, thus, no copper can be reduced at the ITO surface.

Silver has a work function of $\varepsilon_M = 4.05 - 4.6$ eV and is much closer to the work function of copper. Thus, by applying an external negative voltage to ITO and the seed-layer, copper deposition should first occur at the silver surface.

This theory is supported by the fact that copper deposition is observable on the cell edges in Figure 7.3.2. Figure 7.3.4 shows the cell edge before plating and SEM images of the edge and areas close to the edge after plating with copper.

One can see that the edge of the active cell area differs from the rest of the active area. EDX measurements in different areas of the edge or close to the edge show differences in ITO composition.

At the outer part of the edge of the active cell area, a high copper deposition can be seen and measured. The EDX measurement of the ITO shows tin and indium but no measurable concentration of oxygen. Considering the dependence of the ITO conductivity on the oxygen concentration, the area at the outer side of the active cell area is more conductive than the inner part of the active cell area. Thus, copper is easily deposited (Figure 7.3.4 bottom left).

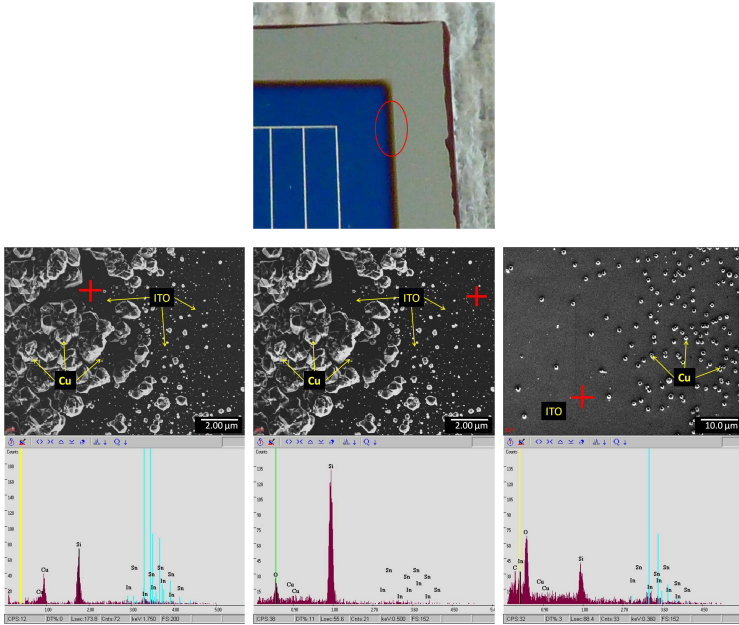


Figure 7.3.4: Top: Photograph of HIT cell edge before plating. The SEM/EDX measured area (results shown in bottom row) is marked with a red cross.

Bottom row: EDX measurements on HIT cell, after ozone cleaning and electroplated copper deposition (Figure ??). EDX measured area is marked with a red cross. Left: Outer part of the cell edge. Middle: Inner part of the cell edge. Right: Distance from cell edge $\sim 50.0 \mu\text{m}$.

Measurements on ITO moving from the edge to the center of the cell show a rising concentration of oxygen and, thus, decreasing conductivity of ITO. Less copper is plated on ITO (Figure 7.3.4 bottom middle and right).

According to Gassenbauer, the work function of the ITO surface should increase when oxidized, e.g., with oxygen plasma treatment or UV-ozone radiation [138–140]. Oxygen diffuses into the surface layers of ITO and saturates the Sn^{4+} species, thus lowering the Fermi

level and increasing the work function. Supposedly, the Schottky barrier should decrease on the samples surfaces which were treated under the UV excimer and copper deposition on ITO should be even easier, which seems, however, to be in contradiction to the experimental observations. In fact, just the opposite can be observed.

However, edges, corners, tips, impurities, and so on are regions of high field density and, thus, areas of high potential drop. Metal deposition can occur.

As was shown by the experiments, the voltage value, which leads to selective deposition of metal on the seed-layer, lies within narrow limits and is dependent on the whole electrochemical system (surface of ITO, electrolyte, additives, counter electrode, etc.).

A possible explanation for the observations could be that the plating process was done within a potential range close to the reduction potential of the plating system which caused impurity effects on the ITO surface to overcompensate the effect of work function differences. However, the deposition on a metal seed-layer on ITO is complex and needs further analysis.

7.3.2 CV measurement results

To evaluate the potential window which would allow for selective metal plating on the metallic seed-layer, cyclic voltametric measurements were carried out with the used copper electrolyte on UV cleaned ITO samples and samples stored in air for several days. The experiment should also show whether a significant difference regarding the electrochemical process occurs depending on UV cleaning. The measurements are shown in Figure 7.3.5.

Both diagrams differ a lot from each other. Especially the behavior on the cathode (ITO) where the reduction of Cu^{2+} to copper takes place differs a lot between the two ITO surfaces. Unfortunately, the reduction peak of copper can not be identified. Only the drop in current (in absolute values) indicates the process of reduction.

For the untreated ITO electrode, the reduction process does not change for several measurement cycles. It starts very early at around $U = -0.05$ V. No peak or reduction potential limits can be identified. The oxidation of copper in the positive potential region (starting at around $U = 0.1$ V and showing a peak at $U = 0.8$ V) does not change significantly after the first two cycles either.

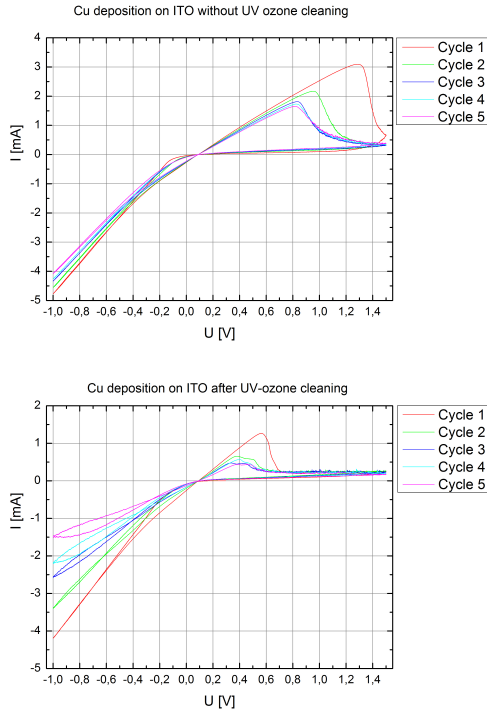


Figure 7.3.5: Cyclic voltammometric measurement diagrams: Copper deposition on ITO without UV cleaning (top) and after cleaning (bottom)

The reduction process of copper on the cleaned (and also oxidized) ITO surface begins as well around the same potential of $U = -0.05$ V. However, each cycle differs from the previous cycle: the slope of the current drop decreases. While the first cycle is quite similar to the measurement progress of the untreated ITO, the slope decreases with every additional measurement cycle. In addition, a *nucleation loop* can be observed starting from cycle number 2. A nucleation loop indicates a kinetic hindrance of nucleation at the surface of the electrode. The potential applied to the electrode is not high enough for ions to pass

the *Helmholtz-layer*¹. Only a few ions are able to pass and nucleate at the surface. Little by little more ions nucleate at the surface and a second ionic layer is formed which is then more easily passed by further ions. The integral of the loop is proportional to the required activation energy which is necessary for the ions to overcome the Helmholtz layer [144]. The increasing loop integral and the decreasing reduction current imply an increasing hindrance for the nucleation of copper at the ITO surface.

The oxidation of copper in the positive potential region (starting at around $U = 0.1$ V and showing a peak of $U = 0.4-0.55$ V) does also show a small drop with each cycle. In addition, compared to the aged ITO samples, the measured flowing oxidation current is less. Thus, copper oxidation seems easier compared to the oxidation process on an aged ITO surface. This implies that the deposition on the cleaned ITO surface is more difficult than on the non-treated ITO.

The observation of both samples after the CV measurement showed that no copper was applied to the UV cleaned sample, whereas the uncleaned sample was covered with copper. Whether the oxidation of the ITO and the correlated potential change in work function is the main reason for the behavior of the ITO surface towards the electrolyte or if potential impurities at the surface played the more important role could not be identified by these experiments. A lot more precise manipulation of the ITO surface would be necessary to get to the bottom of this question.

The CV measurements show no peak for the copper reduction and are difficult to interpret. In addition, no simple CuSO_4 solution was used, rather, an industrially available electrolyte which contains several additives for better plating qualities. The additives also influence the redox reactions which further exacerbates analysis. Variation of the potential scan rate gave no more relevant results.

Further analysis of the plating process on ITO surfaces has to be done in order to understand the undergoing processes more clearly

¹The Helmholtz-layer is an ionic double layer at the surface of an electrode: The surface of the electrode is charged and the ionic species with opposite charge will be concentrated close to the surface. A second ionic layer of the same charge as the electrode is formed next to the first. Ions which should be oxidized or reduced at the surface of the electrode have first to pass this double ionic layer, respectively. An illustration of the Helmholtz-layer can be found in the appendix B.1.2.

and help to evaluate the exact plating conditions for a fast and reliable plating process for selective deposition of the conductive metal on the seed-layer metallization on unprotected ITO.

7.4 Summary

In this chapter it was shown that selective electrochemical deposition of copper on metal seed-layers on ITO is possible, without further protection of the ITO surface.

The deposition has to be done on a cleaned ITO surface. The selective plating is possible within narrow applied current ranges.

The process was analyzed with SEM, EDX and CV measurements. The reasons for the selective metal deposition on ITO within these electrical limits were discussed. The composition of ITO and, thus, its properties is important for a successful process.

With further analysis, proper process parameters could be evaluated, making the selective plating on metal seed-layers on ITO a reliable metallization alternative to metal evaporation and silver rich polymer pastes. This would allow for the use of copper as a conductive metal layer without any further diffusion barrier, thereby lowering the production costs for new and alternative cell concepts.

8 MOD Ink Metallization of Silicon Solar Cells

The results of this chapter have been partially compiled within the Master's thesis of Yaara Tamari [145].

In this chapter the functionality of a particle- and lead-free metal-organic decomposition (MOD) ink used for contacting SiN_x coated crystalline silicon solar cells is described and analyzed. After a short introduction in Section 8.1 the experiments underlying this chapter are depicted (Section 8.2). The requirements for a stable ink composition based on the neodecanoates of silver, bismuth and zinc are described in Section 8.3.1. Different printing techniques, formulation of an MOD paste and the plating process on an MOD seed-layer are characterized in Sections 8.3.3 to 8.3.5. It will be shown that contact formation to the emitter is possible < 500 °C along with very short tempering times (Section 8.3.2). Based on the experimental results, an advanced contact formation model was developed and is described in detail in Section 8.3.6. The contact formation was analyzed in detail with FIB, SEM and EDX measurements and results are discussed in Section 8.3.7. Electrical results of the MOD ink applied on a crystalline silicon solar cell and solar cell results are given in Section 8.3.8. The behavior of the MOD ink as metallization ink are compared to that of a seed-layer metallization formed by a thick film screen printing paste in Section 8.3.9. Finally, Section 8.4 gives a short summary of the chapter.

8.1 Introduction

In order to be competitive, electricity production from solar cells has to be cheaper and/or more eco-friendly compared to conventional power plants. To achieve this goal, the efficiency of solar cells needs to rise and/or the production costs have to be reduced. One costly pro-

duction step in solar cell production is metallization. The high silver consumption and processing temperatures lead to high costs. In addition, the present conventional metallization pastes contain lead, which is toxic and might be forbidden by RoHS in the near future. Metal pastes are being processed at high temperatures of around 900 °C and form the contact to the emitter as well as the conducting metal grid needed to extract the current from the cell. The formulation of a metal paste is, therefore, always a compromise between contact formation and conductivity, which can lead to efficiency losses.

This chapter deals with so called MOD (*metal organic decomposition*) inks, which contain metal organics that can be reduced to the metal at low temperatures and which are able to contact the silicon solar cell through the passivation layer formed by SiN_x . MOD inks are particle-free and the particular ink discussed here does not contain lead. The ink can be printed with contactless printing processes such as ink jet printing or aerosol jet printing instead of using the common screen printing process. This gives more freedom in choice of printing technique and substrate. In addition, ink jet and aerosol jet printing are low cost printing techniques, capable of achieving very narrow line widths of 10 μm (aerosol jet [19]) and < 35 μm (ink jet [20]), respectively.

The metal organics can be converted into pure metal either by decomposition or by reducing reactions. These processes can be carried out in the gas phase (*metal organic chemical vapor deposition*, MOCVD) or by wet chemical processing or even through solid state reactions. The decomposition or reducing reaction can be performed at elevated temperatures or even at room temperature.

Silver is the element with the highest conductivity and a high oxidation resistance. Therefore, many approaches have been made to develop a low temperature curable silver coating process. Several base materials have been studied to be used as the metal source: AgNO_3 [82, 146], silver citrate [147], silver neodecanoate [81, 148], among others [16]. Thermal and especially photochemical stability is a challenge for silver salt based inks, as most of the silver salts are very easily reduced, which is also the reason why those compounds can achieve high conductivities under moderate processing conditions such as mild reducing agents or elevated decomposition temperatures. Many silver salts can be decomposed at temperatures between 150 - 250 °C [40]. Without further stabilizers higher silver metal loading

can be achieved with metal organic based inks in comparison to water based ink formulations. In addition, as achievement of a smooth and clean metallization so to be aspired, foreign components should be easy to remove. Organic rests often decompose to volatile compounds, which leave the metallization layer during decomposition very easily.

Today's MOD silver inks are developed for the low temperature metallization of temperature sensitive substrates. The main goal is to achieve the highest conductivity at low temperatures.

Teng has demonstrated resistivities of $\rho = 108 \cdot 10^{-8} \Omega\text{m}$ after curing the metallized samples at $T = 150 \text{ }^\circ\text{C}$ for 15 min, which dropped even as low as $\rho = 17.8 \cdot 10^{-8} \Omega\text{m}$ after curing for longer than 60 min. Resistivity has been further decreased by curing at higher temperatures ($T = 230 \text{ }^\circ\text{C}$) and by curing for 50 min, reaching $\rho = 3.1 \cdot 10^{-8} \Omega\text{m}$ [148], which is already close to the bulk resistivity of silver ($\rho_{\text{Ag bulk}} = 1.58 \cdot 10^{-8} \Omega\text{m}$). Other metals such as Al, Cu and Au have also been used in MOD ink formulations [16][149].

The MOD ink is designed to contact the silicon solar cells through the passivation layer SiN_x at low temperatures. To complete the metallization on the solar cell, the seed-and-plate approach is used in this work. The conductive layer is formed by an additional plating step. This allows independent optimization of contact formation to the emitter and of the conductivity.

8.2 Experimental

Specifications of chemicals:

Silver nitrate: ABCR, 99.9% ACS

Neodecanoic acid: ABCR, prime grade

Zinc neodecanoate: ABCR, Zn 17.9-18.2%

Bismuth neodecanoate: Sigma-Aldrich

Xylene: Sigma-Aldrich, Xylenes, reagent grade

N-Methyl-2-pyrrolidone: Sigma-Aldrich, ACS reagent, >99%

Acetone: Applichem, ACS ISO

Ethanol: Rectapur, 90%, denatured with methanole GPR

Table 8.2.1: Xylene/NMP mixtures for solvent evaluation

wt% NMP	wt% Xylene
30	70
40	60
50	50
60	40
70	30
80	20
90	10
100	0

8.2.1 Ink formulation

Solvent mixture

Different solvent formulations of N-methyl-2-pyrrolidone (NMP) and Xylene were mixed and homogenized according to Table 8.2.1.

The evaporation time of the mixtures were measured with a goniometer. The drops were placed on a microscope slide and measurements were done in sessile drop mode. The solvent drop was left to evaporate at room temperature. Pictures of the drop were taken with a frame rate of 13 pictures/s. The volume of the drops was determined with the goniometer software. The drop volume was plotted against the drop age. The plots were linearly fitted according to equation 8.1.

$$V_D = v_{ER} * t_D + V(t_D = 0) \quad (8.1)$$

with V_D representing the drop volume, v_{ER} the evaporation rate and t_D the drop age.

The slope of the linear fit yields the evaporation rate.

Synthesis of silver neodecanoate

9.347 ml (50 mmol) neodecanoic acid were slowly added to 50 ml of a 1 M ammonia solution and left to mix for 1 h. 8.49 g (50 mmol) silver nitrate were dissolved in 10 ml deionized water and added slowly to the stirring solution. The suspension was stirred for 20 min to complete the reaction and a glue-like white substance of silver neodecanoate was

formed. The suspension was then decanted and washed with deionized water three times. The substance was filtrated over a vacuum pump, washed with ethanol three times and with a small amount of acetone to form a colorless solid. The solid was tried until it came apart as a fine powder, thus indicating high aridity.

Ink stability

The ink stability was analyzed in dependence of the overall metal concentration by formulating different ink solutions with varying metal concentration. The metal organyls were dissolved in a mixture of NMP:Xylene = 2:1. The solutions were partially stored in darkness at room temperature for several days. Color changes and residues implied formation of silver nanoparticles. (Metal contents in % are referred to *as metal mass*.)

1. Two component solution series silver/zinc: Variation of overall metal content
Metal organic contents (referred to as 100% metal mass): 96% silver neodecanoate, 4% zinc neodecanoate
Overall metal neodecanoate content: 14 wt%, 17 wt%, 20 wt%
Storing time: <1h
2. Two component solution series silver/bismuth: Variation of overall metal content
Metal organic content (referred to as 100% metal mass): 96% silver neodecanoate, 4% bismuth neodecanoate
Overall metal neodecanoate content: 14 wt%, 17 wt%, 20 wt%
Storing time: <1h
3. Two component solution series: Variation of bismuth content
Metal organic content (referred to as 100% metal mass): 1%, 2%, 4% bismuth neodecanoate, 99%, 98%, 96% silver neodecanoate
Overall metal neodecanoate content: 10 wt%
Storing time: <1h
4. Three component solution series: Variation of zinc content
Metal organic content (referred to as 100% metal mass): 1% bismuth neodecanoate, 3%, 4%, 5%, 6%, 7% zinc neodecanoate,

rest: silver neodecanoate

Overall metal neodecanoate content: 10 wt%, 11 wt%, 12 wt%, 13 wt%, 14 wt%, 15 wt%, 16 wt%

Storing time: <1h

5. Three component solution series: Variation of overall metal content

Metal organic contents (referred to as 100% metal mass): 93% silver neodecanoate, 6% zinc neodecanoate, 1% bismuth neodecanoate

Overall *metal neodecanoate* content: 10 wt%, 12 wt%, 14 wt%, 16 wt%, 18 wt%, 20 wt%

Storing time: 20 d.

6. Three component solution series: Variation of overall metal content

Metal organic contents (referred to as 100% metal mass): 94% silver neodecanoate, 5% zinc neodecanoate, 1% bismuth neodecanoate

Overall *metal* content: 18 wt%, 22 wt%, 26 wt%, 30 wt%, 35 wt%, 40 wt%

Storing time: 4 d.

Etching component

The amount of bismuth which is necessary to penetrate the silicon nitride layer, was determined by fully processing different inks with varying bismuth neodecanoate contents.

The inks investigated were formulated according to the following recipes. (Metal contents in % are referred to as *metal mass*.)

1. Ink 1:

Solvent: NMP:Xylene = 2:1

Overall *metal* content = 26 wt%

Zinc neodecanoate: 5%

Silver neodecanoate: 94%

Bismuth neodecanoate: 1%

2. Ink 2:

Solvent: NMP:Xylene = 2:1

Overall *metal* content = 26 wt%
Zinc neodecanoate: 5%
Silver neodecanoate: 93%
Bismuth neodecanoate: 2%

3. Ink 3:

Solvent: NMP:Xylene = 2:1
Overall *metal* content = 26 wt%
Zinc neodecanoate: 5%
Silver neodecanoate: 92%
Bismuth neodecanoate: 3%

4. Ink 4:

Solvent: NMP:Xylene = 2:1
Overall *metal* content = 26 wt%
Zinc neodecanoate: 5%
Silver neodecanoate: 90%
Bismuth neodecanoate: 5%

Inks were dropped on SiN_x (PECVD, thickness: 70-75 nm) coated wafers with alkaline etched random pyramid texture and sintered at 480 °C for 15 min on a hot plate after drying for 5 min at 100 °C.

Etching

To evaluate the quality of the SiN_x etch, the silver and glass layers were etched off.

Silver etch:

The samples are placed in half concentrated (~ 32, 5%) HNO₃ until no silver is visible to the naked eye anymore (<1 min). The samples are cleaned with deionized water.

Glass etch:

After removal of silver the glass layer is etched in 1% HF. The etching time is adapted to the layer thickness of the samples and etching is finished when no glass is visible to the naked eye anymore (<1 min). The samples are cleaned in deionized water and dried in the air stream.

Characterization

The samples were characterized via SEM measurement. Cross sections were prepared with an ion beam miller.

Final ink formulation

This formulation was based on 100 g ink with a total metal content of 26 wt%. The metal fractions were 91 % silver, 6 % zinc and 3 % bismuth, respectively. Metal contents in % were referred to as *metal mass*.

9.73 g (24 mmol) of zinc neodecanoate and 2.69 g (3.7 mmol) of bismuth neodecanoate were dissolved in 17.6 g (1.78 mmol) of N-methyl-2-pyrrolidone and 8.8 g (83 mmol) of Xylene. To the stirring solution 61.18 g (219 mmol) of silver neodecanoate were added and stirring continued until the solution became clear.

The whole procedure was performed under avoidance of light exposure and the final ink was stored in the dark.

8.2.2 Tempering process

TG-DSC characterization was done using an STA 449 F3-Jupiter TG-DSC measurement tool by NETZSCH. Aluminum crucibles with open lid were used. Heating rate was 5 °C/min. Temperature and calorimetric corrections specific to each TG-DSC setup were used. The measurement chamber was flooded with compressed air with a gas flow rate of 50 ml/min. The balance was protected by a nitrogen gas flow of 20 ml/min. Weight determination was done just before the measurement.

Silicon nitride penetration

For evaluation of the proper tempering temperature and time to successfully penetrate the silicon nitride layer, the MOD ink was tempered on SiN_x coated wafers (PECVD, 70-75 nm, alkaline etched random pyramid texture).

The ink was applied to the substrates and dried at 100 °C on a hot plate.

Tempering was done on a hot plate at 300 °C, 350 °C, 400 °C, 450 °C, 500 °C, 550 °C and 600 °C for 5 min.

Etching

To evaluate the quality of the SiN_x etch, the silver and glass layers were etched off.

Silver etch:

The samples are placed in half concentrated ($\sim 32, 5\%$) HNO_3 until no silver is visible to the naked eye anymore (<1 min). The samples are cleaned with deionized water.

Glass etch:

After removal of silver the glass layer is etched in 1 % HF. The etching time is adapted to the layer thickness of the samples and etching is finished when no glass is visible to the naked eye anymore (<1 min). The samples are cleaned in deionized water and dried in the air stream.

Characterization

The samples were characterized via SEM measurement. Cross sections were prepared with an ion beam miller.

8.2.3 Aerosol jet printing

Substrate

Mono-crystalline silicon wafers with alkaline etched random pyramid texture with a 70-75 nm thick PECVD SiN_x anti-reflection coating and a phosphorous diffused emitter with a sheet resistance of $60 \Omega/\text{sq}$ were used. The back contact was formed by screen printed aluminum paste fired prior to front side metallization at 900°C peak temperature. The $156.0 \times 156.0 \text{ cm}^2$ wafers were cut with a dicing saw into $5.2 \times 5.2 \text{ cm}^2$ pieces.

Ink

This formulation was based on 100 g of ink with a total metal content of 26 wt%. The metal fractions were 91 % silver, 6 % zinc and 3 % bismuth, respectively. Metal contents in % were referred to as *metal mass*.

9.73 g (24 mmol) of zinc neodecanoate and 2.69 g (3.7 mmol) of bismuth neodecanoate were dissolved in 17.6 g (1.78 mmol) of N-methyl-2-pyrrolidone and 8.8 g (83 mmol) of Xylene. To the stirring solution 61.18 g (219 mmol) of silver neodecanoate was added and stirring continued until the solution became clear.

The whole procedure was performed under avoidance of light exposure and the final ink was stored in the dark.

Printing

Aerosol jet printing was done with an M3D system from OPTOMECH INC. Gas flow had always been adjusted to the ink with each printing process. The chuck was heated to 120 °C and a print head with 8 nozzles and a 150 µm nozzle size was used. The number of printing layers is also dependent on the gas flow settings and ink behavior. Within a batch the number of layers was chosen in such a way that a closed metallization finger could be observed with the confocal microscope.

Tempering

The samples were dried at 100 °C on a hot plate. Tempering was done on a hot plate at 480 °C for 15 min.

Characterization

Characterization was done by confocal microscope imaging.

8.2.4 Screen printing**Substrate**

Mono-crystalline silicon wafers with alkaline etched random pyramid texture with a 70-75 nm thick PECVD SiN_x anti-reflection coating and a phosphorous diffused emitter with a sheet resistance of 60 Ω/sq were used. The back contact was formed by screen printed aluminum paste fired prior to front side metallization at 900 °C peak temperature. The 156.0 x 156.0 cm² wafers were cut with a dicing saw into 5.2 x 5.2 cm² pieces.

Paste

This formulation was based on 100 g of paste with a total metal content of 26 wt%. The metal fractions were 91 % silver, 6 % zinc and 3 % bismuth, respectively. Metal contents in % were referred to as *metal mass*.

2 g of ethyl cellulose (300 cP) were dissolved in 17.6 g (1.78 mmol) of N-methyl-2-pyrrolidone and 8.8 g (83 mmol) of Xylene. 9.73 g (24 mmol) of zinc neodecanoate and 2.69 g (3.7 mmol) bismuth neodecanoate were added. To the stirring dispersion 61.18 g (219 mmol) of silver neodecanoate were added and left stirring until the solution became clear.

The whole procedure was performed under avoidance of light exposure and the final ink was stored in the dark.

Printing

Screen printing was done with a half-automated screen printer EKRA STS E5. The screen openings of fingers were 100 μm , finger spacing $d = 2$ mm, mesh/inch = 280 in^{-1} , thread size 0.032 mm. The grid dimension was 5.0 x 5.0 cm^2 with one busbar in the middle and 26 fingers perpendicular to the busbars.

Tempering

The samples were dried at 100 $^{\circ}\text{C}$ on a hot plate. Tempering was done on a hot plate at 480 $^{\circ}\text{C}$ for 15 min.

Characterization

Characterization was done by confocal microscope imaging.

8.2.5 Plating

Substrate

As substrates, tempered samples from aerosol jet printing and screen printing were used.

Plating

Light induced plating was carried out. A setup such as the one shown in Figure 3.3.1 was used. Plating was done by applying 0.35 V to the back contact of the solar cell. An illumination intensity of 0.5 W was set. Plating duration was 5 min and 3 min, respectively. Commercially available silver and copper electrolytes were used, respectively. After plating samples were cleaned with deionized water and dried in an air stream.

Characterization

Characterization was done using a confocal microscope and SEM imaging. Cross sections were prepared with an ion beam miller.

8.2.6 Contact formation model

Substrate

Mono-crystalline silicon wafers with alkaline etched random pyramid texture with a 70-75 nm thick PECVD SiN_x anti-reflection coating and a phosphorous diffused emitter with a sheet resistance of 60 Ω/sq were used.

MOD ink

This formulation was based on 100 g of ink with a total metal content of 26 wt%. The metal fractions were 91 % silver, 6 % zinc and 3 % bismuth, respectively. Metal contents in % were referred to as *metal mass*.

9.73 g (24 mmol) of zinc neodecanoate and 2.69 g (3.7 mmol) of bismuth neodecanoate were dissolved in 17.6 g (1.78 mmol) of N-methyl-2-pyrrolidone and 8.8 g (83 mmol) of Xylene. To the stirring solution 61.18 g (219 mmol) of silver neodecanoate were added and stirring continued until the solution became clear.

The whole procedure was done under avoidance of light exposure and the final ink was stored in the dark.

Bismuth neodecanoate solutions

Bismuth neodecanoate was soluted in a mixture of NMP:Xylene = 1:1. Solution with bismuth neodecanoate concentrations of 10 - 100 % (steps of 10 %) were applied dropwise to wafer substrates, dried at 100 °C and tempered at different temperatures between 350 °C -550 °C (steps of 50 °C, additionally 480 °C) on a hot plate for 15 min. The layers were etched off and the results analyzed by SEM imaging.

Bismuth-/silver neodecanoate ink

(Two component ink)

To evaluate the role of bismuth and silver in the contact formation process, several solutions with different bismuth to silver ratios were applied dropwise to wafer substrates. The samples were divided in two groups. Group 1 was tempered at 480 °C for 15 min. Group 2 was tempered at 520 °C for 15 min. After drying (at 100 °C) and tempering the metal and glass layer were etched back and the results analyzed by SEM imaging.

The two component inks were formulated according to the following procedure and Table 8.2.2.

The formulations were based on 1 g of ink with a total metal organic content of 20 wt%. As solvent a mixture of NMP:Xylene = 1:1 was used.

First bismuth neodecanoate was dissolved in the solvent. Afterwards, silver neodecanoate was added. The solution was stirred until it became clear.

The whole procedure was done under avoidance of light exposure

Table 8.2.2: Bismuth to silver neodecanoate proportions (neo = neodecanoate)

Bi-neo/Ag-neo [wt%/wt%]	Bi/Ag [mol/mol]	m(Bi-neo) [mg]	m(Ag-neo) [mg]
1:9	1:23	20	180
1:4	1:11	40	160
1:2	1:5	70	130
1:1	1:2.6	100	100
2:1	1:1.4	130	70
4:1	1.6:1	160	40
9:1	3.5:1	180	20

and the final ink was stored in the dark.

Tempering

The MOD ink samples were dried at 100 °C on a hot plate. Tempering was done on a hot plate at 480 °C for 15 min.

Etching

To evaluate the quality of the SiN_x etch, the silver and glass layers were etched back.

Silver etch:

The samples are placed in half concentrated (~ 32, 5%) HNO₃ until no silver is visible anymore (<1 min). The samples are cleaned with deionized water.

Glass etch:

After removal of silver the glass layer is etched in 1 % HF. The etching time is adapted to the layer thickness of the samples and etching is finished when no glass is visible anymore (<1 min). The samples are cleaned in deionized water and dried in the air stream.

SiN_x etching

To evaluate the etching ability of the MOD ink in dependence of the silicon nitride thickness, the silicon nitride layer of wafer substrates with an initial silicon nitride layer of 70-75 nm thickness was etched according to the following procedure.

The wafers were etched in a solution of buffered hydro fluoride acid with 5-7 % HF and 10-25 % ammonium fluoride (commercial etch

solution).

The wafers were initially etched for 30 min until the silicon nitride surface became hydrophobic. Further etching removed the silicon nitride. Etching times and resulting (estimated from etching time) silicon nitride thicknesses are given in Table 8.2.3.

Characterization

Characterization was done by SEM imaging in combination with FIB tomography and EDX analysis. FIB slices had a thickness of 10 nm. Cross sections were prepared with an ion beam miller.

Table 8.2.3: Etching times for silicon nitride etching

Time [s]	Resulting SiN _x thickness [nm]
257	60
514	50
772	40
1028	30
1285	20

8.2.7 Contact quality

Substrate

Mono-crystalline silicon wafers with alkaline etched random pyramid texture with a 70-75 nm thick PECVD SiN_x anti-reflection coating and a phosphorous diffused emitter with a sheet resistance of 60 Ω/sq were used.

MOD ink

This formulation is based on 100 g of ink with a total metal content of 26 wt%. The metal fractions are 91 % silver, 6 % zinc and 3 % bismuth, respectively. Metal contents in % are referred to as *metal mass*.

9.73 g (24 mmol) of zinc neodecanoate and 2.69 g (3.7 mmol) of bismuth neodecanoate were dissolved in 17.6 g (1.78 mmol) of N-methyl-2-pyrrolidone and 8.8 g (83 mmol) Xylene. To the stirring solution 61.18 g (219 mmol) of silver neodecanoate were added and stirring continued until the solution became clear. The whole procedure was performed under avoidance of light exposure and the final ink was stored in the dark.

Tempering

The MOD ink samples were dried at 100 °C on a hot plate. Tempering was done on a hot plate at 480 °C for 15 min.

Etching

To evaluate the quality of the SiN_x etch, the silver and glass layers were etched back.

Silver etch:

The samples are placed in half concentrated (~ 32,5%) HNO₃ until no silver is visible anymore (<1 min). The samples get cleaned with deionized water.

Glass etch:

After removal of silver the glass layer is etched in 1 % HF. The etching time is adapted to the layer thickness of the samples and etching is finished when no glass is visible anymore (<1 min). The samples get cleaned in deionized water and dried in the air stream.

Characterization

Characterization was done by SEM imaging in combination with FIB tomography and EDX analysis. For FIB tomography each FIB milling step had a of 10 nm. SEM images were taken after each milling step. Cross sections were additionally prepared with an ion beam miller.

8.2.8 Conductivity, contact resistance and cell results

Screen printing samples as described in Section 8.3.4 were used.

Substrate

Mono-crystalline silicon wafers with alkaline etched random pyramid texture with a 70-75 nm thick PECVD SiN_x anti-reflection coating and a phosphorous diffused emitter with a sheet resistance of 60 Ω/sq were used. The back contact was formed by screen printed aluminum paste fired prior to front side metallization at 900 °C peak temperature. The 156.0 x 156.0 cm^2 wafers were cut with a dicing saw into 5.2 x 5.2 cm^2 pieces.

Paste

This formulation was based on 100 g of paste with a total metal content of 26 wt%. The metal fractions were 91 % silver, 6 % zinc and 3 % bismuth, respectively. Metal contents in % were referred to as *metal mass*.

2 g of ethyl cellulose (300 cP) were dissolved in 17.6 g (1.78 mmol) of N-methyl-2-pyrrolidon and 8.8 g (83 mmol) of Xylene. 9.73 g (24 mmol) of zinc neodecanoate and 2.69 g (3.7 mmol) of bismuth neodecanoate were added. To the stirring dispersion 61.18 g (219 mmol) of silver neodecanoate were added and left stirring until the solution became clear.

The whole procedure was done under avoidance of light exposure and the final ink was stored in the dark.

Printing

Screen printing was done with the half-automated screen printer EKRA STS E5. The screen openings of fingers were 100 μm , finger spacing $d = 2$ mm, mesh/inch = 280 in^{-1} , thread size 0.032 mm. The grid dimension was 5.0 x 5.0 cm^2 with one busbar in the middle and 26 fingers perpendicular to the busbars.

Tempering

The samples were dried at 100 °C on a hot plate. Tempering was done on a hot plate at 480 °C for 15 min.

Plating

Light induced plating was carried out. A setup such as the one shown in Figure 3.3.1 was used. Plating was done by applying 0.35 V to the back contact of the solar cell. An illumination intensity of 0.5 W/m² was set. Plating duration was 5 min and 3 min, respectively. A silver and copper electrolyte were used, respectively. After plating samples were cleaned with deionized water and dried in an air stream.

Characterization

Samples were characterized with SunsV_{OC} measurements, IV-curve measurements, electroluminescence measurements and TLM measurements.

IV-curve measurements were done with a reference cell at 25 °C and an illumination of 1000 W/m².

A voltage of 651 mV was applied to the metallized samples for 2 s to measure electroluminescence.

The contact resistance was measured by a TLM measurement setup. Contact resistivity was determined measuring eight silver lines. The applied current was set to $I = 10$ mA.

8.3 Results and discussion

8.3.1 Ink formulation

Solvent mixture

The MOD ink formulation used for this work is based on the work of Binder and was further developed and investigated [18, 150].

The main ink components are based on metal organyls¹ soluted in an organic solvent. According to Vest [151] silver neodecanoate fulfills the most important criteria for ink formulation (stability in air, low decomposition temperature, high metal content) and has a very high

¹Although the metal neodecanoates used in this work are strictly speaking no metal organyls, we will proceed with the term for simplicity.

solubility in Xylene. Thus, a very high metal proportion in the ink is possible.

In the following experiments silver neodecanoate, bismuth neodecanoate and zinc neodecanoate were used. Silver neodecanoate is the basic metal compound used to form the conductive metal grid on the solar cell. Bismuth neodecanoate was used as etching component to penetrate the SiN_x anti-reflection coating layer on the wafer, as was shown by Hörteis and Kalio [35, 41]. Zinc neodecanoate was used to improve the contact formation to the emitter [35]. The chemical structure of the neodecanoates is shown in Figure 8.3.1.

Xylene has a very high vapor pressure [152]. It was, therefore, mixed with N-methyl-2-pyrrolidon (NMP) which is a common solvent for printing applications. To determine the best proportion for maintaining high solubility on the one hand and moderate evaporation on the other, the evaporation rates of different Xylene:NMP mixtures were investigated with a goniometer. Drop volumes were measured against time and the evaporation rate calculated from the slope of measured data (see Figure 8.3.2).

With increasing amount of NMP the evaporation rate for the solvent mixture drops. For printing purposes the evaporation rate should be moderate: it must be high enough to allow for fast drying of the ink after printing but low enough to avoid drying of the ink and clogging while still inside the print head.

Based on the data above a mixture of Xylene:NMP = (1:1) would have been chosen. Due to higher evaporation rates caused by the air flow necessary to obtain a printable aerosol stream, this ratio turned out to be still too exhalable for aerosol jet printing. Thus, the final solvent ratio used was Xylene:NMP = (2:1).

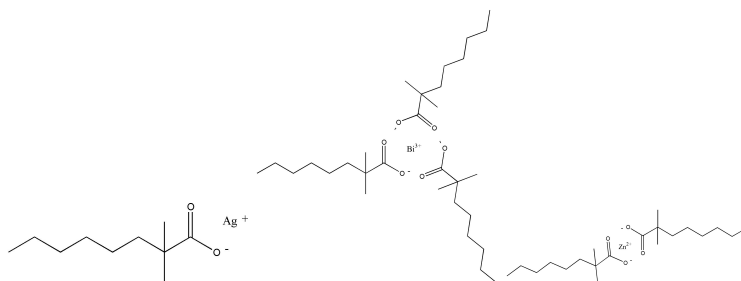


Figure 8.3.1: Chemical structures of metal neodecanoates (from left to right): silver neodecanoate, bismuth neodecanoate, zinc neodecanoate

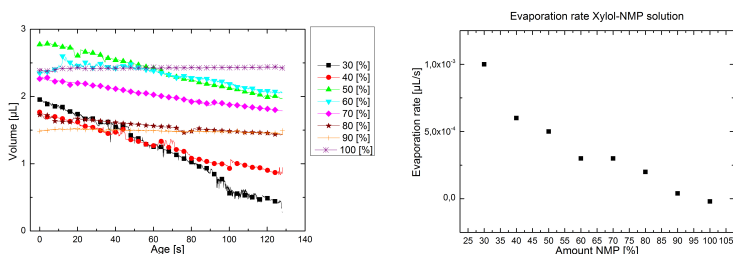


Figure 8.3.2: Evaporation of Xylene:NMP mixtures. Amount of NMP is given in % (left: measurement; right: calculated evaporation rate)

Silver neodecanoate synthesis

Silver neodecanoate is very sensitive to light, which causes reduction to silver (photographic process [153]. The stability of the ink is also very dependent on the quality of the used silver neodecanoate. For this reason silver neodecanoate was synthesized right before use, as described by Shim [65].

Some experience of the synthesis is necessary in order to gain impurity-free silver neodecanoate. The most critical part is the drying step. Already minor remains of salts or solvents can lead to impurities within the final product. Figure 8.3.3 shows a sample of silver neodecanoate



Figure 8.3.3: Silver neodecanoate (brown color implies impurities)

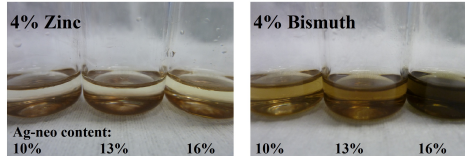


Figure 8.3.4: Solution series 1 and 2. Left: Zinc series with 4% zinc neodecanoate and varying neodecanoate content of 14 wt%, 17 wt% and 20 wt%; Right: Bismuth series with 4% bismuth neodecanoate and varying neodecanoate content of 14 wt%, 17 wt% and 20 wt%

of lesser quality due to impurities.

Ink stability

The overall metal organic concentration influences the quality and long term stability of the MOD ink. High amounts of metal ions trigger the formation of silver nanoparticles, which is indicated by an orange and later greenish color of the solution and by precipitates for very high concentrations, respectively. The nature of ions also influences the ink stability in different ways. To find a stable ink recipe with maximal metal content, several neodecanoate mixtures were investigated. The results are shown below.

A photograph of solution series 1 and 2 with increasing silver neodecanoate content is shown in Figure 8.3.4.

Bismuth ions seem to have a higher impact on the ink stability than zinc ions. The color change caused by reduced silver nanoparticles is more intense for the bismuth solution series. The influence of zinc is much less significant, which can also be seen from Figure 8.3.6 below.

To confirm this result, a two component solution series of bismuth

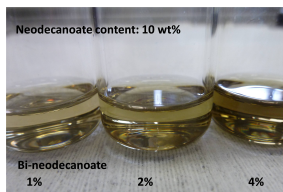


Figure 8.3.5: Bismuth neodecanoate content solution series

Solid % (neo)	10	11	12	13	14	15	16
3% Zn-Neo 1% Bi-Neo 96% Ag-Neo							
4% Zn-Neo 1% Bi-Neo 95% Ag-Neo							
5% Zn-Neo 1% Bi-Neo 94% Ag-Neo							
6% Zn-Neo 1% Bi-Neo 93% Ag-Neo							
7% Zn-Neo 1% Bi-Neo 92% Ag-Neo							

Figure 8.3.6: Zinc neodecanoate content solution series in the presence of 1% bismuth neodecanoate and varying overall metal concentration

and silver neodecanoate with varying bismuth neodecanoate content was investigated and is shown in Figure 8.3.5 (solution series 3).

The greenish color already indicates the formation of silver nanoparticles even at very low bismuth neodecanoate contents of only 1%. In regard to ink stability the bismuth metal content should be kept as low as possible.

The tolerance of silver neodecanoate towards zinc ions in the presence of bismuth neodecanoate was investigated and is shown in Figure 8.3.6 (solution series 4).

The solution series shows that the zinc neodecanoate content also has a certain impact on the ink stability. The influence increases with increasing overall metal content (columns of Figure 8.3.6). However,

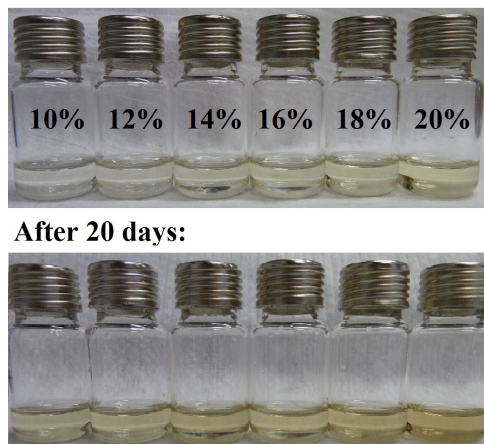


Figure 8.3.7: MOD ink stability series for various *metal organic contents* (wt%): just after formulation (top row) and after 20 days storage in darkness (bottom row)

the overall metal content itself has the major impact on the ink stability, as can be seen from the color change along the rows in Figure 8.3.6.

Regarding these results, the dependency of the overall concentration of metal organics and the ink stability over time was examined. Solution series 5 is shown in Figure 8.3.7. A series of different metal organic concentrations (wt%) is shown right after formulation and after 20 days of storage. Light also leads to reduction of silver ions, which is the reason why the ink should be stored in darkness.

It has to be emphasized, that the quality of silver neodecanoate is the most critical factor regarding the ink stability. Impurities lead to a fast reduction of silver ions to silver nanoparticles. With increasing experience of silver neodecanoate synthesis, the quality of the silver salt increased. In consequence, the concentration of soluted metal organic could be increased. Note that in the following Figure 8.3.8 (solution series 6), concentration values specify *metal content* (not metal organic content).

As a result of the stability experiments a 26 wt% metal content was chosen for experiments as a compromise between ink stability and

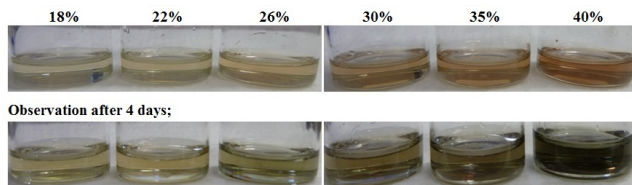


Figure 8.3.8: MOD ink stability for very high *metal contents* (wt%): right after formulation (top row) and after 4 days storage in darkness (bottom row)

metal amount.

Etching component

The amount of bismuth was determined by fully processing different inks at 480 °C for 5 min with varying bismuth neodecanoate contents.

Figure 8.3.9 shows the results.

The opening of the ARC improved with increasing bismuth metal content from 1 to 5 wt%. Higher bismuth amounts are favorable in terms of etching ability. First silver crystallites within the silicon nitride layer can be observed for a bismuth metal content of 1 wt%. Clear poor formation and partially open silicon as well as silver crystals are formed with 3 wt% bismuth content. However, the SiN_x layer at the pyramid tips is still not open. This is the case for bismuth contents of 5 wt%.

Final ink formulation

Silver is the element which forms the conductive layer after tempering of the ink. Therefore, silver is the main metal component within the ink formulation. Bismuth allows the etching of silicon nitride and higher amounts are favorable for good contact formation. However, the ink stability is strongly influenced by bismuth ions. As a compromise between ink stability and etching ability, a 3 wt% bismuth metal concentration was chosen for further experiments. As zinc is only used for contact improvement, 6 wt% zinc metal content was chosen according to metallization ink developed by Hörteis [51]. The solvent which fits the demanded parameters best was determined to be a mixture of NMP:Xylene = 2:1.

The final ink composition was as follows:

- Metal content: 26 wt% (17 wt% silver, 3 wt% bismuth, 6 wt% zinc)
- 74 wt% solvent (NMP:Xylene = 2:1)

8.3.2 Tempering process

Sintering conditions were investigated by processing the ink at several temperatures and via TG-DSC (cp. Chapter 4) measurements on silicon wafers with random pyramid texture and PECVD deposited SiN_x coating of 70-75 nm thickness.

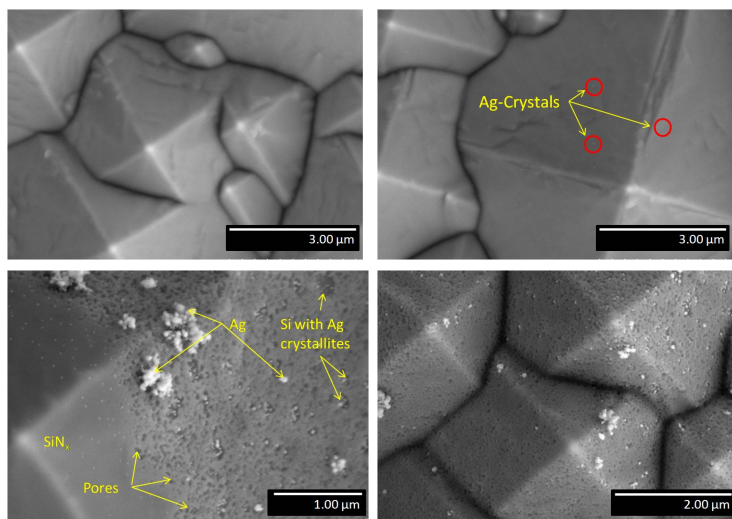
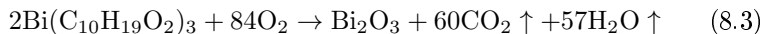
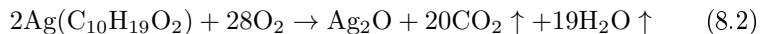


Figure 8.3.9: SEM images of etched SiN_x layers by MOD ink with varying Bi concentration.

Top row left: 1% Bi - no etching; right: 2% Bi - single Ag crystals visible. Bottom row left: 3% Bi - pore formation at pyramid tips and silver dendrites. right: 5% Bi - pore formation over the whole pyramids and silver dendrites

All ink components (except for the solvents) were measured separately in advance to verify the decomposition characteristics. All neodecanoates decompose up to 450 °C. The measurements are shown in the Appendix B.1.3.

The decomposition reactions are proposed to take place according to the following formulas:



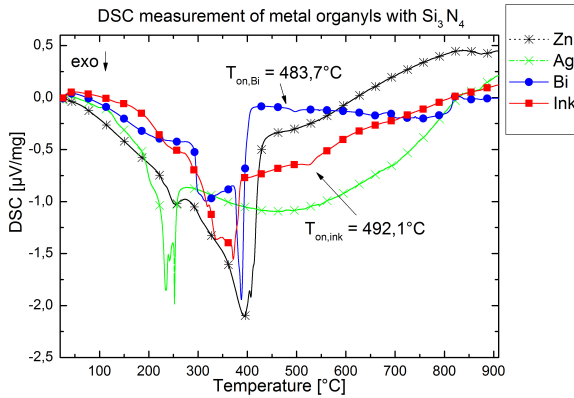
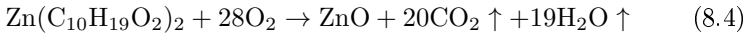


Figure 8.3.10: DSC measurements of the reactions between the different metal organyls and Si_3N_4 : onset temperatures mark the beginning of reactions between the compounds.



All metal neodecanoates as well as the complete ink formulation were mixed with Si_3N_4 and the reactions were measured by TG-DSC as shown in Figure 8.3.10.

The DSC measurements show the exothermic decomposition reactions of the organyls up to 450 °C, which is also supported by the TG analysis (data shown in the Appendix B.1.3).

The curves showing the reactions of bismuth neodecanoate + Si_3N_4 and ink + Si_3N_4 show additional exothermic reactions at 483.7 °C and 492.1 °C, respectively, indicating that a reaction with Si_3N_4 occurred. Figure 8.3.10 shows no reactions between silver neodecanoate + Si_3N_4 and zinc organyle + Si_3N_4 between 450-800 °C, respectively. Therefore, one can assume that the bismuth compound is the active etching component of the ink.

Bismuth neodecanoate and zinc neodecanoate show additional reactions above 600 °C: bismuth neodecanoate reacts endothermically at around 690 °C and 812 °C, respectively. According to Kalio, bismuth

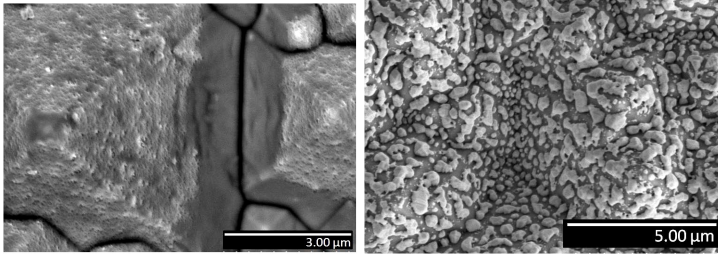


Figure 8.3.11: Left: SEM image of an MOD ink etching of an SiN_x layer on a textured silicon wafer tempered for 5 min at 450 °C after an HNO_3 and an HF etch. Right: SEM image of silver clump formation after ink tempered at 550 °C.

glass shows exothermic reactions with SiN_x starting at 550 °C [41]. An additional endothermic peak has been observed at around 810 °C by Kalio as well, but has not been further discussed in his work. Possible endothermic reactions are melting, evaporation and non-oxidative chemical reactions. Since no mass change could be measured anymore, no reaction with nitrogen can be assumed. Thus, melting of a glass formed from bismuth and Si_3N_4 could be possible. Due to SEM observations (which are discussed in more detail later in this chapter), which indicate ARC penetration already starting at low temperatures, processing temperatures and, thus, reactions above 550 °C were not further analyzed.

Besides TG-DSC measurements, samples with ink on SiN_x coated wafers were sintered at different temperatures for 5 min, respectively. Afterwards, the silver and glass layers were etched off by HNO_3 and HF. In Figure 8.3.11 the results for a sample tempered at 450 °C after etch off of the silver and glass layer and a sample tempered at 550 °C before etch off are shown.

The temperature variation indicates the start of the ARC etching already at 450 °C. Figure B.1.9 (in the Appendix) shows that no etching appears below 450 °C. SiN_x penetration is not more effective for higher temperatures (Figure B.1.9). For higher temperatures ≥ 550 °C silver clumps form at the wafer surface. No continuous silver layer is formed anymore as could be observed up to 500 °C (Figure B.1.9). The

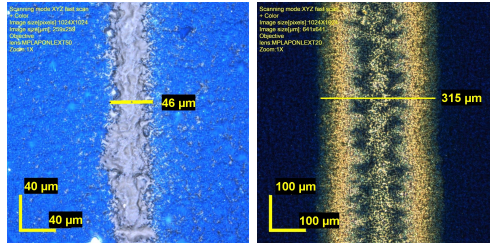


Figure 8.3.12: Confocal microscope images of aerosol jet printed finger. Left: after printing. Right: after tempering

clump formation might cause conductivity and, thus, plating issues.

During experiments longer tempering times of 15 min and 30 min were tested as well. No difference in the etching quality could be observed.

Regarding these results and taking the DSC measurements into account, which show an effective reaction of bismuth neodecanoate and Si_3N_4 at around 484 °C, a sintering temperature of 480 °C was chosen for further experiments. Although 5 minutes would be enough, a longer sintering time of 15 min was chosen to ensure completion of the silicon nitride penetration reaction.

8.3.3 Aerosol jet print of MOD inks

To ensure absence of particles the MOD ink was printed directly after formulation. Aerosol printed lines reached high amounts of applied ink and narrow width as shown in Figure 8.3.12.

Line heights lie at around 2-3 μm with little overspray. The printer chuck was heated during printing to ensure immediate evaporation of the solvents and narrow line widths. After curing, the ink spread out and reached line widths to around 200 μm . A typical *coffee ring effect*² can be observed: ink is concentrated at the edge and the middle

²The coffee ring effect describes the pattern which is left over after the solvent of a dispersion coated on a surface evaporated. Typically, the particles are drawn from the center of the coating to the edges due to the evaporation of the solvent. Often a high concentration of particles can also be observed in the center of the coating. Because the pattern of the particles reminds of a stain left over from a coffee spill, this phenomenon is called the “coffee ring effect”.

of the line. The line height was no longer measurable. The reason for this extreme ink spread arises from the ink components themselves; bismuth and zinc neodecanoate are highly viscous liquids. The viscosity drops dramatically by sample heating and the neodecanoates spread across the sample before decomposition. The influence of the wafer surface was not analyzed in detail within this work but one could expect that the amount of spreading is also dependent on the surface morphology. Because the spreading is caused by the liquid neodecanoates themselves, either a mask has to be applied to the wafer surface in advance, thereby acting as a barrier for the ink, or the liquid ink components have to be substituted by solid yet soluble metal organics.

Multiple printed lines are wider and give higher amounts of applied ink. However, those lines also spread widely and gave only slightly better contact and plating results.

8.3.4 Screen printing of MOD pastes

The intention of screen printing was to apply more ink in one printing step than with aerosol jet printing. Furthermore, screen printing is the standard metallization technique for silicon solar cell manufacturing which enables better comparability of the results with standard metallisation.

To apply the MOD ink to screen printing, the formulation has to be altered in order to meet rheological requirements. To thicken the ink and add thixotropic behavior, ethyl cellulose, a widely used organic compound in paste manufacturing, was added to the solvent mixture. The additional particles improve the quality demands on silver neodecanoate so as to avoid early formation of nanoparticles.

Photographs of samples after printing and curing are shown in Figure 8.3.13. In addition, an image taken with the confocal microscope of a cured screen printed line is shown as well.

The screen printed samples show the same characteristics as the aerosol jet printed samples. Because more ink per unit area could be applied, the spreading of the ink even caused fingers broader than those of the aerosol jet printed samples. Higher regions on the tempered sample imply higher amounts of silver in these regions. The confocal microscope image shows three regions of the MOD ink after tempering. The main region with a width of 784 μm is the main re-

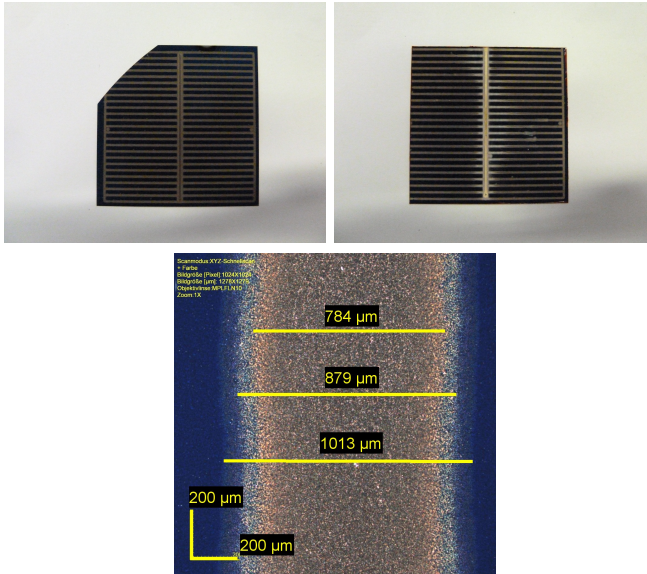


Figure 8.3.13: Photographs of screen-printed MOD ink samples: Top left: After printing. Top right: After curing at 480 °C for 15 min. Bottom: Confocal microscope image of a metallized finger. Finger widths are shown.

gion of metallization. Most silver is deposited in this region. Contact formation is most likely made here. The ink spread beyond this region with varying silver application. The second region might still possess enough silver to cause plating on top; however, the third region is likely to not be conductive enough to cause metal application. The reason for the different ink/paste application regions is the ability of the solvent to solute and transport the organyls and the adhesion of the organyls to the substrate surface. With decreasing the amount of solvent, less metal organyls can be transported, while at the same time, the affinity of the organyls towards the substrate surface rises compared to the solubility in the solvent. The coffee ring effect is also present, which is indicated by the light edges of region one. It is not as distinct as for the aerosol jet application because the binder within the paste decreases the capillary effect and, thus, the forces causing

the ink/paste and the organyls to spread.

8.3.5 Plating on the MOD seed-layer

To thicken the conductive layer, light induced plating was used. As described in Section 3.3.4 LIP uses the current generated by an illuminated solar cell to generate electrons at the surface of the wafer, which act as the reducing agent for metal ions in the electrolyte. The process is only functional, if a contact between seed-layer and emitter is formed. A working LIP process indicates a working contact between seed-layer metallization and emitter. If the conductivity of the seed-layer is adequate, the whole area which is connected to one contact point between metallization and emitter without interruption can be plated, even though contact may not have been formed over the whole plated area. Thus, a working LIP process only indicates a general contact formation but gives no information about the overall contact quality or the region where the contact was formed. A schematic illustration and a photograph of the experimental setup are shown in Figure 8.3.14.

The first grids plated for 5 min showed poor adhesion, which failed the tape test. Therefore, plating time was reduced to 3 min. Grid adhesion was improved and sufficient for further characterization.

With shorter plating times less metal is deposited to the seed-layer (cp. Chapter 3). This could also be observed for experiments described in this work. Thinner metal layers possess less internal stress which could cause adhesion failure. Another explanation could be that the interface between seed-layer and emitter is damaged by the electrolyte, as is known for nickel electrolytes [154, 155].

In Figure 8.3.15 plating results on aerosol jet printed lines and screen printed samples are shown.

The results show that plating is possible on aerosol jet printed seed layers as well as on the screen printed layers. This means that the silicon nitride layer of the cells was penetrated and contact formation to the emitter of the solar cell was done. Plating is possible with silver as well as with copper.

For the aerosol jet printed finger, plating produced a final finger width of 590 μm . Compared to the initial seed-layer (Figure 8.3.12) the finger width more than doubled. For the screen printed layer the plated area contributes to the main seed layer region shown in Figure

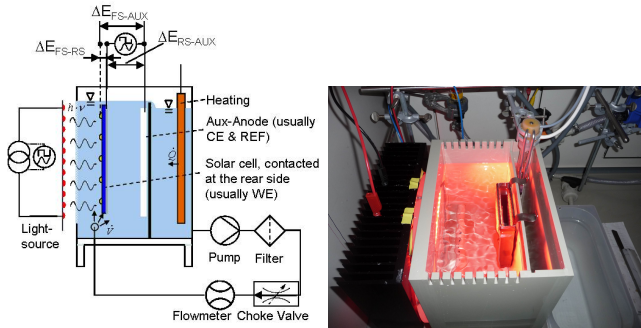


Figure 8.3.14: Schematic illustration of plating setup (left) and photograph of plating experimental setup (right). ΔE_{FS-RS} the potential difference between the front and rear side of the cell, ΔE_{FS-AUX} the potential difference between the front side of the cell and the anode, ΔE_{RS-Aux} the potential difference between the rear side of the cell and the potential of the anode.

8.3.13 (in both pictures the same finger is shown but not necessarily the same region).

For the aerosol jet printed finger an irregularity can be observed. Normally, silver would plate evenly in all directions. However, plating resulted in an intensive broadening of the finger width from $315 \mu\text{m}$ of the sintered finger to $590 \mu\text{m}$ after plating (Figures 8.3.12 and 8.3.15). Interestingly, a growth in height of $< 1 \mu\text{m}$ could be observed according to SEM measurements (Figure 8.3.16). As one can see from Figure 8.3.16, the seed layer is very thin (20-30 nm). Therefore, the conductivity of the seed layer is low and plating is slow, which could explain the small amount of applied plated silver. However, the silver application to the sides of the originally seeded area is much bigger. A possible explanation could be that very small amounts of the ink spread over a full width of $450 \mu\text{m}$. However, this theory could not be confirmed (e.g. optically with a confocal microscope). Further investigations have to be done regarding this effect.

As already described the working of light induced plating indicates whether the MOD seed-layer made contact to the emitter of the solar

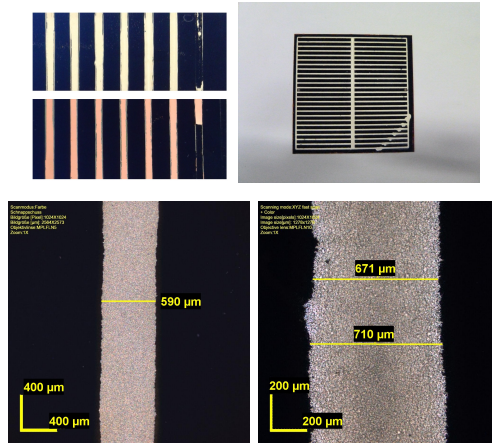


Figure 8.3.15: Photographs and confocal microscope images of MOD ink and paste metalized samples after LIP plating. Top row (Photographs) left: Aerosol jet printed samples with silver plating (top) and copper plating (bottom). Right: Silver plated screen printed sample. Bottom row (confocal microscope images and measurements) left: Silver plated aerosol jet printed finger. Right: Silver plated screen printed finger

cell. Figure 8.3.16 shows a photograph and a confocal microscope image of a non-uniform plated sample, contacted with the metal organyl decomposition ink.

The contact formation is not sufficient for all samples to be able to produce a smooth and even application of metal over the whole metallized grid. Non-uniform conductivity caused by uneven amounts of silver throughout the metal grid is also a reason for non-uniform plating results.

On the other hand, a uniform metallization does not necessarily mean a uniform contact formation by the seed-layer, but may also be caused by a good conductivity throughout the seed layer, which leads to uniform plating over the metal grid, although only few contact points might be present. High amounts of silver, which can be recognized by lighter regions of the metallization (Figure 8.3.13), con-

dition good conductivity in this region. However, if plating by the LIP process is possible, contact to the emitter was made. The quality of the contact has to be analyzed differently (for example, by contact resistance measurements).

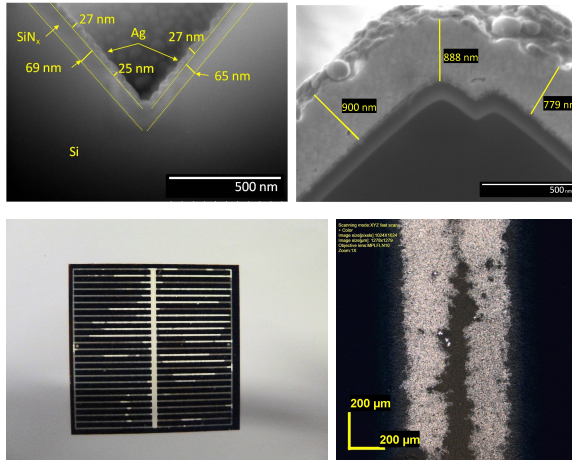


Figure 8.3.16: Images of MOD ink/paste contacted and partially plated samples. Top row (SEM images) left: Cross section of sample with MOD seed layer, applied by aerosol jet printing and cured at 480 °C for 15 min. Seed layer is formed by silver (silver-glass) nanoparticles. Right: Cross section of plated sample contacted by MOD ink applied by aerosol jet printing. Seed layer not visible anymore. Overall layer thickness < 1 μm. Bottom row left: Photograph of poorly plated screen printed sample with MOD paste seed layer. Right: Confocal microscope image of poorly plated screen printed sample with MOD paste seed layer

8.3.6 Contact formation model

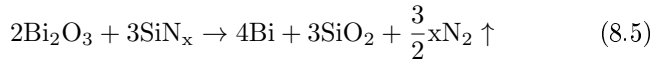
SiN_x penetration

The contact formation model for thick film silver metallization on crystalline silicon solar cells was discussed in Section 2.2.4. During development of the MOD ink, the results of the experiments denote that this contact formation model has to be altered for the process of MOD ink contact formation.

The contact formation was examined with SEM and EDX measurements more deeply. By means of those measurements two closely related but extended contact formation models will be proposed.

Recollecting Section 2.2.4, according to Schubert [39], pure lead is formed by the reaction of lead oxide with silver nitride and silicon (cp. Equations 2.3 and 2.4) to open the ARC layer.

In the MOD ink, bismuth (neodecanoate) was used, which is able to substitute lead in thick film metallization pastes, as mentioned in Chapter 2.2.3. The reactions of bismuth oxide with silicon nitride and silicon are similar to the reaction of lead oxide.



However, bismuth neodecanoate is not able to penetrate the silicon nitride layer, but forms Bi₂O₃ according to Equation 8.3, which was also confirmed by the reaction of pure bismuth neodecanoate with a silicon nitride covered wafer as shown in Figure 8.3.17. No etching of SiN_x by Bi₂O₃ is observed after etch off of bismuth oxide by HF. This is also true of higher annealing temperatures and different bismuth neodecanoate concentrations (not shown). Consequently, pure bismuth oxide is not able to penetrate the silicon nitride at reaction temperatures as low as T = 550 °C.

This is in contrast to the observations with TG-DSC measurements discussed in Section 8.2 (Figure 8.3.10). A possible explanation would be that the reaction in the DSC was done with pure bismuth neodecanoate and Si₃N₄ powder, which has a very high surface area compared to the denser, more compact PECVD-deposited layer of SiN_x. Bismuth neodecanoate is a highly viscous liquid and is, therefore, able

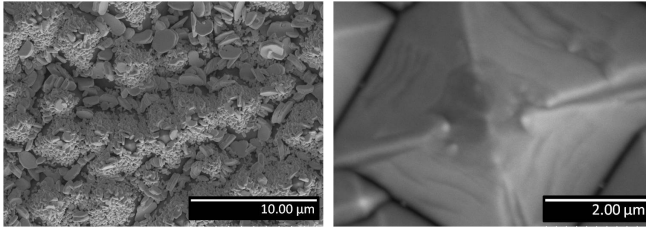


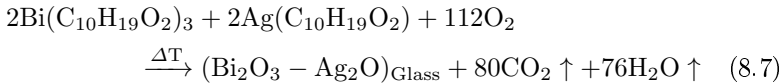
Figure 8.3.17: SEM image of Bi_2O_3 on a textured and SiN_x -coated wafer. Left: Bi_2O_3 particles (50 wt% solution cured at 480 °C for 15 min) before HF etch. Right: No etching of ARC occurred.

to wet the nitride powder almost completely, which leads to a much larger active reaction area compared to a bismuth neodecanoate drop on top of the ARC layer on a small wafer piece.

These observations contradict the model of Schubert [39], which, in addition, does not explain that no lead precipitates could be found next to silver crystallites [156, 157].

Silver neodecanoate alone is also not able to react with SiN_x at these low temperatures, which can be seen from the DSC measurements shown above (Figure 8.3.10). No reaction with SiN_x can be observed.

However, when applying a two component ink to the substrate, a glass layer is formed on the silicon nitride surface, which is covered by conductive silver (Figure 8.3.18). The glass phase is formed in-situ at 450-480 °C supposedly according to Equation 8.7.



After the removal of the silver layer by HNO_3 , the glass layer is more clearly visible. Etch off of the glass layer by HF reveals openings and partial removal of the SiN_x ARC layer even at low curing temperatures of 480 °C, as shown in Figure 8.3.19. Several bismuth neodecanoate to silver neodecanoate ratios were formulated (description in Section 8.2) and investigated (Figure 8.3.19).

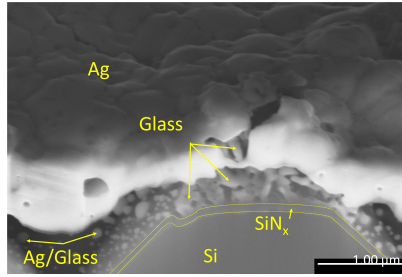


Figure 8.3.18: SEM cross section of MOD metallized SiN_x coated silicon wafer: Layer sequence is visible and marked

As shown in Figure 8.3.19 the thickness or quality of the glass formation on top of the silicon nitride layer tends to increase with increasing silver content. With the highest bismuth to silver ratio no sufficient glass phase is formed. The thickest glass phases are formed with Bimetal to Ag-neo-ratios between 4:1 and 1:4 (see Appendix B.1.3). Glass formation seems to decrease again for decreasing bismuth to silver ratios. However, the SiN_x etching effect is still higher than for high bismuth ratios. Although almost all of the ink formulations affect the SiN_x surface, the formulation with a ratio of 1 seems to be the most effective. Large areas of open silicon can be seen, as is shown in the EDX images in Figure 8.3.20. Black areas show open silicon, gray regions are formed either from SiN_x or from glass remains and bright residues are alloys of bismuth and silver and/or pure silver and/or glass residues with very high metal ratios and metal precipitates, respectively (Figure 8.3.20).

By comparing the etching results at the two different sintering temperatures 480 °C and 520 °C (cp. Appendix B.1.3), it seems that higher sintering temperatures improve the etching results. However, for decreasing ratios starting at ratio 1, etching at 480 °C seemed more effective than at 520 °C. This implies that temperature and bismuth to silver ratio are not the only important factors influencing the etching process.

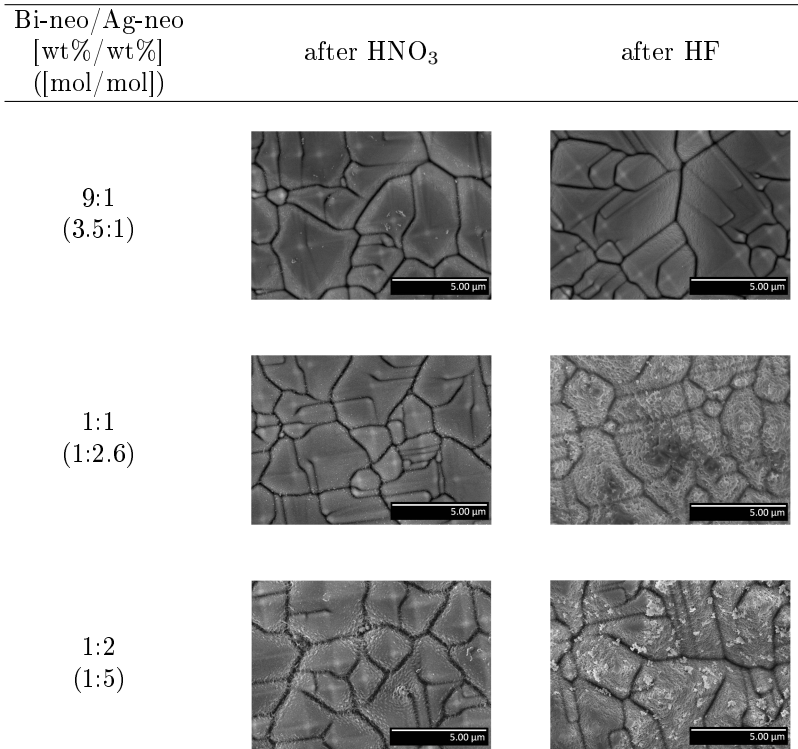


Figure 8.3.19: Proportions and SEM images of Bi-/Ag-neodecanoate variations on SiN_x. Images after HNO₃ treatment show glass formation on wafer surface (left). Images after HF treatment show wafer surface with etched SiN_x layer and silver-bismuth-glass residues (right) (neo = neodecanoate). (The whole measurement series is given in the Appendix B.1.3.)

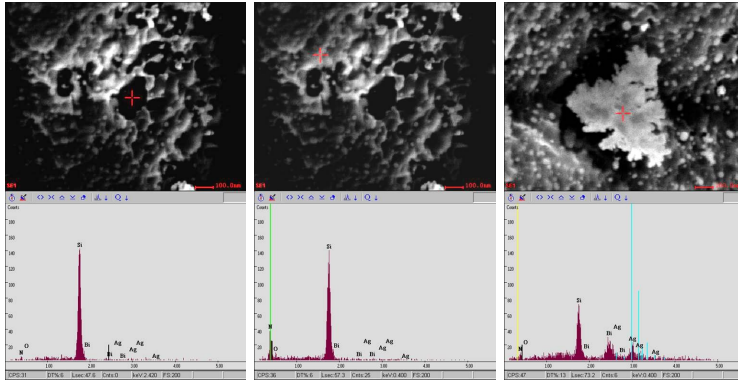
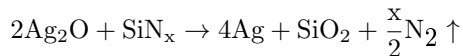
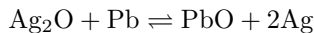
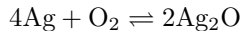


Figure 8.3.20: SEM and corresponding EDX images. Left: Si. Middle: SiN_x . Right: Ag-Bi-alloy.

When considering, that unlike the silver containing glass, Bi_2O_3 is not able to penetrate the SiN_x , one is lead to the conclusion that it is not bismuth but silver, more precisely silver oxide, which is the main etching component in metallization pastes and inks. This has already been discussed by Hong et al [43] for thick film metallization pastes. There, he suggested that silver oxide is the main oxidation and, thus, main etching component in the ink and paste formulations [43]. According to Hong et al., the reaction of lead (or bismuth, respectively) is suppressed by the reactions of silver ions according to Equations 2.5, 2.6 and 2.7.



This suggestion is supported by the fact that the silicon nitride layer is not etched equally over the whole glass covered area, but is penetrated through pores - which are formed by silver (or silver alloy) residues, as shown in Figure 8.3.21.

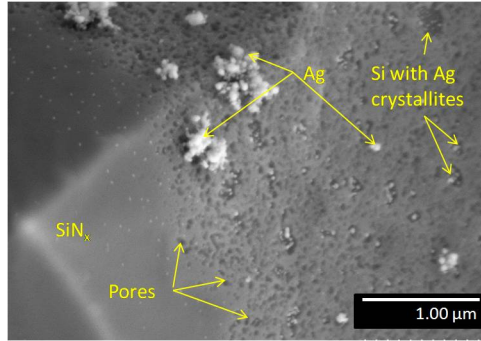


Figure 8.3.21: SEM image of SiN_x coated wafer opened by MOD ink and after metallization etch off by HNO_3 and HF: Pore etching through silver or silver-bismuth alloy

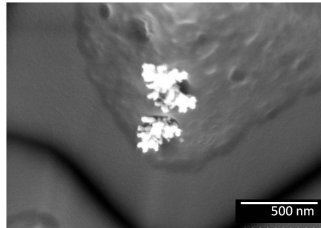


Figure 8.3.22: SEM picture of silver dendrites in an SiN_x pore

Pore formation can clearly be seen on the surface of the SiN_x coating. Remains of non-etched silver or silver-bismuth alloy can be observed. These residues are located under the glass layer and are, therefore, not etched by HNO_3 or HF. A second HNO_3 etching step would also remove these residues.

Unfortunately, EDX resolution is not high enough to verify whether the metal penetrating the ARC is pure silver or a silver-bismuth alloy since in most cases only silver can be detected. However, one has to keep in mind that the amount of bismuth within the ink is low.

A dendrite which seems to be grown out of the ARC layer is shown in Figure 8.3.22.

The theory of silver as the actual etching component can further

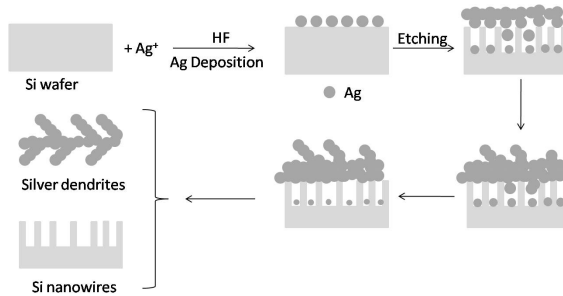


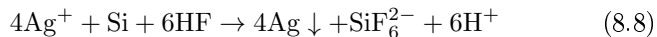
Figure 8.3.23: Schematic illustration of a possible etching process of silicon by silver ions and HF (retraced from [158])

be supported as it resembles the production process of black silicon [158].

The silicon appears black because the surface has a special texture to suppress light reflection almost completely and, thus, avoid optical losses. The silicon surface is covered with silicon needles which are etched by a silver nitrate containing HF solution.

Figure 8.3.23 schematically shows the etching process. Silver ions form precipitates on top of the silicon and oxidize silicon at the interface. The silicon oxide is etched and dissolved by HF. More silver ions are reduced at the formed precipitates and “etch” vertically through the silicon.

The summarized chemical reaction is described by Equation 8.8:



More evidence of silver oxide as the actual etching component is given by examination of the SEM images and EDX measurements shown in Figure 8.3.24 and 8.3.25.

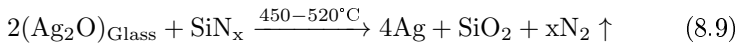
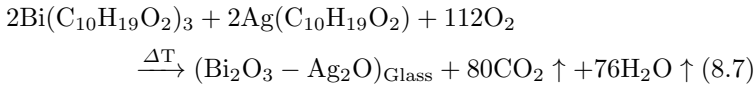
After curing of the MOD ink on a Si wafer at 480 °C for 15 min and a following back etch with HNO₃ and HF, only metals and metal glass residues remained, which have been able to penetrate the ARC layer. Two metal glass residues are shown in Figure 8.3.24. The effectivity of etching is higher for the residue on the right-hand side. EDX measurements (Figure 8.3.25) show that the silver ratio is higher in this residue.

These observations do not exclude the possibility of bismuth oxide (or lead oxide, respectively) being able to act as an etching component as well, as already indicated by the TG-DSC measurements above. However, the reaction of the pure oxides can only occur at higher temperatures, as shown by Kalio [41]. In the presence of silver ions and silver oxide, respectively, the suggestion of Hong et al., that silver suppresses the reduction of bismuth oxide while at the same time being reduced itself seems evident. Redox potentials³ of silver and bismuth also support this theory: $E^0(\text{Ag}/\text{Ag}^+) = +0.799 \text{ V}$; $E^0(\text{Bi}/\text{Bi}^{3+}) = +0.317 \text{ V}$ [40]. Silver has the higher potential, which means it is easier reducible than bismuth, which is why bismuth can not act as an reductive for silver.

However, silver oxide is not stable at temperatures $>160 \text{ }^\circ\text{C}$ [40], at which point it decomposes. That means that the etching silver oxide has to be stabilized in a glass matrix. This matrix is formed by lead oxide and bismuth oxide, respectively.

From SEM and EDX analysis it can be assumed that glass formation is essential to etch through the anti-reflection coating. Furthermore, glass can only be formed with both bismuth and silver at those low temperatures, as can be seen from measurement series in the Appendix (B.1.3) as well as from Kalio's observations of reactions by silver to silicon by Kalio [41] (2.2.4).

Summarizing the results, the silicon nitride layer is penetrated by silver oxide stabilized in a silver-bismuth-glass, which is itself formed in-situ. The etching process is proposed to follow Formulas 8.7, 8.9 and 8.10.



³Here the standard potential in aqueous solutions E^0 at $\text{pH} = 0$ are compared. The higher (more positive) the potential the easier is the reduction of the element, or in other words bismuth can reduce silver ions to silver and is oxidized to Bi^{3+} but silver cannot reduce bismuth ions to bismuth and be oxidized to Ag^+ .

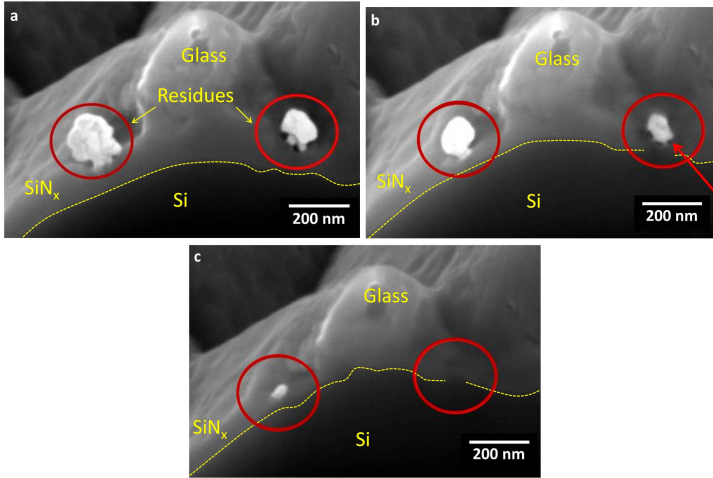
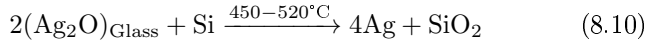


Figure 8.3.24: SEM image of cross section of MOD ink residues after etch off on an alkaline etched random pyramid textured Si wafer with SiN_x coating (SiN_x: lighter part; dark areas: silicon). Image series after FIB milling. a) Residues on ARC layer. b) Penetration and opening of the ARC layer by right residue. c): Small opening of ARC layer at position of right residue.



The glass formed here by silver and bismuth is likely to be a so-called “inverted glass” [159]. These glasses possess < 50% of oxygen polyhedrons and normally contain two network modifiers of different size and charge. Almost no long oxygen polyhedron chains are formed, which is why inverted glasses possess unique properties such as very low softening temperatures [159]. Because the glass phase is formed in-situ during decomposition of the neodecanoates in the MOD ink, reaction temperatures with the ARC are lower (starting at 450 °C) than observed by Kalio (530 °C for Pb glass and 550 °C for Bi glass, respectively)[41].

A second possibility for the glass formation would be that bismuth

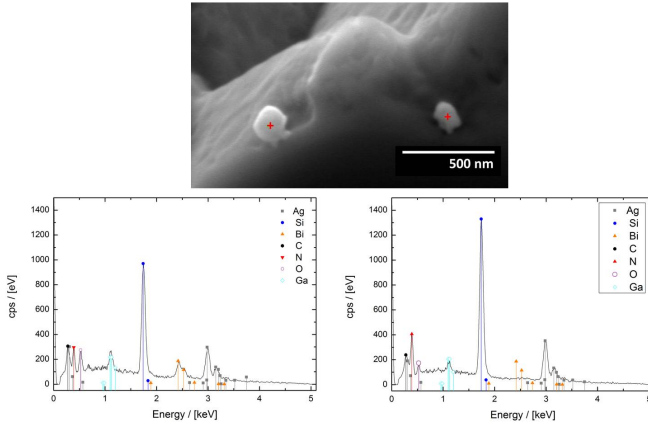
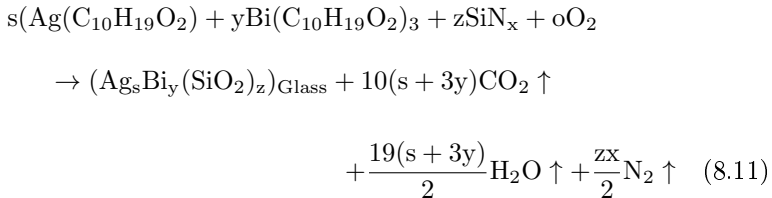


Figure 8.3.25: SEM image of residues with marked positions of EDX spot measurements (top) and EDX spectra (bottom) of the residues shown in Figure 8.3.24 (gallium present due to FIB milling): Left residue contains a high content of bismuth (bismuth oxide) and only weakly penetrates the ARC layer. Right residue contains almost only silver (silver oxide) and does penetrate the ARC layer more clearly.

(neodecanoate) and silver (neodecanoate) form a glass phase *together* with silicon nitride and silicon, respectively. This would also explain why the tempering time is very short and why no better etching results can be detected after longer tempering periods (see Section 8.3.2). The chemical reaction could follow Formula 8.11. After the glass formation process, excess silveroxide is reduced at the silicon interface according to Formula 8.10.



If silicon nitride is part of the glass formation reaction, a sufficient amount of glass building components in the MOD ink (for example Ag and Bi) is available to effectively open the silicon nitride layer. For this composition the “etching” result and contact formation are most efficient even at low temperatures. The ideal molar ratio for bismuth to silver lies between 1:2.6 to 1:20 according to glass formation results (Figure B.1.3). In this case, a silicon oxide glass with very high amounts of the network modifiers silver and bismuth would be formed.

The silver or silver/bismuth dendrites could either precipitate after the glass formulation at the silicon/glass surface during the rapid cooling process of the samples (during tempering on a hot plate, samples get removed from the still hot hot plate) or are formed from excess.

As can be seen in Figure 8.3.19 no ink formulation was able to penetrate the silicon nitride layer over a larger area, but only locally through pores. This might be because the content of silver oxide within the glass phase is not adequate or the glass composition is not adequate and uniform over the whole area. At higher temperatures, such as during conventional fast firing processes, bulk silver could be a source for both further silver diffusion into the glass phase as well as for the formation of silver oxide.

Better penetration of ARC by MOD ink could be observed on printed bus bars, which are thicker and, therefore, contain more paste and silver in a given area. But still, the amount of silver oxide (or glass composition) seems not to be high enough. In addition, bismuth neodecanoate is a highly viscous liquid. During the firing process, viscosity of the compound decreases, which leads to very high wettability of the wafer surface and large blending of the ink. Only a very small amount of ink per unit area of silicon nitride remains to etch the ARC layer and the opening is only local, as illustrated in Figure 8.3.26.

The assumption is examined in more detail by analyzing different regions of drop samples more closely. Figure 8.3.27 shows pictures of a mixture of bismuth- and silver neodecanoate (1:9) after both, sintering at 480 °C for 15 min and etch off of the metallization by HNO₃ and HF. Comparison with the corresponding SEM pictures indicates that regions which are covered by a thicker layer of silver and, thus, a thicker amount of ink after deposition tend to be more effectively etched than regions with less ink application.

It could also be observed that silver dendrites are mainly present

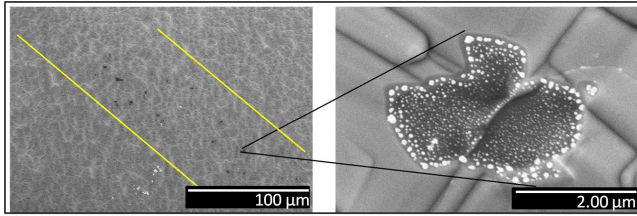


Figure 8.3.26: SEM images of contact points after HNO_3 and HF etch back: yellow lines indicate printed metallization line (left). Contact point with silver crystallites (right)

at the pyramid tips when the etching process is overall poor. This is reasonable as reactions most likely occur at regions with high energies. Etches and tips are defect regions in the crystal lattice and, therefore, regions of higher energy compared to the “defectless” crystal lattice.

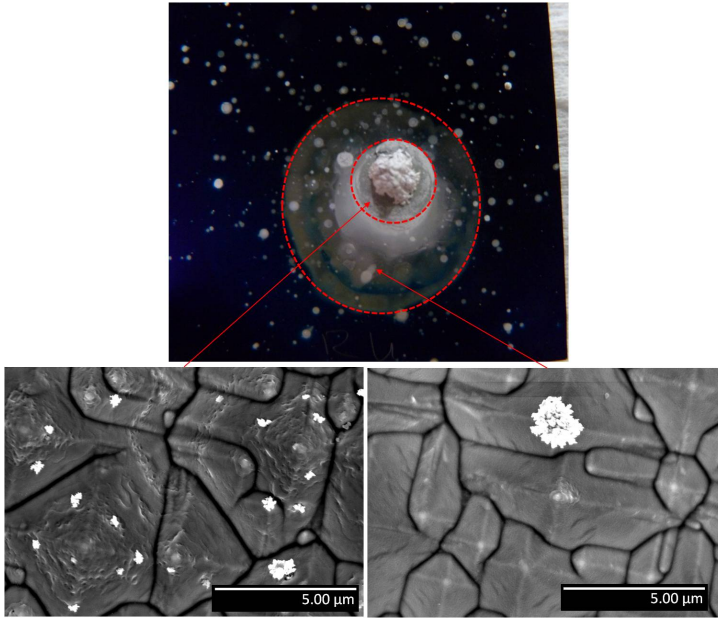


Figure 8.3.27: Top: Photograph of Bi-/Ag-neodecanoate (1:9) on SiN_x wafer after sintering at 480 °C for 15 min. Bottom: SEM pictures show more effective etching at regions with a high amount of silver (left) and poor etching with a low amount of silver (right)

To investigate whether the amount of ink per unit area necessary to penetrate the ARC layer is too low, silicon nitride layers of varying layer thicknesses (20-60 nm) were tested. Results are shown in Figure 8.3.28. Note the different magnifications.

A complete opening over the whole treated sample area could not be achieved, yet when the thickness of SiN_x layer is below 50 nm bigger areas of open nitride can be observed. This indicates that the amount of ink per unit area is important for the ARC opening result.

In summary, the contact formation process by bismuth- and silver neodecanoic ink is assumed to follow either a two step glass formation and nitride layer penetration mechanism according to Formulas 8.7,

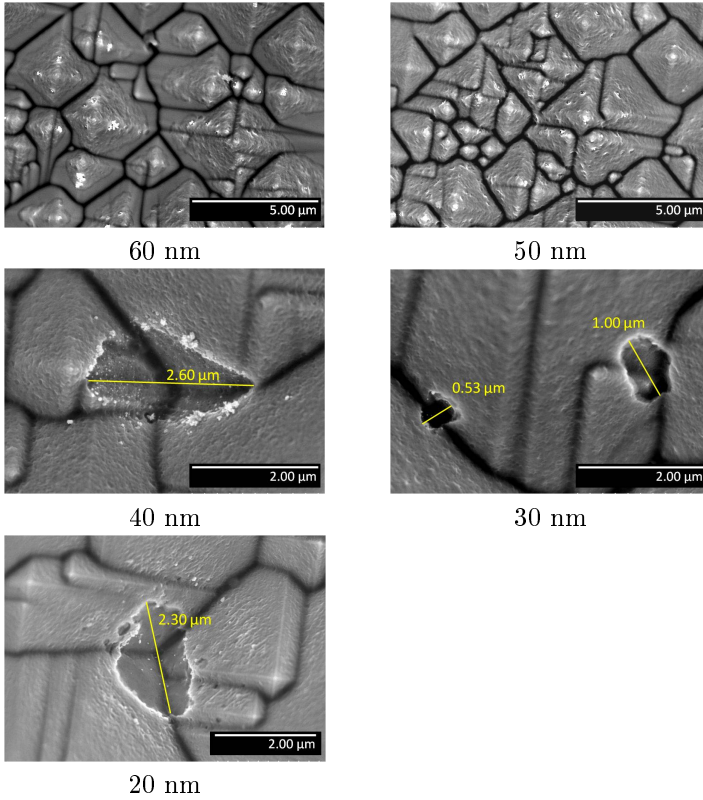
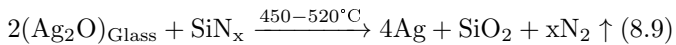
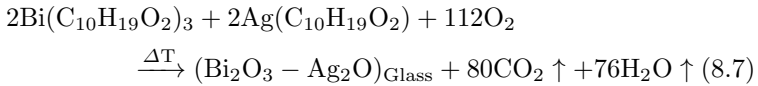
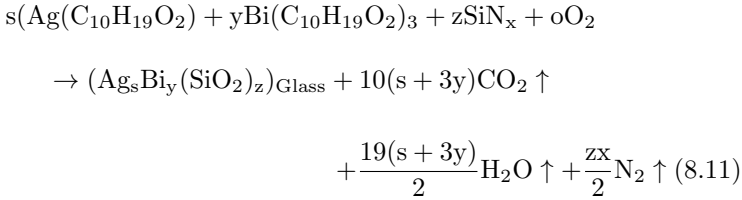
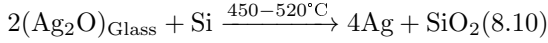


Figure 8.3.28: SEM pictures of etching results with varying SiN_x layer thicknesses

8.9 and 8.10 or a one step process with consumption of silicon nitride for glass formation according to Formula 8.11.





Both contact formation models are closely related. In the one step model however, SiN_x is *necessary* for glass formation and ARC opening. It also seems more likely regarding the short reaction times.

What both approaches have in common is that silver, in due proportion, is crucial for the penetration through SiN_x and contact formation to the emitter for this kind of glass.

Glass formation, the bismuth to silver ratio and the amount of ink per area are the most important factors for the good etching results of the ink.

In theory every ink composition, which is able to remove SiN_x either by dissolving or consumption, should be able to open the ARC layer. However, for the contact formation, a conductive metal is necessary. If the metal containing ink would be able to open the ARC layer uniformly over the whole metallized area, than only the contact formation, more precisely, the contact resistance to the emitter would be important for the choice of metal, for example titanium. The conductive layer will be formed by the plating step. However, if the ink is not able to open the whole area, then a good conductivity of the contacting metal is also necessary to ensure a uniform plating process.

In any case, the ink components for an MOD ink are not limited to silver and bismuth or lead, respectively. Essential is the ability to form a glass which is able to penetrate silicon nitride either by dissolution or by consumption.

8.3.7 Contact quality

After discussing the penetration of the anti-reflection coating in detail, the quality of the local contact points has to be examined more closely as well.

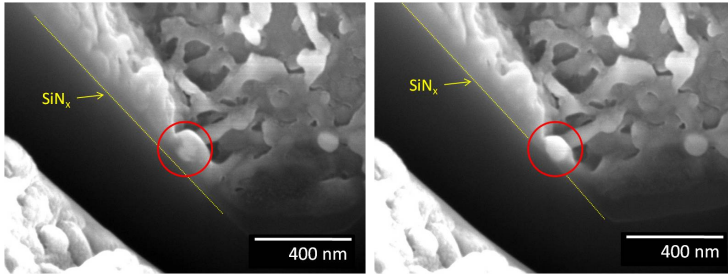


Figure 8.3.29: SEM images of MOD ink on alkaline etched random pyramid textured Si wafer with SiN_x layer after etch back with HNO_3 . Glass layer is still present. SEM images taken between FIB milling steps. Red marking shows region of high metal concentration with ARC penetration underneath. Yellow dashed line marks the SiN_x surface.

Cross sections polished by the focused ion beam (FIB) and observed by SEM show the contact formation beneath the SiN_x layer (Figures 8.3.29, 8.3.30 and 8.3.31). Within the glass, there are regions where a high amount of metal is concentrated which is able to penetrate the ARC layer locally.

The SiN_x layer is only penetrated at very small spots, where the metal concentration is high. Underneath the ARC coating the Ag-Bi-glass forms a contact to the silicon which is bigger than the penetration spot (Figure 8.3.30). This implies that silicon is more easily removed than SiN_x , which is reasonable to assume since silicon is more reactive than silicon nitride.

Figure 8.3.31 shows a cave formation at a contact point between the passivation layer and silicon. Whether the silicon is soluted within the Ag-Bi-glass can not be detected.

Cave formation is also a good explanation for poor adhesion between the metallization seed-layer and wafer. In addition, it is known that the electrolytes can be aggressive towards the seed-layer regarding the adhesion [154, 155]]. Which effect causes the corrosion of the adhesion layer is not yet known exactly, but one can assume that the electrolyte is able to diffuse into the contact caves and destroys the local adhesive

points at the contact points.

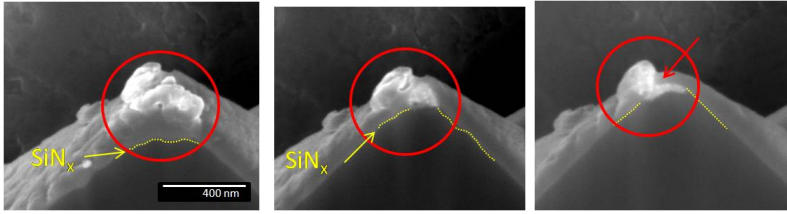


Figure 8.3.30: SEM images of contact point. Images were taken between FIB cuts. Yellow dashed line marks the SiN_x/Si interface. Left: Ag-Bi-glass on top of SiN_x layer. Middle: Contact point formed beneath SiN_x layer. Right: Contact point connection to Ag-Bi-glass precipitate on top of SiN_x layer.

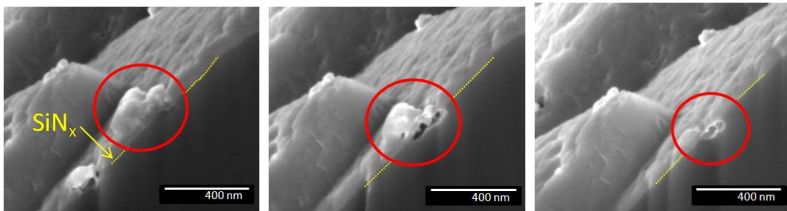


Figure 8.3.31: SEM images of contact point. Images were taken between FIB cuts. Yellow dashed line marks the SiN_x/Si interface. Cave formation is visible and marked.

8.3.8 Conductivity, contact resistance and cell results

The lateral conductivity of the metal grid applied via MOD seed-layer printing and plating is dominated by the plated silver layer on top of the seed-layer and not directly by the MOD ink. The quality of the plated layer is influenced by many factors and can not be discussed in this thesis. The interested reader is, therefore, referred to the literature [160].

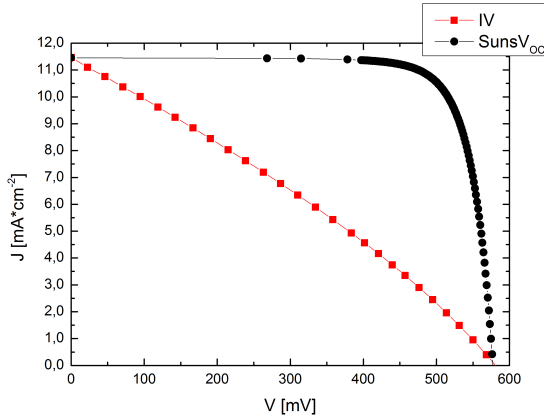


Figure 8.3.32: SunsV_{OC} and IV-measurement curves representative of the cell batch

In the previous Section, the contact formation by the MOD ink was discussed in detail. Within the following section, the results of solar cells contacted with the MOD ink and further metallized by light induced plating will be discussed.

A batch of test cells was contacted via screen printing with MOD ink and further metallized by silver LIP. IV-curves and SunsV_{OC} curves of the cells were measured, EL images were taken and the contact resistance of the metallization to the emitter was measured.

In Figure 8.3.32 a representative illuminated IV-curve of a fully metallized cell (MOD ink seed-layer and LIP silver plating) is shown in comparison to a SunsV_{OC} curve after metallization with the MOD ink.

The curve progression of the SunsV_{OC} measurement is independent from the metallization and can be used for identification of cell degradation caused, for example, by emitter damage. Emitter damage can occur after metallization in the event that the metal grows through the emitter, thereby contacting the cell base and causing shunts between the emitter and the cell base.

As shown in Figure 8.3.32 the SunsV_{OC} curve progression exhibits a typical diode curve. The corresponding average measured pseudo

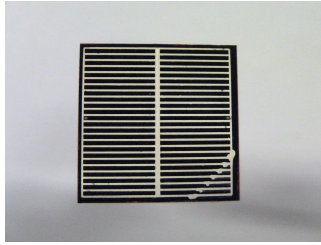


Figure 8.3.33: Photograph of fully metalized cell sample: the shaded cell area is very high and should normally not exceed 5-10 %

fill factor was $pFF = 81 \%$. Before metallization the cells showed a pFF of 80 %. The difference is within the measurement error range. A comparison of the different $SunsV_{OC}$ measurements before MOD ink application, after MOD ink curing and after plating are shown in the Appendix B.1.10.

The average open circuit voltage of the cell samples was $V_{OC} = 575$ mV and was measured with $SunsV_{OC}$. IV-curve samples showed even higher open circuit voltage values: $V_{OC} = 593$ mV. After complete metallization (MOD ink application, curing and plating) the cells had an average open circuit voltage of $V_{OC} = 571$ mV.

The results show that cell degradation did not appear. Thus, the metallization process caused no damage to the p-n-junction - for example, through short cuts caused by silver crystallites connecting emitter and cell base. It evidences that the cell performance itself is not affected by this metallization process.

The drop in fill factor for the illuminated IV-curve in Figure 8.3.32 can be explained by a high contact resistance. The MOD ink did not develop enough contact points to the emitter. In addition, plating results were also not ideal (very thin metallization - see also Section 8.3.5). This caused a high series resistance. As a result, the created current was not effectively extracted from the cell. The active cell area was small due to the spreading of the ink along with the resulting broad metalized fingers and busbar. This can be seen in Figure 8.3.33, which shows a photograph of a fully metalized cell. All of these factors lead to the loss in fill factor.

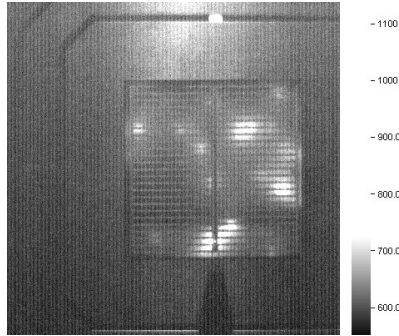


Figure 8.3.34: Electroluminescence image of fully metalized cell sample: light spots show active contact points. Dark areas show inactive cell area (Image contrast increased for better visibility of contact points)

The contact resistance was measured using the transfer length method (TLM). Contact resistance is also a function of contact area. Due to the poor etching results of the MOD ink the overall opening of the SiN_x layer was approximately less than 1% of the metalized area. Electroluminescence images (Figure 8.3.34) show the active contact points, which penetrated the ARC layer and made contact to the emitter.

Due to the very low active contact area, the normalized contact resistance measured achieved $R_c * W = 5\text{-}10 \text{ } \Omega\text{cm}$ and a specific contact resistance of around $\rho_c = 200\text{-}300 \text{ m}\Omega * \text{cm}^2$, which is quite high compared to standard metallization methods (specific contact resistances of screen printed thick film pastes is acceptable for $\rho_c < 5 \text{ m}\Omega * \text{cm}^2$ and good for $\rho_c < 1 \text{ m}\Omega * \text{cm}^2$ [41]).

8.3.9 Comparison to high temperature metallization pastes

Considering both metallization techniques - high temperature metallization and MOD ink metallization - only the seed-layer metallization concept with an additional plating step can be compared.

High temperature thick film metallization pastes have to be “fired” at $800\text{-}900 \text{ } ^\circ\text{C}$ to form a contact to the emitter. MOD inks have only

to be processed at rather low temperatures of < 500 °C. In addition, the metal content of this seed-layer ink is only 26 wt% compared to 60-80 wt% for seed-layer thick film metallization pastes.

The theories of contact formation also differ. High temperature thick film metallization paste contact the solar cell by penetrating the ARC layer through a redox reaction within a liquid glass phase (cp. Section 2.2.4). Silver diffuses from the silver bulk phase through the liquid glass phase and reprecipitates at the interface.

The etching process by MOD ink metallization seems very dependent on the composition of the glass phase. A liquid phase process such as proposed for high temperature metallization cannot occur because the reaction temperature is too low. A solid state diffusion process is also unlikely. The diffusion rate, which is necessary to explain, that contact formation is already done after 5 min at relatively low temperature would be too high. In addition, if solid state diffusion would be responsible for the etching and crystal formation, longer reaction times would have caused better results, which was not the case. The whole etching process has to take place at quite the same time as the decomposition of the ink components and glass formation. The proper ratio of bismuth neodecanoate to silver neodecanoate is crucial for an effective ARC opening. The ARC layer is most likely opened by consumption through the glass formation reaction as has been proposed above.

High temperature metallization with thick film paste and the low temperature process with the MOD ink have in common that the ARC area opened through both processes is local rather than over the full area. Using high temperature metallization pastes, the number of contacting points and silver crystallites increase with increasing peak temperature [35]. Comparing these results with the MOD ink, low temperature metallization shows that the number *and* area of active SiN_x layer openings mostly depend on the amount of ink applied per unit area.

Comparison of the geometry of the crystallites formed from high temperature pastes with that of those formed from MOD inks shows, that high temperature metallization pastes form triangular shaped contact points (compare Figure 8.3.35 left) while MOD inks develop dendritic crystals with no defined geometry (Figure 8.3.35 right).

In addition, to the increasing number of contact points with increasing firing temperature, the penetration depth of silver crystals

formed by high temperature metallization pastes also increases by several nanometers [35]. This may cause short circuits of the solar cell when using shallow emitters which are only a few nanometers thick. The silver crystallites grow through the emitter and also contact the basis. Hence, the right peak firing temperature has to be tested whenever a paste component or the cell has been altered. This effect has not yet been observed for MOD inks and is also less likely at the low processing temperatures $< 500\text{ }^{\circ}\text{C}$.

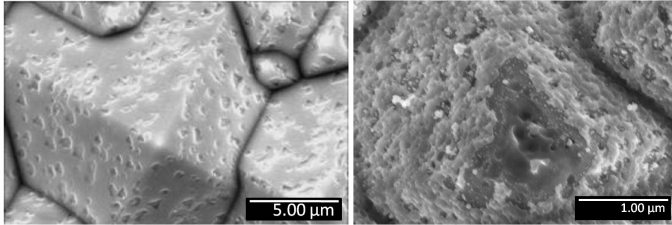


Figure 8.3.35: SEM pictures of silver crystallite imprints: high temperature paste [35] (left), MOD ink (right) (Note different magnification)

8.4 Chapter Summary

In this chapter, a new metallization method based on a metal-organic decomposition (MOD) ink for contacting SiN_x coated crystalline silicon solar cells was introduced. The basic requirements for the formulation were described and the contact formation process analyzed in detail.

The ink is based on metal neodecanoates of silver, bismuth and zinc which decompose below 450 °C. The metal content is only 26 wt%. The ink, partially, forms a glass phase at the interface to the substrate. This glass layer is covered by a bulk silver layer. The synthesis of silver neodecanoate was described and the importance of the quality of silver neodecanoate for the ink stability was established and emphasized. It is possible to add a binder and gain a screen printable paste. Contact formation to the emitter takes place at 450 °C within 5 min.

The impact of ink composition with respect to the silver and bismuth neodecanoate ratio was studied in detail. Based on these results, it has been determined that the latest ink formulation has to be altered for future work. The ideal silver to bismuth ratio is assumed to lie between 2.6:1 and 20:1. In addition, the amount of ink per unit area is important for an effective silicon nitride opening.

Based on these results, two advanced contact formation models for MOD inks were introduced. Both models are closely related.

Within the first model, bismuth neodecanoate and silver neodecanoate form a stable glass matrix. The stabilized silver oxide then affects and removes the SiN_x layer. The glass phase is formed prior to the etching process. In this case, the amount of silver oxide within the glass matrix has to be maximized.

Within the second model it is suggested that the silicon nitride is consumed during the glass formation process and, hence, is a necessary part of the glass matrix. In this case, the bismuth to silver ratio is crucial for forming an ideal glass matrix, which consumes a maximum of SiN_x . With an optimal glass component ratio, ideal contact formation could be achieved at low temperatures without lead while using advanced printing techniques. Regarding the processing time, this model seems to be more likely.

It has been shown, that silicon is more effectively soluted by the glass phase than SiN_x . This results in cave formation at the contact points and beneath the SiN_x layer. This, in combination with the low active

contact area, may be the reason for the poor adhesion of the applied seed-layer.

Due to the use of the high viscous liquids bismuth neodecanoate and zinc neodecanoate, the ink spreads out during the tempering process, which affects the contact formation and involving very broad metal grids.. Alternative bismuth organics (and zinc organics) must be found to avoid blending during tempering.

Due to the poor etching results of the applied ink, only a few contact points were formed on the solar cells and thus, contact resistivity was overall quite poor. This caused a decreased fill factor. The contact points could be detected by electroluminescence imaging. However, the MOD ink does not damage the emitter-base interface. The pseudo fill factor before and after metallization exceeded 80 %.

Comparison of MOD ink seed-layer metallization with thick film paste seed-layer metallization shows that MOD ink is not yet competitive due to poor contact formation and poor adhesion. However, problems such as shunting of the solar cells due to extensive silver crystallite growth through the emitter and into the base, which can be the case for thick film metallization pastes, were not observed for MOD inks so far. In addition, processing temperatures for thick film metallization pastes have to be evaluated each time the formulation or the sample differs. MOD inks can be processed at low temperatures of 450 °C in any formulation. The inks can be applied using advanced printing techniques which principally allow printing of very narrow finger widths and the use of mechanically delicate substrates.

9 Summary and Outlook

The present work aimed to analyze alternative metallization concepts for silicon solar cells. Cost reduction by lowering the process temperature and reduce the silver consumption make silicon solar cells more competitive energy source. Two different metallization concepts aiming at the application on different cell concepts were investigated.

A metallization process based on silver nanoparticles is needed to contact advanced and temperature-sensitive solar cell concepts like HIT cells or organic solar cells. The approach was inspired by silver nanoparticle inks developed for the use on printable and flexible electronics and mainly meant for application on polymeric substrates like PET.

The suitability of silver nanoparticles as low-temperature metallization material for solar cells was investigated. Simple inks and pastes were formulated to investigate the general sintering behavior of silver nanoparticles within such formulations.

Usually, metal nanoparticles are getting sintered using a thermal process. However, most often this requires temperatures > 200 °C and long processing times. Therefore, an alternative sintering technique, *chemical sintering* was used, which allows sintering of silver nanoparticles even at room temperature. The silver nanoparticles were exposed to HCl vapor, which triggered the sintering of the particles. The chlorine ions are the crucial component in this process. They substitute the protective capping agent from the particle surface, causing collision between the particles, which starts the particle sintering.

In this work, both sintering strategies were combined. The samples were first chemically sintered and then tempered. Based on this concept, inks and pastes were formulated and tested. As a result, line resistivities down to $\rho = 2.30 \cdot 10^{-8}$ Ω m for a simple ink formulation and $\rho = 3.16 \cdot 10^{-8}$ Ω m for a hydroxy ethylene cellulose containing paste could be achieved for low curing temperatures of $T = 200$ °C and $T = 300$ °C and short curing times of 15 min, respectively. This

compares to only **1.5 and 2 times** of the resistivity of bulk silver, respectively. Commercially available inks are usually thermally sintered and reach such values only after 30 min of thermal sintering [80]. Chemical sintering alone achieves values five times of the conductivity of bulk silver [83]. Comparing the paste results, commercially available polymer pastes, which are used for the metallization of temperature sensitive cells today, only reach values of $\rho = 1 \cdot 10^{-7} \Omega\text{m}$ at tempering temperatures $\leq 220 \text{ }^\circ\text{C}$ [62].

Longer curing times of 15 min compared to 10 s for inks are necessary for paste sintering to remove the binder from the silver layer and gain best conductivities.

To improve the understanding of the effect of organic additives in the ink and paste formulations on the chemical sintering process, the influence of organics was analyzed in detail. It could be shown, that the chemistry of these organics has to be adjusted to the desired sintering process and temperature. For chemical sintering, capping agents should contain oxygen containing functional groups as anchor groups to the silver surface. Chemical sintering is less effective with nanoparticles protected with nitrogen containing organics. This concept is transferable to other additives in inks and pastes.

Most of the sensitive cell concepts require ITO (indium tin oxide) on the surface to improve the current transport from the cell to the metal grid. Nanoparticle inks, which are available on the market today, are usually designed to be printed on organic substrates like PET and only to transport current, but not to extract the charge carriers from the substrate. Thus, contact resistance to the substrate is not an issue. However, it could be shown, that the choice of organics within the inks and pastes is even more crucial for contact resistance than for the lateral resistance of the sintered silver layers. With this in mind, very good contact formation for the inks and pastes formulated in this work were achieved: lateral contact resistances of $R_c * W = \mathbf{0.166} \Omega\text{cm}$ for inks and $R_c * W = \mathbf{0.068} \Omega\text{cm}$ for pastes applied to ITO were measured. Typical values for screen printed polymer pastes are between $R_c * W < 0.3\text{-}0.5 \Omega\text{cm}$ [135, 136].

Further improvement of the silver nanoparticle regarding size distribution and stability can further improve the electrical properties of the sintered silver tracks.

Alternative sintering agents based on chlorine containing salts were investigated. The salts were directly added to the inks in low concen-

trations. During drying of the printed silver layers, the chlorine ion concentration should rise and finally reach a critical concentration to trigger particle sintering. However, the particle sintering was limited to local *sinter islands* and was not effective to form a closed sintered silver layer. In addition, the stability of the ink is reduced.

Using silver nanoparticle inks has the advantage to apply those inks by low-cost and fast ink jet or aerosol jet printing. The ink formulations have to be adjusted to the substrate in order to avoid unwanted effects like ink bleeding or repelling, or adhesion failure. It is, therefore, crucial to determine the surface properties of the substrates.

Within this work, the surface properties of ITO were investigated. It was shown, that ITO possesses a very high surface energy and hydrophilicity right after deposition. However, the behavior changes drastically within only a few hours from hydrophilic to hydrophobic. The effect can be “reseted” by cleaning the surface with ozone produced by a UV excimer. The state of the ITO surface has influence on the ink formulation as well as on the timescale of ink application. In addition, it influences the metal adhesion to the surface.

Based on the results of this work, the next steps in silver nanoparticle ink development will be the addition of adhesion promoters as well as other additives adjusting wettability properties, surface tension etc. in order to complete the formulation.

It was demonstrated that the silver nanoparticle ink formulations are suitable for seed-layer metallization on ITO. To obtain a full metallization, the seed-layer has to be thickened. This can be done by electrochemical metal deposition. The whole metallization process is called *seed-and-plate*.

To thicken the silver seed-layer by plating, the cell has to be dipped into a plating bath. The ITO surface is highly conductive which causes the thread of metal deposition on the surface. It was investigated, if selective plating on a seed-layer is possible without further protection of the ITO surface. It could be shown that the process is possible in a narrow range of applied plating current. ITO forms a barrier against copper diffusion, thus, the seed-and-plate approach using copper as conductive material is an additional possibility to lower the cell production costs. To improve the selective plating process further experiments are necessary to fully understand the underlying processes.

The results demonstrate that metallization based on silver nanoparticles is a promising alternative for low-temperature metallization on ITO and mass production. The requirements on ink and paste formulations based on silver nanoparticles in order to meet solar cell demands were investigated and are now the basics for further metallization development. The investigation of the surface properties of ITO complete the informations which are necessary to know to formulate inks and pastes which meet the special requirements to contact solar cells, and which are not fulfilled by commercially available inks. Improvement of silver particles can further increase the quality and performance of the inks.

With the demonstration of selective electrochemical metal deposition on a metal seed-layer on unprotected ITO, it was shown, that a full metallization process based on the silver nanoparticle inks is possible. The seed-and-plate approach can be used without additional processing steps. The possibility of using copper as deposition metal reduces the process costs. This opens the path to an efficient and low cost metallization process and allows for mass production of temperature sensitive solar cell concepts.

The second metallization concept investigated in this work, aims to contact standard silicon solar cells at moderate temperatures below 500 °C.

The approach was inspired by MOD (metal organic decomposition) inks, which were originally design for use on temperature-sensitive substrates. These MOD inks contain only silver to develop a lateral conductive layer for printed electronics, comparable to the approaches with silver nanoparticles.

MOD inks used in this work contain no particles and are **free of lead**. They contain bismuth and zinc neodecanoate apart from silver neodecanoate to form a contact through the ARC layer covering the solar cell surface. The inks have a low metal content compared to thick film metallization pastes and form a contact to the emitter already at **450 °C**, a temperature much lower than the typical firing temperature of screen-printing pastes (800-900 °C).

The contact formation process of this new metallization approach was investigated in detail and two closely related contact formation models were proposed.

The first model deviated from the current contact formation model

developed for firing through thick film silver pastes. The model was altered according to the results obtained in this work. It is suggested that **silver is the key etching component** within the ink/paste formulation and has to be stabilised as silver oxide within a glass matrix.

In addition to this model, a second contact formation model was proposed. Silicon nitride as anti-reflection coating is not penetrated by the glass, which is formed by the ink components, but is dissolved during the glass formation process and, thus, consumed during the contact formation process. It is part of the glass and, as such, even necessary for the contact formation to the emitter. Excess silver oxide is being reduced at the silicon interface and forms the contact to the emitter. In principle, only the ability of the glass to consume silicon nitride is limiting the performance of the ink. Other glass composition than used here are imaginable. To enable the use of the seed-and-plate approach, a metal which is able to form a conductive layer should be involved.

The ink does form a contact to the emitter without damaging the emitter-base interface. The pseudo fill factor before and after the metallization with the MOD ink was $\text{pFF} \geq 80\%$.

The ink is meant as seed-layer metallization, forming the contact. Light induced plating (LIP) uses the current induced by the operating solar cell itself, to reduce silver ions from the plating bath. Silver deposition via LIP is possible on contacts formed by the MOD ink and thus, the newly introduced MOD ink is suitable for the seed-and-plate process. It makes low temperature metallization for industrial silicon solar cells possible by reducing the silver consumption at the same time. Production cost can be significantly reduced.

The next steps will be to adapt the ink formulation in terms of bismuth to silver ratio according to the results of this work, to improve the contact quality. To avoid bleeding of the ink, a change of the bismuth and silver compounds may be necessary.

The metallization approaches introduced in this work, have the potential to lower production costs of already established cell designs as well as help to introduce new cell concepts to mass production. This way, costs of €/kWh can be further lowered, making energy production from solar cell conversion a competitive and serious alternative to fossil fuels.

Publications

Tamari, Y.; Gautrein, A.; Schmiga, C.; Binder, S.; Glatthaar, M. and Glunz, S. W. Synthesis of a Lead- and Particle-free Metal-organic Ink for Front Side Metallization of Crystalline Silicon Solar Cells, *Energy Procedia*, 2014, 55, 708 - 714

Gautrein, A.; Tamari, Y.; Mondon, A.; Schmiga, C.; Glunz, S.W. and Tremel, W. Metal organic decomposition (MOD) ink for contacting silicon solar cells: Contact formation model and influence of ink composition on glass formation, *submitted*

Gautrein, A.; Schmiga, C.; Tremel, W.; Glunz, S.W. Improvement of Low-Temperature Sintering Process of Silver Nanoparticles for Temperature-Sensitive Solar Cell Concepts, *submitted*

Kraft, A.; Pernia, Y.; Kalio, A.; Gautrein, A.; Ni, L.; Bartsch, J.; Glunz, S. and Reinecke, H. Origin of corrosion effects in solar cell contacts during electrochemical nickel deposition, *Journal of Applied Electrochemistry*, Springer Netherlands, 2015, 45, 95-104

Gautrein, A.; Schmiga, C.; Glatthaar, M.; Tremel, W.; Glunz, S.W. Nanometallic silver inks for metallization of ITO-coated silicon solar cells: Influence of organic components, *Proc. 29th EU PVSEC 2014*. Amsterdam, The Netherlands

Bibliography

- [1] *Fraunhofer Institute for Solar Energy Systems database*, 2015.
- [2] IEA. Key energy world statistics. *International Energy Agency*, 2014.
- [3] Harald Andruleit, Andreas Bahr, Hans Georg Babies, Dieter Franke, Jürgen Meßner, Roberto Pierau, and Sarah Weihmann Schauer, Michael Sandro Schmidt. Energiestudie 2013 : Reserven, Ressourcen und Verfügbarkeit von Energierohstoffen (17), 2013.
- [4] Peter Würfel. *Physics of Solar Cells From Principles to New Concepts*. 2005.
- [5] S. De Wolf, A. Descoedres, Z. C. Holman, and C. Ballif. High-efficiency silicon heterojunction solar cells: a review. *Green*, 2 (1):7–24, 2012.
- [6] Jeff Clark. Casey Research, Mai 2015. <https://www.caseyresearch.com/articles/a-photovoltaic-silver-bull-in-china>.
- [7] ISFH. ISFH Konstanz, Mai 2015. http://www.isfh.de/institut_solarforschung/silberverbrauchskosten.php.
- [8] DuPont. April 2015. <http://www.dupont.com/products-and-services/solar-photovoltaic-materials/photovoltaic-metallization-pastes/products/solamet-pv-low-temp-silver-paste.html>.
- [9] Heraeus. April 2015. http://heraeus-pvsilverpaste.com/en/products/novelcellpastes/sol500series/sol9383_2.aspx.

- [10] M. Abdelhamid, R. Singh, and M. Omar. Review of Microcrack Detection Techniques for Silicon Solar Cells. *Photovoltaics, IEEE Journal of*, 4(1):514–524, Jan 2014.
- [11] Achim Kraft, Christian Wolf, Jonas Bartsch, and Markus Glatthaar. Characterization of Copper Diffusion in Silicon Solar Cells. *Energy Procedia*, 67(0):93 – 100, 2015. ISSN 1876-6102. Proceedings of the Fifth Workshop on Metallization for Crystalline Silicon Solar Cells.
- [12] J. Bartsch. *Advanced Front Side Metallization for Crystalline Silicon Solar Cells with Electrochemical Techniques*. PhD thesis, Albert-Ludwigs-Universität Freiburg im Breisgau, 2011.
- [13] A. Mondon, M.N. Jawaid, J. Bartsch, M. Glatthaar, and S.W. Glunz. Microstructure analysis of the interface situation and adhesion of thermally formed nickel silicide for plated nickel-copper contacts on silicon solar cells. *Solar Energy Materials and Solar Cells*, 117(0):209 – 213, 2013. Dye Sensitized Solar Cells, Organic, Hybrid Solar Cells and New Concepts Dye Sensitized Solar Cells, Organic, Hybrid Solar Cells and New Concepts.
- [14] Michael Rauer, Andrew Mondon, Christian Schmiga, Jonas Bartsch, Markus Glatthaar, and Stefan W. Glunz. Nickel-plated Front Contacts for Front and Rear Emitter Silicon Solar Cells. *Energy Procedia*, 38(0):449 – 458, 2013. Proceedings of the 3rd International Conference on Crystalline Silicon Photovoltaics (SiliconPV 2013).
- [15] K. Masuko, M. Shigematsu, T. Hashiguchi, D. Fujishima, M. Kai, N. Yoshimura, T. Yamaguchi, Y. Ichihashi, T. Mishima, N. Matsubara, T. Yamanishi, T. Takahama, M. Taguchi, E. Maruyama, and S. Okamoto. Achievement of More Than 25Silicon Heterojunction Solar Cell. *Photovoltaics, IEEE Journal of*, PP(99):1–3, 2014.
- [16] Alexander Kamyshny, Joachim Steinke, and Shlomo Magdassi. Metal-based Inkjet Inks for Printed Electronics. *The Open Applied Physics Journal*, 4:19–36, 2011.
- [17] Shlomo Magdassi, editor. *The Chemistry of Inkjet Inks*, volume 20. World Scientific, 2010.

- [18] Yaara Tamari, Aline Gautrein, Christian Schmiga, Sebastian Binder, Markus Glatthaar, and Stefan W. Glunz. Synthesis of a Lead- and Particle-free Metal-organic Ink for Front Side Metallization of Crystalline Silicon Solar Cells. *Energy Procedia*, 55(0):708 – 714, 2014. Proceedings of the 4th International Conference on Crystalline Silicon Photovoltaics (SiliconPV 2014).
- [19] B. King. Maskless mesoscale material deposition. *Electronic Packaging and Production*, 2003.
- [20] J.P. Hermans, P.Papet, K. Pacheco, W.J.M. Brok, B. Strahm, J. Rochat, T. Söderström, and Y. Yao. Advanced metallization concepts by inkjet printing. *Proceedings of 29th European Photovoltaic Solar Energy Conference and Exhibition*, 2014.
- [21] M. Hörteis and S.W. Glunz. Fine line printed silicon solar cells exceeding 20 *Progress in Photovoltaics: Research and Applications*, 16(7):555–560, 2008.
- [22] T.H.J. van Osch, J. Perelaer, A.W.M. deLaat, and U.S. Schubert. Inkjet Printing of Narrow Conductive Tracks on Untreated Polymeric Substrates. *Advanced Materials*, 20(2):343–345, 2008.
- [23] Ph. Buffat and J-P. Borel. Size effect on the melting temperature of gold particles. *Phys. Rev. A*, 13:2287–2298, Jun 1976. doi: <http://dx.doi.org/10.1103/PhysRevA.13.2287>.
- [24] A. Goetzberger, B. Voß, and J. Knobloch. *Sonnenenergie: Photovoltaik; Physik und Technologie der Solarzelle*. B.G. Teubner Stuttgart 1997, 2 edition, 1997.
- [25] C. Honsberg and S. Bowden. Pveducation.org, September 2014. URL <http://pveducation.org>.
- [26] Stefan Goßner. *Grundlagen der Elektronik*. Shaker Verlag, 2011.
- [27] D. Meier and D.K. Schroder. Contact resistance: Its measurement and relative importance to power loss in a solar cell. *Electron Devices, IEEE Transactions on*, 31(5):647–53, May 1984.
- [28] K. Hajmrle and R. Angers. Sintering study of silver particles by in situ electron microscopy. *Metallurgical Transactions*, 5(4): 817–822, 1974.

- [29] K.A. Schroder. *Mechanism of Photonic Curing: Process High Temperature Films on Low Temperature Substrates*, volume 2. NCC Nano, 2011. ISBN ISBN: 978-1-4398-7139-3.
- [30] Wilfried G.J.H.M. van Sark, Francesco Roca, and Lars Korte. *Physics and Technology of Amorphous-Crystalline Heterostructure Silicon Solar Cells*. Springer-Verlag Berlin Heidelberg, 2012.
- [31] D. S. Ginley, H. Hosono, and D. C. Paine. *Handbook of transparent conductors*. Springer, 2010.
- [32] Julia E. Medvedeva and Chaminda L. Hettiarachchi. Tuning the properties of complex transparent conducting oxides: Role of crystal symmetry, chemical composition, and carrier generation. *Phys. Rev. B*, 81:125116, Mar 2010. doi: <http://dx.doi.org/10.1103/PhysRevB.81.125116>.
- [33] Thomas Young. An essay on the cohesion of fluids. *Philosophical Transactions of the Royal Society of London*, 95:65–87, 1805.
- [34] Joseph M. Luther Octavi Semonin and Matthew C. Beard. Multiple exciton generation in a quantum dot solar cell. *SPIE Newsroom*, 2012.
- [35] Matthias Hörteis. *Fine-line printed contacts on crystalline silicon solar cells*. PhD thesis, University of Konstanz, 2009.
- [36] S.M. Sze. *Physics of Semiconductor Devices*. New York: John Wiley and Sons, 1981.
- [37] D.K. Schroder and D.L. Meier. Solar cell contact resistance - a review. *IEEE Trans. Electron Devices*, pages 637–47, 1984.
- [38] A. Mette. *New concepts for front side metallization of industrial silicon solar cells*. PhD thesis, University of Freiburg, 2007.
- [39] Gunnar Schubert. *Thick film metallisation of crytsalline silicon solar cells*. PhD thesis, University of Konstanz, 2006.
- [40] Holleman and Wiberg. *Lehrbuch der Anorganischen Chemie*. de Gruyter, 2007.

- [41] André Kalio. *Study of contact formation using leaded and lead-free silver model pastes on advanced crystalline silicon solar cells*. PhD thesis, Technical Faculty of Albert-Ludwigs-University Freiburg, 2014.
- [42] D.M. Huljic, D. Biro, R. Preu, C.C. Castillo, and R. Ludemann. Rapid thermal firing of screen printed contacts for large area crystalline silicon solar cells. *Proceedings of the 28th IEEE Photovoltaics Specialists Conference*, 2000.
- [43] Kyoung-Kook Hong, Sung-Bin Cho, Jae Sung You, Ji-Weon Jeong, Seung-Mook Bea, and Joo-Youl Huh. Mechanism for the formation of Ag crystallites in the Ag thick-film contacts of crystalline Si solar cells. *Solar Energy Materials and Solar Cells*, 93(6-7):898 – 904, 2009. 17th International Photovoltaic Science and Engineering Conference.
- [44] CRCT ThermalFact Inc. Factsage(v6.3 ed.), 2013. URL www.factsage.com.
- [45] W. Schatt and H. Worch. *Werkstoffwissenschaft*. Wiley-VCH Verlag GmbH, 2003.
- [46] S. Kontermann. *Characterization and modeling of contacting crystalline silicon solar cells*. PhD thesis, University of Konstanz, 2009.
- [47] Stefan Kontermann, Alexander Ruf, and Ralf Preu. Quantitative comparison of simulated and experimental silver crystal formation at the interface of silver thick film contacts on n-type silicon. *Energy Procedia*, 8(0):455 – 460, 2011. Proceedings of the SiliconPV 2011 Conference (1st International Conference on Crystalline Silicon Photovoltaics).
- [48] K. Suganuma, S. Sugihara, and K. Okazaki. Interface microstructure between silicon and silver formed after eutectic brazing reaction. *Journal of Materials Science*, 29(16):4371–4378, 1994.
- [49] Randall M. German, Pavan Suri, and Seong J. Park. Review: liquid phase sintering. *Journal of Materials Science*, 44(1):1–39, 2009.

- [50] Enrique Cabrera, Sara Olibet, Joachim Glatz-Reichenbach, Radovan Kopecek, Daniel Reinke, and Gunnar Schubert. Experimental evidence of direct contact formation for the current transport in silver thick film metallized silicon emitters. *Journal of Applied Physics*, 110(11):114511, 2011.
- [51] Matthias Hörteis, Tobias Gutberlet, Armin Reller, and Stefan W. Glunz. High-Temperature Contact Formation on n-Type Silicon: Basic Reactions and Contact Model for Seed-Layer Contacts. *Advanced Functional Materials*, 20(3):476–484, 2010.
- [52] E. Cabrera, S. Olibet, D. Rudolph, J. Glatz-Reichenbach, R. Kopecek, D. Reinke, A. Gotz, and G. Schubert. Impact of Si surface topography on the glass layer resulting from screen printed Ag-paste solar cell contacts. In *Photovoltaic Specialists Conference (PVSC), 2012 38th IEEE*, pages 000204–000208, June 2012.
- [53] Ching-Hsi Lin, Song-Yeu Tsai, Shih-Peng Hsu, and Ming-Hsun Hsieh. Investigation of Ag-bulk/glassy-phase/Si heterostructures of printed Ag contacts on crystalline Si solar cells. *Solar Energy Materials and Solar Cells*, 92(9):1011 – 1015, 2008.
- [54] Kurt R. Mikeska, Zhigang Li, Paul D. VerNooy, Liang Liang, Alan F. Carroll, Jessica Chou, and Karu Shih. New Thick Film Paste Flux for ConContact Silicon Solar Cells. *Proceedings of the 26th European Photovoltaic Solar Energy Conference and Exhibition, Hamburg, Germany*, 2011.
- [55] Seung H Ko, Heng Pan, Costas P Grigoropoulos, Christine K Luscombe, Jean M J Fraechet, and Dimos Poulidakos. All-inkjet-printed flexible electronics fabrication on a polymer substrate by low-temperature high-resolution selective laser sintering of metal nanoparticles. *Nanotechnology*, 18(34):345202, 2007.
- [56] M. L. Allen, Mikko Aronniemi, Tomi Mattila, Ari Alastalo, Kimmo Ojanper, Mika Suhonen, and Heiki Sepp. Electrical sintering of nanoparticle structures. *Nanotechnology*, 19(17): 175201, 2008.

- [57] J. Perelaer, B.-J. de Gans, and U.S. Schubert. Ink-jet Printing and Microwave Sintering of Conductive Silver Tracks. *Advanced Materials*, 18(16):2101–2104, 2006.
- [58] Jolke Perelaer, Mark Klokkenburg, Chris E. Hendriks, and Ulrich S. Schubert. Microwave Flash Sintering of Inkjet-Printed Silver Tracks on Polymer Substrates. *Advanced Materials*, 21(47):4830–4834, 2009.
- [59] Ingo Reinhold, Chris E. Hendriks, Rebecca Eckardt, Johannes M. Kranenburg, Jolke Perelaer, Reinhard R. Baumann, and Ulrich S. Schubert. Argon plasma sintering of inkjet printed silver tracks on polymer substrates. *J. Mater. Chem.*, 19:3384–3388, 2009.
- [60] Michael Layani and Shlomo Magdassi. Flexible transparent conductive coatings by combining self-assembly with sintering of silver nanoparticles performed at room temperature. *J. Mater. Chem.*, 21:15378–15382, 2011.
- [61] Yuning Li, Yiliang Wu, and Beng S. Ong. Facile Synthesis of Silver Nanoparticles Useful for Fabrication of High-Conductivity Elements for Printed Electronics. *Journal of the American Chemical Society*, 127(10):3266–3267, 2005.
- [62] Julia R. Greer and Robert A. Street. Thermal cure effects on electrical performance of nanoparticle silver inks. *Acta Materialia*, 55(18):6345 – 6349, 2007.
- [63] Inyu Jung, YunHwan Jo, Inyoung Kim, and HyuckMo Lee. A Simple Process for Synthesis of Ag Nanoparticles and Sintering of Conductive Ink for Use in Printed Electronics. *Journal of Electronic Materials*, 41(1):115–121, 2012.
- [64] Alexander Kamyshny and Shlomo Magdassi. Conductive Nanomaterials for Printed Electronics. *Small*, 10(17):3515–3535, 2014. ISSN 1613-6829.
- [65] In-Keun Shim, Young Il Lee, Kwi Jong Lee, and Jaewoo Joung. An organometallic route to highly monodispersed silver nanoparticles and their application to ink-jet printing. *Materials Chemistry and Physics*, 110:316 – 321, 2008.

- [66] Thomas D. Schladt. *Design of Multifunctional Magnetic Nanomaterials for Biomedical Applications*. PhD thesis, Johannes-Gutenberg-Universität Mainz, 2010.
- [67] Thanh-Dinh Nguyen and Trong-On Do. *Nanocrystal*. InTech, 2011. ISBN 978-953-307-199-2.
- [68] C. B. Murray, C. R. Kagan, and M. G. Bawendi. Synthesis and Characterization of Monodisperse Nanocrystals and Close-packed Nanocrystal Assemblies. *Annual Review of Materials Science*, 30(1):545–610, 2000.
- [69] Younan Xia, Yujie Xiong, Byungkwon Lim, and S.E. Skrabalak. Shape-Controlled Synthesis of Metal Nanocrystals: Simple Chemistry Meets Complex Physics? *Angewandte Chemie International Edition*, 48(1):60–103, 2009.
- [70] Jongnam Park, Jin Joo, Soon Gu Kwon, Youngjin Jang, and Taeghwan Hyeon. Synthesis of Monodisperse Spherical Nanocrystals. *Angewandte Chemie International Edition*, 46(25):4630–4660, 2007.
- [71] Hongshui Wang, Xueliang Qiao, Jianguo Chen, Xiaojian Wang, and Shiyuan Ding. Mechanisms of PVP in the preparation of silver nanoparticles. *Materials Chemistry and Physics*, 94:449 – 453, 2005.
- [72] G.S. Métraux and C.A. Mirkin. Rapid Thermal Synthesis of Silver Nanoprisms with Chemically Tailorable Thickness. *Advanced Materials*, 17(4):412–415, 2005.
- [73] Sang Hyuk Im, Yun Tack Lee, Benjamin Wiley, and Younan Xia. Large-Scale Synthesis of Silver Nanocubes: The Role of HCl in Promoting Cube Perfection and Monodispersity. *Angewandte Chemie*, 117(14):2192–2195, 2005.
- [74] Xiaohu Xia, Jie Zeng, Brenden McDearmon, Yiqun Zheng, Qingge Li, and Younan Xia. Silver Nanocrystals with Concave Surfaces and Their Optical and Surface-Enhanced Raman Scattering Properties. *Angewandte Chemie*, 123(52):12750–12754, 2011.

- [75] C. Ducamp-Sanguesa, R. Herrera-Urbina, and M. Figlarz. Synthesis and characterization of fine and monodisperse silver particles of uniform shape. *Journal of Solid State Chemistry*, 100(2):272 – 280, 1992.
- [76] Dongjo Kim, Sunho Jeong, Bong Kyun Park, and Joocho Moon. Direct writing of silver conductive patterns: Improvement of film morphology and conductance by controlling solvent compositions. *Applied Physics Letters*, 89(26):264101, 2006.
- [77] K. Vanheusden, K. Kunze, H. Kim, A. Stump, A. Schult, M. Hampden-Smith, C. Edwards, A. James, J. Caruso, T. Kodas, et al. Metal nanoparticle compositions, August 24 2006. US Patent App. 11/331,211.
- [78] Z. Radivojevic, K. Andersson, K. Hashizume, M. Heino, M. Mäntysalo, P. Mansikkamäki, Y. Matsuba, and N. Tereda. Optimised curing of silver ink jet based printed traces. *Proceedings of Thermionic Conference 2006, France*, page 166, 2006.
- [79] Michael Grouchko, Alexander Kamyshny, Cristina Florentina Mihailescu, Dan Florin Anghel, and Shlomo Magdassi. Conductive Inks with a "Built-In" Mechanism That Enables Sintering at Room Temperature. *ACS Nano*, 5(4):3354–3359, 2011.
- [80] Cabot. CCl300 Technical Datasheet. Technical report, Cabot International.
- [81] Angela L. Dearden, Patrick J. Smith, Dong-Youn Shin, Nuno Reis, Brian Derby, and Paul O'Brien. A low curing temperature silver ink for use in ink-jet printing and subsequent production of conductive tracks. *Macromolar Rapid Communications*, 26:315–8, 2005.
- [82] N.M. Reinartz. Silver-containing inkjet ink, June 22 2006. WO Patent App. PCT/US2005/045,482.
- [83] Shlomo Magdassi, Michael Grouchko, Oleg Berezin, and Alexander Kamyshny. Triggering the Sintering of Silver Nanoparticles at Room Temperature. *ACS Nano*, 4(4):1943–1948, 2010. PMID: 20373743.

- [84] W. Zapka, W. Voit, C. Loderer, and P. Lang. Low Temperature Chemical Post-Treatment of Inkjet Printed Nano-Particle Silver Inks. *NIP24: Intern. Conf. on Digital Printing Technologies and Digital Fabrication, Proceeding*, page 906, 2008.
- [85] Michael Layani, Michael Grouchko, Shai Shemesh, and Shlomo Magdassi. Conductive patterns on plastic substrates by sequential inkjet printing of silver nanoparticles and electrolyte sintering solutions. *J. Mater. Chem.*, 22:14349–14352, 2012.
- [86] K.A. Shroder, K.M. Martin, D.K. Jackson, and S.C. McCool. Method and apparatus for curing thin films on low-temperature substrates at high speeds, March 18 2014. US Patent 8,674,618.
- [87] Furlan W.F. Schroder K.A., McCool S.C. *Broadcast Photonic Curing of Metallic Nanoparticle Films*, volume 3. Nanotech, 2006. ISBN ISBN:0-9767985-8-1.
- [88] E. Yablonoitch, T. Gmitter, R. M. Swanson, and Y. H. Kwark. A 720 mV open circuit voltage SiO_x:c-Si:SiO_x double heterostructure solar cell. *Applied Physics Letters*, 47(11):1211–1213, 1985.
- [89] M. Taguchi, M. Tanaka, T. Matsuyama, T. Matsuoka, S. Tsuda, S. Nakano, Y. Kishi, and Y. Kuwano. Tech. Digest 5th International Photovoltaic Science and Engineering Conference, Kyoto, Japan. 1990.
- [90] W. Fuhs, K. Niemann, and J. Stuke. Heterojunctions of Amorphous Silicon and Silicon Single Crystals. *AIP Conference Proceedings*, 20(1):345–350, 1974.
- [91] J. I. Pankove and M. L. Tarnng. Amorphous silicon as a passivant for crystalline silicon. *Applied Physics Letters*, 34(2):156–157, 1979.
- [92] Yoshihiro Hamakawa, Kouha Fujimoto, Kouji Okuda, Yoshio Kashima, Shuichi Nonomura, and Hiroaki Okamoto. New types of high efficiency solar cells based on a-si. *Applied Physics Letters*, 43(7):644–646, 1983.

- [93] Stefaan De Wolf and Michio Kondo. Nature of doped a-Si:H/c-Si interface recombination. *Journal of Applied Physics*, 105(10):103707, 2009.
- [94] L. Barraud, Z.C. Holman, N. Badel, P. Reiss, A. Descoeurdes, C. Battaglia, S. De Wolf, and C. Ballif. Hydrogen-doped indium oxide/indium tin oxide bilayers for high-efficiency silicon heterojunction solar cells. *Solar Energy Materials and Solar Cells*, 115(0):151 – 156, 2013.
- [95] J. Bardeen. Surface States and Rectification at a Metal Semiconductor Contact. *Phys. Rev.*, 71:717–727, May 1947.
- [96] D. Braun. Untersuchung der elektronischen Struktur von Indiumoxid mittels ARPES und STS. Master’s thesis, Humboldt-University Berlin, 2012.
- [97] Tobias Koeniger. *Leitfähige Beschichtungen aus Indium-Zinn-Oxid Nanopartikeln für Flexible Transparent Elektroden*. PhD thesis, University of Erlangen-Nürnberg, 2008.
- [98] Andreas Klein, Christoph Körber, André Wachau, Frank Säuberlich, Yvonne Gassenbauer, Steven P. Harvey, Diana E. Profit, and Thomas O. Mason. Transparent Conducting Oxides for Photovoltaics: Manipulation of Fermi Level, Work Function and Energy Band Alignment. *Materials*, 3(11):4892–4914, 2010.
- [99] L.H. Lee. *Fundamentals of Adhesion*. Springer Science & Business Media, 1990.
- [100] Frederick M. Fowkes. Attractive forces at interfaces. *Industrial and Engineering Chemistry*, 56(12):40–52, 1964.
- [101] D. K. Owens and R. C. Wendt. Estimation of the surface free energy of polymers. *Journal of Applied Polymer Science*, 13(8):1741–1747, 1969.
- [102] W. Rabel. Einige Aspekte der Benetzungstheorie und ihre Anwendung auf die Untersuchung und Veränderung der Oberflächeneigenschaften von Polymeren. *Farbe und Lacke*, 77(10):997–1005, 1971.

- [103] GmbH Krüss. *Benutzerhandbuch "Drop Shape Analysis DSA1 v 1.90 für Kontaktwinkelmess-System DSA100"*. Krüss GmbH, Hamburg, 2004.
- [104] Methode nach Owens, Wendt, Rabel und Kaelble (OWRK). Homepage, Oct 2014. URL <http://www.kruss.de/de/service/schulung-theorie/glossar/methode-nach-owens-wendt-rabel-und-kaelble-owrk/>.
- [105] M. Galiazzo. Reliable double printing of ag-contacts for c-si cell manufacturing. In *2nd workshop on solar cell metallization*, Konstanz, Germany, 2010.
- [106] A.J. Bard and L.R. Faulkner. *Electrochemical Methods, Fundamentals and Application*. John Wiley & Sons, New York, 2001.
- [107] V.M. Schmidt. *Elektrochemische Verfahrenstechnik*. Wiley VCH, Weinheim, Germany, 2003.
- [108] C.C. Hamann and W. Vielstich. *Elektrochemie*. Wiley, VCH, Weinheim, Germany, 2005.
- [109] A.A. Milchev. *Electrocrystallization: Fundamentals of Nucleation and Growth*. Kluwer Academic Publishers Group, Norwell, USA, 2002.
- [110] W. Späth. Verfahren zur galvanischen Abscheidung einer Metallschicht auf der Oberfläche eines Halbleiterkörpers, 1975.
- [111] S.H. Hsieh, C.M. Chien, W.L. Liu, and W.J. Chen. Failure behavior of ITO diffusion barrier between electroplating Cu and Si substrate annealed in a low vacuum. *Applied Surface Science*, 255(16):7357 – 7360, 2009.
- [112] Ankit Khanna, Zhi Peng Ling, Vinodh Shanmugam, Matthew B. Boreland, Isao Hayashi, Daniel Kirk, Hideki Akimoto, Armin G. Aberle, and Thomas Mueller. Screen printed metallisation for silicon heterojunction solar cells. *Proceedings of the 28th European Photovoltaics Solar Energy Conference, Paris, France*, pages 1336–1339, 2013.

- [113] V. Akhavan, K. Schroder, D. Pope, I. Rawson, A. Edd, and S. Farnsworth. Reacting Thick-Film Copper Conductive Inks with Photonic Curing. Online, 2013.
- [114] Vahid Akhavan, Kurt Schroder, Dave Pope, and Stan Farnsworth. Process Thick-Film Printed Metal CuO Reduction Ink with PulseForge Tools, 2013. URL https://www.novacentrix.com/sites/default/files/files/Novacentrix%20Tech%20Coatings%200313_final.pdf.
- [115] R.A. Sinton and A.Cuevas. A quasi-steady-state open-circuit voltage method for solar cell characterization. *Proceedings of the 16th Eu-PVSEC*, pages 1152–1155, 2000.
- [116] W. Shockley. Research and Investigation of Inverse Epitaxial UHF Power Transistor. Technical report no. al-tdr-64-207, Air Force Atomic Laboratory, Air Force Systems Command, Wright-Patterson Air Force Base, Ohio, 1964.
- [117] H. Murrmann and D. Widmann. Current Crowding on Metal Contact to Planar Devices. *IEEE Trans. Electron Dev.*, ED-16: 1022–1024, Dec. 1969.
- [118] H. Murrmann and D. Widmann. Messungen des Übergangswiderstandes zwischen Metall und Diffusionsschicht in Si-Planarelementen. *Solid-State Electronics*, 12:879–86, 1969.
- [119] H.H. Berger. Models for Contact to Planar Devices. *Solid-State Electronics*, 15:145–158, Feb. 1972.
- [120] H.H. Berger. Contact Resistance and Contact Resistivity. *J. Electrochem. Soc.*, 119:507–514, April 1972.
- [121] D.P. Kennedy and P.C. Murley. A Two-Dimensional Mathematical Analysis of the Diffused Semiconductor Resistor. *IBM J. Res. Dev.*, 12:242–250, May 1968.
- [122] D.K. Schroder. *Semiconductor Material and Device Characterization*. New York: John Wiley & Sons, 1990.
- [123] R. Franke. *Simultaneous Thermal Analysis - Methods, Function principles*. Netzsch Gerätebau GmbH.

- [124] Yuning Li, Yiliang Wu, and Beng S. Ong. Facile Synthesis of Silver Nanoparticles Useful for Fabrication of High-Conductivity Elements for Printed Electronics. *Journal of the American Chemical Society*, 127(10):3266–3267, 2005.
- [125] Nikhil R. Jana and Xiaogang Peng. Single-Phase and Gram-Scale Routes toward Nearly Monodisperse Au and Other Noble Metal Nanocrystals. *Journal of the American Chemical Society*, 125(47):14280–14281, 2003.
- [126] T. C. Leung, C. L. Kao, W. S. Su, Y. J. Feng, and C. T. Chan. Relationship between surface dipole, work function and charge transfer: Some exceptions to an established rule. *Phys. Rev. B*, 68:195408, Nov 2003.
- [127] Gmelin. *Handbuch der Anorganischen Chemie*, volume 8, chapter Silber Teil 6B. 1975.
- [128] Helge Hannebauer, Tom Falcon, Rene Hesse, Thorsten Dullweber, and Rolf Brendel. 18.9 Print-on-Print Process. *Proceedings of the 26th European Photovoltaic Solar Energy Conference and Exhibition, Hamburg, Germany*, 2011.
- [129] K. Hajmrle and R Angers. Sintering study of silver particles by in situ electron microscopy. *Metallurgical Transactions*, 5(4): 817–822, 1974.
- [130] Glenn Elert. April 2015. <http://physics.info/expansion>.
- [131] Accuratus. April 2015. <http://accuratus.com/silinit.html>.
- [132] K. Tu, J.W. Mayer, and L.C. Feldman. *Electronic Thin Film Science: For Electrical Engineers and Materials Scientists*. Macmillan, 1992.
- [133] Maximilian Ludwig and Dietmar Scherff. *Optimierung von a-Si:H/c-Si-Heterostruktur-Solarzellen*. PhD thesis, Open University of Hagen, 2010.
- [134] N. Chitvoranund, S. Jiemsirilers, and D.P. Kashima. Effects of surface treatments on adhesion of silver film on glass substrate fabricated by electroless plating. *Journal of Australian Ceramics Society*, 49(1):62–69, 2013.

- [135] D. Borchert, T. Brammer, O. Voigt, H. Stiebig, A. Gronbach, M. Rinio, J. T. M. Kenanoglu, G. Willeke, H. Windgassen, W. A. Nositschka, and H. Kurz. Large area (n) a-Si:(H) (p) c-Si heterojunction solar cells with low temperature screen printed contacts. *19th European Photovoltaic Solar Energy Conference*, 2004.
- [136] R. Gogolin, M. Turcu, R. Ferré, R. Brendel, N.-P. Harder, and J. Schmidt. 730 mV Bifacial Screen Printed a-Si:H/c-Si Heterojunction Solar Cells: Open-Circuit Voltage and Fill Factor Effect from a-Si:H Layer Thickness and Front Metallization. *Proceedings of the 28th European Photovoltaic Solar Energy Conference*, 2013.
- [137] Yvonne Gassenbauer and Andreas Klein. Electronic and Chemical Properties of Tin-Doped Indium Oxide (ITO) Surfaces and ITO/ZnPc Interfaces Studied In-situ by Photoelectron Spectroscopy. *The Journal of Physical Chemistry B*, 110(10):4793–4801, 2006. PMID: 16526716.
- [138] Yvonne Gassenbauer and Andreas Klein. Electronic surface properties of rf-magnetron sputtered In₂O₃:Sn. *Solid State Ionics*, 173:141 – 145, 2004. Proceedings of EMRS Symposium K on Solid State Ionics: High Temperature vs. Low Temperature Defect Chemistry.
- [139] Y. Gassenbauer, R. Schafranek, A. Klein, S. Zafeiratos, M. Hävecker, A. Knop-Gericke, and R. Schlögl. Surface states, surface potentials, and segregation at surfaces of tin-doped in₂o₃. *Phys. Rev. B*, 73:245312, Jun 2006.
- [140] Y. Gassenbauer, R. Schafranek, A. Klein, S. Zafeiratos, M. Hävecker, A. Knop-Gericke, and R. Schlögl. Surface potential changes of semiconducting oxides monitored by high-pressure photoelectron spectroscopy: Importance of electron concentration at the surface. *Solid State Ionics*, 177:3123 – 3127, 2006. Proceedings of the E-MRS Symposium P on Solid State Ionics: Mass and Charge Transport at Various Length Scales.

- [141] P.A. Newman. *Stratospheric Ozone - An Electronic Textbook, Chapter 5*. Mai 2015. http://www.ccpo.odu.edu/~lizsmith/SEES/ozone/oz_class.htm.
- [142] C. Bischof and W. Possart. *Adhäsion - Theoretische und experimentelle Grundlagen*. Akademie-verlag Berlin, 1982.
- [143] W.M. Haynes, editor. *CRC Handbook of Chemistry and Physics*. 95th edition, 2014-2015. URL <http://www.hbcnetbase.com/>.
- [144] Jürgen Heinze, Armin Rasche, Markus Pagels, and Beate Geschke. On the Origin of the So-Called Nucleation Loop during Electropolymerization of Conducting Polymers. *The Journal of Physical Chemistry B*, 111(5):989–997, 2007. PMID: 17266253.
- [145] Yaara Tamari. *Novel Technology for Front-side Metallization of Solar Cells Using Particle-free Metal-organic Ink*. PhD thesis, University of Freiburg, 2014.
- [146] Zhuo Wang, Wenwen Wu, Qunbao Yang, Yongxiang Li, and Chang-Ho Noh. In-situ fabrication of flexible vertically integrated electronic circuits by inkjet printing. *Journal of Alloys and Compounds*, 486(1-2):706 – 710, 2009.
- [147] Xiaolei Nie, Hong Wang, and Jing Zou. Inkjet printing of silver citrate conductive ink on PET substrate. *Applied Surface Science*, 261:554–560, 2012.
- [148] K.F. Teng and R.W. Vest. Metallization of solar cells with ink jet printing and silver metallo-organic inks. *IEEE Transactions on components, hybrids, and manufacturing technology*, 11(3): 291–7, 1988.
- [149] Claudia Schoner, André Tuchscherer, Thomas Blaudeck, Stephan F. Jahn, Reinhard R. Baumann, and Heinrich Lang. Particle-free gold metal-organic decomposition ink for inkjet printing of gold structures. *Thin Solid Films*, 531(0):147 – 151, 2013.
- [150] S. Binder. Entwicklung und Evaluierung von metallorganischen Tinten zur Kontaktierung von Solarzellen. Master’s thesis, Hochschule Mannheim, 2008.

- [151] G.M. Vest and R.W. Vest. MOD Silver Metallization for Photovoltaics. Technical report, United States Department of Energy, 1985.
- [152] Yong Zhou, Jiangtao Wu, and Eric W. Lemmon. Thermodynamic Properties of o-Xylene, m-Xylene, p-Xylene, and Ethylbenzene. *Journal of Physical and Chemical Reference Data*, 41(2):023103–023103–26, 2012.
- [153] L. Smart and E. Moore, editors. *Einführung in die Festkörperchemie*. Friedrich Vieweg & Sohn Verlagsgesellschaft GmbH, Braunschweig, Wiesbaden, 2 edition, 1997.
- [154] Achim Kraft, Yutriz Pernia, Andre Kalio, Aline Gautrein, Limeng Ni, Jonas Bartsch, Stefan Glunz, and Holger Reinecke. Origin of corrosion effects in solar cell contacts during electrochemical nickel deposition. *Journal of Applied Electrochemistry*, 45(1):95–104, 2015.
- [155] A. Kraft, Y. Pernia, L. Ni, A. Filipovic, A. Hähnel, A. Graff, J. Bartsch, and M. Glatthaar. Microstructure Analysis of the Interaction between Watts-Type Nickel Electrolyte and Screen Printed Solar Cell Contacts. *ECS Journal of Solid State Science and Technology*, 3(4):Q55–Q60, 2014.
- [156] Huster F. Schubert G. and Fath P. Current Transport Mechanism in printed Ag thick film contacts to an n-type emitter of a crystalline silicon solar cell. *19th European Photovoltaic Solar Energy Conference, Paris*, 2004.
- [157] C. Ballif, D. M. Huijic, A. Hessler-Wyser, and G. Willeke. Nature of the Ag-Si interface in screen-printed contacts: a detailed transmission electron microscopy study of cross-sectional structures. *Photovoltaic Specialists Conference, 2002. Conference Record of the Twenty-Ninth IEEE*, 2002.
- [158] T. Qiu, X.L. Wu, G.G. Siu, and P.K. Chu. Intergrowth mechanism of silicon nanowires and silver dendrites. *Journal of Electronic Materials*, 35(10), 2006.
- [159] Theodor L. Chvatal. Glasses with high content of silver oxide, 1974.

- [160] Yuliy D. Gamburg and Giovanni Zangari. *Theory and Practice of Metal Eelectrodeposition*. Springer, 2011.

Danksagung

Gestrichen wegen Datenschutz

A Appendix

A.1 Theory

A.1.1 Additional data for Chapter 2

Fermi-Dirac distribution

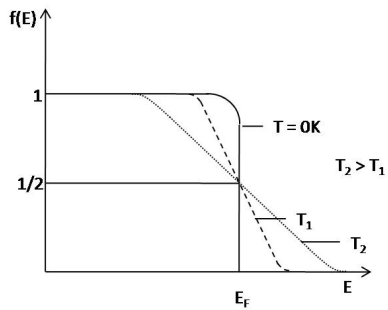


Figure A.1.1: Fermi-Dirac distribution at several temperatures

TCOs and properties

Table A.1.1: Properties relevant to TCO materials and applications (data from[31])

General criteria	Opto-electronic criteria	Processing criteria
Green materials	Visible trans- parency	Deposition tempera- tures and conditions
Green processing	Conductivity	Annealing stability
Cost	Carrier concentra- tion	Compatibility with vac- uum of non-vacuum pro- cessing
Availability	Mobility	Chemical stability
Ease of application	Infrared trans- parency	Etchability, patterning and electrical contacts
	High mobility	Interfacial chemistry and surface states
	High mobility with low carrier concen- tration	Ionic diffusion proper- ties
	Suitability to flexi- ble electronics	Temperature sensitivity
	Work function	Atmospheric sensitivity

Table A.1.2: TCO materials for various applications (data from [31])

Property application	Material		
	Simple	Binary	Ternary
Highest transparency	ZnO:F	Cd ₂ SnO ₄	
Highest conductivity	In ₂ O ₃ :Sn		
Highest plasma frequency	In ₂ O ₃ :Sn		
Highest work function	SnO ₂ :F	ZnSnO ₃	[Zn _{0.45} In _{0.88} Sn _{0.66} O ₃]
Lowest work function	ZnO:F		
Best thermal stability	SnO ₂ :F	Cd ₂ SnO ₄	
Best mechanical durability	SnO ₂ :F		
Best chemical durability	SnO ₂ :F		
Easiest to etch	ZnO:F		
Best resistance to H plasmas	ZnO:F		
Lowest deposition temperature	In ₂ O ₃ :Sn ZnO:B a-InZnO		
Least toxic	ZnO:F SnO ₂ :F		
Lowest cost TFT channel layer	SnO ₂ :F ZnO	a-InZnO a-ZnSnO	InGaO ₃ (ZnO) ₅ a-InGaZnO
Highest mobility	CdO In ₂ O ₃ :Ti In ₂ O ₃ :Mo		
Resistance to water	SnO ₂ :F		

A.1.2 Additional data for Chapter 3

Aerosol jet printing system

The aerosol can be created with a compressed air nebulizer or with an ultrasonic nebulizer. The compressed air nebulizer allows a wider range of ink characteristics (particle size and viscosity). However, this technique necessitates a virtual impactor which concentrates the created aerosol as a high aerosol density (10^{16}m^{-3}), produced with small gas flow rates (50-120 ml/min) and a mean droplet size of 1-3 μm are necessary for aerosol jet printing [35]. A schematic drawing of a pneumatic atomizer and a virtual impactor are given in Figure A.1.2.

The pneumatic impactor consists of one or more orifices which are set perpendicular to a vertical liquid feed channel within a cylindrical metallic rod. To create an aerosol, compressed gas is accelerated over the liquid feed channel, and due to the Venturi effect, ink is pressed into the channel where the ink is atomized by the gas stream. Most of the created aerosol, especially large droplets, impact at the wall of the jar and is recollected.

The created droplets which are transported by the gas flow, now have to pass the virtual impactor to reduce the transport gas flow (which is too high for deposition), separate bigger droplets from smaller ones and concentrate the aerosol. The virtual impactor, as shown in Figure A.1.2, consists of two oppositely directed funnels, also called jets. Those jets are separated by a small gap. The jet diameter and the gap size define the particle or droplet separation. Larger droplets with a higher inertial momentum follow the main gas stream and overcome the gap. Smaller particles and the excess gas (atomization gas) are guided out of the system. The two jets are encapsulated in a vacuum chamber and a pump helps separating the atomizing gas from the aerosol. The remaining concentrated aerosol is forwarded into the deposition head, which is schematically shown in Figure A.1.3.

The print head consists of two interconnected tubes. The aerosol stream is guided through the inner tube while a so called sheet gas flows inside the outer tube. The sheet gas envelopes and focuses the aerosol jet and keeps it from touching the wall. A narrow jet exits the tip of the nozzle and gets deposited on the substrate. The ratio of aerosol gas to sheet gas influences the jet diameter.

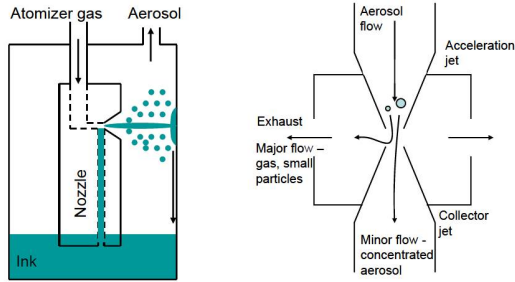


Figure A.1.2: Schematic drawing of a pneumatic impactor (left) and a virtual impactor (right)[35]

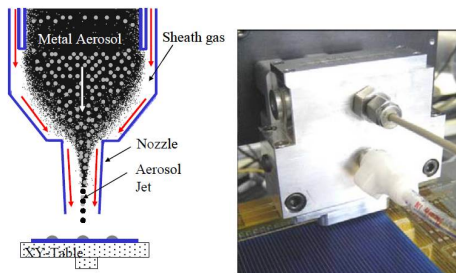


Figure A.1.3: Scheme of aerosol printing head (left) and photograph of 10 nozzle print head as used at Fraunhofer ISE (right) [35]

B Appendix

B.1 Measurements

B.1.1 Additional data for Chapter 5

TG-DSC measurement

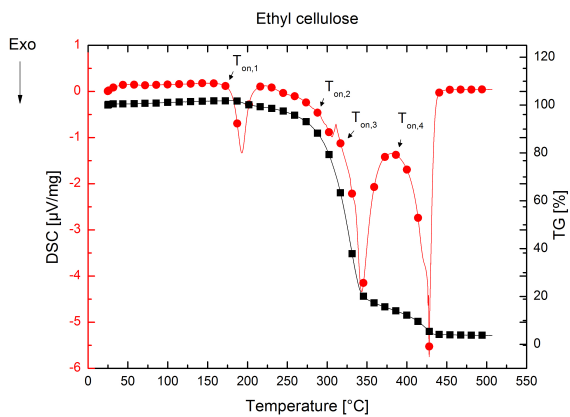


Figure B.1.1: TG-DSC measurement of EC

Illustrations



Figure B.1.2: Linkam TS 1500

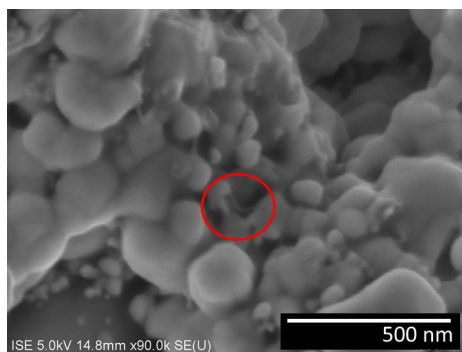


Figure B.1.3: SEM image of nanoparticles in ink formulation sintered in HCl vapor and treated at 200 °C for 15 min: Organic residues

B.1.2 Additional data for Chapter 7

Electric double layer on electrodes in electrolyte solutions [106]

The *inner plane* of an electrolyte closest to the electrode contains solvent ions and ions, which are said to be *specifically adsorbed*. This layer is also called the *Helmholtz layer* or *Stern layer*. The locus of the electrical center of the specifically adsorbed ions is called the *inner Helmholtz plane* (IHP) and is located at a distance χ_1 . The total charge density of ions in this plane is σ^i [$\mu\text{C}/\text{cm}^2$]. Solvated ions can only approach the metal surface to a distance χ_2 . The electrical center of the solvated ions forms the *outer Helmholtz plane* (OHP). The solvated ions can only interact through long distance ranged electrostatic forces and are therefore independent on the chemical properties of the ions. These ions are also called *nonspecifically absorbed*. Thermal agitation causes the nonspecifically adsorbed ions to be distributed in a volume reaching into the bulk of the solution. This volume is called *diffuse layer*. The diffuse layer has a total charge density of σ^d . The thickness of the diffuse layer depends on the ion concentration.

The Helmholtz layer significantly influences the redox reactions at the electrodes and thus the reduction of metal ions on the metal surface.

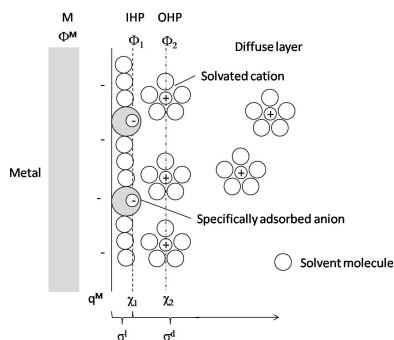


Figure B.1.4: Illustration of Helmholtz-plane. M = Metal, ϕ = Electrostatic potential, *IHP* = Inner Helmholtz plane, *OHP* = Outer Helmholtz plane, q = charge, χ = Distance, σ = charge density (retraced from [106])

B.1.3 Additional data for Chapter 8

Additional TG-DSC data

Table B.1.1: Measured and theoretical mass loss of metal organyl and MOD ink decomposition

Compound	Mass loss measured [%]	Theoretical mass loss [%]
Zinc neodecanoate	86.3	84.0
Bismuth neodecanoate	80.4	71.1
Silver neodecanoate	58.3	61.3
MOD ink solid content 26 wt%	78.10	74.0

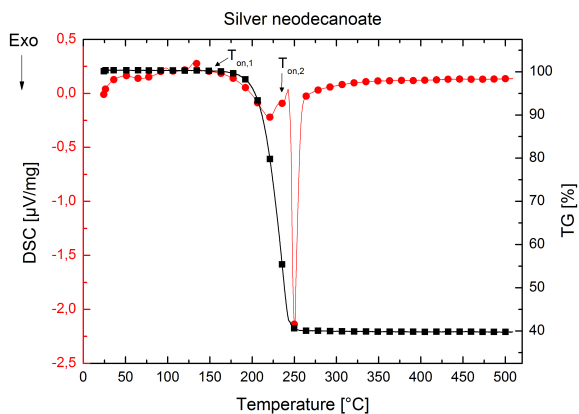


Figure B.1.5: TG-DSC measurement of silver neodecanoate.
 $T_{on,1} = 152 \text{ }^{\circ}\text{C}$, $T_{on,2} = 246 \text{ }^{\circ}\text{C}$ $\Delta m = -60.5 \text{ } \%$

The mass loss determined by TG measurement is given in Table B.1.1. The theoretical loss in case of total decomposition and evaporation of solvent is also given.

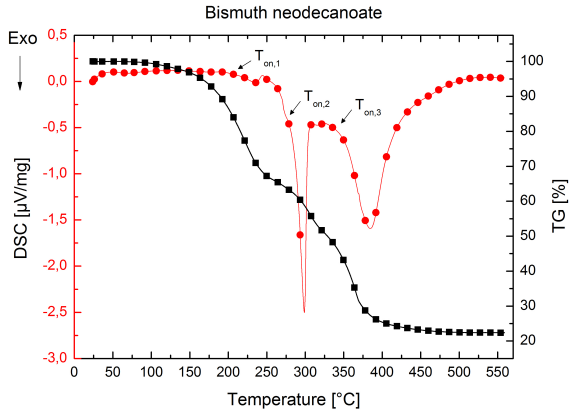


Figure B.1.6: TG-DSC measurement of bismuth neodecanoate. $T_{on,1} = 215$ °C, $T_{on,2} = 286$ °C, $T_{on,3} = 355$ °C, $\Delta m_1 = -34.3$ %, $\Delta m_2 = -14.3$ %, $\Delta m_3 = -29.0$ %, $\Delta m_{ges} = -77.6$ %

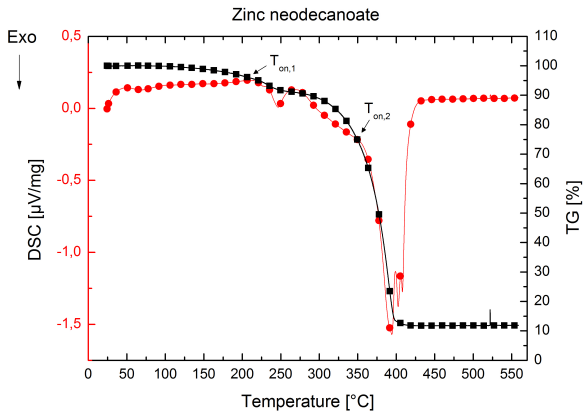


Figure B.1.7: TG-DSC measurement of zinc neodecanoate. $T_{on,1} = 198$ °C, $T_{on,2} = 371$ °C, $\Delta m_1 = -9.2$ %, $\Delta m_2 = -78.3$ %, $\Delta m_{ges} = -87.5$ %

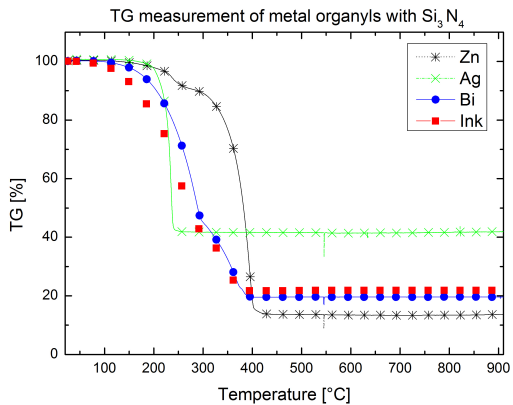


Figure B.1.8: TG measurement of reaction of metal organyls and MOD ink with Si_3N_4

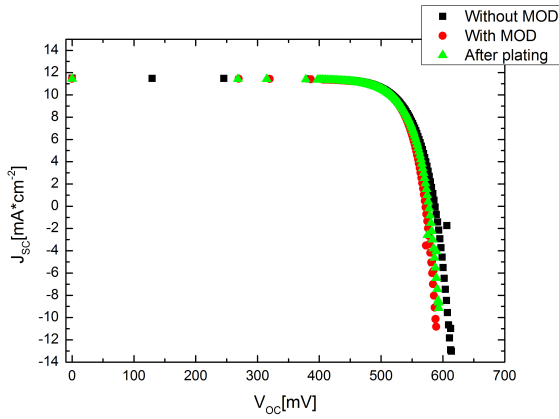
Additional SEM data regarding tempering temperature evaluation

Figure B.1.10: Suns V_{OC} measurements of cell batch metallized with MOD ink and LIP plating before MOD ink application and curing, after MOD curing and after LIP plating.

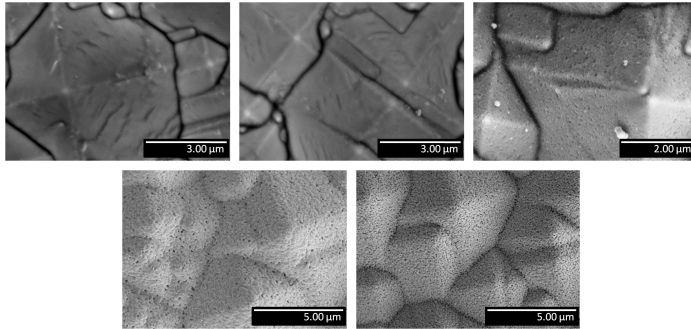
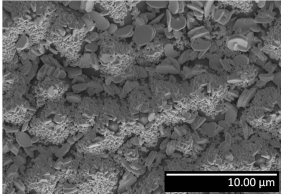
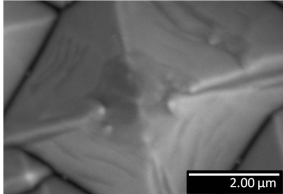


Figure B.1.9: MOD ink on SiN_x coated wafer tempered for 5 on a hot plate

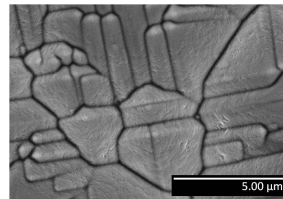
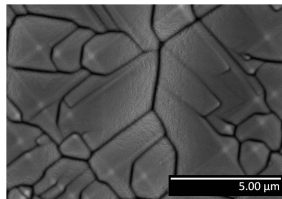
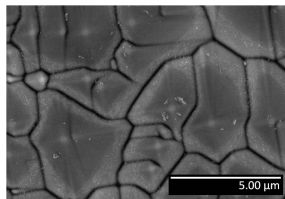
Top row left: 350 °C - no etching of SiN_x layer; middle: 400 °C - few Ag residues, no visible etching. Right: 500 °C - pores in SiN_x visible comparable to etching at 450 °C (Figure 8.3.11); Bottom row left: Closed silver layer at tempering at 450 °C before etch back. Right: Closed silver layer at tempering at 500 °C before etch off (note different scales!)

Additional SEM data regarding bismuth - to silver neodecanoate ratio

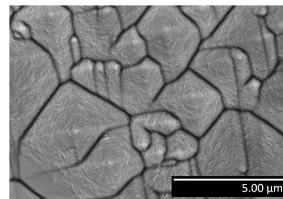
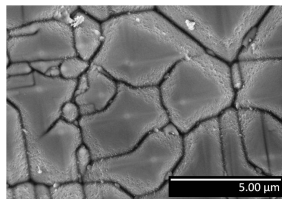
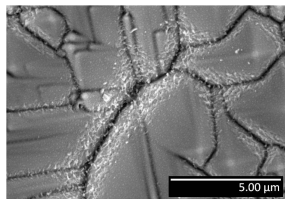
Table B.1.2: Proportions and SEM images of Bi-/Ag-neodecanoate variation on SiNx images after HNO treatment show glass formation on wafer surface (middle); images after HF treatment show wafer surface with etched SiNx layer and silver-bismuth-residues (right)

Bi-neo/Ag- neo [wt%/wt%] ([mol:mol])	after HNO ₃ (480 °C)	after HF (480 °C)	after HF (520 °C)
1:0 (1:0)			

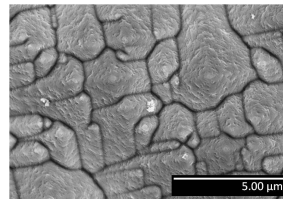
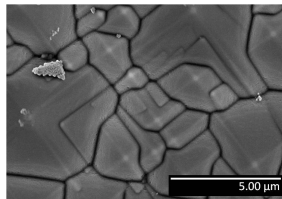
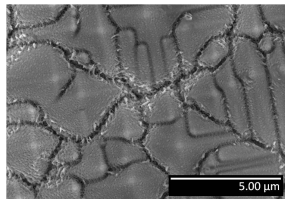
9:1
(3.5:1)



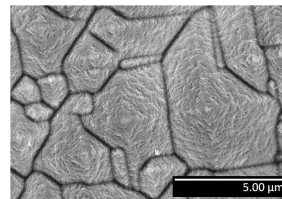
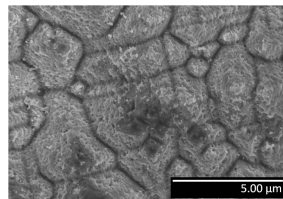
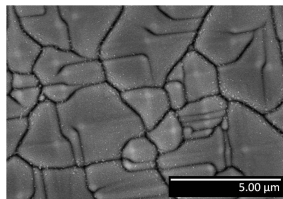
4:1
(1.6:1)



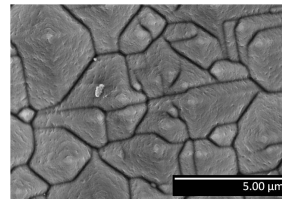
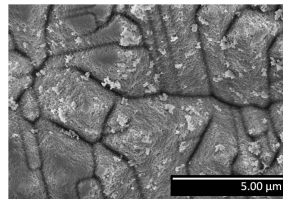
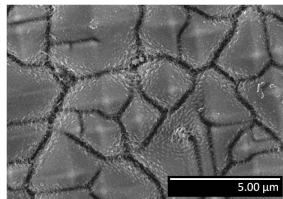
2:1
(1:1.4)



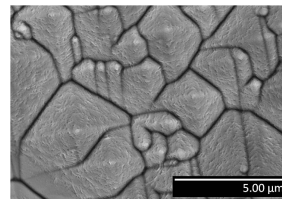
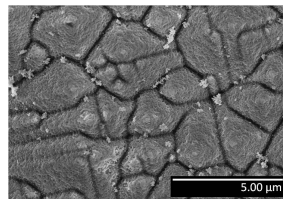
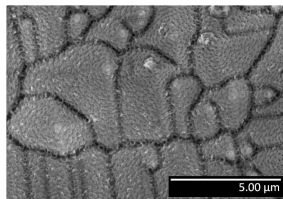
1:1
(1:2.6)



1:2
(1:5)



1:4
(1:11)



1:9
(1:23)

